

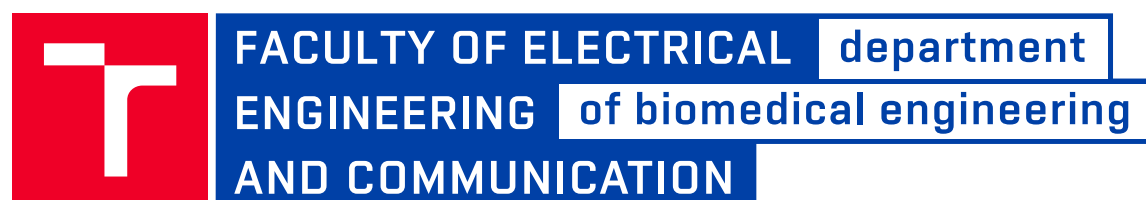
QUANTITATIVE PERFUSION IMAGING USING
ULTRASONOGRAPHY AND MRI

HABILITATION THESIS

AUTHOR

Ing. RADOVAN JIŘÍK, Ph.D.

BRNO 2022



QUANTITATIVE PERFUSION IMAGING USING
ULTRASONOGRAPHY AND MRI

KVANTITATIVNÍ ZOBRAZOVÁNÍ PERFUZE POMOCÍ
ULTRASONOGRAFIE A MRI

HABILITATION THESIS
HABILITAČNÍ PRÁCE

AUTHOR
AUTOR PRÁCE

Ing. RADOVAN JIŘÍK, Ph.D.

BRNO 2022

ACKNOWLEDGEMENT

I would like to thank my wife Hanka and our family for their patience and support. I am especially very grateful to my mentor and good friend, prof. Torfinn Taxt, for his guidance and support both on the personal and professional level. I would also like to thank my colleagues who have been precious members of our "perfusion" team: my (now former) Ph.D. students Michal Bartoš, Martin Mézl, Jiří Kratochvíla, Ondřej Macíček, Lucie Krátká and Lenka Dvořáková, my dear colleagues Olivier Keunen, Zenon Starčuk, jr. and Pavel Rajmic, my medical-doctor colleagues Michal Standara, Kim Nylund, Odd Helge Gilja, and many others who have directly and indirectly contributed to our work, especially my colleagues at Institute of Scientific Instruments, Czech Academy of Sciences and at Department of Biomedical Engineering, Brno University of Technology.

Brno

.....

(author's signature)

CONTENTS

List of symbols, physical constants and abbreviations	11
Introduction	13
1 Theory of perfusion imaging	15
1.1 Short history overview	19
1.2 Basic pharmacokinetic models	22
1.2.1 Models for non-diffusible contrast agents	24
1.2.2 Models for diffusible contrast agents	26
1.3 Main problems	29
2 Contribution of the author's team	31
2.1 Ultrasound perfusion imaging	31
2.2 MR perfusion imaging	33
3 Conclusions	35
Bibliography	39
4 Selected journal papers	49
4.1 Ultrasound perfusion imaging	49
4.1.1 Paper I	49
4.1.2 Paper II	61
4.2 MR perfusion imaging	72
4.2.1 Paper III	72
4.2.2 Paper IV	84
4.2.3 Paper V	96
4.2.4 Paper VI	110

LIST OF FIGURES

1.1	Perfusion-imaging process. Example images from MR perfusion imaging of tumor-bearing mice, axial slice, tumor (hyper-intense contrast-agent-uptaking area in the upper right area of images) located in the flank of the hind limb.	16
1.2	Schematic of a perfusion unit assumed by pharmacokinetic models.	22

LIST OF TABLES

1.1	Overview of the most usual perfusion parameters.	17
1.2	Perfusion parameters estimated using different pharmacokinetic models. Primary perfusion parameters – one of possible choice of model parametrization (shows the number of unknown parameters of the given model), derived perfusion parameters – remaining perfusion parameters that can be derived from the primary perfusion parameters.	24
1.3	Pharmacokinetic models for non-diffusible contrast agents.	26
1.4	First-generation pharmacokinetic models for diffusible contrast agents.	27
1.5	Second-generation pharmacokinetic models for diffusible contrast agents.	28

LIST OF SYMBOLS, PHYSICAL CONSTANTS AND ABBREVIATIONS

2CX	2-compartment exchange (model)
AIF	arterial input function
ASL	arterial spin labeling
ATH	adiabatic approximation of the tissue homogeneity (model)
CT	computed tomography
DCATH	distributed-capillary adiabatic tissue homogeneity (model)
DCE-MRI	dynamic contrast-enhanced magnetic resonance imaging
DCE-US	dynamic contrast-enhanced ultrasonography
DP	distributed-parameter (model)
DSC-MRI	dynamic susceptibility contrast-enhanced magnetic resonance imaging
EES	extravascular extracellular space
GCTT	Gamma Capillary Transit Time (model)
IVIM	intravoxel incoherent motion
IRF	impulse residue function
MR	magnetic resonance
MRI	magnetic resonance imaging
PET	positron emission tomography
ROI	region of interest
SNR	signal-to-noise ratio
SPECT	single-photon emission computed tomography
TH	tissue-homogeneity (model)

INTRODUCTION

The word *perfusion* describes, in general, the passage of a fluid through natural channels in a tissue. In the most cases, this general meaning is narrowed to blood, and perfusion is understood as circulation of blood through tissues. The topic of this habilitation thesis, perfusion imaging, relates to methods providing parameters describing perfusion. Examples of such perfusion parameters are blood flow, blood volume, vessel-wall permeability expressed per unit mass or unit volume of tissue. These parameters describe the physiological state of the tissue on the microvascular level. They are important biomarkers in many clinical and biological applications. Perfusion imaging is important especially in oncology, where it provides a noninvasive way to early identification of tumor types. Furthermore, it provides an early-stage insight into the efficacy of tumor treatment since the reaction to tumor treatment is much faster on the microvascular level expressed by perfusion parameters (days to weeks) than on the macroscopic level expressed by standard anatomical images (months). That means that perfusion imaging can give a substantially earlier evaluation of the treatment process than the standard criteria based on measurements of tumor volume from anatomical images. Hence, such early evaluation of the treatment response is a key to qualified decisions on the treatment strategy, which can ultimately prolong or safe lives and substantially decrease health-care costs.

Perfusion imaging is a valuable tool also in preclinical research, especially in testing of new treatment strategies on animals (e.g. antiangiogenic treatment in oncology) and drug-delivery paths (e.g. drug delivery through the blood brain barrier in neurology).

However, in many applications, current perfusion imaging methods are not sufficiently reliable for routine clinical use, where they remain mostly at the experimental level, although their principles have been known for several decades.

The topic of perfusion imaging is a unique multidisciplinary field. It combines the physics of the image acquisition processes, knowledge of physiology and mathematics needed for understanding and modeling of the perfusion process, as well as the field of signal and image processing needed for image reconstruction and image pre- and post-processing. An important part of pharmacokinetic-model fitting in perfusion imaging is also understanding of approaches to inverse problem solving. Furthermore, identification of relevant applications for perfusion imaging and management of the examined subjects (patients, animals), as well as interpretation of the results often requires medical, veterinarian or biological expertise. This multidisciplinary character of perfusion imaging is one of the reasons of the author's enthusiasm

for this field. The combination of the above mentioned disciplines overlaps very well with the curriculum taught at the Department of Biomedical Engineering at Brno University of Technology. The author has introduced perfusion imaging, to a smaller or larger extent, into several courses, including Biological system modeling, Models in Biology and Epidemiology, Systems Biology, Traditional Medical and Ecological Imaging Systems and Imaging Systems with Nonionizing Radiation.

The research and teaching activity of the author in the field of perfusion imaging started in 2004 as a natural continuation of the cooperation with prof. Torfinn Taxt at University of Bergen, Norway, and his colleagues. The know-how in this field was gradually gained from the Norwegian partners and extended further, mainly in frame of research projects including colleagues from the Institute of Scientific Instruments of the Czech Academy of Sciences, Department of Biomedical Engineering at Brno University of Technology, the author's bachelor, master and doctoral students, as well as colleagues from the cooperating institutes.

The thesis is written as a collection of selected journal papers with an introduction. The introduction is meant as an explanation of the perfusion imaging field, starting with a general description, which is gradually narrowed down to ultrasound and magnetic-resonance (MR) perfusion imaging and their specifics. Furthermore, the focus is put on the specific topics where the author sees the main contribution of his group.

1 THEORY OF PERFUSION IMAGING

Most perfusion imaging methods, including the class of methods related to the focus of the author's group, are based on intravenous administration of a contrast agent and imaging of the tissue of interest before, during and after the administration. The recorded image sequence is subsequently processed. Contrast agents are sometimes referred to as indicators or tracers. The word indicator refers to a substance introduced into a physiological system that can be detected and give information about the system. A tracer is a type of indicator that has the same chemical structure as a systemic substance of interest [1].

For these techniques, the process of perfusion imaging can be divided into the following parts (Fig. 1):

- Data acquisition – acquisition of raw image data upon contrast-agent administration.
- Image-sequence reconstruction – reconstruction of an image sequence from the acquired raw image data.
- Preprocessing – e.g. motion correction due to cardiac and/or respiration, noise suppression.
- Conversion from image intensity to contrast-agent concentration.
- Extraction of contrast-agent concentration curves from the converted image sequence – for each voxel of interest or for each region of interest (ROI); in the following text, the term ROI will be used, without a loss of generality, for the case of single voxels or a set of voxels belonging to a presumably homogeneous tissue.
- Pharmacokinetic-model fitting – In quantitative perfusion-imaging methods, a pharmacokinetic model is then fitted to these contrast-agent concentration curves. The estimated parameters of the model and their combinations are the sought perfusion parameters of the given ROI (see Tab. 1.1 below for a list of perfusion parameters).
- Visualization, interpretation – e.g. perfusion-parameter maps overlaid over an anatomical image; followed by interpretation of the results, possibly classification.

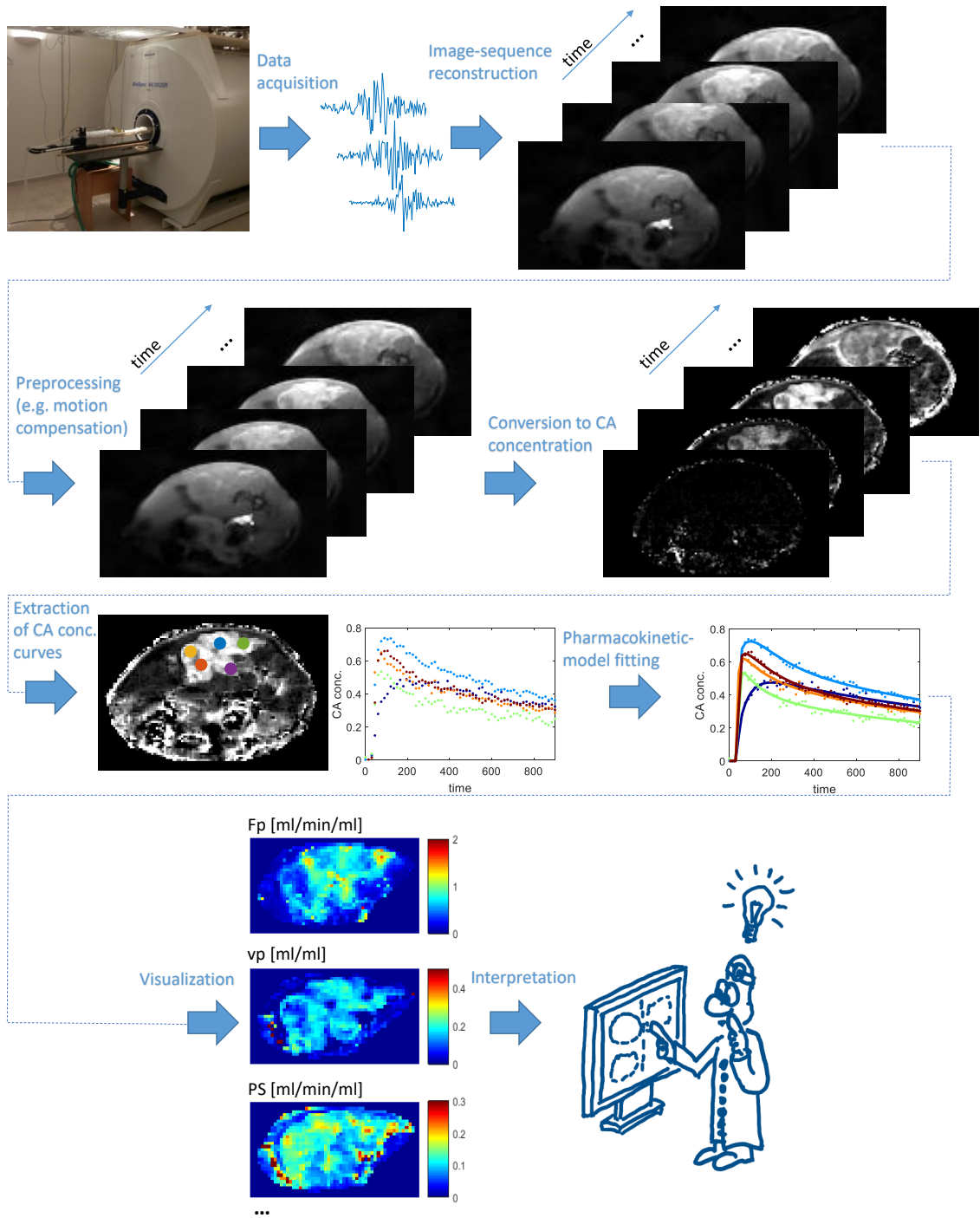


Fig. 1.1: Perfusion-imaging process. Example images from MR perfusion imaging of tumor-bearing mice, axial slice, tumor (hyper-intense contrast-agent-uptaking area in the upper right area of images) located in the flank of the hind limb.

Quantity	Description	Unit
F_p	Plasma flow	ml/min/ml
F_b	Blood flow	ml/min/ml
PS	Permeability-surface area product (measure of vessel-wall "leakiness" for the contrast agent)	ml/min/ml
v_p	Plasma volume	ml/ml
v_b	Blood volume	ml/ml
v_e	Volume of the extravascular extracellular space (EES)	ml/ml
E	Extraction fraction (fraction of contrast-agent particles that are extracted into the interstitium)	-
T_c	Capillary mean transit time (average time needed for a contrast-agent particle to pass through the perfusion unit)	min
K^{trans}	Volume transfer constant (compound parameter: $K^{trans} = EF_p$)	1/min
k_{ep}	Interstitial-to-plasma rate constant (compound parameter: $k_{ep} = EF_p/v_e$)	1/min
σ, α	Parameters describing the the statistical distribution of the capillary transit times (used in DCATH and GCTT models, σ, α capture the structure of the microvessels)	min, -
BAT	Bolus arrival time (delay between the global AIF and the local perfusion-unit-specific local AIF)	min

Tab. 1.1: Overview of the most usual perfusion parameters.

To narrow down the scope of this text, it is important to mention also perfusion-analysis methods that are not in focus of our work and will not be considered in the following sections. In one group of these methods, only so called semi-quantitative parameters of the contrast-agent concentration curves are estimated, without proper pharmacokinetic modeling of their course. Such semi-quantitative perfusion parameters are for example slope of the initial rising phase of the contrast-agent inflow or the area under the curve within some time window. Several semi-quantitative approaches to perfusion imaging are based on models of contrast-agent concentration curves that are fitted to the measured data. Some of these models might be denoted as pharmacokinetic models as they describe mathematically the physiology of the vascular system. For example the gamma-variate model [2, 3] is related to a series of compartments¹ that represent neighboring sections of the vascular system. Other such pharmacokinetic models are for example the lagged-normal [4, 3], the Local Density Random Walk (LDRW) and the First Passage Time (FPT) models [5, 3]. Use of these models is typical for perfusion imaging using ultrasonography. The problem of this approach is that they describe the shape of the contrast-agent bolus and the whole vascular system from the location of bolus administration to the tissue ROI. This means that the estimated parameters of these models depend not only on the tissue ROI but also on the bolus-administration procedure and on the physiology of the arterial tree proximal to the tissue ROI. This makes these methods hardly reproducible and comparable among different imaging centers.

An even more simplistic approach, falling also into the field of *perfusion imaging*, includes only the acquisition part. The acquired image sequence is then visually (subjectively) assessed without any modeling or estimation of semi-quantitative parameters.

Both the semi-quantitative and visual approaches are not in the focus of our work as they depend on the used contrast agent, its administration, the imaging device itself, the acquisition setup and the operator (in the latter case). The trend in modern medical imaging is to use an imaging device not as a "snapshot camera", but rather as a measuring apparatus that can measure selected biomarkers, in physical units, independently of the acquisition details and vendors of the used devices. Use of such user- and vendor-independent quantitative imaging methods minimizes the subjectivity of radiographer's decision and allows for multicentric studies. Thus, only the quantitative approaches (based on pharmacokinetic modeling allowing separation of the administered bolus shape and the properties of the proximal

¹In pharmacokinetics, a compartment is an idealized well-mixed volume with homogeneous concentration of the observed substance.

arterial tree from the perfusion properties of the tissue ROI) have been in focus of our work, hence the name *quantitative* in the title of the thesis. Thus, the following text deals only with the quantitative perfusion imaging methods.

A plethora of perfusion imaging approaches exist. They vary based on

- the contrast-agent administration method (e.g. bolus, dual-bolus, infusion),
- imaging modality (e.g. positron emission tomography, computed tomography, MR imaging), the selected acquisition method and its setup,
- method for conversion from image intensity to contrast-agent concentration,
- pharmacokinetic model,
- approach to model fitting,
- other specifics related to the application, e.g. acquisition synchronized with cardiac and sometimes respiration activity, together with the subsequent image registration is needed for cardiac applications.

Perfusion imaging methods should not be confused with flow velocity imaging where blood velocity and flow is measured in big vessels using e.g. Doppler ultrasonography or MR velocity imaging techniques. In perfusion imaging, perfusion parameters are measured on the microvascular level the extents of which are far lower than the spatial resolution achievable with standard medical imaging modalities. The perfusion parameters refer to average quantities within the ROI (e.g. a voxel), for example average blood volume within the ROI.

1.1 Short history overview

Measuring of perfusion started in nuclear medicine in early 1960s as a preclinical (i.e. applicable to laboratory animals) measurement method. It was based on administration of radioactive microspheres (preferably by a catheter as a bolus into left atrium or left ventricle). After the first passage through the vasculature, the microspheres remained trapped in the arterioles or capillaries. Subsequently, the animals were sacrificed and tissue samples harvested. Then, the number of microspheres was measured using scintigraphy. [6, 7]

The first application of radiolabeled microspheres in man for assessment of perfusion was done in 1964 by Wagner et al. [8] where albumin-based microspheres were used for assessment of pulmonary blood flow. The radioactivity was originally detected by rectilinear scanners (a radiation detector physically moved over the surface of the patient), later replaced by gamma cameras in late 1960s.

From 1990s, use of radiolabeled microspheres in preclinical quantification of perfusion was partly substituted by use of fluorescent microspheres [9].

Perfusion imaging based on radiolabeled substances developed further. Planar imaging was replaced by tomographic imaging, namely by single-photon emission computed tomography (SPECT) and later by positron emission tomography (PET). For routine clinical practice, SPECT was introduced in the late 1980s [10]. PET imaging is a more expensive and technologically more complex imaging modality with shorter-lived and less easily obtainable radioisotopes than in SPECT imaging. PET has been considered to be a research tool for a long time. Compared to SPECT, PET provides higher spatial resolution and allows for smaller radioactive doses [11]. The most SPECT and PET perfusion imaging methods rely on static cumulative (uptake) images acquired after the radiotracer has accumulated in the tissue. In contrast to radiolabeled microspheres mentioned above, the SPECT/PET radiotracers do not accumulate intravascularly but extravasate and take part in metabolic changes in the cells [11].

Later, absolute quantification of blood flow has been pursued, especially using PET with the $H_2^{15}O$ tracer. This approach is based on dynamic imaging acquired before, during and after administration of the tracer and application of pharmacokinetic models to the acquired image sequences in the postprocessing step [12]. The pharmacokinetics-based $H_2^{15}O$ PET perfusion imaging has become gold standard in myocardial perfusion imaging [10, 11]. These pharmacokinetics-based techniques are closely related to the focus of the author's research group.

Computed Tomography (CT) perfusion imaging is based on intravenous administration of an iodinated contrast agent and dynamic CT scanning, followed by pharmacokinetic modeling of the acquired image sequences, similarly to $H_2^{15}O$ PET perfusion imaging mentioned above. The basics of CT perfusion imaging were laid down in 1979 [13] and 1980 [14] (before $H_2^{15}O$ PET perfusion imaging). However clinical application, mainly in acute-stroke and tumor patients, came much later.

Perfusion imaging in magnetic resonance is a term referring to several groups of methods. The first group is based on administration of an exogenous contrast agent, similarly to CT and PET/SPECT mentioned above. The most MR contrast agents are chelates of gadolinium. Their concentration is related to shortening of T_1 , T_2 and T_2^* relaxation times. Depending on the measured relaxation time, the contrast-agent based methods are further categorized into *Dynamic Contrast-Enhanced (DCE) Magnetic Resonance Imaging (MRI)* (based on T_1 -weighted image sequences) and *Dynamic Susceptibility Contrast-enhanced (DSC) MRI* (based on T_2 - or T_2^* -weighted

image sequences).

The basics of DSC-MRI date back to late 1980th when Villringer et al. [15] used a gadolinium-based contrast agent on rats (in brain) and showed contrast-agent curves related to concentration and suggested their use for perfusion imaging. DSC-MRI on human became reality in the 1990th [16, 17, 18]. The main application of DSC-MRI has been stroke imaging where it provides, in combination with diffusion-weighted MRI, identification of the so called penumbra – the potentially salvageable brain tissue.

DCE-MRI started in early 90th, with applications in cardiology [19] (myocardium perfusion of an isolated rat’s heart and of healthy human subjects in vivo), neurology [20, 21, 22] (assessment of blood-brain-barrier permeability in multiple-sclerosis and brain-tumor patients). The main domain of DCE-MRI has been tumor imaging.

Another group of MR-perfusion-imaging methods does not require application of any exogenous contrast agent. These methods rely on an endogenous contrast agent being blood. In this case, blood is labeled ”magnetically” by the MR scanner’s coil system, i.e. by a defined modification of the magnetic moment of the blood flowing to the regions of interest. These so called Arterial Spin Labeling (ASL) methods are known since 1992 [23] and have become very popular, partly also in the clinics in the recent decade. Another MR perfusion imaging method with no need for an exogenous contrast agent is the Intravoxel Incoherent Motion (IVIM) technique, known from 1986 [24]. It is related to diffusion MRI as blood flow mimics a water-molecule diffusion process. The ASL and IVIM techniques are out of the scope of this text.

Ultrasound perfusion imaging (Dynamic Contrast-Enhanced Ultrasonography – DCE-US) is also based on administration of an exogenous contrast agent. Ultrasound contrast agents are gas-filled microbubbles of the size of several micrometers. The contrast mechanisms have been known from 1968 [25]. Ultrasound contrast agents were commercially available since 1991 (Echovist, Bayer Shering Pharma AG). Nonlinear properties of microbubbles are used in various contrast imaging modes of ultrasonographs. The main domain of contrast agent use in ultrasonography is cardiology where it has been used for better delineation of the heart cavities. There are two main approaches in ultrasound perfusion imaging: bolus tracking and burst-replenishment.

Bolus-tracking methods are similar to the above mentioned $H_2^{15}O$ PET, CT and DCE/DSC-MRI perfusion imaging methods based on administration of a contrast-agent bolus. Bolus-tracking ultrasound perfusion imaging has been first used in

2000 for assessment of myocardial perfusion [26] and in brain perfusion [27].

Burst-replenishment methods assume continuous infusion of a contrast agent with intermittent applications of high-energy ultrasound pulses which destroy the microbubbles in the imaging plain. The following replenishment of the contrast agent is imaged and analyzed. Burst-replenishment ultrasound perfusion imaging has been first reported in 1998 for myocardial perfusion [28].

1.2 Basic pharmacokinetic models

In this section, pharmacokinetic modeling as the core of perfusion imaging will be shortly described. In pharmacokinetic modeling, a tissue ROI is treated as a perfusion unit with an arterial input, venous output and the microvascular segment in between (Fig. 1.2). Only tissue ROIs with small vessel size are assumed so that the vessels can be viewed as a statistical set of randomly organized structures [29]. This limits the vessel size to the maximum diameter of several hundreds μm , corresponding to small arteries, arterioles, capillaries², venules and small veins [30].

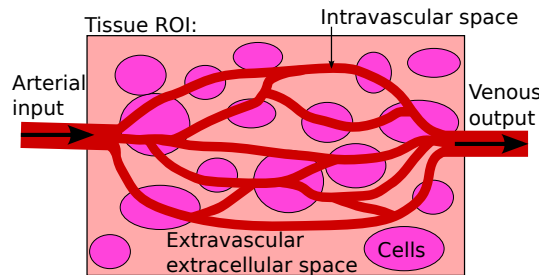


Fig. 1.2: Schematic of a perfusion unit assumed by pharmacokinetic models.

The ROI consists of the intravascular and the extravascular extracellular space (EES)³ and the intracellular space. As this text is focused on ultrasonography- and MRI-based perfusion imaging, only the contrast agents used with these modalities will be considered further on. Ultrasound contrast agents remain only in the intravascular space, due to their large size on the order of micrometers, and do not diffuse through the vessel wall. Hence the term *non-diffusible contrast agents*. Thus, only the intravascular space needs to be modeled in this case.

²A specific case is DSC-MRI based on T_2 -weighted acquisition which is sensitive predominantly to the signal from capillaries but not from larger vessels; this property is related to the nature of the acquisition process.

³This term is used in literature on perfusion imaging, although it is not accurate, as it could also include other volumes which are not captured by the pharmacokinetic models, such as lymphatic vessels, brain ventricles, etc. – the term interstitial space would be more appropriate.

On the other hand, MR contrast agents are much smaller and extravasate to the EES. Thus, MR contrast agents are referred to as *diffusible contrast agents*. It is also a known fact that MR contrast agents do not diffuse further into the cells. Hence, in MR perfusion imaging the intravascular space and the EES are modeled. An exception is brain imaging with intact blood brain barrier, which makes the vessel wall impermeable also for MR contrast agents. This is mostly the case of DSC-MRI in stroke.

A perfusion unit, described using a pharmacokinetic model, is assumed to be a linear stationary system [31]. An "input signal" of the modeled perfusion unit is the so called *Arterial Input Function* (AIF). It is the arterial input in Fig. 1.2, i.e. the time course of the contrast-agent concentration in the arterial input of the ROI. As the intravascular distribution volume, accessible to the contrast agent, is blood plasma, AIF is usually expressed as the contrast-agent concentration in plasma, $c_p(t)$. In the most perfusion imaging techniques, the AIF is assumed to be known, either from literature (population-based models) or from a measurement in some large artery (see below).

A straightforward interpretation of Fig. 1.2 assigns the output of the perfusion unit to the time course of the contrast-agent concentration in the venous output, $c_v(t)$. However, this signal is not accessible for measurement (as the size of these single draining vessels is far below the achievable spatial resolution). However, it is instructive to stay at this formulation of the system's output. In this case, the output is given as

$$c_v(t) = F_p(c_p * h)(t). \quad (1.1)$$

The scaling constant F_p is flow of blood plasma (defined as plasma flow per unit tissue volume), see Tab. 1.1 for overview of perfusion parameters. The symbol $*$ is time-domain convolution, The function $h(t)$ is the so called *transport function*. In the theory of systems, $h(t)$ is the perfusion-unit's impulse response function. Another interpretation of $h(t)$ is the probability distribution of contrast-agent-particle transit times. The expectation of $h(t)$ is the mean transit time of contrast-agent particles through the perfusion unit. The function $h(t)$ acts as a propagator through the perfusion unit. [31]

In perfusion imaging, the measured signal, i.e. the "output signal" of the perfusion unit, is the time course of the contrast-agent concentration within the tissue ROI, $c_t(t)$, not in its venous output $c_v(t)$. Hence, the impulse response of the perfusion unit is referred to as *Impulse Residue Function* (IRF), $R(t)$ [31], sometimes also called impulse response function. It is interpreted as the probability that the contrast-agent particle is present in the perfusion unit at time t following an instantaneous bolus of the contrast agent at the arterial input (Dirac-pulse AIF)

at time $t = 0$. From the definition, it follows that the IRF is a non-increasing function satisfying $R(t = 0) = 1$. It is related to the transport function as follows:

$$R(t) = 1 - \int_0^t h(\tau) d\tau. \quad (1.2)$$

The contrast-agent concentration within the tissue unit is then expressed as

$$c_t(t) = F_p(c_p * R)(t). \quad (1.3)$$

This is the basic pharmacokinetic model used in perfusion-imaging literature. The pharmacokinetic models differ based on the form of $R(t)$. In the following text, different formulations of the IRF, $R(t)$, will be reviewed. The perfusion parameters accessible using the different pharmacokinetic models are summarized in Tab. 1.2.

Model	Primary perfusion parameters	Derived perfusion parameters
Non-diffusible models		
Nonparametric	F_p, v_p	T_c
Compartment	F_p, v_p	T_c
Plug-flow	F_p, v_p	T_c
Diffusible models, 1st generation		
Tofts	K^{trans}, v_e	k_{ep}
Extended Tofts	K^{trans}, v_e, v_p	k_{ep}
Patlak	K^{trans}, v_p	-
Diffusible models, 2nd generation		
2CX	F_p, v_p, v_e, PS	$T_c, E, K^{trans}, k_{ep}$
TH	F_p, v_p, v_e, PS	$T_c, E, K^{trans}, k_{ep}$
ATH	F_p, v_p, v_e, PS	$T_c, E, K^{trans}, k_{ep}$
DP	F_p, v_p, v_e, PS	$T_c, E, K^{trans}, k_{ep}$
DCATH	$F_p, v_p, v_e, PS, \sigma$	$T_c, E, K^{trans}, k_{ep}$
GCTT	$F_p, v_p, v_e, PS, \alpha$	$T_c, E, K^{trans}, k_{ep}$

Tab. 1.2: Perfusion parameters estimated using different pharmacokinetic models. Primary perfusion parameters – one of possible choice of model parametrization (shows the number of unknown parameters of the given model), derived perfusion parameters – remaining perfusion parameters that can be derived from the primary perfusion parameters.

1.2.1 Models for non-diffusible contrast agents

Some perfusion-imaging methods are based on a nonparametric approach, where a non-parametric IRF is assumed [32]. According to the general pharmacokinetic

model (Eq. (1.3)), the measured tissue concentration curves, $c_t(t)$, are deconvolved with the AIF, $c_p(t)$, which yields an estimate of $F_p \cdot R(t)$. Regularization, such as Tikhonov regularization or truncated singular value decomposition, is sometimes used to deal with the ill-posedness of the deconvolution problem [33].

Then, F_p is estimated from $F_p \cdot R(t)$ as the first sample (because $R(t = 0) = 1$) or as its maximum. Plasma volume, v_p , (Tab. 1.1) is calculated as the ratio of areas under the tissue and AIF curves:

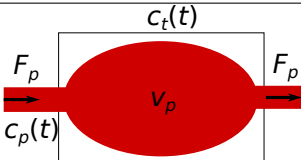
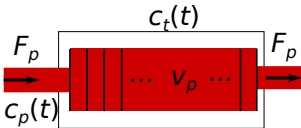
$$v_p = \frac{\int_0^{\text{inf}} c_t(t) dt}{\int_0^{\text{inf}} c_p(t) dt}. \quad (1.4)$$

The mean transit time, T_c , (Tab. 1.1) is derived from F_p and v_p according to the central volume principle [34] as

$$T_c = v_p / F_p. \quad (1.5)$$

Compared to non-parametric IRF, use of parametric IRF imposes additional assumptions about the perfusion unit, which can stabilize estimation of the perfusion parameters by limiting the set of possible solutions. This is however at the cost of decreased realism of the pharmacokinetic model because each IRF model brings a certain degree of simplification. The most broadly used parametric IRF models of the intravascular space (Tab. 1.3) are the compartment and plug-flow models. A compartment model describes the intravascular space as a well-mixed volume with a homogeneous contrast-agent concentration. Such model is suitable for a chaotic microvascular structure with no prevailing orientation of the vessels, such as the brain microvasculature for example. The dynamics of the contrast-agent distribution in a one-compartment perfusion unit can be described by a 1st-order ordinary differential equation. The solution leads to the convolutional model Eq. (1.3) with $R(t) = \exp(-t \cdot F_p / v_p)$ [35]. Fitting this model to the measured signal, $c_t(t)$, yields estimates of F_p and v_p (and T_c from the central volume principle).

A plug-flow model describes the microvasculature as a tube or a set of parallel tubes where all particles move with the same velocity. This relates to erythrocytes acting as "plugs" because they have a slightly larger size than the lumen of capillaries. When deformed erythrocytes are passing through the capillaries, they induce the same velocity of the plasma space between them. A plug-flow model is suitable for tissues with unidirectionally organized vessels, e.g. some muscle structures. The IRF of a plug-flow perfusion unit is $R(0 \leq t \leq T_c) = 1$ and $R(t) = 0$ elsewhere [35].

Compartment model	
<ul style="list-style-type: none"> • homogeneous contrast-agent concentration • exponential IRF 	
Plug-flow model	
<ul style="list-style-type: none"> • constant speed of contrast-agent particles • boxcar IRF 	

Tab. 1.3: Pharmacokinetic models for non-diffusible contrast agents.

1.2.2 Models for diffusible contrast agents

This section reviews pharmacokinetic models modeling the contrast-agent distribution within both the intravascular space and the EES. For these models, the approach of a non-parametric IRF has been used rarely [36]. In Eqs. (1.4), (1.5), the distribution volume, v_p , of the non-diffusible-contrast-agent case needs to be replaced by the distribution volume of the diffusible-contrast-agent case being $v_p + v_e$. The mean transit time, T_c , in Eq. (1.5) is replaced by the mean transit time of contrast-agent particles through the whole perfusion unit including the EES.

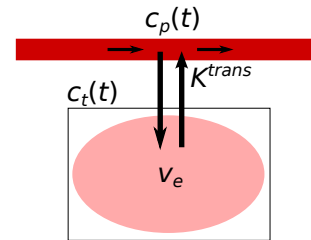
Parametric IRF models of diffusible contrast agents are of various degrees of complexity. As for the intravascular space, some models assume this space has negligible contribution and do not model it, e.g. the Tofts model [21, 37]. In the extended Tofts or the Patlak models, the intravascular signal is included but the structure of the intravascular space is not modeled (as it is irrelevant for the assumed high-flow conditions) [36]. These models are referred to as 1st-generation models (Tab. 1.4), dating back to the 1990s, where the quality of acquired MRI data was not sufficient to extract F_p, PS, T_c and E . This became possible later, with the so called 2nd-generation models, such as the 2CX, TH, ATH, DP, DCATH and GCTT models (see Tab. 1.5 for the full names, schematics and short descriptions). These models are based on a compartment or plug-flow model of the intravascular space and on a compartment or distributed-parameter model of the EES. The advantage of the 2nd-generation models is that they provide a more complete set of perfusion parameters than the 1st-generation models. For example the perfusion parameter K^{trans} provided by the 1st-generation models is affected by both plasma flow, F_p , and the permeability-surface area product, PS (describing the "leakiness" of the vessel wall for the contrast agent). Hence, the 1st-generation models do not allow differentiating the effects of blood flow and permeability. Separating the flow and permeability properties gives important information about the tissue

microvasculature state. This is provided by the 2nd-generation models. On the other hand, the 2nd-generation models are more complex and require better data quality.

A thorough description of the pharmacokinetic models is beyond the scope of this introduction. The reader can refer to several reviews on this topic [31, 36, 38].

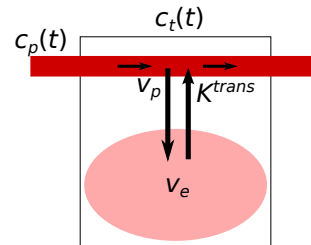
Tofts model

- only EES assumed
- EES modeled as a compartment



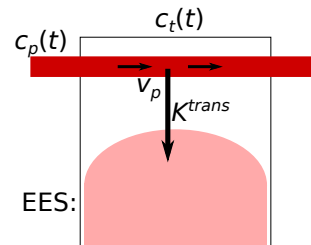
Extended Tofts model

- vascular signal considered
- structure of the intravascular space not modeled (high plasma flow assumed)



Patlak model

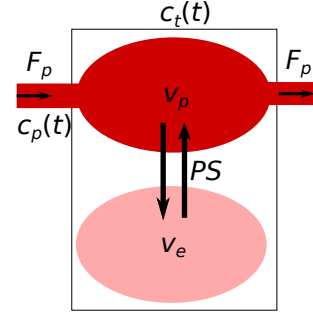
- vascular signal considered
- structure of the intravascular space not modeled (high plasma flow assumed)
- backflux from the EES to the vascular space neglected (uptake model)



Tab. 1.4: First-generation pharmacokinetic models for diffusible contrast agents.

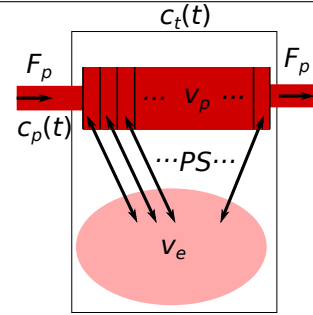
2-Compartment eXchange (2CX) Model

- intravascular space modeled as a compartment
- EES modeled as a compartment



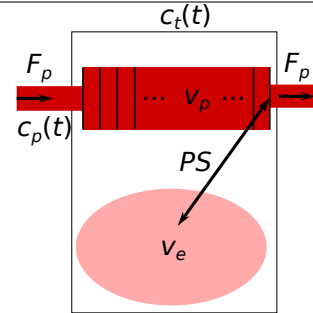
Tissue-Homogeneity (TH) model

- plug-flow model of the vascular space
- EES modeled as a compartment
- no analytic time-domain expression of the IRF, $R(t)$, only frequency-domain expression available



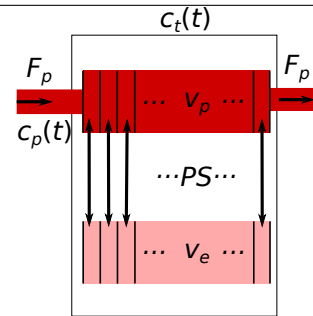
Adiabatic approximation of the Tissue Homogeneity model (ATH)

- plug-flow model of the vascular space
- EES modeled as a compartment
- assumption of much faster intravascular contrast-agent dynamics compared to the dynamics in the EES



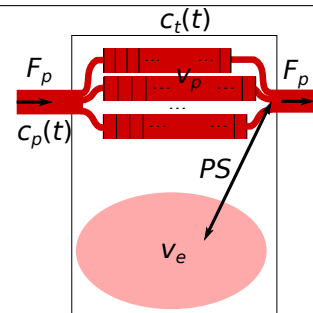
Distributed-Parameter (DP) model

- plug-flow model of the vascular space
- distributed model of the EES
- contrast-agent exchange only between the corresponding intravascular-space and EES units
- no exchange (diffusion) between the neighboring EES units assumed



Distributed-Capillary Adiabatic Tissue Homogeneity (DCATH) and Gamma Capillary Transit Time (GCTT) models

- as the ATH model but multiple intravascular paths with different transit times assumed
- additional perfusion parameter describing the statistical distribution of the mean capillary transit times



Tab. 1.5: Second-generation pharmacokinetic models for diffusible contrast agents.

1.3 Main problems

Perfusion imaging using MRI and ultrasonography have been known since the 1980th / late 1990th. However, in the most clinical applications, current perfusion imaging methods are not sufficiently reliable for routine clinical use, where they remain mostly at the experimental level. Due to the vast variability of the available methods and due to their poor reproducibility among different scanners and scanner setups, there is a lack of standardization of the perfusion-imaging procedures. The situation is even worse in preclinical use, with a substantially smaller number of users, and hence lower business profit and interest of the scanner vendors.

One exception, in MRI, is DSC-MRI in stroke patients. Although the majority acute stroke examinations are made using CT, DSC-MRI is an officially approved standardized option, used in advanced medical imaging centers.

The Main reasons for the prevailing experimental character of perfusion imaging with MR and ultrasonography can be summarized as follows.

- There is still a dominating tendency to use simplistic semi-quantitative methods where the estimated perfusion parameters depend on the contrast-agent administration, on the properties of the proximal arterial system of the patient and on the scanner and its setup.

This clearly leads to the need for fully quantitative perfusion imaging methods. These methods model the shape of the contrast-agent bolus entering the analyzed tissue ROI (perfusion unit), i.e. the AIF, which captures the influence of the contrast-agent administration process and the influence of the arterial tree proximal to the tissue ROI. This means that the convolutional model (Eq. (1.3)) needs to be the model of choice in quantitative perfusion imaging.

- Related to the previous point is the need for accurate estimation of the AIF. The AIF is commonly considered equal for all voxels of the examined tissue (global AIF). In most studies, it is measured (extracted from the acquired image sequence) in a big artery or taken as a parametric population-based AIF from literature. In MRI, the measured AIF is distorted by flow artifacts, partial volume effects, saturation, T_2^* effects and dispersion of the contrast-agent bolus between the AIF measurement location and the examined tissue. In DCE-US, deriving the AIF from an arterial ROI in the measured image sequence is an even more problematic task than in MRI, mainly due to attenuation of the contrast agent (dependent on the contrast-agent concentration, i.e. changing throughout the acquisition time). In addition, similar problems as in DCE-MRI arise: motion artifacts, low spatial resolution, blood-velocity dependence of the backscattered signal and dispersion of the contrast-agent bolus.

On the other hand, use of a population-based AIF, as another possibility to determine the AIF, ignores the differences in the vascular tree between different individuals and depends on the acquisition protocol and the contrast-agent-administration procedure used when these "standard" AIFs were established.

- In DCE-MRI, still mostly 1st-generation pharmacokinetic models are used. As mentioned above, they provide ambiguous information concerning the common parameters K^{trans} and k_{ep} which mix together the effects of plasma flow and vessel wall permeability without a chance to distinguish between them. Furthermore, these models are too simplistic for many tissue types and lead to biased perfusion-parameter estimates.

A solution is to use more complex, 2nd-generation, models. However this leads to higher demands on the temporal resolution and signal-to-noise ratio (SNR), often ill-conditioned model fitting and higher sensitivity to the accuracy and precision of the AIF. Hence these models are still not much used.

2 CONTRIBUTION OF THE AUTHOR'S TEAM

The general aim of our group concerning both ultrasound and MRI perfusion imaging was and is to contribute to reliable quantitative perfusion analysis that gives accurate perfusion parameters independent of the contrast-agent-administration procedure, image-data acquisition methods and their setup, and the subject-specific properties of the arterial tree proximal to the ROI. Achieving this helps to bring ultrasound and MRI perfusion imaging closer to routine clinical practice and improve the diagnostics in many clinical and preclinical applications.

In the following text, our contribution is described more specifically, split into items. In most cases, an item corresponds to 1 or 2 journal paper(s) (co)authored by our group, possibly accompanied by our related conference contributions. The main journal papers, constitute attachments of the habilitation thesis.

2.1 Ultrasound perfusion imaging

The author believes that his group has contributed to introduction of quantitative perfusion imaging into DCE-US to replace the semi-quantitative methods. As pointed out earlier, the majority of DCE-US was done in a semi-quantitative manner.

The burst-replenishment DCE-US method is a semi-quantitative approach by nature, unless the parameters of the replenishment-curve model are scaled with respect to the arterial signal (as an analogy to the AIF in the bolus-tracking methods). To the author's knowledge, at the publication time of our first papers in DCE-US [39, 40, 41] (2010-2013), there were only three papers of two groups on quantitative burst-replenishment DCE-US (with normalization with respect to the arterial signal) [42, 43, 44], all applied to cardiac perfusion imaging.

A similar situation was present in bolus-tracking DCE-US. To the author's knowledge, at the publication time of our first papers in DCE-US there were two papers of one group [45, 46] using the convolution model Eq. (1.3) for estimation of the mean transit time, T_c , and slightly later, in 2012, another group published a convolution-based approach where all three available perfusion parameters were estimated (T_c , F_b , v_b) [47, 48].

The main contribution of our group in the field of DCE-US can be summarized as follows.

- We have introduced deconvolution-based perfusion imaging to bolus-tracking DCE-US and validated the methodology on a flow phantom [39, 49] and on pig's heart [50].

- We have newly formulated the standard burst-replenishment DCE-US method, using the convolutional formalism (i.e. using the convolution model Eq. (1.3)). This made it possible to combine the burst-replenishment approach with deconvolution-based bolus-tracking. In this combined approach, we called *Bolus & Burst*, the contrast agent is administered as a bolus and image data recorded as in the bolus-tracking method, but in addition, during the same image-recording session a high-energy burst is applied in the later slow-dynamics phase. Simultaneous processing of the bolus and replenishment signals leads to more robust perfusion analysis than processing of the bolus or replenishment signals alone. Having the bolus and replenishment signals interconnected through the convolutional model represents sufficient information to estimate the AIF together with the IRF (parametrized by the sought perfusion parameters T_c, F_b, v_b). This approach is called blind deconvolution – “blind” because both components of the convolution (Eq. (1.3)) are unknown. This approach avoids the problems connected to measuring the AIF or using population-based AIFs (see above). The author considers the *Bolus & Burst* method as the core of our contribution in DCE-US. We have published the methodology paper as [40] (*Paper I* of this habilitation thesis).
- We have extended our original *Bolus & Burst* method with a more accurate model [51]. In [41] (*Paper II* of this habilitation thesis), we have validated this extended *Bolus & Burst* method on clinical data from Crohn’s disease patients where we have shown that it could be used as a treatment-stratification method for patients with Crohn’s disease, particularly to distinguish between inflammatory and fibrous wall thickening of the gastrointestinal tract.
- The *Bolus & Burst* method was further tested on patients with exocrine pancreatic failure [52]. Interobserver agreement for repeated recordings using the same ultrasound scanner and agreement between results on two different scanner systems were evaluated.
- Another successful validation study of the *Bolus & Burst* method was done on patients with insufficiency of pancreas related to cystic fibrosis and on healthy volunteers [53].
- The *Bolus & Burst* processing chain was further extended by automatic compensation of motion using translational and non-rigid image registration with a temporal continuity assumption [54].
- We have further developed the *Bolus & Burst* method by implementing new AIF models suitable for DCE-US of small animals [55, 56] and illustrated the method on tumor-bearing mice and compared the results with DCE-MRI [57], all presented so far as conference proceedings papers.

2.2 MR perfusion imaging

In MR, convolution-based quantitative perfusion imaging has been more common than in ultrasonography. The main focus of our group has been DCE-MRI. Here, the most widely used pharmacokinetic models are the 1st-generation models, such as the Tofts and extended Tofts models. Our contribution was towards reliable DCE-MRI based on 2nd-generation models.

Our main effort was focused on accurate estimation of the AIF, which avoids the problems connected to measured or population-based AIFs. The main approach, similarly to our DCE-US work, was blind deconvolution, where both the IRF and AIF are estimated from the measured tissue concentration curves. Blind-deconvolution estimation of the AIF was proposed by the group of Edward DiBella (Univ. of Utah, USA) [58, 59, 60], with applications in DCE-MRI using 1st-generation pharmacokinetic models. At approximately the same time, the group of Torfinn Taxt (Univ. of Bergen, Norway) introduced blind-deconvolution AIF estimation into DSC-MRI [61, 62, 63]. Having a close cooperation with Torfinn Taxt and his group (and later partly with DiBella's group), we have built on this work. Together with Torfinn Taxt and his colleagues, we have applied blind-deconvolution AIF estimation to DCE-MRI using 2nd-generation pharmacokinetic models. Use of 2nd-generation models is more sensitive to the accuracy of AIF estimation and presents a more difficult problem than use of the 1st-generation models.

The main contribution of our group in DCE-MRI can be summarized as follows. Estimation of the AIF using blind deconvolution:

- We have proposed blind-deconvolution AIF estimation method with 2nd-generation pharmacokinetic models and a nonparametric AIF [64, 65] and validated them on DCE-MRI recordings from mice with induced muscle inflammation.
- DCE-MRI data processing and analysis based on blind deconvolution from the previous point was the core of our part in two major preclinical studies on tumor-bearing rats and the effects of antiangiogenic treatment with bevacizumab [66, 67]. The experimental setup and analysis methods, including our perfusion-imaging methodology, have revealed new insights into the physiological background of the treatment processes.
- We have further extended the above mentioned blind-deconvolution AIF estimation to use a semi-parametric AIF (initial rapidly changing part of the AIF was left nonparametric, while the "tail" was mathematically modeled), leading to more accurate AIF estimates [68]. The method was validated on recordings from mice with induced muscle inflammation.

- We have also contributed to blind-deconvolution AIF estimation with fully parametric AIF models to further constrain the AIF estimation process (used in connection with 2nd-generation pharmacokinetic models). In [69] (*Paper III* of this habilitation thesis), we have proposed such method for clinical DCE-MRI and validated it on renal-cell-carcinoma patients. In [70] (*Paper IV* of this habilitation thesis), we have proposed such method with an AIF model tailored to small-animal DCE-MRI and validated it within a study on tumor-bearing mice.
- the above mentioned blind deconvolution method with semi-parametric AIF was applied on a longitudinal preclinical study where the time development of bevacizumab's effects was studied at several time points during the treatment [71] (*Paper V* of this habilitation thesis). With our perfusion-imaging methodology we have contributed to gain new insights into the dynamics of the treatment effect.

Other topics:

- We have proposed a new estimation scheme for an advanced 2nd-generation model (DCATH) with a continuous formulation of all perfusion parameters, including the bolus arrival time, thanks to its estimation in the frequency domain [72]. This allows us to use standard gradient-based optimization algorithms in pharmacokinetic-model fitting of the tissue concentration time sequences. In addition to perfusion parameters, we have estimated also their confidential intervals. We have newly proposed a method for estimation of the confidential intervals of the perfusion parameters derived from the primary ones parametrizing the IRF.
- To increase the robustness of DCE-MRI with 2nd-generation models, we have incorporated spatial regularization into pharmacokinetic-model fitting. Hence, the model-fitting process was not done separately for each voxel, as usual, but simultaneously for all voxels with induced similarity of the neighboring voxels, based on the (edge-preserving) total variation (TV) regularization [73], (*Paper VI* of this habilitation thesis).

3 CONCLUSIONS

Our main contribution to ultrasound and MRI perfusion imaging was in fully quantitative perfusion analysis, as a means of reliable measurement of perfusion biomarkers, reproducible across different imaging scanners and differences in their acquisition setup (and independent of patient-specific arterial-tree properties). We have been pursuing the idea of treating ultrasonography and MRI not only as an imaging tool but rather as measuring devices.

In this respect, our main contribution in DCE-US was introducing a novel method, *Bolus & Burst*, which combines the bolus tracking and burst-replenishment methods, both formulated using convolution-based pharmacokinetic models. The perfusion-analysis process is performed using blind deconvolution which avoids the need for measurement of the AIF. This makes *Bolus & Burst* robust with respect to estimation errors due to AIF-measurement artifacts.

In DCE-MRI, we have followed the same idea of avoiding the need to measure the AIF by the use of blind-deconvolution, with a special focus on the use of 2nd-generation pharmacokinetic models, where the requirements on the accuracy and precision of AIF estimates are higher than for the more commonly used 1st-generation pharmacokinetic models. We have also contributed to improved reliability of perfusion analysis using 2nd-generation pharmacokinetic models by proposing a proper continuous formulation of the pharmacokinetic model and by introducing edge-preserving spatial regularization into the perfusion analysis.

The topic of perfusion analysis has been the core of several successfully defended bachelor, diploma and Ph.D. theses led by the author and several related theses led by his colleagues. The topic of perfusion imaging has been also introduced into several courses at Brno University of Technology, Dept. of Biomedical Engineering.

Our work in the field of quantitative perfusion analysis brought us in closer contact with broader national and international scientific community, often thanks to our long-term cooperation with Torfinn Taxt from University of Bergen, Norway. Our cooperation with the Institute of Medicine, University of Bergen, Norway and the National Centre of Ultrasound in Gastroenterology at Haukeland University Hospital, Bergen, Norway (Odd Helge Gilja, Kim Nylund, Trond Engjom) has been very fruitful in sense of validation of our DCE-US *Bolus & Burst* method on actual clinical applications. Our cooperation with the Department of Biomedicine, University of Bergen, Bergen, Norway (Rolf Bjerkvig, Eskil Eskilsso, Nina Obad) and the Luxembourg Institute of Health (Olivier Keunen) has helped us to apply our MR perfusion-analysis methods to actual problems in search for antiangiogenic cancer treatment. Finally, we have also started active cooperation with the group of

Edward DiBella, University of Utah, USA, in the field of DCE-MRI of myocardium [74]. This field represents a challenge due to complicated acquisition connected to cardiac and respiratory motion and it is one of our future orientations.

The increasing number of interested users of our perfusion-imaging methods has brought us to development of an online tool for perfusion analysis, called PerfLab <http://perflab.cerit-sc.cz/>, currently implemented as a prototype version. It is designed as a web-based database of studies, datasets and batches of perfusion analyses, providing a step-by-step perfusion analysis of DCE-US and DCE-MRI data. The web-based graphical user interface guides the user in entering the processing parameters, drawing ROIs, plotting of their concentration curves, browsing through the image sequences in each processing step and previewing of the resulting perfusion maps. The web-based character of PerfLab avoids the need for installation of any software, except for the web browser. For clinical users, the data can be imported through the service ReDiMed (<https://www.medimed.cz/en/redimed>) directly from the radiology workstation. Import of the DCE-US/DCE-MRI data is available for several clinical and preclinical scanners. PerfLab has been partly tested by our colleagues at the University of Bergen, Luxembourg Institute of Health and Stanford University. Our further development of this online software tool is directed towards thorough evaluation on clinical and preclinical data, dissemination and possibly future research and/or commercial use.

The current research focus of our group extends the above described work in several directions. First, we have implemented modern compressed-sensing DCE-MRI acquisition schemes based on sparse data sampling and spatially regularized image-sequence reconstruction to overcome the limits of standard MRI acquisition given by the Nyquist theorem [75, 76]. This approach provides increased spatial and/or temporal resolution or improved spatial coverage of the organ of interest. The spatial-regularization term can also be learned using modern deep-learning approaches, to provide even higher efficiency of the acquisition/reconstruction process which is a further natural extension of the compressed-sensing techniques.

On the level of applications (of DCE-MRI), the above described perfusion-analysis acquisition/processing methodology becomes more challenging when applied in the fields of cardiology and stroke imaging, where we intend to extend our know-how and hopefully contribute to the current state of the art. In cardiology, the main challenge is to synchronize the data acquisition process with the cardiac and respiratory motion while acquiring enough data for reliable image reconstruction and subsequent perfusion analysis. In stroke imaging, the main challenge is the low SNR of DCE-MRI data due to the blood brain barrier (preventing the contrast agent from extravasation) but allows quantification of subtle blood-brain-barrier

disruption [77, 78].

BIBLIOGRAPHY

- [1] N. A. Lassen, W. Perl, W. A. Perl, Tracer Kinetic Methods in Medical Physiology, Raven Press, 1979.
- [2] T. HK, S. CF, W. RE, M. HD, INDICATOR TRANSIT TIME CONSIDERED AS A GAMMA VARIATE, *Circulation research* 14 (1964) 502–515. doi:10.1161/01.RES.14.6.502.
- [3] C. Strouthos, M. Lampaskis, V. Sboros, A. Mcneilly, M. Averkiou, Indicator dilution models for the quantification of microvascular blood flow with bolus administration of ultrasound contrast agents, *IEEE Transactions on Ultrasonics, Ferroelectrics, and Frequency Control* 57 (6) (2010) 1296–1310. doi:10.1109/TUFFC.2010.1550.
- [4] J. B. Bassingthwaight, F. H. Ackerman, E. H. Wood, Applications of the Lagged Normal Density Curve as a Model for Arterial Dilution Curves, *Circulation Research* 18 (4) (1966) 398–415. doi:10.1161/01.RES.18.4.398.
- [5] M. MISCHI, Z. D. PRETE, H. H. M. KORSTEN, INDICATOR DILUTION TECHNIQUES IN CARDIOVASCULAR QUANTIFICATION, 2007, pp. 89–155. doi:10.1142/9789812771377_0004.
- [6] M. A. Heymann, B. D. Payne, J. I. Hoffman, A. M. Rudolph, Blood flow measurements with radionuclide-labeled particles, *Progress in Cardiovascular Diseases* 20 (1) (1977) 55–79. doi:10.1016/S0033-0620(77)80005-4.
- [7] H. N. Wagner, B. A. Rhodes, Y. Sasaki, J. P. Ryan, Studies of the circulation with radioactive microspheres (1969). doi:10.1097/00004424-196911000-00004.
- [8] H. N. Wagner, D. C. Sabiston, M. Iio, J. G. McAfee, J. K. Meyer, J. K. Langan, Regional Pulmonary Blood Flow in Man by Radioisotope Scanning, *JAMA: The Journal of the American Medical Association* 187 (8) (1964) 601–603. doi:10.1001/jama.1964.03060210051012.
- [9] G. RW, B. S, B. M, Validation of fluorescent-labeled microspheres for measurement of regional organ perfusion, *Journal of applied physiology (Bethesda, Md. : 1985)* 74 (5) (1993) 2585–2597. doi:10.1152/JAPPL.1993.74.5.2585.
- [10] A. Notghi, C. S. Low, Myocardial perfusion scintigraphy: past, present and future doi:10.1259/bjr/14625142.

- [11] R. S. Driessen, P. G. Raijmakers, . . Wijnand, J. Stuijzand, . . P. Knaapen, Myocardial perfusion imaging with PET, *The International Journal of Cardiovascular Imaging* 33 (2017) 1021–1031. doi:10.1007/s10554-017-1084-4.
- [12] S. V. Nesterov, C. Han, M. Mäki, S. Kajander, A. G. Naum, H. Helenius, I. Lisinen, H. Ukkonen, M. Pietilä, E. Joutsiniemi, J. Knuuti, J. Knuuti, S. V. Nesterov, M. Mäki, A. G. Naum, H. Helenius, H. Ukkonen, M. Pietilä, . E. Joutsiniemi, Myocardial perfusion quantitation with 15 O-labelled water PET: high reproducibility of the new cardiac analysis software (Carimasâ,,), *Eur J Nucl Med Mol Imaging* 36 (2009) 1594–1602. doi:10.1007/s00259-009-1143-8.
- [13] H. R. Heinz, P. Dubois, D. Osborne, B. Drayer, W. Barrett, Dynamic Computed Tomography Study of the Brain, *Journal of Computer Assisted Tomography* 3 (5) (1979) 641–649. doi:10.1155/2015/397521.
- [14] L. Axel, Cerebral blood flow determination by rapid-sequence computed tomography. A theoretical analysis, *Radiology* 137 (3) (1980) 679–686. doi:10.1148/radiology.137.3.7003648.
- [15] A. Villringer, B. R. Rosen, J. W. Belliveau, J. L. Ackerman, R. B. Lauffer, R. B. Buxton, Y. S. Chao, V. J. Wedeenand, T. J. Brady, Dynamic imaging with lanthanide chelates in normal brain: Contrast due to magnetic susceptibility effects, *Magnetic Resonance in Medicine* 6 (2) (1988) 164–174. doi:10.1002/mrm.1910060205.
- [16] R. R. Edelman, H. P. Mattle, D. J. Atkinson, T. Hill, J. P. Finn, C. Mayman, M. Ronthal, H. M. Hoogewoud, J. Kleefeld, Cerebral blood flow: Assessment with dynamic contrast-enhanced T2*-weighted MR imaging at 1.5 T, *Radiology* 176 (1) (1990) 211–220. doi:10.1148/radiology.176.1.2353094.
- [17] B. R. Rosen, J. W. Belliveau, B. R. Buchbinder, R. C. McKinstry, L. M. Porkka, D. N. Kennedy, M. S. Neuder, C. R. Fisel, H. J. Aronen, K. K. Kwong, R. M. Weisskoff, M. S. Cohen, T. J. Brady, Contrast agents and cerebral hemodynamics, *Magnetic Resonance in Medicine* 19 (2) (1991) 285–292. doi:10.1002/mrm.1910190216.
- [18] S. Warach, J. F. Dashe, R. R. Edelman, Clinical outcome in ischemic stroke predicted by early diffusion-weighted and perfusion magnetic resonance imaging: A preliminary analysis, *Journal of Cerebral Blood Flow and Metabolism* 16 (1) (1996) 53–59. doi:10.1097/00004647-199601000-00006.

- [19] D. J. Atkinson, D. Burstein, R. R. Edelman, First-pass cardiac perfusion: Evaluation with ultrafast MR imaging (1990). doi:10.1148/radiology.174.3.2305058.
- [20] H. B. Larsson, M. Stubgaard, J. L. Frederiksen, M. Jensen, O. Henriksen, O. B. Paulson, Quantitation of blood-brain barrier defect by magnetic resonance imaging and gadolinium-DTPA in patients with multiple sclerosis and brain tumors, *Magnetic Resonance in Medicine* 16 (1) (1990) 117–131. doi:10.1002/mrm.1910160111.
- [21] P. S. Tofts, A. G. Kermode, Measurement of the blood brain barrier permeability and leakage space using dynamic MR imaging. 1. Fundamental concepts, *Magnetic Resonance in Medicine* 17 (2) (1991) 357–367. doi:10.1002/mrm.1910170208.
- [22] G. Brix, W. Semmler, R. Port, L. R. Schad, G. Layer, W. J. Lorenz, Pharmacokinetic parameters in cns gd-dtpa enhanced mr imaging, *Journal of Computer Assisted Tomography* 15 (4) (1991) 621–628.
- [23] J. A. Detre, J. S. Leigh, D. S. Williams, A. P. Koretsky, Perfusion imaging, *Magnetic Resonance in Medicine* 23 (1) (1992) 37–45. doi:10.1002/mrm.1910230106.
- [24] D. Le Bihan, E. Breton, D. Lallemand, P. Grenier, E. Cabanis, M. Laval-Jeantet, MR imaging of intravoxel incoherent motions: Application to diffusion and perfusion in neurologic disorders, *Radiology* 161 (2) (1986) 401–407. doi:10.1148/radiology.161.2.3763909.
- [25] R. Gramiak, P. M. Shah, Echocardiography of the Aortic Root, *Investigative Radiology* 3 (5) (1968) 356–366.
- [26] J. R. Lindner, F. S. Villanueva, J. M. Dent, K. Wei, J. Sklenar, S. Kaul, Assessment of resting perfusion with myocardial contrast echocardiography: Theoretical and practical considerations, *American Heart Journal* 139 (2) (2000) 231–240. doi:10.1016/S0002-8703(00)90231-X.
- [27] M. Wiesmann, G. Seidel, Ultrasound perfusion imaging of the human brain, *Stroke* 31 (10) (2000) 2421–2425. doi:10.1161/01.STR.31.10.2421.
- [28] K. Wei, A. R. Jayaweera, S. Firoozan, A. Linka, D. M. Skyba, S. Kaul, Quantification of myocardial blood flow with ultrasound-induced destruction

- of microbubbles administered as a constant venous infusion, *Circulation* 97 (5) (1998) 473–483. doi:10.1161/01.CIR.97.5.473.
- [29] V. G. Kiselev, On the theoretical basis of perfusion measurements by dynamic susceptibility contrast MRI, *Magnetic Resonance in Medicine* 46 (6) (2001) 1113–1122. doi:10.1002/mrm.1307.
- [30] N. Herring, *Levick's introduction to cardiovascular physiology, sixth edition.. Edition*, 2018.
- [31] S. P. Sourbron, D. L. Buckley, Tracer kinetic modelling in MRI: estimating perfusion and capillary permeability, *Physics in Medicine and Biology* 57 (2) (2011) R1–R33. doi:10.1088/0031-9155/57/2/R1.
- [32] L. Østergaard, ISMRM Perfusion Workshop Invited Paper Principles of Cerebral Perfusion Imaging by Bolus Tracking (2005). doi:10.1002/jmri.20460.
- [33] S. Sourbron, R. Luypaert, P. V. Schuerbeek, M. Dujardin, T. Stadnik, Choice of the regularization parameter for perfusion quantification with MRI, *Physics in Medicine & Biology* 49 (14) (2004) 3307. doi:10.1088/0031-9155/49/14/020.
- [34] P. Meier, K. L. Zierler, On the Theory of the Indicator-Dilution Method for Measurement of Blood Flow and Volume.
- [35] L. Østergaard, R. M. Weisskoff, D. A. Chesler, C. Gyldensted, B. R. Rosen, High resolution measurement of cerebral blood flow using intravascular tracer bolus passages. Part I: Mathematical approach and statistical analysis, *Magnetic Resonance in Medicine* 36 (5) (1996) 715–725. doi:10.1002/MRM.1910360510.
- [36] S. P. Sourbron, D. L. Buckley, Classic models for dynamic contrast-enhanced MRI., *NMR in biomedicine* 26 (8) (2013) 1004–27. doi:10.1002/nbm.2940.
- [37] P. S. Tofts, G. Brix, D. L. Buckley, J. L. Evelhoch, E. Henderson, M. V. Knopp, H. B. Larsson, T. Y. Lee, N. A. Mayr, G. J. Parker, R. E. Port, J. Taylor, R. M. Weisskoff, Estimating kinetic parameters from dynamic contrast-enhanced T1-weighted MRI of a diffusable tracer: Standardized quantities and symbols., *JMRI* 10 (3) (1999) 223–32.
- [38] T. S. Koh, S. Bisdas, D. M. Koh, C. H. Thng, Fundamentals of tracer kinetics for dynamic contrast-enhanced MRI, *Journal of Magnetic Resonance Imaging* 34 (6) (2011) 1262–1276. doi:10.1002/jmri.22795.

- [39] M. Mézl, R. Jiřík, V. Harabiš, R. KolářTM, Quantitative ultrasound perfusion analysis in vitro, *ANALYSIS OF BIOMEDICAL SIGNALS AND IMAGES*, Proceedings of Biosignal (2010) 279–283.
- [40] R. Jiřík, K. Nylund, O. H. Gilja, M. Mézl, V. Harabiš, R. Kolář, M. Standarda, T. Taxt, Ultrasound Perfusion Analysis Combining Bolus-Tracking and Burst-Replenishment, *IEEE Transactions on Ultrasonics, Ferroelectrics, and Frequency Control* 60 (2) (2013) 310–319.
- [41] K. Nylund, R. Jiřík, M. Mézl, S. Leh, T. Hausken, F. Pfeffer, S. Ødegaard, T. Taxt, O. H. Gilja, Quantitative Contrast-Enhanced Ultrasound Comparison Between Inflammatory and Fibrotic Lesions in Patients with Crohn’s Disease, *Ultrasound in Medicine & Biology* 39 (7) (2013) 1197–1206. doi:10.1016/j.ultrasmedbio.2013.01.020.
- [42] R. Vogel, A. Indermuhle, J. Reinhardt, P. Meier, P. T. Siegrist, M. Namdar, P. A. Kaufmann, C. Seiler, The quantification of absolute myocardial perfusion in humans by contrast echocardiography: Algorithm and validation, *Journal of American College of Cardiology* 45 (5) (2005) 754–762.
- [43] T. Rutz, S. F. de Marchi, M. Schwerzmann, R. Vogel, C. Seiler, Right ventricular absolute myocardial blood flow in complex congenital heart disease, *Heart* 96 (13) (2010) 1056–1062.
- [44] H. Komatsu, S. Yamada, H. Iwano, M. Okada, H. Onozuka, T. Mikami, S. Yokoyama, M. Inoue, S. Kaga, M. Nishida, C. Shimizu, K. Matsuno, H. Tsutsui, Angiotensin II receptor blocker, valsartan, increases myocardial blood volume and regresses hypertrophy in hypertensive patients, *Circulation Journal* 73 (11) (2009) 2098–2103.
- [45] P. C. Li, C. K. Yeh, S. W. Wang, Time-intensity-based volumetric flow measurements: An in vitro study, *Ultrasound in Medicine and Biology* 28 (3) (2002) 349–358. doi:10.1016/S0301-5629(01)00516-6.
- [46] P. C. Li, M. J. Yang, Transfer function analysis of ultrasonic time-intensity measurements, *Ultrasound in medicine & biology* 29 (10) (2003) 1493–1500. doi:10.1016/S0301-5629(03)00968-2.
- [47] M. Gauthier, F. Tabarout, I. Leguerney, M. Polrot, S. Pitre, P. Peronneau, N. Lassau, Assessment of Quantitative Perfusion Parameters by Dynamic Contrast-Enhanced Sonography Using a Deconvolution Method An In Vitro and In Vivo Study, *Journal of Ultrasound in Medicine* 31 (2012) 595–608.

- [48] M. Gauthier, S. Pitre-Champagnat, F. Tabarout, I. Leguerney, M. Polrot, N. Lassau, Impact of the arterial input function on microvascularization parameter measurements using dynamic contrast-enhanced ultrasonography., *World journal of radiology* 4 (7) (2012) 291–301. doi:10.4329/wjr.v4.i7.291.
- [49] M. Mézl, R. Jiřík, V. Harabiš, R. Kolář, M. Standara, K. Nylund, O. H. Gilja, T. Taxt, Absolute ultrasound perfusion parameter quantification of a tissue-mimicking phantom using bolus tracking, *IEEE Transactions on Ultrasonics, Ferroelectrics, and Frequency Control* 62 (5) (2015) 983–987. doi:10.1109/TUFFC.2014.006896.
- [50] M. Mézl, R. Jiřík, K. Matre, K. Grong, P.-R. Salminen, M. T. Lonnebakken, T. Taxt, Quantitative myocardial perfusion analysis with contrast-enhanced ultrasound bolus tracking - preliminary animal results, in: *2013 IEEE International Ultrasonics Symposium (IUS)*, IEEE, 2013, pp. 541–544. doi:10.1109/ULTSYM.2013.0140.
- [51] R. Jiřík, K. Nylund, T. Taxt, M. Mézl, T. Hausken, V. Harabiš, R. Kolář, M. Standara, O. H. Gilja, Parametric ultrasound perfusion analysis combining bolus tracking and replenishment, in: *2012 IEEE International Ultrasonics Symposium*, IEEE, 2012, pp. 1323–1326. doi:10.1109/ULTSYM.2012.0330.
- [52] M. Stangeland, T. Engjom, M. Mézl, R. Jiřík, O. H. Gilja, G. Dimcevski, K. Nylund, Interobserver Variation of the Bolus-And-Burst Method for Pancreatic Perfusion with Dynamic-Contrast-Enhanced Ultrasound, *Ultrasound International Open* 3 (3) (2017) E99–E106. doi:10.1055/s-0043-110475.
- [53] T. Engjom, K. Nylund, F. Erchinger, M. Stangeland, B. Lærum, M. Mézl, R. Jiřík, O. Gilja, G. Dimcevski, Contrast-enhanced ultrasonography of the pancreas shows impaired perfusion in pancreas insufficient cystic fibrosis patients, *BMC Medical Imaging* 18 (1) (2018). doi:10.1186/s12880-018-0259-3.
- [54] S. Schäfer, K. Nylund, F. Sævik, T. Engjom, M. Mézl, R. Jiřík, G. Dimcevski, O. H. Gilja, K. Tönnies, Semi-automatic motion compensation of contrast-enhanced ultrasound images from abdominal organs for perfusion analysis., *Computers in biology and medicine* 63 (2015) 229–37. doi:10.1016/j.compbiomed.2014.09.014.
- [55] M. Mézl, R. Jiřík, K. Souček, R. Kolář, Evaluation of accuracy of bolus and burst method for quantitative ultrasound perfusion analysis with various

arterial input function models, 2015 IEEE International Ultrasonics Symposium (IUS) (1) (2015) 1–4. doi:10.1109/ULTSYM.2015.0482.

- [56] M. Mézl, R. Jiřík, L. Dvořáková, E. Dražanová, R. Kolář, Comparison of arterial input function models for small-animal ultrasound perfusion imaging, in: IEEE International Ultrasonics Symposium, IUS, Vol. 2016-Novem, 2016. doi:10.1109/ULTSYM.2016.7728503.
- [57] R. Jiřík, K. Souček, M. Mézl, M. Bartoš, E. Dražanová, F. Dráfi, L. Grossová, J. Kratochvíla, O. Macíček, K. Nylund, A. Hampl, O. H. Gilja, T. Taxt, Z. Starčuk, Blind deconvolution in dynamic contrast-enhanced MRI and ultrasound., in: Conf Proc IEEE Eng Med Biol Soc., Vol. 2014, Institute of Electrical and Electronics Engineers Inc., 2014, pp. 4276–9. doi:10.1109/EMBC.2014.6944569.
- [58] D. Y. Riabkov, E. V. R. D. Bella, Estimation of Kinetic Parameters Without Input Functions : Analysis of Three Methods for Multichannel Blind Identification, IEEE T Bio-Med Eng 49 (11) (2002) 1318–1327.
- [59] J. U. Fluckiger, M. C. Schabel, E. V. R. DiBella, Model-Based Blind Estimation of Kinetic Parameters in Dynamic Contrast Enhanced (DCE)-MRI, Magnetic Resonance in Medicine 62 (6) (Dec. 2009).
- [60] M. C. Schabel, J. U. Fluckiger, E. V. R. DiBella, A model-constrained Monte Carlo method for blind arterial input function estimation in dynamic contrast-enhanced MRI: I. Simulations, Physics in Medicine and Biology 55 (16) (2010) 4783–4806.
- [61] G. R. T. T, Iterative blind deconvolution in magnetic resonance brain perfusion imaging, Magnetic resonance in medicine 55 (4) (2006) 805–815. doi:10.1002/MRM.20850.
- [62] R. Grü, B. T. Bjørnarå, G. Moen, T. Taxt, Magnetic Resonance Brain Perfusion Imaging With Voxel-Specific Arterial Input Functions, J. Magn. Reson. Imaging 23 (2006) 273–284. doi:10.1002/jmri.20505.
- [63] R. Grü, T. Taxt, Cepstral Estimation of Arterial Input Functions in Brain Perfusion Imaging, J. Magn. Reson. Imaging 26 (2007) 773–779. doi:10.1002/jmri.21115.
- [64] T. Taxt, R. Jiřík, C. B. Rygh, R. Gruner, M. Bartos, E. Andersen, F. R. Curry, R. K. Reed, Single-Channel Blind Estimation of Arterial Input Function

and Tissue Impulse Response in DCE-MRI, *IEEE Transactions on Biomedical Engineering* 59 (4) (2012) 1012–1021. doi:10.1109/TBME.2011.2182195.

- [65] T. Taxt, T. Pavlin, R. K. Reed, F.-R. Curry, E. Andersen, R. Jiřík, Using Single-Channel Blind Deconvolution to Choose the Most Realistic Pharmacokinetic Model in Dynamic Contrast-Enhanced MR Imaging, *Applied Magnetic Resonance* 46 (6) (2015) 643–659. doi:10.1007/s00723-015-0679-y.
- [66] O. Keunen, M. Johansson, A. Oudin, M. Sanzey, S. A. A. Rahim, F. Fack, F. Thorsen, T. Taxt, M. Bartos, R. Jiřík, H. Miletic, J. Wang, D. Stieber, L. Stuhr, I. Moen, C. B. Rygh, R. Bjerkvig, S. P. Niclou, Anti-VEGF treatment reduces blood supply and increases tumor cell invasion in glioblastoma, *Proceedings of the National Academy of Sciences* 108 (9) (2011) 3749–3754. doi:10.1073/pnas.1014480108.
- [67] E. Eskilsson, G. Rosland, K. Talasila, S. Knappskog, O. Keunen, A. Sottoriva, S. Foerster, G. Solecki, T. Taxt, R. Jirik, S. Fritah, P. Harter, K. Vålk, J. Al Hossain, J. Joseph, R. Jahedi, H. Saed, S. Piccirillo, I. Spiteri, L. Leiss, P. Euskirchen, G. Graziani, T. Daubon, M. Lund-Johansen, P. Enger, F. Winkler, C. Ritter, S. Niclou, C. Watts, R. Bjerkvig, H. Miletic, EGFRvIII mutations can emerge as late and heterogenous events in glioblastoma development and promote angiogenesis through Src activation, *Neuro-oncology* 18 (12) (2016).
- [68] T. Taxt, R. K. Reed, T. Pavlin, C. B. Rygh, E. Andersen, R. Jiřík, Semi-parametric arterial input functions for quantitative dynamic contrast enhanced magnetic resonance imaging in mice, *Magnetic Resonance Imaging* 46 (2018) 10–20. doi:10.1016/J.MRI.2017.10.004.
- [69] J. Kratochvíla, R. Jiřík, M. Bartoš, M. Standara, Z. Starčuk, T. Taxt, Distributed capillary adiabatic tissue homogeneity model in parametric multi-channel blind AIF estimation using DCE-MRI, *Magn Reson Med* 75 (3) (2016) 1355–1365. doi:10.1002/mrm.25619.
- [70] R. Jiřík, T. Taxt, O. Macíček, M. Bartoš, J. Kratochvíla, K. Souček, E. Dražanová, L. Krátká, A. Hampl, Z. Starčuk, Blind deconvolution estimation of an arterial input function for small animal DCE-MRI, *Magnetic Resonance Imaging* 62 (2019) 46–56. doi:10.1016/J.MRI.2019.05.024.
- [71] N. Obad, H. Espedal, R. Jiřík, P. O. Sakariassen, C. Brekke Rygh, M. Lund-Johansen, T. Taxt, S. P. Niclou, R. Bjerkvig, O. Keunen, Lack of functional

- normalisation of tumour vessels following anti-angiogenic therapy in glioblastoma, *Journal of Cerebral Blood Flow & Metabolism* 38 (10) (2018) 1741–1753. doi:10.1177/0271678X17714656.
- [72] M. Bartoš, R. Jiřík, J. Kratochvíla, M. Standara, Z. Starčuk, T. Taxt, The precision of DCE-MRI using the tissue homogeneity model with continuous formulation of the perfusion parameters., *Magnetic resonance imaging* 32 (5) (2014) 505–13. doi:10.1016/j.mri.2014.02.003.
- [73] M. Bartoš, P. Rajmic, M. Šorel, M. Mangová, O. Keunen, R. Jiřík, Spatially regularized estimation of the tissue homogeneity model parameters in DCE-MRI using proximal minimization, *Magnetic Resonance in Medicine* 82 (6) (2019) 2257–2272. doi:10.1002/mrm.27874.
- [74] R. Jiřík, J. Mendes, Y. Tian, G. Adluru, E. DiBella, Hybrid Estimation of the Arterial Input Function Using Blind Deconvolution and the Measured Blood Pool Signal, in: *ISMRM Proceedings 2018*, 2018, p. 2965.
- [75] M. Mangová, P. Rajmic, R. Jiřík, Dynamic magnetic resonance imaging using compressed sensing with multi-scale low rank penalty, in: *2017 40th International Conference on Telecommunications and Signal Processing, TSP 2017*, Vol. 2017-Janua, 2017. doi:10.1109/TSP.2017.8076094.
- [76] R. Jiřík, M. Marie, P. Rajmic, O. Macíček, K. Souček, Z. Starčuk, Advanced pharmacokinetic modeling in small-animal compressed-sensing DCE-MRI, in: *ESMRMB 2019 Congress*, Elsevier, Rotterdam, 2019, pp. S346–S348. doi:10.1007/s10334-019-00755-1.
- [77] R. Jiřík, M. Marie, P. Rajmic, L. Krátká, L. Dvořáková, E. Dražanová, Z. Starčuk, Absolute Quantification of Brain Perfusion using Golden Angle Compressed Sensing DCE-MRI, in: *ISMRM Proceedings 2017*, 2017, p. 6400.
- [78] R. Jiřík, L. Krátká, J. Kratochvíla, O. Macíček, Y. Tian, P. Scheer, J. Hložková, M. Bartoš, E. DiBella, Z. Starčuk, Blood Flow and Permeability Imaging in a Rat Stroke Model Using 3D Compressed-Sensing DCE-MRI, in: *ISMRM Proceedings 2020*, 2020, p. 3771.

4 SELECTED JOURNAL PAPERS

4.1 Ultrasound perfusion imaging

4.1.1 Paper I

R. Jiřík, K. Nylund, O.H. Gilja, M. Mézl, V. Harabiš, R. Kolář, M. Standara, T. Taxt, Ultrasound perfusion analysis combining bolus-tracking and burst-replenishment, IEEE Trans. Ultrason. Ferroelectr. Freq. Control. 60 (2013) 310–319.

<https://doi.org/10.1109/TUFFC.2013.2567>.

(IF 1.503)

Author's contribution:

- co-author of the main idea
- methodological design
- implementation
- data processing
- data evaluation
- paper writing

Ultrasound Perfusion Analysis Combining Bolus-Tracking and Burst-Replenishment

Radovan Jiřík, Kim Nylund, Odd Helge Gilja, Martin Mézl, Vratislav Harabiš, Radim Kolář, Michal Standara, and Torfinn Taxt

Abstract—A new signal model and processing method for quantitative ultrasound perfusion analysis is presented, called bolus-and-burst. The method has the potential to provide absolute values of blood flow, blood volume, and mean transit time. Furthermore, it provides an estimate of the local arterial input function which characterizes the arterial tree, allowing accurate estimation of the bolus arrival time. The method combines two approaches to ultrasound perfusion analysis: bolus-tracking and burst-replenishment. A pharmacokinetic model based on the concept of arterial input functions and tissue residue functions is used to model both the bolus and replenishment parts of the recording. The pharmacokinetic model is fitted to the data using blind deconvolution. A preliminary assessment of the new perfusion-analysis method is presented on clinical recordings.

I. INTRODUCTION

PERFUSION imaging is an important method for diagnosis and therapy monitoring in ischemic and oncologic illnesses. It is also a promising tool for discrimination between cancer and inflammation [1]. One of the first indications of quantitative ultrasound perfusion analysis [or dynamic contrast enhanced ultrasonography (DCE-US)] was in echocardiography, for the assessment of myocardial perfusion. In contrast to other imaging modalities used in

perfusion analysis, ultrasound imaging has the advantage of being real-time and it is a low-cost application. On the other hand, ultrasound images are often of poor quality and suffer from many artifacts (e.g., attenuation) which make quantitative perfusion analysis difficult.

The basic idea of perfusion imaging is to record the time-dependent change of the contrast-agent concentration in a tissue of interest following intravascular administration. Ultrasound contrast agents (gas-filled microbubbles) do not leak into the extravascular space. For such contrast agents, blood flow, F_b , blood volume, V_b , and mean transit time (MTT) can be estimated. Currently, two main approaches are used for quantitative ultrasound perfusion analysis: burst-replenishment and bolus-tracking.

The burst-replenishment (reperfusion) method [2] is widely used in experimental research. The application fields cover mostly myocardial perfusion [2], [3], but also cerebral [4], renal [5], [6], and liver perfusion [7]. The contrast agent is administered as an infusion. This technique is based on bubble destruction in the analyzed region of interest (ROI) using one or several pulses with high mechanical index (MI), usually around 1, followed by low-MI imaging sensitive to microbubbles (e.g., pulse inversion, power modulation, or power modulated pulse inversion imaging [8]).

The reperfusion time curve acquired after bubble destruction can be modeled as an increasing exponential function or a more complex function [6], [9], [10]. The maximum of the curve, A , is proportional to the fractional blood volume, V_b . Using the estimate of the exponential-function time constant, β , the quantity $A\beta$ is proportional to the blood flow per tissue volume.

The problem with this approach is that the quantities β and $A\beta$ are only proportional to the perfusion parameters. The proportionality constants are unknown and depend on many factors (e.g., infusion dosage and rate, clearance of the contrast agent, settings of the ultrasound scanner, and attenuation) which vary between examinations and also within the image (attenuation). To our knowledge, the only DCE-US approach providing absolute values of the perfusion parameters is based on the method proposed in [11], in which the additional information for absolute quantification is the image intensity in the blood pool (ROIs placed in the ventricle). However, this approach has been used only in cardiology so far [12], [13].

Bolus-tracking is an acquisition technique in which the tracer concentration curves are measured during the passage of a contrast agent bolus. The analysis of the image intensity curves (mean image intensity within tissue ROIs

Manuscript received August 3, 2012; accepted November 22, 2012. This work has been supported by the projects of the Czech Science Foundation, numbers GA102/09/1690 and GA102/12/2380; by the projects of the European Commission and Ministry of Education, Youth, and Sports of the Czech Republic (Application Laboratories of Microtechnologies and Nanotechnologies number CZ.1.05/2.1.00/01.0017 and Regional Centre for Applied Molecular Oncology number CZ.1.05/2.1.00/03.0101); by the research frame number MZMOU2005 FUNDIN, sponsored by the Ministry of Health of the Czech Republic; and by the European Regional Development Fund, Project FNUSA-ICRC (number CZ.1.05/1.1.00/02.0123). The study was also supported by MedViz (<http://medviz.uib.no/>), an interdisciplinary research cluster at Haukeland University Hospital, University of Bergen, and Christian Michelsen Research AS.

R. Jiřík is with the Institute of Scientific Instruments, Academy of Sciences of the Czech Republic, Brno, Czech Republic (e-mail: jirik@isibrno.cz).

R. Jiřík, M. Mézl, and R. Kolář are with the International Clinical Research Center, Center of Biomedical Engineering, St. Anne's University Hospital Brno, Brno, Czech Republic.

K. Nylund and O. H. Gilja are with the Institute of Medicine, University of Bergen, Bergen, Norway, and the National Centre for Ultrasound in Gastroenterology, Haukeland University Hospital, Bergen, Norway.

V. Harabiš is with the Department of Biomedical Engineering, Brno University of Technology, Brno, Czech Republic.

M. Standara is with the Masaryk Memorial Cancer Institute, Brno, Czech Republic.

T. Taxt is with the Department of Biomedicine, University of Bergen, Bergen, Norway.

DOI <http://dx.doi.org/10.1109/TUFFC.2013.2567>

versus time) allows estimation of several semiquantitative tissue parameters (e.g., peak intensity, area under the curve, time to peak) [14], [15] or quantitative parameters (e.g., local diffusion-related parameter and mean transit time [16]), which are related to real physical perfusion parameters. The problem with most of the present bolus-tracking methods (except for [16] and [17]) is that the delay and shape of the time-concentration curve in the local arterial input of the tissue [called the arterial input function (AIF)] are ignored. This leads to a nonunique interpretation of the estimated parameters because they mix the effect of the AIF and the tissue perfusion parameters. Furthermore, it limits the reproducibility of the method because the AIF is determined by the bolus administration and is also dependent on the patient-specific vascular tree.

In this paper, a combination of the bolus-tracking and burst-replenishment methods is proposed, called bolus and burst. It takes advantage of the simpler contrast-agent application in bolus-tracking and the possibility of absolute quantification of physical perfusion parameters in the burst-replenishment method. In addition, by utilizing information from both the bolus-tracking and burst-replenishment data, our method can provide potentially more robust MTT estimates than a standard replenishment technique. The proposed bolus-and-burst acquisition is based on bolus administration of the contrast agent. Low-MI imaging pulses are used to record the bolus-phase sequence. In the later wash-out phase of the bolus, when the tracer concentration decays rather slowly, a high-intensity ultrasound pulse sequence is applied to the imaged region to destroy the contrast agent in the imaging plane. The following replenishment phase is recorded using low-MI imaging pulses for a time interval of about 30 s. During this phase, a constant infusion-like state is assumed. The final phase, in which the contrast-agent concentration decays, is excluded from the replenishment phase to keep this assumption approximately valid. In [18]–[20], similar acquisition schemes combining the bolus-tracking and burst-replenishment methods have been published. However, only the replenishment part was used for estimation of A and β , (and absolute blood velocity derived using the imaging-plane width), and the bolus phase was used for normalization of A [19] or correction of the decay phase [18].

To allow estimation of physical perfusion parameters (blood volume, blood flow, and MTT), the pharmacokinetic models of the two methods are reformulated and a new estimation method is suggested. The bolus-tracking part is modeled as in perfusion analysis of other modalities [positron emission tomography (PET), single-photon emission computed tomography (SPECT), computed tomography (CT), and magnetic resonance imaging (MRI)], where the AIF is measured, estimated, or known as a population-based curve. According to [8], this has not been applied in ultrasound perfusion analysis. Only recently, two studies on this approach have been published [17],

[21]. Measurement of the AIF in a blood pool, as done in [17], [21], is difficult in DCE-US because of attenuation and low spatial resolution of ultrasound images. Here, the need for an AIF measurement is avoided by estimating it using the burst-replenishment part of the recording. To do this, the replenishment phase is modeled in terms of a known AIF and the tissue residue function. In addition to the perfusion parameters, the new approach provides an estimate of the local AIF, which characterizes the arterial tree.

II. PHARMACOKINETIC MODEL

The pharmacokinetic model for the bolus part is known from PET, SPECT, CT, and MRI [22], [23]:

$$C_{\text{bolus}}(t) = F_b \text{AIF}(t) * R(t). \quad (1)$$

$C_{\text{bolus}}(t)$ is the contrast-agent concentration in the ROI, $*$ stands for convolution, F_b is the blood flow per unit tissue volume (in milliliters per minute per milliliter of tissue), $\text{AIF}(t)$ is the contrast agent concentration in the arterial input of the ROI and $R(t)$ is the dimensionless tissue residue function, i.e., the fraction of the contrast agent remaining in the analyzed tissue ROI at time t after an instantaneous contrast agent bolus into the tissue ROI [i.e., a Dirac delta function as $\text{AIF}(t)$]. The function $R(t)$ is a monotonic decreasing positive function starting at 1 [i.e., $R(0) = 1$] [23].

For a one-compartment model of the ROI, $R(t) = \exp(-(F_b/V_b)t)$, where V_b is the blood volume per unit tissue volume (in milliliters per 100 mL of tissue) [22], [23].

The new formulation of a pharmacokinetic model for the replenishment phase is based on the assumption of a step-function character of the AIF, i.e., zero before the replenishment part (meaning all microbubbles have been destroyed) and constant during the replenishment part, meaning a constant infusion-like input. The step-function AIF leads to a modified version of (1):

$$C_{\text{repl}}(t) = F_b C_0 H(t) * R(t), \quad (2)$$

where $C_{\text{repl}}(t)$ is the contrast agent concentration in the ROI, C_0 is the contrast agent concentration in the arterial input of the ROI at the plateau [equal to the $\text{AIF}(t)$ from (1) at the plateau i.e., before the high-energy pulse sequence], and $H(t)$ is a Heaviside (unit) step function (zero before and one during the replenishment phase). This model of replenishment is general and does not impose any constraints to the microvascular tree within the ROI.

For a one-compartment model of the ROI, where $R(t) = \exp(-(F_b/V_b)t)$ as for the bolus part, the monoexponential model in [2] is obtained (see Appendix A for derivation):

$$C_{\text{repl}}(t) = A(1 - e^{-\beta t}), \quad (3)$$

where $A = V_b C_0$ and $\beta = F_b/V_b$, which agrees with the known formulation, e.g., [11]. Hence, in this model, A is proportional to blood volume (or cross-sectional blood area) and $A\beta$ is proportional to blood flow.

III. SIGNAL PROCESSING

Standard preprocessing is needed to estimate tracer concentration curves for each ROI from the DCE-US recording, including linearization of video data and ROI selection, see e.g., [24].

Having the tracer concentration curves $k \cdot C(t)$ for each ROI (where k is a scaling constant determined by the imaging ultrasound scanner, bolus dose, and attenuation), they must be split into the bolus part, $k \cdot C_{\text{bolus}}(t)$, and the replenishment part, $k \cdot C_{\text{repl}}(t)$. Then, the models [(1) and (2)] are fitted to the curves as described subsequently. This model fitting provides an estimate of $R(t)$, using $R(0) = 1$.

A. Parameter Estimation

The tissue residue function $R(t)$ can be estimated either as a nonparametric curve (constrained to be positive-valued and monotonic decreasing, in accordance with the physical model) or as a parametric (here one-compartment) approximation. In both cases, $R(t)$ gives an estimate of MTT, because $\text{MTT} = \int_0^\infty R(t)dt$ for the nonparametric model of $R(t)$ [22] and for the one-compartment model $R(t) = \exp(-(F_b/V_b)t)$, where $\text{MTT} = V_b/F_b$.

Subsequently, V_b can be estimated according to the formula used in perfusion imaging with other modalities [22], [23]

$$V_b = \frac{1 - \text{Hct}}{1 - r\text{Hct}} \frac{\int_0^\infty C(t)dt}{\int_0^\infty \text{AIF}_a(t)dt}, \quad (4)$$

where $C(t)$ is the contrast agent concentration in the tissue ROI following a bolus application, $\text{AIF}_a(t)$ is the contrast agent concentration measured in a big artery feeding the ROIs, Hct is the hematocrit in large vessels, and r is the ratio between the hematocrit in small and large vessels. Here, $C(t)$ is approximated by the measured tracer concentration curve $kC_{\text{bolus}}(t)$. Similarly, $\text{AIF}_a(t)$ can be theoretically approximated by the measured arterial tracer concentration curve $k\text{AIF}_a(t)$, assuming the same proportionality constant k as for the tissue ROI. The integral $k \int_0^\infty \text{AIF}_a(t)dt$ in the denominator is a constant for a given bolus application in the whole image (although the shape of the curve varies slightly with the location in the arterial tree, the integral remains constant, see Appendix B). Assuming the integral $k \int_0^\infty \text{AIF}_a(t)dt$ (later denoted as the constant $k\text{AIF}_{\text{int}}$) can be estimated using a scaling procedure described later, (4) can be used for estimation of V_b .

Using the central volume theorem [22], the blood flow, F_b , is finally calculated as

$$F_b = \frac{V_b}{\text{MTT}}. \quad (5)$$

B. Scaling Procedure

The scaling procedure is the most difficult part of absolute quantification. The scaling constant $k\text{AIF}_{\text{int}}$ can be estimated in several ways.

One option is to select the imaging plane so that an AIF ROI can be placed inside a large artery feeding the analyzed tissue (e.g., in [11] the AIF ROI was placed in the left ventricle close to the myocardium tissue ROIs). The constant $k\text{AIF}_{\text{int}}$ can be set to the integral of the tracer concentration curve in the AIF ROI. The drawback of this approach is that especially the peak of this measured AIF curve is distorted by attenuation, which introduces an error. Another problem of measuring a time intensity curve in an artery is the dependence of the backscattered signal amplitude on blood velocity and pressure (the mean of which is different in large arteries and in microcapillaries) [25], [26].

Another approach is to estimate the level of the measured AIF curve in a short time interval at the tail (calculated e.g., as the area under the curve in this interval) where the AIF curve is fairly smooth and the contrast-agent concentration is fairly small so that the attenuation caused by the contrast agent is negligible. At this later stage, the contrast agent concentration in the arterial and venous tree is the same, hence the ROI could also be selected in a vein instead of a big artery. This later-part AIF level can then be imposed to each estimate of $\text{AIF}(t)$ in (1) in the curve fitting. This imposes an absolute scaling of the AIF in the fitting procedure and leads to estimation of absolute F_b according to (1). Subsequently, V_b is calculated according to (5). The drawback of this approach is the low signal-to-noise ratio in the later part of the AIF curve and blood velocity- and pressure-dependence of the backscattered signal, which introduces an estimation error.

The scaling can also be done using a ROI placed in a reference tissue with a known value of F_b or V_b (from literature or from a reference perfusion imaging with another modality). Then, the constant $k\text{AIF}_{\text{int}}$ is set to yield this known value of F_b or V_b according to (5).

Finally, a standardized acquisition protocol can be used with the same setting of the ultrasound scanner (same ultrasound power, focal point depth, etc.), a standardized position of the probe and a bolus dose normalized with respect to the patient weight. This will allow use of a population-based scaling constant $k\text{AIF}_{\text{int}}$, in a similar way as in blind AIF estimation in DCE-MRI [27]. This constant could be found, for example, by acquiring an AIF from a nearby feeding artery using a separate recording with a low-contrast-agent bolus (as used in this paper later) using the same ultrasound-scanner setting.

This approach assumes that the influence of the attenuation caused by tissue is the same in the recordings across all patients or corrected for by time gain compensation or a more advanced method. Also, for this approach, the problem of blood velocity- and pressure-dependence of the backscattered signal remains present.

If none of these methods can be used, only the relative values of V_b and F_b can be estimated. This approach still allows comparison of these perfusion parameters between tissues within the ultrasound image.

C. Blind Deconvolution

The models fitted to the bolus and replenishment signals are convolutional, hence, the curve fitting problem can be formulated as a deconvolution problem. The least-mean-squares curve fitting is used here. This corresponds to the maximum likelihood deconvolution for Gaussian noise distribution [28] (used in scheme 1, described subsequently). In scheme 2, an additional assumption of smoothness and positivity of the AIF is used. This leads to the maximum *a posteriori* (MAP) deconvolution [28]. The two deconvolution approaches fall into the deconvolution group called Bayesian deconvolution [29]. Two curve fitting schemes are proposed; scheme 1 is used here for initial estimation of $R(t)$ and AIF(t) and these estimates are further refined in scheme 2.

- Scheme 1: A straightforward approach is to use the replenishment part to estimate $R(t)$ and subsequently to use this estimate and the bolus-part curve $C_{\text{bolus}}(t)$ to estimate AIF(t). This would correspond to the quantitative parameter estimation using the replenishment method in [11] with the advantage of bolus administration instead of infusion, and with an additional feature estimated for each ROI—the local AIF, for the vascular tree characterization.
- Scheme 2: A more robust approach to estimate $R(t)$ and AIF(t) is to apply curve fitting of both the bolus and replenishment parts simultaneously, using a blind multichannel deconvolution [30]. Here, both parts are considered as two independent measurements with the same unknown convolutional kernel, $R(t)$, and different arterial components of the convolution. The arterial component in the bolus part is an unknown function $F_b k \text{AIF}(t)$. In the replenishment part, the arterial component is $F_b k C_0 H(t)$, which is a known function except for the scaling factor $F_b k C_0$. When including additional *a priori* information in the estimation process (positivity and smoothness of the AIF), scheme 2 leads to an estimation scheme which is more robust with respect to low signal-to-noise ratio, speckle, and movement artifacts.

The blind multichannel deconvolution is formulated as the following optimization problem:

$$\begin{aligned}
 R(p), F_b k \text{AIF}(n) &= \arg\{\min(J_{\text{bolus}} + J_{\text{repl}} + J_{\text{prior}})\} \\
 J_{\text{bolus}} &= \sum_{n=1}^N [k C_{\text{bolus}}(n) - F_b k \text{AIF}(n) * R(n)]^2 \\
 J_{\text{repl}} &= \sum_{m=1}^M [k C_{\text{repl}}(m) - F_b k C_0 H(m) * R(m)]^2 \\
 J_{\text{prior}} &= \lambda \sum_{n=1}^N [k \text{AIF}(n) * L(n)]^2.
 \end{aligned} \tag{6}$$

Because of the discrete character of the signals, the time variable t is replaced with indices n , m , and p . Denoting the signal lengths of the bolus and replenishment parts in samples as N and M , respectively, the tissue residue function, $R(p)$, is estimated for $p = 1 \dots P$, where P is the maximum of N and M . The first two terms of the criterion function, J_{bolus} and J_{repl} , are the maximum-likelihood terms describing the fidelity of the measured signals $k C_{\text{bolus}}(n)$ and $k C_{\text{repl}}(m)$ to the model. The third term, J_{prior} , is the prior term penalizing high-frequency components of AIF(n). The parameter λ is a weighting factor affecting the smoothness of the resulting AIF estimation. $L(n)$ is the Laplacian operator (high-pass filter) defined as a sequence $[-1, 2, -1]$. This prior term formulation is also known as Tikhonov regularization [31]. To provide a unique solution of the optimization, the constraint $R(0) = 1$ is applied.

The optimization algorithm used here is the Broyden–Fletcher–Goldfarb–Shanno (BFGS) quasi-Newton method with a cubic line search procedure [32], [33] as implemented in the Matlab Optimization toolbox (The MathWorks, Inc., Natick, MA), function `fminunc`.

IV. DATA AND EVALUATION METHODS

The bolus-and-burst method was tested on data sets recorded from 8 patients with Crohn’s disease included in a broader clinical study. Group 1 consisted of 5 patients operated on because of stenotic disease or failure of medical treatment. Group 2 consisted of 3 patients starting medical treatment because of an acute flare up. The treatment decisions were based on biochemical markers and clinical, radiological, and endoscopic examinations, and were made before inclusion in the study. The ultrasound acquisition was done using GE Logiq E9 ultrasound scanner (GE Healthcare, Milwaukee, WI) with a linear probe (9L) to acquire the dynamic sequence using the General setting in the contrast mode (power modulation mode, probe frequency 3.5 MHz) with the frame rate 11 Hz, color map 2/0, MI = 0.11. Each patient data set consisted of two recordings (see Fig. 1 for an example). The artery recording was acquired from a region of the right iliac artery with a dose of 0.4 mL of SonoVue (Bracco Imag-

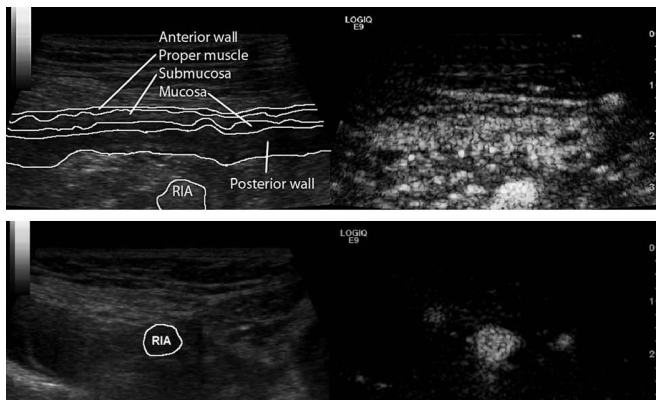


Fig. 1. Example of (top) tissue and (bottom) artery recordings: (left) fundamental-harmonic image, (right) second-harmonic image. RIA denotes the right iliac artery.

ing S.p.A., Milan, Italy) for approximately 60 s and with no high-energy pulses. The tissue recording was acquired with a dose of 4.4 mL of SonoVue for approximately 90 s with the high-energy pulse sequence applied 60 s after the bolus application. The contrast agent was drawn from the same vial. The time delay between the two injections was 5 to 10 min. The length of the replenishment part was set to 12 s based on visual assessment of the tracer concentration curves so that inclusion of the decay part is avoided and, at the same time, that the replenishment part is sufficiently long.

In each tissue recording, one ROI was drawn covering the anterior wall of bowel, including mucosa, submucosa, and muscularis. The average number of pixels in the ROIs was 4952. In each artery recording, one ROI was drawn inside the artery in the upper (proximal) half of the arterial cross section (to minimize attenuation effect). The mean intensity time curve was computed from the mean pixel intensity within the ROI in each frame. Because the image recordings were available as video data, the image intensity curves were transformed to tracer concentration curves (ultrasound intensity, i.e., acoustical units squared) using the linearization described in [24]. The dynamic range and gain values needed for the linearization were obtained from the stored ultrasound-scanner settings. An example of the tracer concentration curves from the data sets in Fig. 1 are shown in Fig. 2. The arterial tracer concentration curves contained repetitive spikes caused by blood flow and pressure pulsation. The signal was filtered using order statistic filtering so that every sample is replaced by the maximum of the neighboring samples within a floating window. The window size was set experimentally to 15 samples (1.4 s) to eliminate the blood flow and pressure oscillation from the signal. The resulting envelope of the signal [see Fig. 2(b)] was used as the reference AIF. The choice of this filtering was based on the resulting estimates of blood flow in the intestinal wall ROIs being closest to the expected values based on the literature, as discussed later. This filtering approximately accounted for the dif-

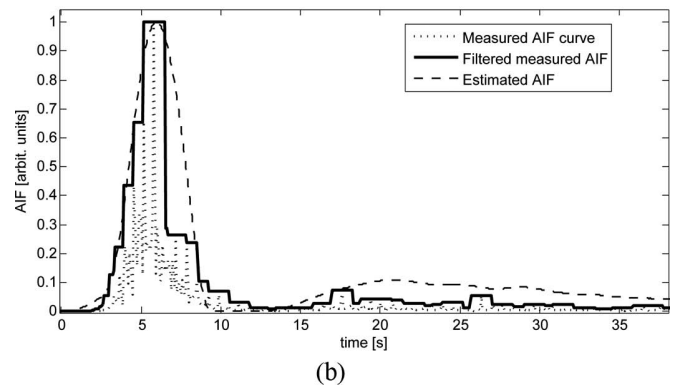
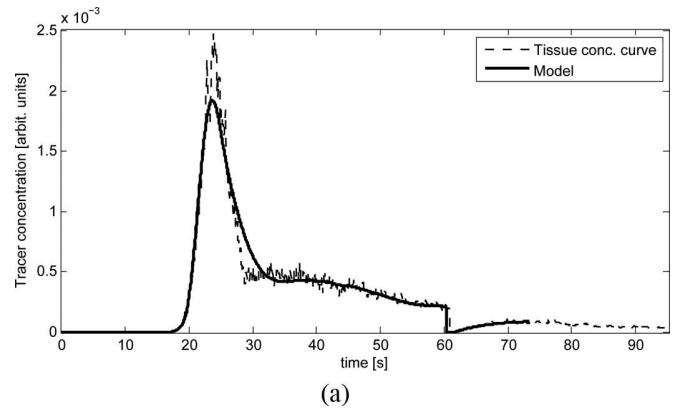


Fig. 2. Tracer concentration curves. (a) Intestinal wall region of interest (ROI) in a tissue recording: (dashed) measured and (solid) fitted curves. (b) Right iliac artery ROI in the artery recording: (solid thin) measured, (solid thick) filtered, and (dashed) estimated from bolus-and-burst method; note the regular peaks of the measured arterial tracer concentration curve which are due to blood pressure oscillation.

ference in attenuation, blood pressure, and velocity in the tissue and artery ROIs. Other alternatives, including median filtering, minimum of the neighboring samples, and low-pass filtering, resulted in blood flow estimates that were too high.

The DCE-US data were processed using the one-compartment pharmacokinetic model described previously to constrain the curve-fitting problem and, hence, to provide more robustness with respect to noise, speckle presence, and movement artifacts.

The evaluation was done as follows. First, the results of the bolus-and-burst method were compared with those of the burst-replenishment method to evaluate the noise-robustness of the two approaches and show their applicability to ROIs of various sizes. The burst-replenishment method was applied to the replenishment part of the tracer concentration curves, whereas the bolus-and-burst method was applied to both the bolus and replenishment parts. The tracer concentration curves were obtained from a homogeneous well-perfused ROI in the intestinal wall. In each experiment, the total number of 608 curves (1 per pixel) were randomly divided into a specified number of groups (here 1, 3, 6, 20, 30, 40, and 60 groups). This

corresponded to ROIs of 608, 202, 101, 30, 20, 15, and 10 pixels, respectively. The evaluation was done for MTT. Then, the accuracy of the AIF estimation was visually evaluated. The measured AIFs were obtained as the tracer concentration curves from ROIs in the right iliac artery in the 8 artery recordings of the corresponding patients. The mean of the measured AIFs was visually compared with the mean of the AIFs estimated from the 8 tissue recordings of the corresponding patients. Before averaging, the AIFs were scaled to a maximum value of 1 and shifted manually so that the first-pass peaks overlapped.

Finally, for completeness and illustration purposes, all perfusion parameters, MTT, V_b , and F_b , were estimated for the intestinal wall ROIs of all 8 patients and related to literature values.

The scaling procedure necessary for absolute quantification of V_b and F_b was done as described here. The test recordings were not sufficiently standardized, in the sense that the depth and ultrasound power at the ROI locations was very variable (area under the curve of the tracer concentration curves varied by a factor of up to 1000 times). Hence, the use of a common scaling factor was not possible. To improve the estimation accuracy, the scaling procedure was done using the measured AIF of each patient. V_b was estimated according to (4), where $C(t)$ was the complete tracer concentration curve including both the bolus and replenishment parts, except for the time span of the high-energy pulse sequence. Hct was set to 0.4 and r to 0.7 [34]. F_b was then derived from MTT and V_b using (5). In the ideal case, for standardized recordings in which the depth and ultrasound power in different acquisitions would be comparable, the need for measured AIFs could be avoided. Only one such AIF measurement would be needed to determine the scaling constant $k_{\text{AIF}_{\text{int}}}$.

V. RESULTS

A comparison of the burst-replenishment and bolus-and-burst methods with respect to the size of the ROI is summarized in Fig. 3. For large ROIs (608, 202, and 101 pixels), both methods gave comparable MTT estimates (7.7 s for the burst-replenishment and 7.1 s for the bolus-and-burst methods) with low standard deviation (1.6 s for the burst-replenishment and 1.3 s for the bolus-and-burst methods). For smaller ROIs, the MTT estimates started to deviate from these values. The burst-replenishment method resulted in clearly higher estimation errors and higher standard deviation than the bolus-and-burst method. Closer inspection of the MTT estimates showed that for ROIs of 15 and 10 pixels, the burst-replenishment method resulted in several outlier MTT estimates (higher than 100 s). No such outlier estimates were obtained using the bolus-and-burst method.

Fig. 4 shows the comparison of the measured and estimated AIFs from the 8 clinical recording sets. The mean of the measured AIFs and the mean of the estimated AIFs

[Fig. 4(a)] show a fairly good fit, especially for the first-pass peak. The second-pass peak of the estimated AIFs was slightly higher compared with the measured AIFs. The time location of the second-pass peak in both the measured and estimated AIFs was approximately the same. Fig. 4(b) shows the variability of the measured and estimated AIFs as confidence intervals (mean curve \pm standard deviation). For the first-pass peak, the intervals match fairly well; for the second-pass peak, the confidence interval of the estimated AIFs was slightly wider.

Table I summarizes the perfusion parameters estimated from the two patient groups. For the 5 patients of group 1, the values are given as mean \pm standard deviation, whereas for the 3 patients of group 2, the values are given for each patient. In [35], blood flow was measured using radioisotope washout technique for patients divided into groups with characteristics corresponding to the groups used here. The blood flow in the intestine wall (including mucosa, submucosa, and muscularis) of this study are included in Table I. Assuming the density of tissue is approximately 1 g/mL, the units used here (mL/min/100 mL tissue) and in [35] (mL/min/100 g tissue) are equivalent. These literature values show a fairly wide range depending on the physiological state of the tissue.

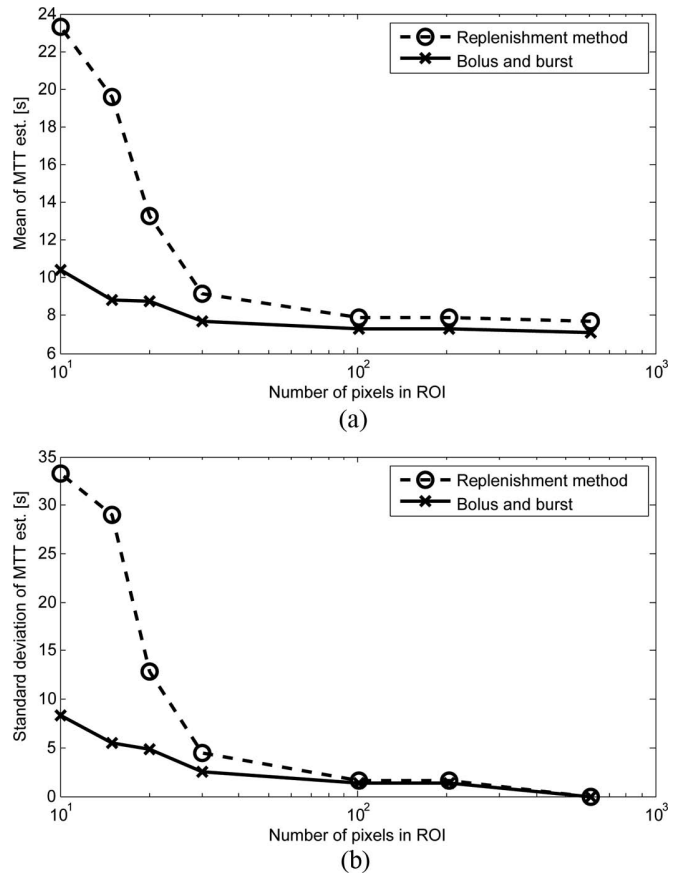


Fig. 3. (a) Mean and (b) standard deviations of mean transit time (MTT) estimates for burst-replenishment and bolus-and-burst methods applied to regions of interest (ROIs) of various size.

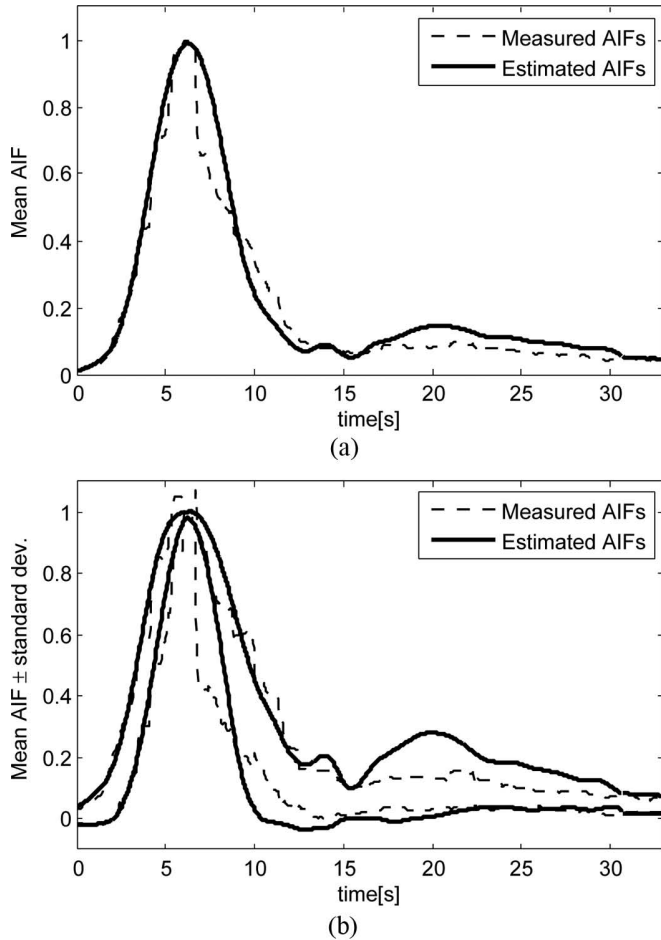


Fig. 4. Estimated and measured arterial input functions (AIFs): (a) mean AIFs and (b) confidence intervals shown as mean \pm standard deviation at each sample.

Although the number of patients used here in the two groups is low for a statistical evaluation, according to Table I, the flow values estimated here are clearly higher than in [35]. The results also indicate that in line with [35] and with physiological expectations, blood flow and blood volume are clearly higher for group 2 than for group 1 with a factor of 4, on average. In [35], the ratio in blood flow between the two groups was 6 for colon and 3 for ileum examinations.

VI. DISCUSSION AND CONCLUSIONS

A new multichannel blind deconvolution method for ultrasound perfusion analysis is proposed. It is based on an acquisition technique combining the bolus-tracking and burst-replenishment methods, an acquisition approach already used in [18]–[20]. Here, the signals corresponding to both parts are modeled according to the concepts of an AIF and a tissue residue function known from bolus-tracking in other imaging modalities. To do this, the model for the replenishment part had to be formulated in terms of an AIF and a tissue residue function.

The new approach can provide absolute physical perfusion parameters, if one of the proposed scaling procedures can be applied. This is possible when a large artery, vein, or a reference tissue (with known blood volume or flow) is available in the imaged area or in a standardized setup with possible population-based scaling. So far, there has been only one method providing absolute perfusion parameters using a DCE-US burst-replenishment method [11], and it was applied only in cardiology. Bolus-and-burst is an alternative to this method using a bolus application which is easier to apply than an infusion application in the burst-replenishment techniques. Furthermore, the proposed scaling procedures also allow absolute quantification of perfusion parameters in other organs than myocardium. Here, the scaling procedures were suggested in the context of the bolus-and-burst technique, but it could also be applied as a modification to the burst-replenishment technique in [11] to extend it for absolute quantification in other organs.

In addition to other known DCE-US methods, the presented method provides an estimate of the local AIF. This avoids the need to directly measure the AIF time course in a feeding artery, except for some type of scaling procedure. The direct AIF measurement is a problematic task, especially for ultrasound imaging because of attenuation of the contrast agent in the artery, movement artifacts, low spatial resolution, and the presence of speckle. In addition, as in other modalities [27], an AIF from a big artery is different from the local AIF because of the bolus dispersion effect, which leads to a broader local AIF. Omitting this effect leads to distorted perfusion parameter estimates. Finally, the comparison of the local tissue-specific AIFs

TABLE I. PERFUSION PARAMETERS ESTIMATED IN SELECTED TISSUE REGIONS OF INTEREST.

	MTT [s]	V_b [mL/100 mL of tissue]	F_b [mL/100 mL of tissue]
Group 1			
Bolus-and-burst	4.6 ± 1.5	5.5 ± 1.8	75.3 ± 31.8
Colon [35]			6–26 (3 patients)
Ileum [35]			6–16 (6 patients)
Group 2			
Bolus-and-burst	5.3, 4.0, 5.1	14.5, 30.1, 15.8	164.3, 451.7, 187.0
Colon [35]			43–155 (5 patients)
Ileum [35]			8–75 (6 patients)

MTT = mean transit time.

between various tissues in the imaged area or between the examinations might be used in the future for characterization of the arterial tree.

The new methodology was illustrated on clinical recordings from 8 Crohn's disease patients. Its correctness was supported by a fairly good agreement between the estimated and separately measured AIFs. The slightly lower level of the second-pass peak maximum in the estimated AIFs could be caused by the attenuation of the contrast agent in the tissue recording, which decreases the tracer concentration curve level more at high concentration (first pass) compared with low concentration (second pass). Scaling according to the first-pass peak in Fig. 4 then leads to increased level of the second pass. Another source of inaccuracy in this comparison is the measured AIFs. They are certainly affected by noise which can distort the result of the order-statistic filtering especially in the presence of outliers, e.g., resulting from motion.

Compared with the burst-replenishment method applied to the same data set within a homogeneous ROI, the bolus-and-burst method was shown to be more noise-robust, and, thus, to allow application to smaller ROIs, leading possibly to estimation of perfusion-parameter maps. This shows the crucial effect of the incorporation of the bolus part of the tissue tracer curve in the estimation process (as assumed for the blind deconvolution scheme 2 in Section III-C).

An attempt to estimate the absolute perfusion parameters using the scaling procedure with the separately measured AIFs was also presented for the patient recordings. Although the number of patients was low for a statistical evaluation, it illustrated a difference in blood flow (and blood volume) values between the two patient groups with a factor similar to that reported in literature [35]. On average, our flow estimates were clearly higher than the values in [35]. The most likely source of possible inaccuracies in our flow estimates is the scaling procedure. Especially, the dependence of the backscattered ultrasound signal intensity on blood flow velocity and pressure must be measured and possibly used for calibration of the signal measurement in arteries. Another source of inaccuracies in the scaling procedure is the attenuation due to the contrast agent and to the tissue itself. Another fact possibly contributing to the mismatch of our flow estimates with the study in [35] could be a different stage of the Crohn's disease in our study and in [35]. In addition, in our study, the ROIs were drawn in the most severely affected parts of the bowel wall, whereas in [35], less affected tissue parts could also have been included in the studied specimens.

To make DCE-US applicable in real clinical setting, the attenuation problem must be solved. Attenuation caused by tissue might be partly compensated by the standard time gain compensation or possibly by some more advanced methods [36]. However, the main problem for DCE-US is the correction of attenuation caused by the contrast agent. It not only affects the scaling procedure but it also distorts the first-pass part of tracer concentra-

tion curves in well perfused tissues. This decreases the level of the first-pass peak compared with the rest of the tracer concentration curves, and it can even result in a valley rather than a peak in the first-pass part caused by very high instantaneous contrast agent concentration. It could be avoided to some extent by using a lower dose of the contrast agent and by using some future imaging techniques which will be more sensitive to the contrast agent [37]–[39]. Another approach is to use a postprocessing approach for estimation of the attenuation coefficient and subsequent attenuation correction [40].

A final important issue is the need for motion compensation. This was avoided here by selecting recordings in which movement artifacts were small. In a real setup, however, the movement must be compensated as well. In case of in-plane movements, image registration can be applied [41]. If movement perpendicular to the imaging plane is unavoidable, the problem can be approached only by using 3-D ultrasound imaging.

APPENDIX A REPLENISHMENT KINETICS

The reformulated kinetic model of the replenishment part according to (2) can be simplified because a convolution of a function [here $R(t)$] with a unit step function is an integral of that function:

$$C_{\text{repl}}(t) = F_b C_0 \int_0^t R(\tau) d\tau. \quad (7)$$

For a one-compartment model, where $R(t) = \exp(-(F_b/V_b)t)$, the integral can be solved analytically:

$$C_{\text{repl}}(t) = V_b C_0 (1 - e^{-(F_b/V_b)t}). \quad (8)$$

Hence, in (3), $A = V_b C_0$ and $\beta = F_b/V_b$.

APPENDIX B INTEGRAL OF AIF

According to the law of conservation of mass, the mass M of contrast agent passing through a given arterial cross-section with flow F is

$$M = F \int_0^{\infty} \text{AIF}_a(t) dt. \quad (9)$$

Along an artery with no branching, both M and F are constant. At branching locations in the arterial tree, these values change but the ratio M/F remains constant. Hence, the integral in (9) remains constant. This assumes no con-

trast-agent leakage in the arterial tree, which is a valid assumption according to physiology.

REFERENCES

- [1] F. Piscaglia, C. Nolsoe, C. F. Dietrich, D. O. Cosgrove, O. H. Gilja, M. Bachmann Nielsen, T. Albrecht, L. Barozzi, M. Bertolotto, O. Catalano, M. Claudon, D. A. Clevert, J. M. Correas, M. D'Onofrio, F. M. Drudi, J. Eyding, M. Giovannini, M. Hocke, A. Ignee, E. M. Jung, A. S. Klausner, N. Lassau, E. Leen, G. Mathis, A. Saftoiu, G. Seidel, P. S. Sidhu, G. ter Haar, D. Timmerman, and H. P. Weskott, "The EFSUMB guidelines and recommendations on the clinical practice of contrast enhanced ultrasound (CEUS): Update 2011 on non-hepatic applications," *Ultraschall Med.*, vol. 33, no. 1, pp. 33–59, 2012.
- [2] K. Wei, A. R. Jayaweera, S. Firoozan, A. Linka, D. M. Skyba, and S. Kaul, "Quantification of myocardial blood flow with ultrasound-induced destruction of microbubbles administered as a constant venous infusion," *Circulation*, vol. 97, no. 5, pp. 473–483, 1998.
- [3] H. J. Paltiel, L. A. Kalish, R. A. Susaeta, F. Frauscher, P. L. O'Kane, and L. G. Freitas-Filho, "Pulse-inversion US imaging of testicular ischemia: Quantitative and qualitative analyses in a rabbit model," *Radiology*, vol. 239, no. 3, pp. 718–729, 2006.
- [4] S.-J. Rim, H. Leong-Poi, J. R. Lindner, D. Couture, D. Ellegala, H. Mason, M. Durieux, N. F. Kassel, and S. Kaul, "Quantification of cerebral perfusion with "real-time" contrast-enhanced ultrasound," *Circulation*, vol. 104, no. 21, pp. 2582–2587, 2001.
- [5] K. Wei, E. Le, J. Bin, M. Coggins, J. Thorpe, and S. Kaul, "Quantification of renal flow with contrast-enhanced ultrasound," *J. Am. Coll. Cardiol.*, vol. 37, no. 4, pp. 1135–1140, 2001.
- [6] O. Lucidarme, S. Franchi-Abella, J. Correas, S. L. Bridal, E. Kurtsovski, and G. Berger, "Blood flow quantification with contrast-enhanced US: "Entrance in the section" phenomenon—Phantom and rabbit study," *Radiology*, vol. 228, no. 2, pp. 473–479, 2003.
- [7] G. J. Lueck, T. K. Kim, P. N. Burns, and A. L. Martel, "Hepatic perfusion imaging using factor analysis of contrast enhanced ultrasound," *IEEE Trans. Med. Imaging*, vol. 27, no. 10, pp. 1449–1457, 2008.
- [8] E. Quaia and T. Bartolotta, *Contrast Media in Ultrasonography: Basic Principles and Clinical Applications* (Medical Radiology series). New York, NY: Springer, 2005.
- [9] M. Arditi, P. J. A. Frinking, X. Zhou, and N. G. Rognin, "A new formalism for the quantification of tissue perfusion by the destruction–replenishment method in contrast ultrasound imaging," *IEEE Trans. Ultrason. Ferroelectr. Freq. Control*, vol. 53, no. 6, pp. 1118–1129, 2006.
- [10] J. M. Hudson, R. Karshafian, and P. N. Burns, "Quantification of flow using ultrasound and microbubbles: A disruption replenishment model based on physical principles," *Ultrasound Med. Biol.*, vol. 35, no. 12, pp. 2007–2020, 2009.
- [11] R. Vogel, A. Indermuhle, J. Reinhardt, P. Meier, P. T. Siegrist, M. Namdar, P. A. Kaufmann, and C. Seiler, "The quantification of absolute myocardial perfusion in humans by contrast echocardiography: Algorithm and validation," *J. Am. Coll. Cardiol.*, vol. 45, no. 5, pp. 754–762, 2005.
- [12] H. Komatsu, S. Yamada, H. Iwano, M. Okada, H. Onozuka, T. Mikami, S. Yokoyama, M. Inoue, S. Kaga, M. Nishida, C. Shimizu, K. Matsuno, and H. Tsutsui, "Angiotensin II receptor blocker, valsartan, increases myocardial blood volume and regresses hypertrophy in hypertensive patients," *Circ. J.*, vol. 73, no. 11, pp. 2098–2103, 2009.
- [13] T. Rutz, S. F. de Marchi, M. Schwerzmann, R. Vogel, and C. Seiler, "Right ventricular absolute myocardial blood flow in complex congenital heart disease," *Heart*, vol. 96, no. 13, pp. 1056–1062, 2010.
- [14] N. Lassau, S. Koscielny, L. Albiges, L. Chami, B. Benatsou, M. Chebil, A. Roche, and B. J. Escudier, "Metastatic renal cell carcinoma treated with sunitinib: Early evaluation of treatment response using dynamic contrast-enhanced ultrasonography," *Clin. Cancer Res.*, vol. 16, no. 4, pp. 1216–1225, 2010.
- [15] X. Gu, H. Zhong, M. Wan, X. Hu, D. Lv, L. Shen, and X. Zhang, "Parametric imaging of blood perfusion with low-cost diagnostic ultrasound equipment," in *IEEE Proc. Ultrasonics Symp.*, 2008, pp. 1338–1341.
- [16] M. P. J. Kuenen, M. Mischi, and H. Wijkstra, "Contrast-ultrasound diffusion imaging for localization of prostate cancer," *IEEE Trans. Med. Imaging*, vol. 30, no. 8, pp. 1493–1502, 2011.
- [17] M. Gauthier, F. Tabarout, I. Leguerney, M. Polrot, S. Pitre, P. Peronneau, and N. Lassau, "Assessment of quantitative perfusion parameters by dynamic contrast-enhanced sonography using a deconvolution method: An in vitro and in vivo study," *J. Ultrasound Med.*, vol. 31, no. 4, pp. 595–608, 2012.
- [18] M. Krix, F. Kiessling, S. Vosseler, I. Kiessling, M. Le-Huu, N. E. Fusenig, and S. Delorme, "Comparison of intermittent-bolus contrast imaging with conventional power Doppler sonography: Quantification of tumour perfusion in small animals," *Ultrasound Med. Biol.*, vol. 29, no. 8, pp. 1093–1103, 2003.
- [19] M. Krix, C. Plathow, F. Kiessling, F. Herth, A. Karcher, M. Essig, H. Schmitteckert, H. U. Kauczor, and S. Delorme, "Quantification of perfusion of liver tissue and metastases using a multivessel model for replenishment kinetics of ultrasound contrast agents," *Ultrasound Med. Biol.*, vol. 30, no. 10, pp. 1355–1363, 2004.
- [20] J.-H. Zhou, L.-H. Cao, J.-B. Liu, W. Zheng, M. Liu, R. Z. Luo, F. Han, and A. H. Li, "Quantitative assessment of tumor blood flow in mice after treatment with different doses of an antiangiogenic agent with contrast-enhanced destruction-replenishment US," *Radiology*, vol. 259, no. 2, pp. 406–413, 2011.
- [21] M. Mezl, R. Jirik, V. Harabis, and R. Kolar, "Quantitative ultrasound perfusion analysis in vitro," in *Proceedings of Biosignal 2010: Analysis of Biomedical Signals and Images*, vol. 20. Brno, Czech Republic, Brno University of Technology, 2010, pp. 279–283.
- [22] P. Tofts, *Quantitative MRI of the Brain: Measuring Changes Caused by Disease*. New York, NY: Wiley, 2005.
- [23] L. Ostergaard, "Principles of cerebral perfusion imaging by bolus tracking," *J. Magn. Reson. Imaging*, vol. 22, no. 6, pp. 710–717, 2005.
- [24] N. G. Rognin, P. Frinking, M. Costa, and M. Arditi, "In-vivo perfusion quantification by contrast ultrasound: Validation of the use of linearized video data vs. raw RF data," in *IEEE Proc. Ultrasonics Symp.*, 2008.
- [25] M. Mischi, A. H. M. Jansen, A. A. C. M. Kalker, and H. H. M. Korsten, "Identification of ultrasound contrast agent dilution systems for ejection fraction measurements," *IEEE Trans. Ultrason. Ferroelectr. Freq. Control*, vol. 52, no. 3, pp. 410–420, 2005.
- [26] M. Mischi, A. H. Jansen, and H. H. Korsten, "Identification of cardiovascular dilution systems by contrast ultrasound," *Ultrasound Med. Biol.*, vol. 33, no. 3, pp. 439–451, 2007.
- [27] T. Taxt, R. Jirik, C. Rygh, R. Grüner, M. Bartos, E. Andersen, F. R. Curry, and R. K. Reed, "Single-channel blind estimation of arterial input function and tissue impulse response in DCE-MRI," *IEEE Trans. Biomed. Eng.*, vol. 59, no. 4, pp. 1012–1021, 2012.
- [28] J. L. Starck, E. Pantin, and F. Murtagh, "Deconvolution in astronomy: A review," *Publ. Astron. Soc. Pac.*, vol. 114, no. 800, pp. 1051–1069, 2002.
- [29] E. Thiébaud and J.-M. Conan, "Strict a priori constraints for maximum-likelihood blind deconvolution," *J. Opt. Soc. Am. A*, vol. 12, no. 3, pp. 458–491, 1995.
- [30] D. Y. Riabkov and E. V. R. Di Bella, "Estimation of kinetic parameters without input functions: Analysis of three methods for multichannel blind identification," *IEEE Trans. Biomed. Eng.*, vol. 49, no. 11, pp. 1318–1327, 2002.
- [31] A. Tarantola, *Inverse Problem Theory and Methods for Model Parameter Estimation*, 1st ed., Philadelphia, PA: Society for Industrial and Applied Mathematics, 2004.
- [32] C. G. Broyden, "The convergence of a class of double-rank minimization algorithms 1. General considerations," *IMA J. Appl. Math.*, vol. 6, no. 1, pp. 76–90, 1970.
- [33] R. Fletcher, "A new approach to variable metric algorithms," *Comput. J.*, vol. 13, no. 3, pp. 317–322, 1970.
- [34] G. Parker and D. Buckley, "Tracer kinetic modelling for T1-weighted DCE-MRI," in *Dynamic Contrast-Enhanced Magnetic Resonance Imaging in Oncology* (Medical Radiology series), A. Jackson, D. Buckley, and G. Parker, Eds., New York, NY: Springer, 2005, pp. 81–92.
- [35] L. Hultén, J. Lindhagen, O. Lundgren, S. Fasth, and C. Åhrén, "Regional intestinal blood flow in ulcerative colitis and Crohn's disease," *Gastroenterology*, vol. 72, no. 3, pp. 388–396, 1977.
- [36] G. Treece, R. Prager, and A. Gee, "Ultrasound attenuation measurement in the presence of scatterer variation for reduction of shad-

- owing and enhancement," *IEEE Trans. Ultrason. Ferroelectr. Freq. Control*, vol. 52, no. 12, pp. 2346–2360, 2005.
- [37] E. Quaia, "Microbubble ultrasound contrast agents: An update," *Eur. Radiol.*, vol. 17, no. 8, pp. 1995–2008, 2007.
- [38] S. Qin, C. F. Caskey, and K. W. Ferrara, "Ultrasound contrast microbubbles in imaging and therapy: Physical principles and engineering," *Phys. Med. Biol.*, vol. 54, no. 6, pp. R27–R57, 2009.
- [39] M. Crocco, P. Pellegretti, C. Sciallero, and A. Trucco, "Combining multi-pulse excitation and chirp coding in contrast-enhanced ultrasound imaging," *Meas. Sci. Technol.*, vol. 20, no. 10, art. no. 104017, 2009.
- [40] S. Mulé, A. De Cesare, O. Lucidarme, F. Frouin, and A. Herment, "Regularized estimation of contrast agent attenuation to improve the imaging of microbubbles in small animal studies," *Ultrasound Med. Biol.*, vol. 34, no. 6, pp. 938–948, 2008.
- [41] R. Kolar, R. Jirik, V. Harabis, K. Nylund, O. H. Gilja, "Registration of ultrasound contrast images for perfusion analysis," in *IEEE Proc. Ultrasonics Symp.*, 2009, pp. 1251–1254.

Authors' photographs and biographies were unavailable at time of publication.

4.1.2 Paper II

K. Nylund, R. Jiřík, M. Mezl, S. Leh, T. Hausken, F. Pfeffer, S. Ødegaard, T. Taxt, O.H. Gilja, Quantitative Contrast-Enhanced Ultrasound Comparison Between Inflammatory and Fibrotic Lesions in Patients with Crohn's Disease, *Ultrasound Med. Biol.* 39 (2013) 1197–1206.

<https://doi.org/10.1016/j.ultrasmedbio.2013.01.020>.

(IF 2.099)

Author's contribution:

- author of the methodology and software used for perfusion analysis (from image import to estimation of perfusion parameters)
- providing consultations on data processing
- paper co-writing

● *Original Contribution*

QUANTITATIVE CONTRAST-ENHANCED ULTRASOUND COMPARISON BETWEEN INFLAMMATORY AND FIBROTIC LESIONS IN PATIENTS WITH CROHN'S DISEASE

KIM NYLUND,^{*†} RADOVAN JIRIK,^{‡§} MARTIN MEZL,[§] SABINE LEH,^{||} TRYGVE HAUSKEN,^{*†}
FRANK PFEFFER,[¶] SVEIN ØDEGAARD,^{*†} TORFINN TAXT,[#] and ODD HELGE GILJA^{*†}

^{*}Institute of Medicine, University of Bergen, Bergen, Norway; [†]National Centre of Ultrasound in Gastroenterology, Haukeland University Hospital, Bergen, Norway; [‡]Institute of Scientific Instruments, Academy of Sciences of the Czech Republic; [§]International Clinical Research Center–Center of Biomedical Engineering, St. Annes University Hospital Brno, Brno, Czech Republic; ^{||}Department of Pathology, Haukeland University Hospital, Bergen, Norway; [¶]Department of Surgical Sciences, University of Bergen, Bergen, Norway; and [#]Department of Biomedicine, University of Bergen, Bergen, Norway

(Received 24 August 2012; revised 25 January 2013; in final form 27 January 2013)

Abstract—The aim of this study was to determine whether there are differences in absolute blood flow between patients with Crohn's disease with inflammation or fibrosis using contrast-enhanced ultrasound. Eighteen patients with fibrotic disease and 19 patients with inflammation were examined. Video sequences of contrast data were analyzed using a pharmacokinetic model to extract the arterial input and tissue residue functions with a custom software, enabling calculation of the absolute values for mean transit time, blood volume and flow. Feasibility of the examination was 89%. The fibrosis group had lower blood volume (0.9 vs. 3.4 mL per 100 mL tissue; $p = 0.001$) and flow (22.6 vs. 45.3 mL/min per 100 mL tissue; $p = 0.003$) compared with the inflammation group. There was no significant difference in mean transit time (3.9 vs. 5.5 s). In conclusion, absolute perfusion measurement in the gastrointestinal wall using contrast-enhanced ultrasound is feasible. There seems to be reduced blood volume and blood flow in patients with fibrotic disease. (E-mail: mpkkn@med.uib.no or kimnylund1@gmail.com) © 2013 World Federation for Ultrasound in Medicine & Biology.

Key Words: Crohn's disease, Inflammatory bowel disease, Intestinal blood flow, Ultrasonography.

INTRODUCTION

Crohn's disease is an inflammatory disease that can affect the entire gastrointestinal (GI) tract, changing between active and inactive disease (Odze 2003). An important challenge in deciding how to treat Crohn's disease is to identify and separate active inflammation from fibrotic lesions, because surgery should be performed if the stenosis is mainly fibrotic. The inflammatory activity in inflammatory bowel disease usually is characterized by neo-vascularization and increased vessel density and fibrosis by comparatively low vessel density; therefore, a non-invasive diagnostic tool for measuring vessel density might be useful for separating mainly inflammatory lesions from mainly fibrotic lesions (Alkim et al. 2009; Danese et al. 2006; Hulten et al. 1977;

Kruschewski et al. 1995). Although small arteries in the GI wall can be seen with ultrasound imaging, there is no imaging method with a penetration and resolution good enough to separate intra-mural micro-vessels in the GI wall (Odegaard et al. 1995). Contrast-enhanced ultrasound (CEUS) is a more feasible and indirect method because as it can be used to evaluate perfusion which is related to vessel density and resistance.

Transabdominal ultrasound of the GI tract is currently an established method for primary diagnosis and follow-up of inflammatory bowel disease. It is mainly used for detection of the affected intestine by measuring GI wall thickness and extent of bowel disease, but it is also useful in detecting abscesses, fistulas and stenosis (Nylund et al. 2010).

High-frequency B-mode ultrasound (>7.5 MHz) in combination with CEUS is a potentially useful tool for evaluating changes in disease activity in the affected intestine (Migaleddu et al. 2009). Certain parameters calculated from time intensity analysis of contrast

Address correspondence to: Kim Nylund, Institute of medicine, University of Bergen, Haukeland University Hospital, 5021 Bergen, Norway. E-mail: mpkkn@med.uib.no or kimnylund1@gmail.com

enhancement have also been shown to reflect the histologic degree of inflammation (Girlich et al. 2011; Ripolles et al. 2013). There are also indications that CEUS can be used to separate inflammation from fibrosis or to predict the need for surgery (Quaia et al. 2012; Ripolles et al. 2013).

Microbubbles are true intra-vascular tracers, and CEUS is a fairly non-invasive method that potentially can be used to measure absolute perfusion (Mezl et al. 2010). Perfusion quantification with CEUS has been used to give relative values of blood flow and blood volume. Previous studies have shown a relationship between various relative perfusions parameters and micro-vessel density (Wang et al. 2007, 2011). Unfortunately, relative values do give rise to problems of reproducibility because data acquired by different scanners can differ. Furthermore, most clinical studies present data for which the perfusion parameters are calculated using the log-converted time-intensity data directly on the ultrasound system or from exported video sequences (Girlich et al. 2011, Girlich et al. 2012; Schirin-Sokhan et al. 2011). However, this method can yield erroneous results because it is not mathematically valid (Peronneau et al. 2010). Raw linear data should be used or, if not available, re-linearized data are an acceptable alternative (Rognin et al. 2008). Finally, because there could be a large variation in patient hemodynamics and because different ultrasound machine vendors have different ways of detecting microbubbles, standardization of relative perfusion parameters is difficult.

As a result, we propose to measure absolute perfusion using a new method called “bolus and burst,” which is a combination of two perfusion quantification techniques—bolus tracking and burst replenishment—and enables the calculation of the arterial input function and thus calculation of absolute perfusion (Hudson et al. 2009; Lassau et al. 2010; Ostergaard 2005).

The two main aims of our study were: (i) to determine whether it was feasible to perform transabdominal absolute perfusion measurements in the intestinal wall using CEUS, and (ii) to determine whether there were differences in perfusion parameters between patients with mainly fibro-stenotic disease and patients with mainly inflammatory disease using CEUS and high frequency ultrasound. We also wanted to determine whether there were differences in the frequency of typical ultrasound findings in Crohn’s disease, GI wall thickness and thickness of individual GI wall layers between the two groups. Accordingly, we chose to compare a group of patients with Crohn’s disease receiving medical treatment for a disease flare-up with a group being treated surgically with fibrosis in the GI wall.

MATERIALS AND METHODS

The study was designed as a prospective, comparative pilot study of two groups of patients with Crohn’s disease with different clinical outcomes.

Patients

Thirty-nine patients with Crohn’s disease were prospectively recruited at Haukeland University Hospital from October 2008 to December 2011. Twenty patients were scheduled for surgery (surgery group) and 19 received medical treatment (medical group). Thirty healthy volunteers were also examined as a control group.

The inclusion criteria were surgical resection owing to stenotic disease or lack of response to medical treatment in the surgery group and fibrosis in the examined bowel segment. In the medical group, patients with flare-up of Crohn’s disease (Crohn’s disease activity index [CDAI] > 150), systemic medical treatment with either steroids (prednisolone or hydrocortisone), or tumor necrosis factor- α inhibitors (adalimumab or infliximab) were included. Exclusion criteria were age less than 18 y, pregnancy and contra-indications to the contrast agent. Patients with no findings on ultrasound were not included. The Regional Ethics Committee West approved the study, and all patients gave their informed consent to participate in the study.

Clinical data and biochemical tests

Patient medical history, current and previous treatment and demographic data were collected through patient interviews or access to the medical records. CDAI and Harvey–Bradshaw index were registered before the ultrasound examination (Best et al. 1979; Harvey and Bradshaw 1980). Blood and stool samples for the biochemical analysis were collected within 1 wk after the ultrasound examination. Hemoglobin (g/dL), leucocyte count (10^9 cells/L), platelet count (10^9 cells/L), albumin, and C-reactive protein (CRP) were measured in blood. The stool was analyzed for calprotectin.

Ultrasound examination

All examinations were performed by the primary investigator (K.N.), who is a medical doctor with an experience of approximately 500 ultrasound examinations of the bowel. Two ultrasound scanners were used for the examination; A Logiq 9 ultrasound scanner (General Electric Healthcare, Milwaukee, WI, USA) with 9L (6–8 MHz, linear) and 12L (9–14 MHz, linear) probes, and a Logiq E9 ultrasound scanner (General Electric Healthcare) with 9L (5.5–9 MHz, linear) and ML6-15 (9–15 MHz, linear) probes. The contrast examination was done with the 9L probe on both machines. The Logiq

9 scanner uses pulse inversion with harmonic imaging and the Logiq E9 amplitude modulation for the detection of ultrasound contrast. The large and small bowels were scanned systematically starting from the right iliac quadrant (Nylund *et al.* 2010). All affected areas were registered, but only the area with the thickest wall was chosen for further investigation with contrast-enhanced ultrasound.

High-frequency B-mode examination. The wall thickness and the thickness of the individual ultrasound wall layers corresponding mainly to the mucosa, submucosa and muscularis propria were measured, and the average of three measurements was selected for further analysis (Nylund *et al.* 2012). The length of affected bowel seen with ultrasound was also measured. The probe with the highest frequency range (12L and ML6-15) was used for the B-mode examination down to 4 cm deep when possible. The 9L was used when there was poor image quality with the high frequency probes or for deeper lying bowel segments. We defined high frequency as center frequency of the ultrasound probe greater than 7.5 MHz. A stenosis on ultrasound was defined as an intestinal section with total wall thickness greater than 3 mm, a narrow or closed off lumen, stiff appearance, and a lack of peristaltic movement (Gasche *et al.* 1999). Ultrasound findings typical for Crohn's disease, such as a thickened muscularis mucosa, changes in echogenicity of the submucosa and muscularis propria and lymphocyte aggregates along the outer border of muscularis propria (Crohn's rosary), were scored according to criteria described previously (Nylund *et al.* 2008). Briefly, the echogenicity of wall layers corresponding to the submucosa and muscularis propria was defined using a semi-quantitative scale of 0–2. For the submucosa, 0 = echo rich, 1 = echo rich with sporadic echo poor elements, and 2 = echo rich with diffuse echo poor elements. Similarly, the echogenicity in the proper muscle was defined as: 0 = echo poor; 1 = echo poor with sporadic echo rich elements; and 2 = echo poor with diffuse echo rich elements. Other ultrasound findings in Crohn's disease such as a stenosis, fistulas, loss of stratification, thickened muscularis mucosa and Crohn's rosary were dichotomized as: 0 = not present and 1 = present.

Doppler examination. Color Doppler was performed with the 12L (Logiq9) and the ML6-15 (Logiq E9) with a velocity scale of ± 2 cm/s for detection of slow flow. Gain was increased until to flash artifacts occurred and then decreased until to the flash artifacts disappeared. Color Doppler was scored using a Likert scale of 0–2, where 0–2, 3–5 and >5 color Doppler signals per square centimeter corresponds to scores of 0, 1 and 2, respectively (Spalinger *et al.* 2000). Pulse wave spectral

Doppler of an artery in the submucosa was performed in triplex mode when possible and the resistive index (RI) of three cycles were measured and averaged.

Perfusion analysis

Contrast-enhanced ultrasound. CEUS was performed using a bolus of 4.4 mL of contrast (Sonovue; Bracco, Milan, Italy) injected over 2 s, followed by a flush of 10 mL 0.9% NaCl over 4 s. The mechanical index was 0.09–0.13, and the frame rate was 4–11 frames/s. Approximately 55 s after injection, the bubbles in the examined plane were burst using a high mechanical index flash, and the scanning continued for an additional 30 s. A continuous video recording including a short pre-bolus phase and bolus and replenishment phases was stored as a single 90-s loop (Fig. 1). The same procedure was performed in the healthy volunteers. To get a recording from both the small intestine and the colon, attempts were made to include both a part of the terminal ileum and the right colon in the imaged section. If the terminal ileum had excessive peristalsis or was covered by the cecum, only the colon was examined.

Post-processing. Cine loops were exported as DICOM files and uploaded to a custom software (DCE-US; <http://www.isibrno.cz/perfusion/>). Perfusion analysis was performed as described by Jirik *et al.* (Jirik *et al.* 2013) with a slight modification described later (Fig. 2). The video recording was down-sampled from 4–11 frames/s to 1–2 frames/s, manually corrected for in plane motion artifacts and re-linearized to obtain a signal proportional to the concentration of the contrast agent (Rognin *et al.* 2008). Next, a region of interest in the anterior bowel wall was chosen for perfusion analysis with the “bolus and burst” algorithm (Jirik *et al.* 2013). This algorithm is a multi-channel, blind deconvolution algorithm based on least-squares fitting of the concentration-time-curve with a pharmacokinetic model. According to the model, the bolus-phase concentration time curve (first 60 s) is a convolution of the arterial input function (AIF) and the tissue residue function (TRF), as commonly used in other modalities (Ostergaard 2005). The AIF is modeled as a sum of non-delayed and delayed log-normal functions (Rognin *et al.* 2008). The replenishment phase (final 30 s) is modeled as a convolution of the same TRF, with the corresponding later part of the AIF modeled as described above. Compared with the “bolus and burst” algorithm (Jirik *et al.* 2013), in which the AIF was non-parametric and the replenishment-phase AIF was assumed constant, the current method allows for more reliable and less biased perfusion analysis (R. Jirik, unpublished observations, 2012). The results were then scaled so that the estimated AIF had the same area under

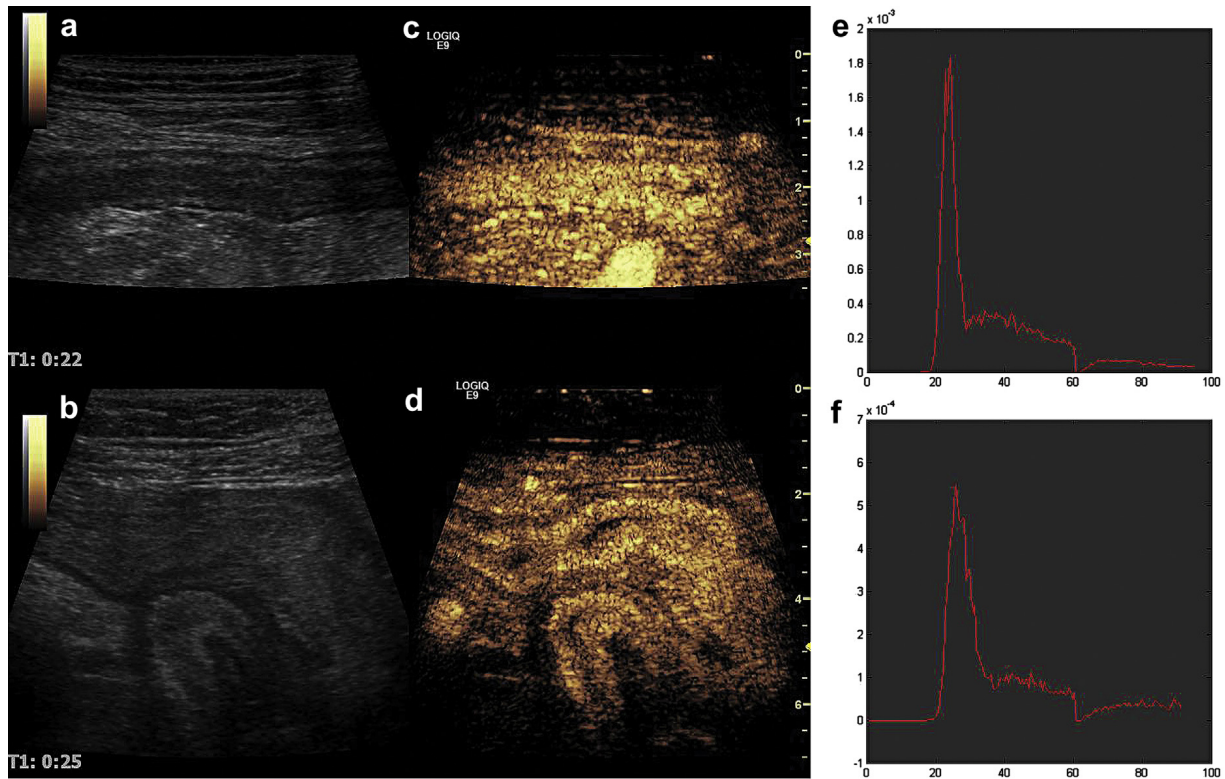


Fig. 1. Peak intensity in terminal ileum in patient receiving medical therapy (a, c, e) and patient undergoing surgery for a stenosis (b, d, f). (a, b) B-mode images of the affected intestine. (c, d) The corresponding contrast image. (e, f) The curve of the re-linearized time-intensity data.

the curve as the AIF measured in an artery in the same video. Three parameters could be derived from the analysis: blood volume (Bv) corresponding to the volume of blood in 100 mL of tissue, mean transit time (MTT) cor-

responding to the average time in seconds that the blood uses for travelling through the region of interest and, finally, blood flow (Bf) corresponding to the volume of blood in milliliters going through 100 mL of tissue per

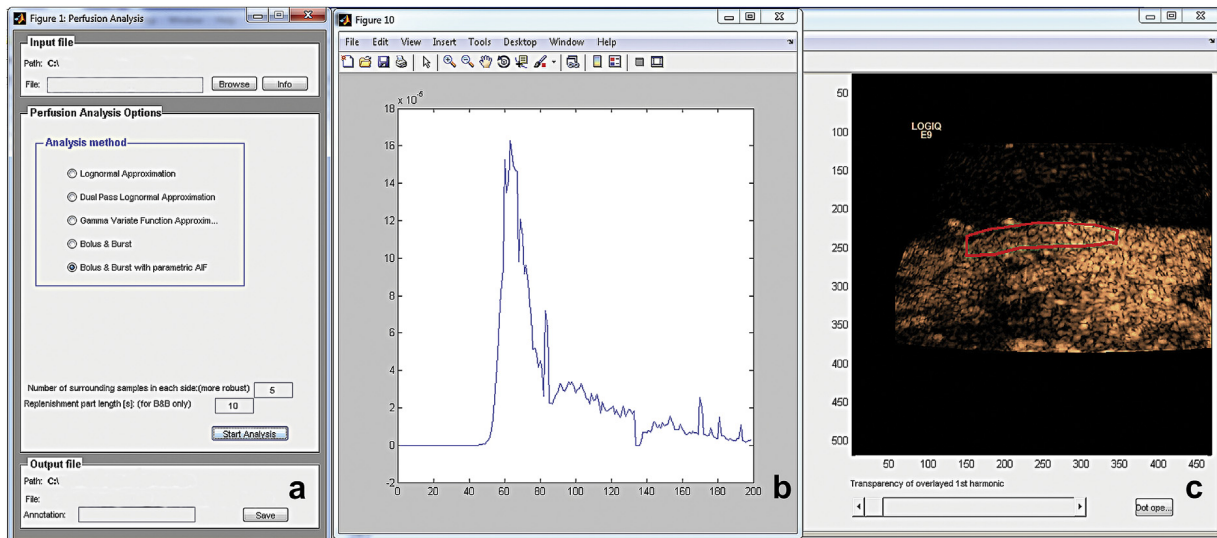


Fig. 2. Perfusion analysis using the DCE-CEUS software on exported DICOM video files from patients with Crohn's disease. (a) Different perfusion analysis methods offered by the software, including the bolus and burst with parametric AIF. (b) The re-linearized intensity values plotted over time (burst excluded). (c) A region of interest drawn in the anterior wall of affected terminal ileum.

minute. These three parameters are inter-dependent according to the formula:

$$Bf = \frac{Bv}{MTT} * 60$$

Thus, MTT is not dependent on the shape of the measured AIF, or on its integral value. In contrast, Bv and Bf values are inversely proportional to this integral value. To test for intra-observer variability in the analysis, 20 CEUS examinations were randomly selected and the analysis was repeated.

Histology

The operation specimens were examined by the primary investigator (K.N.) within 30 min after resection, oriented, cut open longitudinally and mounted on Styrofoam before fixation in 10% buffered formalin. Two-millimeter-thick whole mount slices corresponding to the ultrasound plane were excised by the pathologist with the main investigator present, inked for orientation and embedded in paraffin using standard procedures. Five-micrometer-thick whole mount sections were made and stained with Masson trichrome for visualization of fibrous tissue. Fibrosis in submucosa and the proper muscle was graded semi-quantitatively as previously done by Nylund *et al.* (2008) where 0 = normal, 1 = slight to moderate fibrosis and 2 = severe fibrosis. To separate between fibrotic and non-fibrotic sections, a score of 0 in both wall layers or 0 in the proper muscle and 1 in the submucosa was considered non-fibrotic. All other score combinations were considered fibrotic.

Statistics

The data are presented with median, minimum and maximum values. Comparison between the surgery and medical groups was done using the appropriate statistical tests. Continuous data were analyzed with an unpaired Student's *t*-test if normally distributed and with the non-parametric Mann-Whitney *U* test if not. Dichotomous, categorical data were tested with Fischer's exact test. Likert scaled data with three categories were analyzed using the Freeman-Halston's extension of the Fischer's exact test. To test for associations, Pearson's correlation was used for continuous data. Pearson's correlation coefficient is denoted as *r*. The most promising parameters were examined with a receiver operating characteristic (ROC) analysis to identify a possible cut-off to be used in future studies. Intra-observer variability for the perfusion parameters was assessed using Pearson's correlation coefficient and limits of agreement (mean ± 1.96 standard deviations); *p* < 0.05 was chosen as the level of significance.

RESULTS

Thirty-nine patients were initially included; 20 patients were in the surgery group and 19 patients were in the medical group. Two of the patients in the surgery group did not have significant fibrosis in the resected bowel segment and were excluded. None of the patients in the medical group had been treated previously with balloon dilatation for strictures or stenotic occlusion in the affected area. Absolute perfusion analysis could be performed in 16 patients in the surgery group and 17 patients in the medical group. Overall, technical feasibility was 89%. The contrast examination could be performed in all patients, but the data could not be analyzed in four cases because of a failure to save the video-loop properly (two cases), failure to burst the bubbles (one case) and failure to find an artery in the GI wall for scaling during post-processing (one case). There were no allergic reactions or other side effects to ultrasound contrast during the study.

There were no significant differences in gender and age between the surgery group, the medical group and the healthy control group. Main indications for surgery were stenosis in 15 cases, non-responders to medical treatment in two cases and perforation of the terminal ileum in one case. The surgery group had significantly more stenotic disease than the medical group (*p* < 0.001), had undergone previous resections more frequently (*p* = 0.005), had also more frequent small intestinal affection (*p* = 0.008) and the diagnosis had been known for a longer time (*p* = 0.032). No significant differences in the clinical indices (simple index and CDAI) between the two groups were seen. In addition, there were no differences in biochemical parameters except for leucocyte count and C-reactive protein, which was significantly higher in the medical group (Table 1).

The GI wall measured with ultrasound was significantly thicker in the surgery group than in the medical group (*p* < 0.001; 6.8 [4.5–10.8] vs. 4.9 [2.4–10.1] mm). The individual wall layers corresponding to the mucosa (*p* = 0.013) and the muscularis propria (*p* = 0.001) were thicker in the surgery group (Table 2). The ratio of the submucosa to the total bowel wall thickness was significantly higher (*p* = 0.028) in the medical group (0.44 ± 0.13) versus the surgery group (0.34 ± 0.11). No significant changes in color Doppler score and resistive index between the two groups were seen (Table 2). A thickened muscularis mucosa (*p* = 0.001), echo changes in the submucosa (*p* = 0.016) and Crohn's rosary (*p* = 0.022) were also more prevalent in the surgery group, but there were no differences in the frequency of fistulas, stratification loss, and echo changes of the proper muscle. In the healthy volunteers, there were no significant differences in blood volume, mean transit time and flow between the two locations (Table 3).

Table 1. Clinical variables and biomarkers from blood and faeces in patients with Crohn's disease

Parameter	Surgery group		Medical group		<i>p</i> value
	Median	Min–Max	Median	Min–Max	
Age (y)*	37	19–77	33	20–70	0.673
Time since diagnosis (Years)†	7	0.3–30	1	0.1–22	0.034
CDAI*	255	63–445	247	160–462	0.239
Simple index*	7	2.0–17	8	2.0–20	0.302
Hemoglobin (g/dL)*	12.6	7.4–15.9	13.1	11.5–16.2	0.204
Leucocyte count (10 ⁹ /L)*	7.2	3.4–10.2	9.6	3.9–22.0	0.005
Platelet count (10 ⁹ /L)†	404	275–778	412	167–844	0.663
C-reactive protein (mg/L)†	9	1–58	19	2–338	0.024
Albumin (mg/L)*	40	33–47	40	24–47	0.269
Calprotectin (mg/L)†	249	19–1931	190	19–1279	0.980

CDAI = Crohn's disease activity index.

* Student's *t*-test.

† Mann–Whitney *U* test.

Blood volume was significantly higher in the medical group (3.4 [0.89–9.98] mL per 100 g) compared with the surgery group ($p < 0.001$; 0.9 [0.06–4.54] mL per 100 g). In addition, the blood flow was significantly higher ($p = 0.002$) in the medical group (45.3 [17.3–254.5] mL/min per 100 g) compared with the surgery group (22.6 [0.6–78] mL/min per 100 g). The mean transit time was not significantly different. When the patients with colonic disease were excluded from the analysis, there was still significantly higher blood volume ($p = 0.006$) and blood flow ($p = 0.014$) in the medical group than in the surgical group. There was no comparison with the surgery group because it contained only one patient with colonic disease. Blood volume ($p = 0.002$) and blood flow ($p = 0.005$) was significantly larger in healthy volunteers compared with the surgery group. There were no significant differences in blood volume and blood flow between the healthy and the medical groups, and mean transit time was not significantly different between any of the groups (Table 3).

Testing for the intra-observer variability, we found that Pearson's correlation coefficient was 0.80 ($p < 0.001$) for blood volume, 0.73 for mean transit time

($p < 0.001$) and 0.75 for blood flow ($p < 0.001$). Limits of agreement were 0.1 ± 2.51 for blood volume, -0.04 ± 3.0 for mean transit time and -0.1 ± 46.7 . A scatterplot of the blood volume measurements and a corresponding Bland–Altman plot is shown in Figure 3.

For both groups pooled together, there was a positive correlation between CDAI and blood volume ($r = 0.37$; $p = 0.033$), but there were no significant correlations between perfusion parameters and other clinical or biochemical markers. There was a negative correlation with local blood flow and resistive index ($r = -0.48$; $p = 0.029$; Fig. 4) and blood volume and bowel wall thickness ($r = -0.40$; $p = 0.021$). The measured length of affected intestine also correlated with calprotectin ($r = 0.44$; $p = 0.026$; $n = 28$; Fig. 4) and inversely with albumin ($r = -0.59$; $p < 0.001$).

A *post hoc* ROC analysis was done by combining the parameters blood volume (Vb) and bowel wall thickness (BWT) through simple division. This new variable was named “Vb/BWT-ratio.” In the ROC analysis the area under the curve was 0.92 ($p < 0.001$) and using a cut-off of 0.56 mL per 100 mL/mm gave the best combination of sensitivity (0.82) and specificity (0.94) as a test for predicting surgery or not (Fig. 5).

Table 2. B-mode and Doppler parameters in patients with Crohn's disease

Parameter	Surgery group		Medical group		<i>p</i> value
	Median	Min–Max	Median	Min–Max	
Bowel wall thickness (mm)*	6.8	4.5–10.8	4.9	2.4–10.1	<0.001
Mucosa (mm)†	2.2	1.1–5.8	1.4	0.5–2.5	0.013
Submucosa (mm)†	2.1	1.4–4.8	1.7	1.2–3.8	0.220
Muscularis propria (mm)*	1.8	1.1–4.4	1.3	0.5–2.3	0.001
Length affection (cm)*	10.4	3.2–23.8	12.7	5.1–32.0	0.163
Resistive index*	0.57	0.46–0.76	0.58	0.50–0.75	0.786

* Student's *t* test.

† Mann–Whitney *U* test.

Table 3. Absolute perfusion parameters using CEUS of all GI locations in patients with Crohn's disease*

Location	Parameter	Surgery group			Medical group			Healthy			<i>p</i> value [†]
		Median	Min–Max	<i>n</i>	Median	Min–Max	<i>n</i>	Median	Min–Max	<i>n</i>	
All	Blood volume (mL per 100 mL tissue)	0.9	0.1–4.5	16	3.4	0.9–8.1	17	–	–		<0.001
	Mean transit time	3.9	1.6–9.7		5.5	1.8–9.7		–	–		0.276
	Flow (mL/min per 100 mL tissue)	22.6	0.6–78.0		45.3	17.3–275.1		–	–		0.003
Small intestine	Blood volume (mL per 100 mL tissue)	0.9	0.1–4.3	15	3.8	1.3–7.6	6	3.1	0.4–11.9	20	0.006
	Mean transit time	4.2	1.6–9.7		5.4	2.3–9.7		4.5	2.2–10.9		0.381
	Flow (mL/min per 100 mL tissue)	22.1	0.6–57.0		40.9	29.5–71.9		44.9	6.6–91.2		0.014
Colon	Blood volume (mL per 100 mL tissue)		4.54	1	3.4	0.9–8.1	11	3.2	0.3–11.7	30	NA
	Mean transit time		3.5		5.5	1.8–8.4		4.5	2.1–7.5		NA
	Flow (mL/min per 100 mL tissue)		78.0		45.3	17.3–275.1		39.4	2.2–111.4		NA

CEUS = contrast-enhanced ultrasound; GI = gastrointestinal; NA = not analyzed.

* Mann–Whitney *U* test.

[†] Surgery group versus medical group.

DISCUSSION

We found that the entire GI wall, mucosa and muscularis propria was thicker in patients stratified for surgical treatment for Crohn's disease, whereas blood volume and blood flow was lower. To our knowledge, non-invasive absolute perfusion estimates in the GI wall using CEUS in humans have not been presented previously, although a similar methodology recently has been published using a mouse tumor model (Gauthier *et al.* 2012).

The relationship between the risk for surgical treatment and wall thickness is not a new finding, and this has been shown by several authors, but we have found no reports on the relationship between the thickness of the individual wall layers and the need for surgery (Castiglione *et al.* 2004; Kunihiro *et al.* 2007; Rigazio *et al.* 2009). Normally the echo layer corresponding to the submucosa is thinner or equal to the layer corresponding to the muscularis propria (Nylund *et al.* 2012). A recent study using endoscopic ultrasound showed that thickening of the submucosa is a typical finding in acute Crohn's disease (Fritscher-Ravens *et al.* 2011), which corresponds to our findings in the medical

group. In the surgery group, however, the mucosa and muscularis propria are thicker compared with the submucosa, which seems to suggest that although relative submucosal thickening is a feature of early and acute disease, relative thickening of the mucosa and muscularis propria is a feature of chronic disease and possibly fibrostenotic disease.

A thickened muscularis mucosa, Crohn's rosary and echo changes in the submucosa were all more prevalent in the group treated surgically. These results were expected because these findings are typical of chronic disease and are related to chronic inflammation and fibrosis (Lee *et al.* 1991; Nylund *et al.* 2008; Odze 2003).

There are few reports on absolute perfusion measurements in the intestinal wall in humans. Using a washout technique with a radioactive gas isotope on patients undergoing abdominal surgery, Hulten *et al.* (1976a, 1976b) found that blood flow in the small intestinal wall was 38 (17–75) mL/min per 100 g and in the colon was 18 (8–35) mL/min per 100 g in patients with a healthy bowel. Considering that the average weight of the small intestine is approximately 1300 g and the average flow of the superior mesenteric artery is

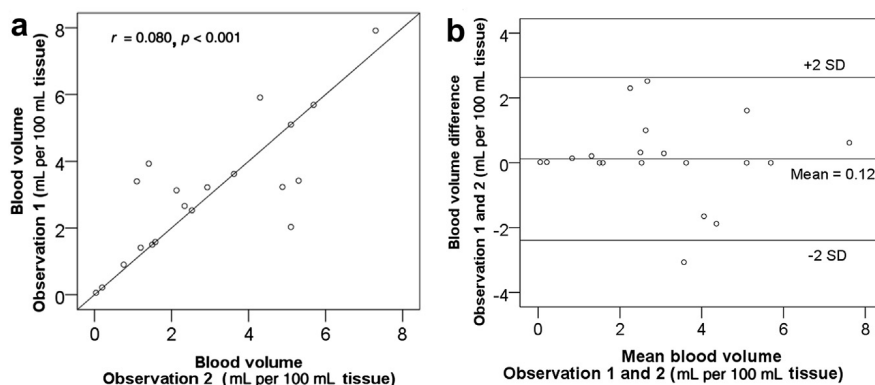


Fig. 3. (a) Scatter plot with line of identity and Pearson's correlation coefficient. (b) Bland–Altman plot for the intra-observer study.

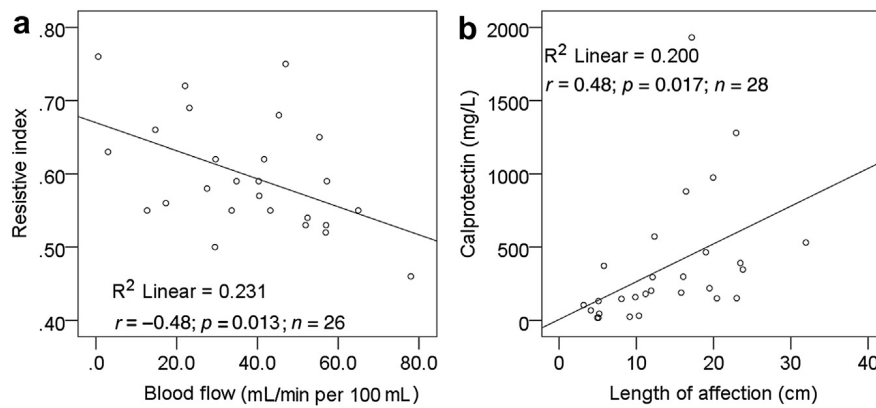


Fig. 4. Scatter plots with linear correlation line and Pearson's correlation coefficient (r) between resistive index and absolute flow (a) and calprotectin and length of affection (b) in patients with Crohn's disease.

500 mL/min during fasting, the average perfusion should be 40 mL/min per 100 g intestine; therefore, these values seem plausible (Hulten et al. 1976a). This finding was later confirmed by Ahn et al. (1986a, 1986b) using laser Doppler also in an intraoperative setting, but they also found higher blood flow in the colon (37 ± 10.4 mL/min per 100 mL tissue) when obtaining measurements transendoscopically in unsedated patients.

Studies of patients with inflammatory bowel disease with the same methodology suggest that Crohn's disease causes increased blood flow in the colon in the acute phase and reduced flow in patients with long-standing disease. In the small intestine, there appears to be no increase in flow in the acute phase, but a decrease as the disease progresses (Hulten et al. 1977; Tateishi

et al. 1997). Our blood flow results seem to coincide fairly well with values reported previously (Ahn et al. 1986a, 1986b; Hulten et al. 1976a, 1976b, 1977; Tateishi et al. 1997).

A benefit of modeling perfusion with the one compartment model is the possibility of differentiating between blood volume and mean transit time (Mezl et al. 2010). Since both neo-vascularization and increased vascular resistance occur in Crohn's disease, these changes might be differentiated because vessel density is related to blood volume, and vessel resistance is related to mean transit time (Alkim et al. 2009; Danese et al. 2006; Funayama et al. 1999; Hatoum et al. 2003; Konerding et al. 2010; Mori et al. 2005). Furthermore, long-standing disease with the development of fibrosis in the submucosa causes a reduction in vessel density and therefore in blood volume (Hulten et al. 1977; Kruschewski et al. 1995). In our patients, we observed a difference in blood volume between the surgical group compared with both healthy volunteers and the medical group. There was however, no significant difference in mean transit time and blood volume between the healthy volunteers and the medical group, when an increased blood volume and prolonged mean transit time would be expected. This finding might be due to the large range of values in the healthy volunteers and the low number of patients in the study.

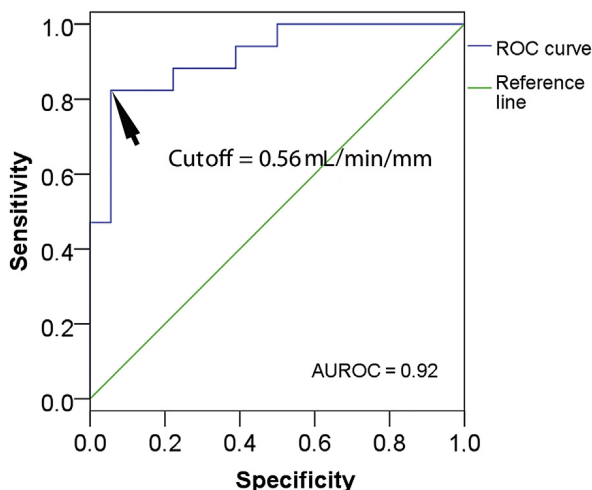


Fig. 5. Receiver operating characteristic (ROC) curve of the parameter combining bowel wall thickness and local blood volume (Vb/BWT ratio) regarding medical or surgical treatment. The area under the ROC curve (AUROC) is 0.92, and the optimal cut-off value is 0.56 mL/min/mm, with a sensitivity of 82% and specificity of 94%.

Limitations

It was technically challenging to identify the bowel wall clearly and adjust for movement in the healthy volunteers. These challenges also applied to the arteries used for scaling, which probably explains the large range of flow values in the healthy volunteers. Furthermore, because an artery contains a large amount of microbubbles, a normal-contrast dose can cause attenuation within the vessel and therefore an underestimation of the time

intensity values in the peak arterial phase. Consequently, using an artery for scaling from the same recording may cause an overestimation of blood volume and blood flow. The problem of attenuation, identification of small arteries and movement can be overcome by using a second low-dose injection from the same vial (one tenth of the original dose) and recording the passage of a bolus over a large artery such as the right iliac artery, for example. We also attempted this approach, but found that Sonovue degraded too fast for the method to be reliable (Kwan and Borden 2010). However, we do not believe that attenuation is of major importance in the small vessels (2 mm or less) that we used for scaling in our study.

The patients were recruited and grouped according to a clinical treatment decision, which caused particular differences in group characteristics. Specifically, there were more patients with stenotic disease and the disease had a longer duration in the surgery group. Because we did not know the histology in the medical group, some might have had fibrotic lesions. Another potential bias was the differences in regard to disease location in the GI tract. Most patients in the surgery group had small intestinal disease, whereas most patients in the medical group had colonic disease. Because previous studies have shown differences in flow in the small intestine and colon in healthy patients, this could influence our results. However, the trend was still the same in a subgroup analysis disregarding the patients with colonic disease. Furthermore, we did not find a significant difference in flow between the ileum and the ascending colon in our control group.

In our study, we had to choose one specific lesion for comparison, possibly introducing a selection bias. Based on previous work by other groups, we defined the most affected area with the thickest bowel wall as the “culprit” lesion (Girlich *et al.* 2011; Girlich *et al.* 2012; Kunihiro *et al.* 2007; Migaletto *et al.* 2009; Ripolles *et al.* 2013; Schirin-Sokhan *et al.* 2011; Spalinger *et al.* 2000). In patients receiving surgery, this area was found in the intestine scheduled for resection. Because CEUS is a 2-D method, we also had to choose a specific section of the bowel wall that could also represent a selection bias regarding choice of lesion and choice of ultrasound plane during CEUS. This problem exists for all 2-D methods, and we tried to solve it by choosing a relatively large region being representative for the lesion. The “bolus and burst” algorithm for calculation of absolute perfusion should also be validated against a gold standard. However, the development of matrix probes enabling 4-D contrast recordings could give a substantial improvement in accuracy. As motion correction becomes more precise, sampling error will be reduced and will enable easier detection and selection of a reference artery.

CONCLUSIONS

Absolute perfusion measurements of the bowel using CEUS and a combination of bolus tracking and burst replenishment is feasible and might be used in the future together with GI wall thickness as a tool for treatment stratification of patients with Crohn's disease, particularly to distinguish between inflammatory and fibrous wall thickening.

Acknowledgments—This study was supported by Medviz, an interdisciplinary research cluster at Haukeland University Hospital, University of Bergen and Christian Michelsen Research AS, by the Czech Science Foundation (project no.GA102/12/2380) and by European Regional Development Fund (Project FNUSA-ICRC, no. CZ.1.05/1.1.00/02.0123). The authors also thank the personnel at the Endoscopy and Ultrasound Unit at Haukeland University Hospital for their support and Dr. Linn Helljesen for help in recruiting healthy patients.

REFERENCES

- Ahn H, Lindhagen J, Lundgren O. Measurement of colonic blood flow with laser Doppler flowmetry. *Scand J Gastroenterol* 1986a;21: 871–880.
- Ahn H, Lindhagen J, Nilsson GE, Oberg PA, Lundgren O. Assessment of blood flow in the small intestine with laser Doppler flowmetry. *Scand J Gastroenterol* 1986b;21:863–870.
- Alkim C, Savas B, Ensari A, Alkim H, Dagli U, Parlak E, Ulker A, Sahin B. Expression of p53, VEGF, microvessel density, and cyclin-D1 in noncancerous tissue of inflammatory bowel disease. *Dig Dis Sci* 2009;54:1979–1984.
- Best WR, Becktel JM, Singleton JW. Rederived values of the eight coefficients of the Crohn's Disease Activity Index (CDAI). *Gastroenterology* 1979;77:843–846.
- Castiglione F, de Sio I, Cozzolino A, Rispo A, Manguso F, Del Vecchio BG, Di GE, Castellano L, Ciacci C, Mazzacca G. Bowel wall thickness at abdominal ultrasound and the one-year-risk of surgery in patients with Crohn's disease. *Am J Gastroenterol* 2004;99:1977–1983.
- Danese S, Sans M, de la MC, Graziani C, West G, Phillips MH, Pola R, Rutella S, Willis J, Gasbarrini A, Fiocchi C. Angiogenesis as a novel component of inflammatory bowel disease pathogenesis. *Gastroenterology* 2006;130:2060–2073.
- Fritscher-Ravens A, Ellrichmann M, Nikolaus S, Arlt A, Sergueev P, Kuehbacher T, Wintermeyer L, Schreiber S, Wietzke-Braun P. 463 endoscopic ultrasound of the colon for the differentiation of Crohn's disease and ulcerative colitis in comparison to healthy controls - a prospective, blinded, comparative study. *Gastrointest Endosc* 2011;73:AB128.
- Funayama Y, Sasaki I, Naito H, Fukushima K, Matsuno S, Masuda T. Remodeling of vascular wall in Crohn's disease. *Dig Dis Sci* 1999;44:2319–2323.
- Gasche C, Moser G, Turetschek K, Schober E, Moeschl P, Oberhuber G. Transabdominal bowel sonography for the detection of intestinal complications in Crohn's disease. *Gut* 1999;44:112–117.
- Gauthier M, Tabarout F, Leguery I, Polrot M, Pitre S, Peronneau P, Lassau N. Assessment of quantitative perfusion parameters by dynamic contrast-enhanced sonography using a deconvolution method: An in vitro and in vivo study. *J Ultrasound Med* 2012;31: 595–608.
- Girlich C, Schacherer D, Jung EM, Schreyer A, Büttner R. Comparison between a clinical activity index (Harvey-Bradshaw-Index), laboratory inflammation markers and quantitative assessment of bowel wall vascularization by contrast-enhanced ultrasound in Crohn's disease. *Eur J Radiol* 2012;81:1105–1109.
- Girlich C, Jung EM, Huber E, Ott C, Iesalnieks I, Schreyer A, Schacherer D. Comparison between preoperative quantitative assessment of bowel wall vascularization by contrast-enhanced ultrasound and operative macroscopic findings and results of

- histopathological scoring in Crohn's disease. *Ultraschall Med* 2011; 32:154–159.
- Harvey RF, Bradshaw JM. A simple index of Crohn's-disease activity. *Lancet* 1980;1:514.
- Hatoum OA, Binion DG, Otterson MF, Gutterman DD. Acquired microvascular dysfunction in inflammatory bowel disease: Loss of nitric oxide-mediated vasodilation. *Gastroenterology* 2003;125:58–69.
- Hudson JM, Karshafian R, Burns PN. Quantification of flow using ultrasound and microbubbles: A disruption replenishment model based on physical principles. *Ultrasound Med Biol* 2009;35:2007–2020.
- Hulten L, Jodal M, Lindhagen J, Lundgren O. Blood flow in the small intestine of cat and man as analyzed by an inert gas washout technique. *Gastroenterology* 1976a;70:45–51.
- Hulten L, Jodal M, Lindhagen J, Lundgren O. Colonic blood flow in cat and man as analyzed by an inert gas washout technique. *Gastroenterology* 1976b;70:36–44.
- Hulten L, Lindhagen J, Lundgren O, Fasth S, Ahren C. Regional intestinal blood flow in ulcerative colitis and Crohn's disease. *Gastroenterology* 1977;72:388–396.
- Jirik R, Nylund K, Gilja OH, Mezl M, Harabis V, Kolar R, Standara M, Taxt T. Ultrasound perfusion analysis combining bolus-tracking and burst-replenishment. *IEEE Trans Ultrason Ferroelectr Freq Control* 2013;60:310–319.
- Konerding MA, Turhan A, Ravnic DJ, Lin M, Fuchs C, Secomb TW, Tsuda A, Mentzer SJ. Inflammation-induced intussusceptive angiogenesis in murine colitis. *Anat Rec* 2010;293:849–857.
- Kruschewski M, Busch C, Dörner A, Lieser W. Angio-architecture of the colon in Crohn disease and ulcerative colitis. Light microscopy and scanning electron microscopy studies with reference to the morphology of the healthy large intestine. *Langenbecks Arch Chir* 1995;380:253–259.
- Kunihiro K, Hata J, Manabe N, Mitsuoka Y, Tanaka S, Haruma K, Chayama K. Predicting the need for surgery in Crohn's disease with contrast harmonic ultrasound. *Scand J Gastroenterol* 2007;42:577–585.
- Kwan JJ, Borden MA. Microbubble dissolution in a multigas environment. *Langmuir* 2010;26:6542–6548.
- Lassau N, Chebil M, Chami L, Bidault S, Girard E, Roche A. Dynamic contrast-enhanced ultrasonography (DCE-US): A new tool for the early evaluation of antiangiogenic treatment. *Target Oncol* 2010;5:53–58.
- Lee EY, Stenson WF, DeSchryver-Kecskemeti K. Thickening of muscularis mucosae in Crohn's disease. *Mod Pathol* 1991;4:87–90.
- Mezl M, Jirik R, Harabis V, Kolar R. Quantitative Ultrasound Perfusion Analysis In Vitro. *Proceedings of Biosignal 2010: Analysis of Biomedical Signals and Images* 2010;20:279–283. Available at: <http://bs2010.biosignal.cz/papers/1068.pdf>.
- Migaleddu V, Scanu AM, Quaia E, Rocca PC, Dore MP, Scanu D, Azzali L, Virgilio G. Contrast-enhanced ultrasonographic evaluation of inflammatory activity in Crohn's disease. *Gastroenterology* 2009; 137:43–52.
- Mori M, Stokes KY, Vowinkel T, Watanabe N, Elrod JW, Harris NR, Lefer DJ, Hibi T, Granger DN. Colonic blood flow responses in experimental colitis: Time course and underlying mechanisms. *Am J Physiol Gastrointest Liver Physiol* 2005;289:G1024–G1029.
- Nylund K, Hausken T, Gilja OH. Ultrasound and inflammatory bowel disease. *Ultrasound Q* 2010;26:3–15.
- Nylund K, Hausken T, Ødegaard S, Eide G, Gilja O. Gastrointestinal wall thickness measured with transabdominal ultrasonography and its relationship to demographic factors in healthy subjects. *Ultraschall Med* 2012;33:E225–E232.
- Nylund K, Leh S, Immervoll H, Matre K, Skarstein A, Hausken T, Gilja OH, Birger NL, Odegaard S. Crohn's disease: Comparison of in vitro ultrasonographic images and histology. *Scand J Gastroenterol* 2008;43:719–726.
- Odegaard S, Kimmey MB, Cheung AHS, Nesje LB, Morild I, Silverstein FE, Martin RW. High frequency endosonography of gastrointestinal arteries: Potential and limitations in vitro. *Eur J Ultrasound* 1995;2:313–319.
- Odze R. Diagnostic problems and advances in inflammatory bowel disease. *Mod Pathol* 2003;16:347–358.
- Ostergaard L. Principles of cerebral perfusion imaging by bolus tracking. *J Magn Reson Imaging* 2005;22:710–717.
- Peronneau P, Lassau N, Leguerney I, Roche A, Cosgrove D. Contrast ultrasonography: Necessity of linear data processing for the quantification of tumor vascularization. *Ultraschall Med* 2010;31:370–378.
- Quaia E, De Paoli L, Stocca T, Cabibbo B, Casagrande F, Cova MA. The value of small bowel wall contrast enhancement after sulfur hexafluoride-filled microbubble injection to differentiate inflammatory from fibrotic strictures in patients with Crohn's disease. *Ultrasound Med Biol* 2012;38:1324–1332.
- Rigazio C, Ercole E, Laudi C, Daperno M, Lavagna A, Crocella L, Bertolino F, Vigano L, Sostegni R, Pera A, Rocca R. Abdominal bowel ultrasound can predict the risk of surgery in Crohn's disease: Proposal of an ultrasonographic score. *Scand J Gastroenterol* 2009; 44:585–593.
- Ripolles T, Rausell N, Paredes JM, Grau E, Martinez MJ, Vizuete J. Effectiveness of contrast-enhanced ultrasound for characterisation of intestinal inflammation in Crohn's disease: A comparison with surgical histopathology analysis. *J Crohns Colitis* 2013;7:120–128.
- Rognin NG, Frinking P, Costa M, Arditi M. In-vivo perfusion quantification by contrast ultrasound: Validation of the use of linearized video data vs. raw RF data. *Ultrasonics Symposium*, 2008. IUS 2008. IEEE 2008;1690–1693 (dx.doi.org/10.1109/ULTSYM.2008.0413).
- Schirin-Sokhan R, Winograd R, Tischendorf S, Wasmuth HE, Streetz K, Tacke F, Trautwein C, Tischendorf JJ. Assessment of inflammatory and fibrotic stenoses in patients with Crohn's disease using contrast-enhanced ultrasound and computerized algorithm: A pilot study. *Digestion* 2011;83:263–268.
- Spalinger J, Patriquin H, Miron MC, Marx G, Herzog D, Dubois J, Dubinsky M, Seidman EG. Doppler US in patients with Crohn's disease: Vessel density in the diseased bowel reflects disease activity. *Radiology* 2000;217:787–791.
- Tateishi S, Arima S, Futami K. Assessment of blood flow in the small intestine by laser Doppler flowmetry: Comparison of healthy small intestine and small intestine in Crohn's disease. *J.Gastroenterol* 1997;32:457–463.
- Wang J, Lv F, Fei X, Cui Q, Wang L, Gao X, Yuan Z, Lin Q, Lv Y, Liu A. Study on the characteristics of contrast-enhanced ultrasound and its utility in assessing the microvessel density in ovarian tumors or tumor-like lesions. *Int J Biol Sci* 2011;7:600–606.
- Wang Z, Tang J, An L, Wang W, Luo Y, Li J, Xu J. Contrast-enhanced ultrasonography for assessment of tumor vascularity in hepatocellular carcinoma. *J Ultrasound Med* 2007;26:757–762.

4.2 MR perfusion imaging

4.2.1 Paper III

J. Kratochvíla, R. Jiřík, M. Bartoš, M. Standara, Z. Starčuk, T. Taxt, Distributed capillary adiabatic tissue homogeneity model in parametric multi-channel blind AIF estimation using DCE-MRI, *Magn Reson Med.* 75 (2016) 1355–1365.

<https://doi.org/10.1002/mrm.25619>.

(IF 3.924)

Author's contribution:

- co-author of the main idea
- methodological design
- setup of the data acquisition method
- guidance in implementation, data processing and evaluation
- paper co-writing

Distributed Capillary Adiabatic Tissue Homogeneity Model in Parametric Multi-channel Blind AIF Estimation Using DCE-MRI

Jiří Kratochvíla,^{1,2*} Radovan Jiřík,² Michal Bartoš,^{1,3} Michal Standara,⁴ Zenon Starčuk Jr.,² and Torfinn Taxt⁵

Purpose: One of the main challenges in quantitative dynamic contrast-enhanced (DCE) MRI is estimation of the arterial input function (AIF). Usually, the signal from a single artery (ignoring contrast dispersion, partial volume effects and flow artifacts) or a population average of such signals (also ignoring variability between patients) is used.

Methods: Multi-channel blind deconvolution is an alternative approach avoiding most of these problems. The AIF is estimated directly from the measured tracer concentration curves in several tissues. This contribution extends the published methods of multi-channel blind deconvolution by applying a more realistic model of the impulse residue function, the distributed capillary adiabatic tissue homogeneity model (DCATH). In addition, an alternative AIF model is used and several AIF-scaling methods are tested.

Results: The proposed method is evaluated on synthetic data with respect to the number of tissue regions and to the signal-to-noise ratio. Evaluation on clinical data (renal cell carcinoma patients before and after the beginning of the treatment) gave consistent results. An initial evaluation on clinical data indicates more reliable and less noise sensitive perfusion parameter estimates.

Conclusion: Blind multi-channel deconvolution using the DCATH model might be a method of choice for AIF estimation in a clinical setup. *Magn Reson Med* 75:1355–1365, 2016. © 2015 Wiley Periodicals, Inc.

Key words: dynamic contrast-enhanced magnetic resonance imaging; multi-channel blind deconvolution; arterial input function; impulse residue function; renal cell carcinoma

INTRODUCTION

Dynamic contrast-enhanced MRI (DCE-MRI) is used for estimation of tissue perfusion parameters, with the main application field in oncology (1,2). The treatment response in terms of changes in perfusion parameters can be observed within days compared with months when evaluating morphological changes with RECIST criteria (3,4).

In quantitative DCE-MRI, the measured tissue tracer concentration sequence in a region of interest (ROI) is modeled as a convolution of the arterial input function (AIF – the tracer concentration sequence in the arterial input of the ROI) and the impulse residue function (IRF) (5–7). The parameters of the IRF are the sought perfusion parameters. These parameters are commonly estimated by (nonblind) deconvolution, where the AIF is assumed to be known. The accuracy of the AIF estimate is crucial for the accuracy of the perfusion parameter estimates. One approach to determine the AIF is to measure it as the tissue tracer concentration sequence in a big feeding artery. However, these measurements are distorted by flow artifacts, partial-volume effect and saturation effects. The saturation effects are due to high tracer concentration in arteries which leads to a nonlinear relationship between the relaxation rate R_1 and the tracer concentration and to the pronounced T_2^* effect. In addition, AIF is distorted by dispersion, i.e., by the transfer function of the vessel segment between the AIF measurement location and the tissue ROI.

Another common approach to AIF estimation is use of a population-based AIF (8), which, in addition, ignores the natural variability of the patient-specific vascular tree and cardiac output.

A less common approach to AIF estimation is blind deconvolution (9–11), where both the IRF and the AIF are estimated simultaneously from the tissue tracer concentration sequences of one ROI (single-channel blind deconvolution) (11) or of more ROIs (multi-channel blind deconvolution) (9,10). Single-channel blind deconvolution inherently estimates the local (ROI-specific) AIF, but it requires use of strong additional constraints and a careful initialization procedure to end up with a correct and

¹Department of Biomedical Engineering, Brno University of Technology, Brno, Czech Republic.

²Institute of Scientific Instruments of the Academy of Sciences of the Czech Republic, Brno, Czech Republic.

³Institute of Information Technology and Automation of the Academy of Sciences of the Czech Republic, Praha, Czech Republic.

⁴Masaryk Memorial Cancer Institute, Brno, Czech Republic.

⁵Department of Biomedicine, University of Bergen, Bergen, Norway.

Grant sponsor: the Czech Science Foundation; Grant number: GA102/12/2380; Grant sponsor: MH CZ - DRO; Grant number: MMCI; 00209805; Grant sponsor: Ministry of Education, Youth and Sports of the Czech Republic; Grant number: LO1212; Grant sponsor: European Regional Development Fund and the state Budget of the Czech Republic; Grant number: RECAMO; CZ.1.05/2.1.00/03.0101; Grant sponsor: Ministry of Education, Youth and Sports of the Czech Republic and European Commission; Grant number: CZ.1.05/2.1.00/01.0017; Grant sponsor: the Meta-Centrum; Grant number: LM2010005; Grant sponsor: the CERIT-SC under the program Centre CERIT Scientific Cloud, part of the Operational Program Research and Development for Innovations; Grant number: CZ.1.05/3.2.00/08.0144.

*Correspondence to: Jiří Kratochvíla, M.Sc., ASCR, Institute of Scientific Instruments, Kralovopolská 147, 612 64 Brno, Czech Republic. E-mail: kratochvila@isibrno.cz

Received 2 October 2014; revised 1 December 2014; accepted 24 December 2014

DOI 10.1002/mrm.25619

Published online 13 April 2015 in Wiley Online Library (wileyonlinelibrary.com).

unique solution (11). For multi-channel blind deconvolution, the uniqueness of the solution is theoretically guaranteed for the noise-less case by means of Z-domain formulation (10), but it allows only estimation of a global AIF which ignores differences in dispersion of the local ROI-specific AIFs. The use of nonparametric (10–14) and parametric (9,15,16) formulations of the AIF have been reported. A realistic parametric AIF model provides strong prior information that regularizes the deconvolution algorithm and, hence, improves the reliability of the AIF estimate.

The IRF of the nonblind approaches is commonly modeled using the extended Tofts models (17–19). More realistic (and much less used) IRF models describe also the intravascular phase of the tracer distribution, either as a compartment (two compartment exchange model, 2CXM) (20,21), using the “plug-flow” assumption (the adiabatic approximation of the tissue homogeneity model, AATH) (22,23) or a set of “plug-flow” capillaries (the distributed capillary adiabatic tissue homogeneity model, DCATH) (24,25).

The parameter estimation of these more complex IRF models requires a high signal-to-noise ratio (SNR) (25) in order not to be ill-posed as they include more perfusion parameters than simpler IRF models. Furthermore, application of these more complex models assumes a high temporal resolution of the acquisition to capture the fast vascular-distribution phase of the bolus. These are the main reasons why most quantitative DCE-MRI studies are based on the Tofts or extended Tofts models. The so far published blind-deconvolution approaches using one of these more complex IRF models are (11) (AATH) and (13) (DCATH). However, both approaches use a nonparametric AIF and the methods were applied to synthetic and pre-clinical data. Only very recent conference contributions (26–28) have reported about blind-deconvolution using one of these more complex IRF models and a parametric AIF. However, these methods were applied to preclinical data and the applied IRF models were the 2CXM (26) and the AATH (27,28).

In this paper, the published multi-channel blind deconvolution methods are extended by replacing the extended-Tofts IRF model by the more realistic DCATH model. Compared with the AATH model, the DCATH model provides a continuous formulation of all parameters including the mean capillary transit time. This allows use of gradient-based optimization.

The commonly used Parker’s AIF model, based on Gaussian, exponential and sigmoid functions (8,29–32), is used here as an alternative to the only AIF model used in blind-deconvolution in clinical applications (9,15,16) (AIF model based on gamma-variate and sigmoid functions). Parker’s AIF model includes 10 parameters while the AIF model in (9,15,16) includes 11 parameters. Thus, the reduced number of AIF parameters partly compensates for the increase of estimated parameters using the more complex IRF model (3 for the extended-Tofts model, 5 for the DCATH model).

The bolus arrival time differences between the tissue ROIs and the AIF are modeled as convolution of the tissue tracer concentration sequences with a narrow Gaussian function. This allows for a continuous formulation

of the delay and can be used in general for any AIF model (including a nonparametric AIF). This is an alternative to the Fourier-domain method (25). In addition, several AIF scaling methods are described and analyzed, because, generally, any blind-deconvolution method provides an AIF estimate with an unknown scaling factor.

The accuracy of AIF estimation versus number of tissue ROIs (channels) and the SNR is evaluated on synthetic data (preliminary simplified evaluation published (33)). Clinical data of renal-cell-carcinoma (RCC) patients before and after the beginning of the antiangiogenic treatment with Axitinib (Pfizer Inc, New York, USA) are used for illustration of the presented method and comparison with use of measured and population-averaged AIFs.

METHODS

The proposed multi-channel blind deconvolution is formulated as minimization of the following function with respect to the parameters of AIF and IRF, including physiological constraints:

$$\sum_m \sum_n [C_t(m, n) - F_p C_p(\Phi, n) * R(\Psi_m, n) * G(\mu_m, n)]^2, \quad [1]$$

where m is the tissue ROI (channel) index, n is the time index, $*$ is time convolution over discrete time n , F_p is plasma flow per unit tissue volume, C_t is the measured tissue tracer concentration sequence, C_p is the AIF (tracer concentration in blood plasma), Φ is the vector of AIF parameters, R is the IRF (DCATH model), Ψ_m is the vector of perfusion parameters for the m -th ROI, G is a narrow Gaussian function modeling the delay between the AIF and $C_t(m, n)$. It is defined as $G(\mu_m, n) = \exp[-(nT_s - \mu_m)^2 / (2\sigma_G^2)]$, with μ_m specifying the delay for the m -th channel signal and the AIF and T_s is the sampling period. The “width” of the narrow Gaussian function, σ_G , is a fixed parameter ensuring that convolution with the Gaussian function affects only the continuous channel-delay with minimal signal distortion of the m -th channel. Active-Set constrained-optimization algorithm (34,35) is used (Matlab Optimization Toolbox, MathWorks, Natick, MA, USA, function *fmincon*) with numerically calculated gradient values. The complexity of the criterial function does not guarantee convergence to the global minimum, but synthetic-data results show reasonable convergence (see below). The optimization scheme is applied directly as a simultaneous minimization of Eq. [1] with respect to the AIF and IRF parameters, compared with (9), where the optimization is implemented as alternating between optimization with respect to the AIF and IRF parameters.

The IRF model (DCATH) is described by four parameters ($\Psi = \{E, k_{ep}, \mu_R, \sigma\}$). We used the truncated normal distribution to describe the probability of transit time according to (24). The DCATH model is defined as:

$$R_v(\Psi, n) = 1 - \left(1 + \operatorname{erf} \left(\frac{\mu_R}{\sqrt{2}\sigma} \right) \right)^{-1} \left(\operatorname{erf} \left(\frac{nT_s - \mu_R}{\sqrt{2}\sigma} \right) + \operatorname{erf} \left(\frac{\mu_R}{\sqrt{2}\sigma} \right) \right) \quad [2]$$

$$R_p(\Psi, n) = E \exp\left(\frac{1}{2}k_{ep}^2\sigma^2 + k_{ep}(\mu_R - nT_s)\right) \\ \left(1 + \operatorname{erf}\left(\frac{\mu_R}{\sqrt{2}\sigma}\right)\right)^{-1} \left(\operatorname{erf}\left(\frac{nT_s - \mu_R}{\sqrt{2}\sigma} - \frac{k_{ep}\sigma}{\sqrt{2}}\right) + \operatorname{erf}\left(\frac{\mu_R}{\sqrt{2}\sigma} + \frac{k_{ep}\sigma}{\sqrt{2}}\right)\right) \\ R(\Psi, n) = R_v(\Psi, n) + R_p(\Psi, n)$$

where E is fraction of the tracer extracted into the parenchymal tissue during vascular passage of the tracer, k_{ep} the rate constant between extravascular extracellular space and blood plasma and is equal to EF_p/v_e , where v_e is volume of extravascular extracellular space, μ_R is the mean of the non-truncated normal distribution of transit time and σ is its standard deviation. If the ratio μ_R/σ is sufficiently small (no greater than $\sim 1/3$ (24)), μ_R can be replaced by the mean capillary transit time T_c , as used below. The erf is the error function and it is defined as:

$$\operatorname{erf}(t) = \frac{2}{\sqrt{\pi}} \int_0^t dx \exp(-x^2). \quad [3]$$

The AIF model (Parker's AIF, $\Phi = \{A_1, B_1, \sigma_1, A_2, B_2, \sigma_2, \alpha, \beta, s, \tau\}$) is formulated as a mixture of two Gaussians and an exponential modulated with a sigmoid function (8):

$$C_p(\Phi, n) = \sum_{i=1}^2 \frac{A_i}{\sigma_i \sqrt{2\pi}} \exp\left(-\frac{(nT_s - B_i)^2}{2\sigma_i^2}\right) + \frac{\alpha \exp(-\beta nT_s)}{1 + \exp(-s(nT_s - \tau))}, \quad [4]$$

where A_i , B_i and σ_i are the parameters of the i -th Gaussian, α and β are the amplitude and decay parameters of the exponential function, s and τ are the steepness and center of the sigmoid.

In general, blind-deconvolution methods provide an AIF estimate with an unknown scaling factor. This factor has to be estimated using some additional information (12). Three methods of scaling are used here. The first method is scaling to the area under the curve (AUC) of a measured AIF. The second method is scaling to the AUC of the "tail" of a measured AIF (the part of the curve after the peak of signal intensity). The third method is a "reference-tissue" scaling where the AIF estimate is scaled so that nonblind deconvolution applied to a reference-tissue region (e.g., muscle) results in an assumed (literature-based) sum of the fractional blood plasma volume (v_p) and v_e . This sum equals the AUC of the IRF. The reference tissue scaling approach used here is similar to (12), but includes also the vascular phase due to the more complex IRF model used here.

AIF scaling with respect to the AUC of the measured AIF is robust as the complete measured AIF signal is used, but suffers from signal distortions affecting mainly the first-pass peak (because of the highest tracer concentration) due to T2* effect, saturation in case of inversion-recovery and saturation-recovery acquisition methods and due to nonlinear relationship between R1 and tracer

concentration for higher concentrations. Scaling to the AUC of the AIF "tail" suffers from low SNR in the later AIF part. The reference-tissue scaling overcomes these problems but relies on the same sum of the fractional blood and extravascular-extravascular volumes for the reference tissue in all examinations.

Evaluation Methods

Synthetic Data

Synthetic tissue tracer time sequences were generated as a convolution of the Parker's AIF model, the DCATH IRF model and the delay-related Gaussian function (quantities C_p , R , G in Eq. [1]). The sampling period of synthetic data (T_s) was set to 1 s. The number of samples was set to 200 for synthetic data. The following parameter values were used for AIF (according to Table 1 in (8)): $A_1 = 0.809$ mmol.min, $A_2 = 0.33$ mmol.min, $B_1 = 0.17046$ min, $B_2 = 0.365$ min, $\sigma_1 = 0.0563$ min, $\sigma_2 = 0.132$ min, $\alpha = 1.05$ mmol, $\beta = 0.1685$ min⁻¹, $s = 38.078$ min⁻¹, $\tau = 0.483$ min. The parameter value ranges of the generated IRFs (one IRF for each channel) were the following: $F_p = [0.3-0.8]$ mL/min/mL tissue, $E = [0.3-0.7]$, $v_e = [0.1-0.3]$ mL/mL tissue, $\mu_R = [0.167-0.417]$ min, $\sigma = [0.1-0.3]$ min. The parameters for the Gaussian function G were: $\sigma_G = 0.0224$ min in all of the performed analyses (including the clinical analyses) and $\mu_m = [0.0167-0.3334]$ min. The σ_G value was a compromise ensuring a constant area under the $G(\mu_m, n)$ curve and avoiding its undersampling-induced time-domain signal-discontinuity on one side, while minimizing signal-shape broadening due to the convolution with $G(\mu_m, n)$ on the other side. White Gaussian noise was added to each generated tissue tracer time sequence. The SNR range was 3 to 950, defined as the mean value of the noise-less signal divided by the standard deviation of the noise. The same SNR was used in each noise realization for all channels.

The presented blind-deconvolution method was applied to the synthetic data for different noise realizations and numbers of channels. The initial AIF-parameter estimates were as follows: $A_1 = 0.6$ mmol.min, $A_2 = 0.4$ mmol.min, $B_1 = 0.1$ min, $B_2 = 0.1$ min, $\sigma_1 = 0.02$ min, $\sigma_2 = 0.3$ min, $\alpha = 0.8$ mmol, $\beta = 0.2$ min⁻¹, $s = 20$ min⁻¹, $\tau = 0.3$ min. The initial IRF-parameter estimates for all channels were: $F_p = 0.2$ mL/min/mL tissue, $E = 0.5$, $v_e = 0.2$ mL/mL tissue, $\mu_R = 5T_s$, $\sigma = T_s$ and the initial delays of the Gaussian function $G(\mu_m, n)$ were $\mu_m = 0.167$ min. For the purpose of this evaluation also other initial AIF-parameter estimates were investigated. They were chosen to represent a narrow, wide, low, and high first-pass peak and several levels of the second-pass peak and the tail. The optimization constraints were F_p : $[10^{-6}-2000]$ mL/min/mL tissue, E : $[0.001-1]$, v_e : $[0.001-1]$ mL/mL tissue, μ_R : $[T_s/2-100T_s]$ min, σ : $[T_s/2-100T_s]$ min. The AIF-parameter constraints were for A_1 and A_2 : $[0.1-1.2]$ mmol.min, σ_1 : $[0.001-0.12]$ min, s : $[1-120]$ min⁻¹ and $[0.01-1.2]$ for the rest of the AIF parameters (in units of the parameters given above). The constraints for the delays μ_m were $[0.01-2]$ min. The selected nonzero lower constraint bounds prevented dividing by zero.

The precision and accuracy of the AIF estimation was measured as a relative L_1 -based error:

$$AIF\%_{ERROR} = \frac{1}{N} \sum_{n=1}^N \left(\frac{1}{W} \sum_{w=1}^W \frac{|\hat{C}_p(w, n) - C_p^{ref}(n)|}{C_p^{ref}(n)} \cdot 100 \right), \quad [5]$$

where N is the number of AIF samples, W is the number of noise realizations, w is the noise-realization index, \hat{C}_p is the estimated AIF and C_p^{ref} is the reference noise-free AIF.

Clinical Data

The evaluation was done on seven clinical examinations of two patients with RCC. The first and the second examination of each patient were acquired in a time interval of two weeks for patient 1 and one week for patient 2. For patient 2, both examinations preceded the treatment. For patient 1, the treatment was initiated between these first two examinations. However, no change was observed in the second examination with respect to the first one, based on radiologist's thorough evaluation of additional MR images acquired within each examination in addition to DCE-MRI: native and postcontrast T1-weighted images, native T2-weighted images, diffusion-weighted (DWI) and apparent-diffusion-coefficient (ADC) images. Hence, the first and second examinations are referred to as baseline for both patients in this evaluation too simplify the results description.

The following examinations (one examination for patient 1 and two examinations for patient 2) were acquired during the Axitinib antiangiogenic treatment with the time interval of 16 weeks for patient 1 and 3 and 29 weeks for patient 2 from the treatment start of each patient. The baseline examinations were used for evaluation of reproducibility, while the follow-up examinations illustrated the response to treatment.

MRI acquisition was done using the Magnetom Avanto 1.5 T MRI scanner (Siemens AG, Munich, Germany). The dynamic sequence was acquired using T1-weighted 2D saturation-recovery prepared Turbo FLASH (nonselective SR pulse), TR/TE/TI 400/1.09/200 ms, flip angle 16°, image matrix 128 × 128 pixels, three coronal slices in the abdominal region. The sampling period, T_s , (acquisition time for one frame, i.e., three slices) was 1200 ms, the dynamic-sequence acquisition time was 10 min. For conversion of signal intensity to R1, three precontrast recordings were acquired using the same pulse sequence with varying TI (500, 1000, 3000 ms), five frames for each TI. Bolus of 7.5 mL of the tracer Gadovist (Bayer Schering Pharma, Berlin, Germany) was manually injected into the antecubital vein.

The image sequences were registered to correct for respiration-related motion artifacts. Manual registration frame-by-frame was used for correction of in-plane shift. Then, using the precontrast recordings and the procedure described in (36), the dynamic image sequence was converted from signal intensity to relaxation rate change, $\Delta R1$, which is directly proportional to the tracer concentration (assuming a linear relationship in the expected concentration range).

The population based Parker's AIF with values from Table 1 in (8) was used as the initial estimate of the AIF to provide proximity of the initial estimate to the real

solution and decreases the risk of the trapping in a local optimum. Initial estimates of the IRF model for each channel were the same as for the synthetic data. For all channels, the initial estimates of the delay-related Gaussian function $G(\mu_m, n)$ were $\mu_m = 0.8$ min – the assumed bolus arrival time of the tracer. The optimization constraints were the same as for the synthetic data. The tracer time sequences used for multi-channel blind deconvolution were derived from five to eight homogenous-tissue ROIs manually drawn by a radiologist within the tumor, psoas muscles, and vertebrae, chosen from all three acquired slices. The tracer concentration time sequences were calculated as the mean within each ROI at every time point. The SNRs of these signals were in the range of 9.7 to 44.5 with the highest SNR values in the tumor rim. For the clinical data, the SNR was estimated as the mean value of the tracer time sequence divided by the standard deviation of its last 2-min segment (assumed constant).

The AIFs estimated by means of blind multi-channel deconvolution were used in pixel-by-pixel nonblind deconvolution (Eq. [1], where C_p is the estimated AIF and $m=1$) to estimate the perfusion-parameter maps. The lower SNR of pixel-based tracer time sequences (from 3 for muscle to 13 for RCC metastasis) suggests that the complete DCATH model cannot be used reliably (25). Hence, the DCATH model was simplified by fixing the parameter σ to a small value, $T_s/2$. This value is high enough to preserve the continuous formulation of the impulse residue function inherent to the DCATH model and low enough to consider the model as an approximation of the AATH model, and μ_R is replaced by T_c in Eq. [2].

The reference tissue for AIF scaling was the psoas muscle. The reference literature-based sum of the fractional blood volume and the extravascular extracellular space volume is 14 mL/100 mL tissue (37,38). Note that blood volume in (37) was converted to blood-plasma volume by multiplication with $(1-rHct)$, where Hct is the large vessel hematocrit and r is the ratio of small to large vessel hematocrit ($r \approx 0.7$, $Hct \approx 0.4$) (39).

The directly estimated perfusion parameters were F_p , E , v_e , and T_c . The perfusion parameters derived from the directly estimated parameters were the blood plasma volume ($v_p = T_c F_p$), the volume transfer constant between blood plasma and extravascular extracellular space ($K_{trans} = F_p E$), the rate constant between extravascular extracellular space ($k_{ep} = E F_p / v_e$) and the permeability surface area product ($PS = -F_p \ln(1-E)$).

Perfusion parameters of the tumor tissue region were estimated for each examination and each slice, using four estimates of AIF: examination-specific blind-deconvolution based AIF, patient specific blind-deconvolution based AIF (average of examination specific blind-deconvolution based AIFs for the given patient), Parker's population AIF and examination specific measured AIF. The measured AIFs were obtained as a pixel-based tissue tracer time sequence in large arteries near the tumor, divided by $1-Hct$ to convert the tracer concentration in blood to the concentration in blood-plasma (7). Furthermore, all above described three types of AIF scaling (see end of the Section Methods) were applied. The resulting

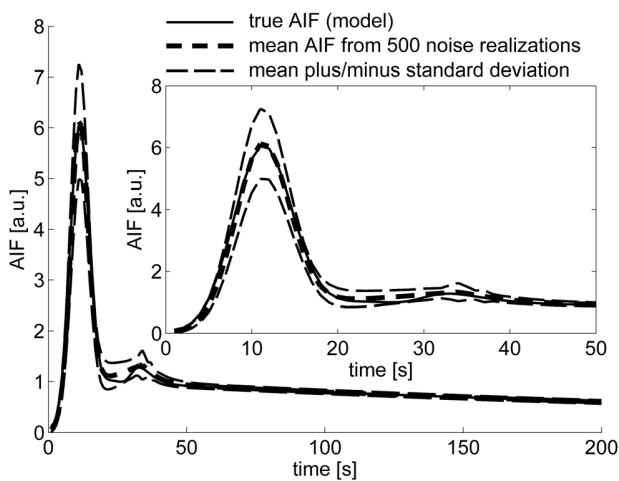


FIG. 1. AIF estimation, four ROIs, SNR 30, 500 noise realizations, inset shows the initial part in detail.

perfusion parameter estimates were compared to each other and with literature values.

RESULTS

Synthetic Data

Blind multi-channel deconvolution with the parameters above was applied to the synthetic data with 500 different noise realizations, four ROIs, and SNR=30 (average SNR in the clinical tissue ROIs). Figure 1 shows the mean estimated AIF ± standard deviation.

Estimation of AIF versus Initial Estimates

The same experiment was repeated for several initial AIF estimates (parameters set manually). The resulted AIF estimation ± standard deviation compared to the true AIF (model) for some initial AIF estimates are shown in Figure 2. The last example of the initial estimate illustrates the case of AIF estimation being trapped in an incorrect local optimum (probably due to the extremely low tail of the initial AIF).

Estimation of AIF versus Number of Channels

The relative L₁-based error (Eq. [5]) and the standard deviation of the error of AIF estimation decreases with increasing number of tissue ROIs (channels), Figure 3. The error of AIF estimation was for four ROIs approximately 6% and less for more ROIs.

Estimation of AIF versus Signal to Noise Ratio

The relative L₁-based error (Eq. [5]) and the standard deviation of the error of AIF estimation decreases with increasing SNR, Figure 4. An AIF-estimation error of approximately 2.5% and less was obtained for SNR higher than 30.

Clinical Data

Figure 5 shows examination-specific blind-deconvolution AIF estimates, measured AIFs and Parker's AIF for all

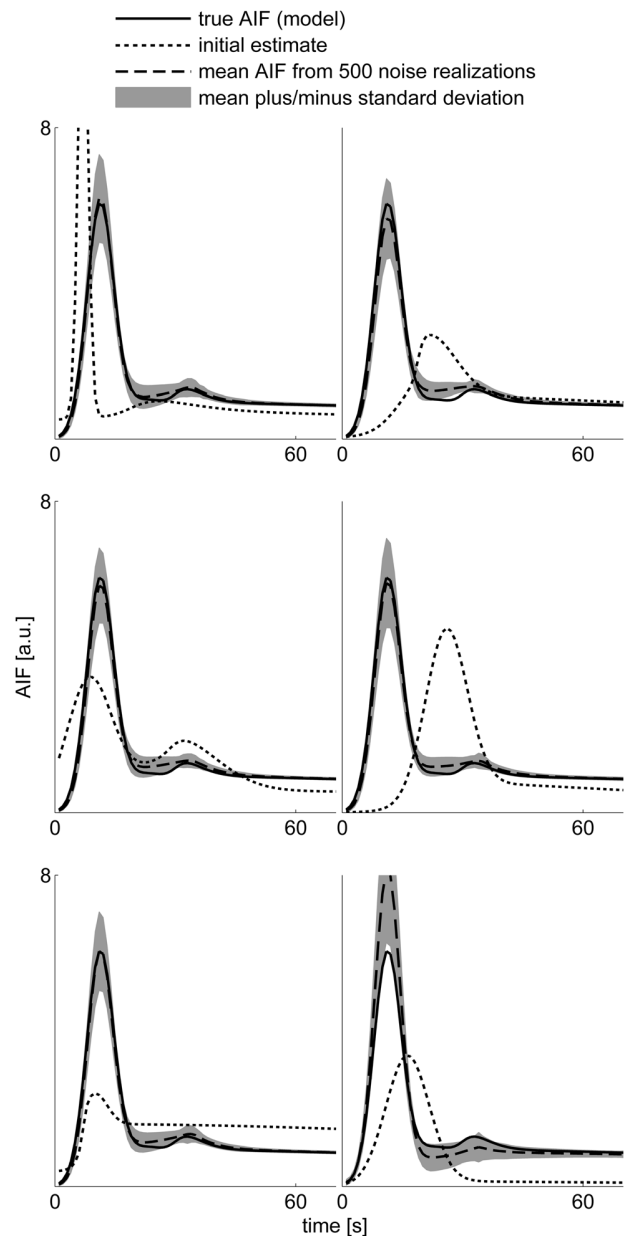


FIG. 2. Dependence of blind deconvolution on the initial AIF estimate, four ROIs, SNR 30, 500 noise realizations.

examinations of the two RCC patients. For better clarity, the time scale was magnified. The blind-deconvolution AIFs were visually similar to Parker's population AIFs. Taking into account the independence of the blind deconvolution algorithm on the initial AIF estimate shown in the simulations, this indicates that Parker's population-based AIF is a realistic AIF estimate. The low level of the first-pass peak in the measured AIFs compared to other AIF types shows the saturation effect.

Figure 6 shows three perfusion-parameter maps of the RCC metastasis obtained using the examination-specific blind-deconvolution AIF for the same slice of the first examination of patient 1.

In each slice, an experienced radiologist delineated the tumor regions. Boxplots were calculated from all pixels

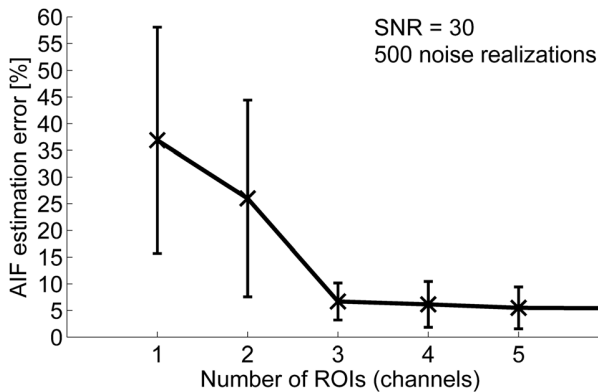


FIG. 3. AIF estimation error (mean plus/minus standard deviation) versus number of ROIs, SNR 30, 500 noise realizations.

of these tumor regions for each perfusion parameter for each patient examination (all three slices) and for each type of AIF estimation.

Boxplots in Figure 7 show a comparison of the AIF scaling methods for two selected perfusion parameters for both patients and all examinations using the examination specific blind-deconvolution AIF estimates. In each boxplot, the central mark is the median, the edges of the box are the 25th and 75th percentiles and the whiskers extend to the most extreme data points not considered outliers. In cases, where the notches in the boxplots do not overlap, the true medians differ with a 95% confidence (40). Scaling to the AUC of the measured AIF and to the AUC of the measured AIF's tail gave substantially less consistent results. More specifically, the reproducibility of the perfusion-parameter estimates for the baseline (ex1 and ex2) examinations was lower and the treatment effect was not according to expectations (see below) for *PS* of patient 2. This indicates that, for our experimental setup, the AIF measurement artifacts connected to high tracer concentration and low SNR in the AIF tail (see section Methods) contribute to the error of AIF scaling more than the variability of $v_e + v_p$ in the reference tissue used in reference-tissue AIF scaling. Further results are shown only for the reference-tissue scaling.

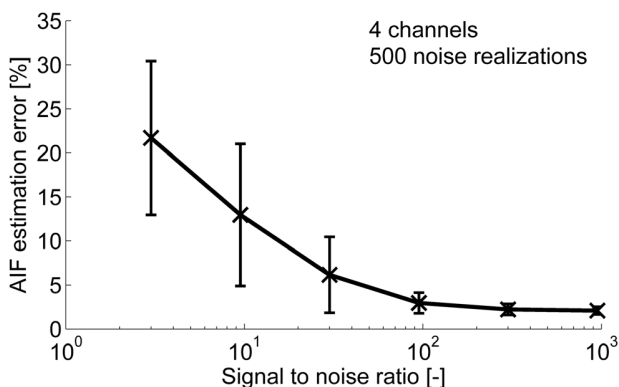


FIG. 4. AIF estimation error (mean plus/minus standard deviation) versus SNR, number of channels 4, 500 noise realizations.

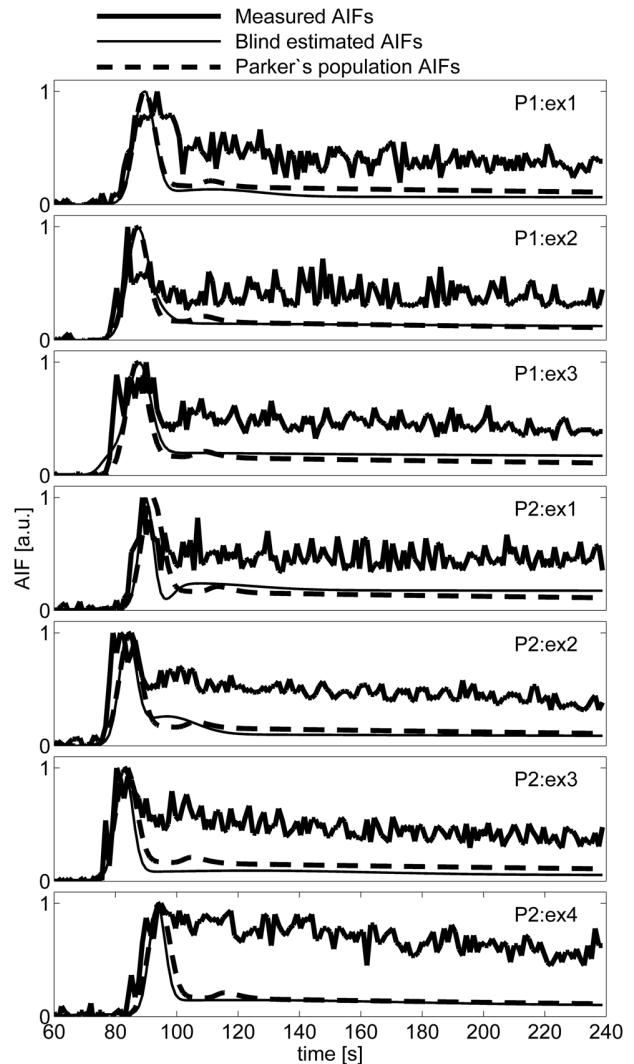


FIG. 5. Examination-specific blind-deconvolution AIF estimates ("Blind estimated AIFs"), measured AIFs and Parker's population AIFs for both RCC patients (P1, P2) and their examinations (ex1-3 for P1 and ex1-4 for P2), magnified in time, normalized to the maximum signal value.

Boxplots in Figure 8 show the time evolution for the selected perfusion parameters for both patients and all examinations using examination-specific and patient-specific blind-deconvolution AIF estimates, measured AIFs and Parker's AIF. Note different y-axes for different AIF estimation methods in Figure 8. The complete set of results and literature values are given in Table 1. The literature based values are taken from studies in (3) and (41). Note that blood flow and blood volume given in (3) were converted to blood-plasma by multiplying with $(1-rHct)$. A Mann-Whitney U-test on a 95% significance level was used to test the null hypothesis that the two baseline examinations resulted in perfusion-parameter estimates with the same medians. This null hypothesis was not rejected ($P > 0.05$) for table values in bold, in almost all cases of the examination-specific blind-deconvolution AIFs: for k_{ep} , K_{trans} , *PS*, and v_e of patient

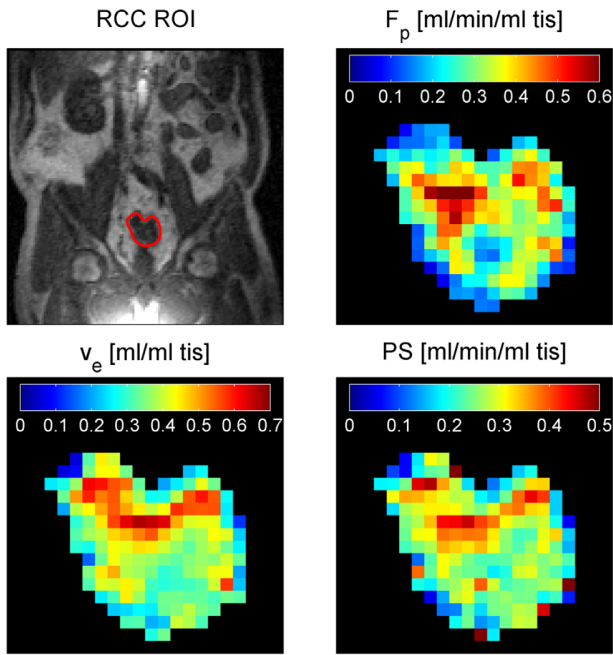


FIG. 6. Examples of three perfusion maps, Patient 1: examination 1, obtained using reference-tissue AIF scaling, examination-specific blind-deconvolution AIF. Tumor ROI delineated in red in the anatomical image and magnified in the perfusion-parameter images.

1 and for E , F_p , K_{trans} , and PS of patient 2. For other types of AIFs, the medians were different ($P < 0.05$), except for the patient-specific blind-deconvolution AIFs for PS and v_p of patient 1 together with E of patient 2, and v_p of patient 1 for the Parker's AIF. These statistical results correspond to overlapping of boxplot notches in Figure 8. In summary, the best reproducibility of the perfusion-parameter estimates for the baseline examinations was achieved for examination-specific blind-deconvolution AIFs. Slightly worse reproducibility was achieved using patient-specific blind-deconvolution AIF and Parker's AIF ranked as the third. Use of the measured AIFs resulted in rejection of the null hypothesis in all cases which indicates the worst reproducibility.

A therapy-induced increase in fibrotic and necrotic tissue is expected, leading to a decrease in v_p (boxplots not shown, see Table 1 and its description below) and hence also in F_p and PS . Therapy-induced blood vessel normalization is also expected, further decreasing PS , but increasing F_p (i.e., opposite effect on F_p than fibrosis and necrosis). The trend in the parameter change was in agreement with the known treatment effects for antiangiogenic therapy.

According to Figure 8, F_p clearly decreases due to therapy with all AIF estimation methods. Hence, the effect of fibrosis and necrosis on F_p seems to be more pronounced than that of vessel normalization. The effect of increased fibrotic-tissue fraction and vessel normalization on v_e is not clearly known, while pronounced necrosis is supposed to increase v_e . The ranking of the AIF estimation methods with respect to the consistency with

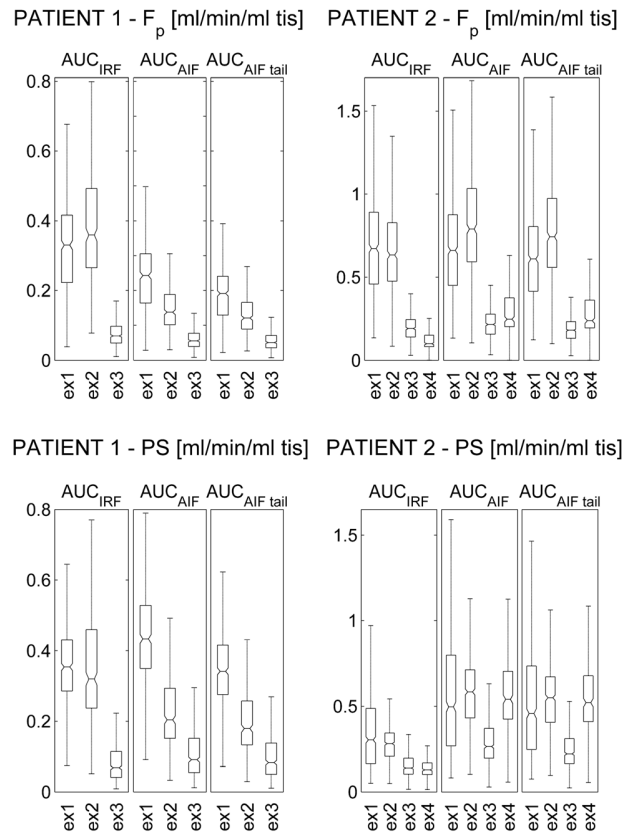


FIG. 7. Comparison of scaling methods on two estimated perfusion parameters of the tumor for all examinations (abbreviated as "ex") of both patients using the examination specific blind-deconvolution AIFs scaled to the reference tissue (AUC_{IRF}), to the AUC of the measured AIF (AUC_{AIF}) and to the tail of the measured AIF ($AUC_{AIF tail}$).

the expected effect of therapy is the same as in the evaluation of reproducibility.

Table 1 shows that the least reliable perfusion parameters in terms of using examination-specific blind-deconvolution AIF were v_p and T_c . Their estimates showed the least reproducible baseline and treatment-effect consistency. This shows that T_c is the perfusion parameter, which is the most difficult one to estimate out of the directly estimated parameters. As v_p is derived from T_c ($v_p = T_c F_p$), the estimation error of T_c is propagated to the estimation error of v_p . According to Table 1, for v_p , the patient-specific blind-deconvolution AIFs resulted in a better reproducibility and consistency with the baseline and assumed therapy effect (decrease) than the examination-specific blind-deconvolution AIFs.

The literature-based RCC perfusion parameter values in Table 1 are divided into untreated patients (before the treatment), and treated patients with antiangiogenic therapy. The effect of the antiangiogenic treatment in (3) and (41) is the same as in our results using blind deconvolution AIFs (decrease of F_p and v_p , increase of E and inconclusive change in v_e). This supports our assumptions about the therapy effects. The estimated perfusion parameter values were mostly in the same range as the literature values.

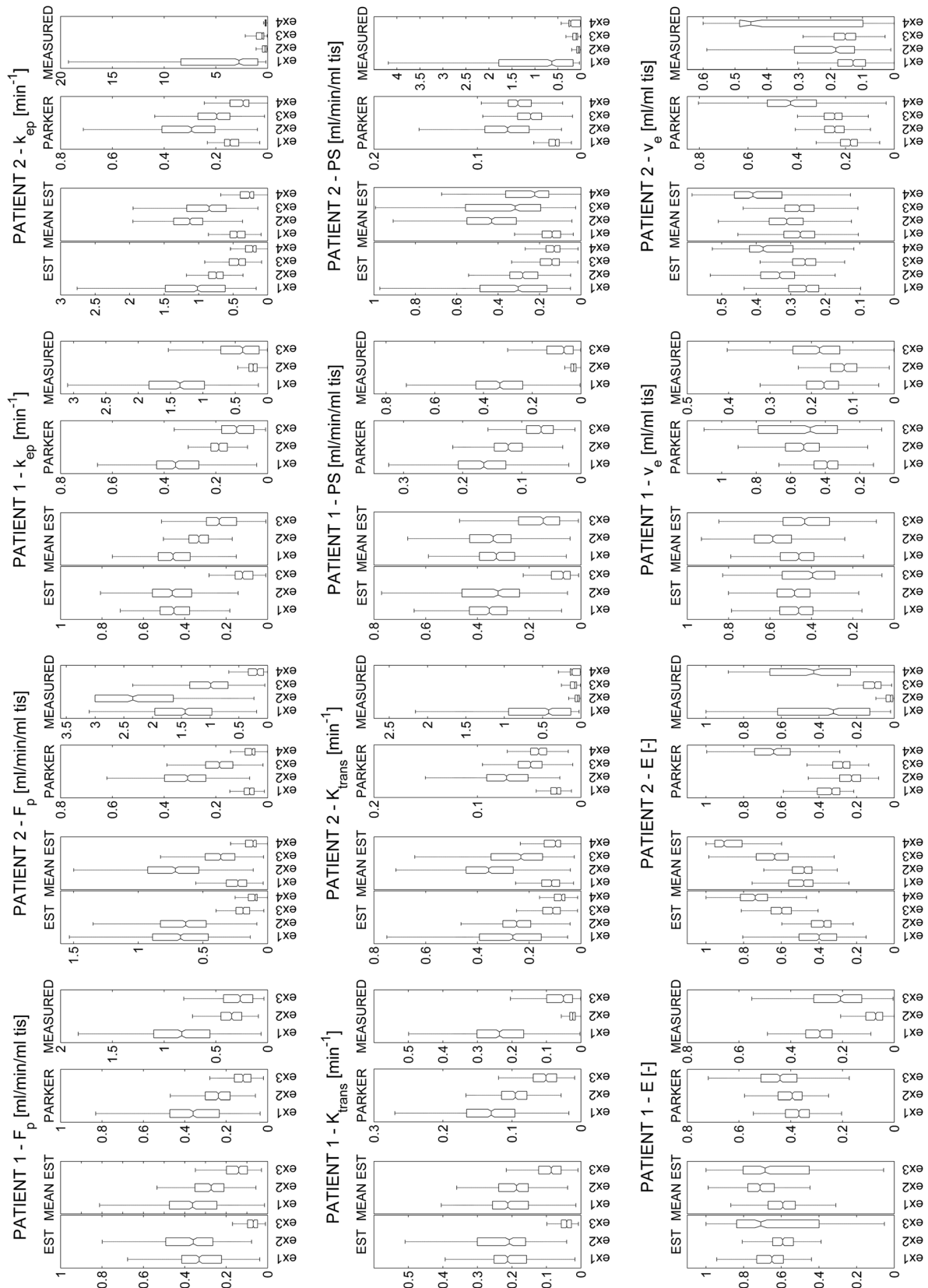


FIG. 8. Time evolution of the tumor perfusion parameters obtained using the examination specific blind-deconvolution AIFs (EST), patient-specific blind-deconvolution AIFs (MEAN EST), Parker’s AIF (PARKER) and examination-specific measured AIF (MEASURED) for the two patients and all of their examinations (abbreviated as “ex”), reference-tissue AIF scaling.

Table 1
Measured and Estimated Perfusion Parameters of RCC Metastasis for Both Patients and Their Examinations Together with Literature Values^a

Parameter	E	F _p	K _{trans}	PS	K _{ep}	T _c	V _p	V _e
	[-]	[ml/min/ml tis]	[min ⁻¹]	[ml/min/ml tis]	[min ⁻¹]	[min]	[ml/ml tis]	[ml/ml tis]
Literature								
Untreated [41]	0.05 ± 0.20	0.82 ± 0.60	-	-	-	-	0.16 ± 0.08	0.09 ± 0.11
Treated [41]	0.28 ± 0.14	0.14 ± 0.07	-	-	-	-	0.04 ± 0.04	0.10 ± 0.06
Untreated [3]	-	1.17 (0.46-1.70)	-	-	-	0.11 (0.09-0.21)	0.07 (0.05-0.11)	-
Treated [3]	-	0.55 (0.31-0.85)	-	-	-	0.15 (0.09-0.21)	0.03 (0.02-0.06)	-
Examination-Specific								
Blind-Deconv. AIFs								
PAT.1 exam. 1	0.65 (0.59-0.73)	0.33 (0.22-0.42)	0.21 (0.16-0.25)	0.35 (0.29-0.43)	0.45 (0.38-0.52)	0.26 (0.20-0.34)	0.09 (0.07-0.11)	0.46 (0.39-0.55)
exam. 2	0.59 (0.54-0.65)	0.36 (0.27-0.49)	0.21 (0.16-0.30)	0.32 (0.24-0.46)	0.46 (0.37-0.56)	0.51 (0.30-0.66)	0.16 (0.13-0.20)	0.48 (0.41-0.57)
exam. 3	0.71 (0.40-0.83)	0.07 (0.05-0.10)	0.04 (0.03-0.06)	0.07 (0.04-0.11)	1.12 (0.07-0.16)	0.40 (0.01-0.72)	0.02 (0.00-0.04)	0.39 (0.29-0.54)
PAT.2 exam. 1	0.40 (0.31-0.51)	0.67 (0.46-0.89)	0.26 (0.15-0.39)	0.30 (0.16-0.49)	1.02 (0.62-1.48)	0.26 (0.23-0.35)	0.18 (0.15-0.22)	0.25 (0.22-0.31)
exam. 2	0.37 (0.34-0.44)	0.63 (0.48-0.83)	0.25 (0.19-0.30)	0.28 (0.21-0.34)	0.74 (0.64-0.86)	0.12 (0.11-0.14)	0.08 (0.06-0.10)	0.33 (0.29-0.39)
exam. 3	0.60 (0.55-0.66)	0.19 (0.14-0.24)	0.11 (0.08-0.15)	0.14 (0.10-0.20)	0.42 (0.32-0.56)	0.56 (0.50-0.66)	0.11 (0.08-0.13)	0.26 (0.23-0.29)
exam. 4	0.74 (0.67-0.82)	0.10 (0.08-0.15)	0.07 (0.06-0.10)	0.13 (0.10-0.17)	0.21 (0.17-0.32)	0.89 (0.70-1.07)	0.09 (0.07-0.12)	0.38 (0.29-0.42)
PAT.1 exam. 1	0.59 (0.53-0.67)	0.36 (0.25-0.47)	0.21 (0.15-0.26)	0.33 (0.26-0.39)	0.46 (0.37-0.53)	0.26 (0.18-0.37)	0.10 (0.07-0.12)	0.46 (0.39-0.55)
exam. 2	0.71 (0.64-0.78)	0.27 (0.21-0.35)	0.19 (0.15-0.24)	0.34 (0.27-0.43)	0.33 (0.29-0.38)	0.34 (0.26-0.52)	0.10 (0.08-0.12)	0.59 (0.50-0.68)
exam. 3	0.69 (0.45-0.80)	0.14 (0.10-0.20)	0.09 (0.06-0.12)	0.15 (0.08-0.24)	0.23 (0.15-0.30)	0.54 (0.03-0.81)	0.06 (0.01-0.10)	0.43 (0.31-0.54)
PAT.2 exam. 1	0.48 (0.43-0.56)	0.23 (0.16-0.32)	0.11 (0.08-0.15)	0.14 (0.10-0.19)	0.44 (0.33-0.54)	0.37 (0.25-0.53)	0.09 (0.07-0.11)	0.27 (0.23-0.32)
exam. 2	0.48 (0.44-0.54)	0.71 (0.53-0.93)	0.36 (0.26-0.44)	0.43 (0.31-0.55)	1.13 (0.94-1.36)	0.13 (0.12-0.15)	0.10 (0.08-0.12)	0.31 (0.26-0.36)
exam. 3	0.64 (0.56-0.73)	0.36 (0.25-0.48)	0.23 (0.15-0.35)	0.32 (0.19-0.56)	0.85 (0.60-1.17)	0.22 (0.18-0.40)	0.09 (0.07-0.11)	0.27 (0.23-0.32)
exam. 4	0.90 (0.81-0.95)	0.11 (0.09-0.17)	0.10 (0.08-0.14)	0.22 (0.16-0.36)	0.26 (0.20-0.40)	0.73 (0.39-1.20)	0.08 (0.06-0.10)	0.41 (0.33-0.46)
PAT.1 exam. 1	0.37 (0.33-0.42)	0.36 (0.23-0.47)	0.13 (0.10-0.17)	0.16 (0.13-0.21)	0.36 (0.27-0.43)	0.43 (0.34-0.63)	0.16 (0.13-0.20)	0.39 (0.33-0.46)
exam. 2	0.39 (0.36-0.45)	0.24 (0.18-0.30)	0.10 (0.08-0.12)	0.12 (0.10-0.15)	0.19 (0.16-0.22)	0.68 (0.56-0.81)	0.16 (0.13-0.20)	0.52 (0.43-0.63)
exam. 3	0.44 (0.38-0.52)	0.12 (0.08-0.16)	0.05 (0.04-0.07)	0.06 (0.05-0.09)	0.12 (0.05-0.18)	0.79 (0.53-1.07)	0.08 (0.05-0.12)	0.48 (0.33-0.79)
PAT.2 exam. 1	0.33 (0.29-0.41)	0.07 (0.05-0.09)	0.02 (0.02-0.03)	0.03 (0.02-0.03)	0.14 (0.11-0.17)	0.68 (0.58-0.85)	0.05 (0.04-0.06)	0.18 (0.15-0.22)
exam. 2	0.23 (0.18-0.29)	0.31 (0.24-0.40)	0.07 (0.05-0.09)	0.07 (0.05-0.09)	0.29 (0.20-0.41)	0.47 (0.43-0.53)	0.14 (0.10-0.17)	0.24 (0.21-0.29)
exam. 3	0.27 (0.24-0.33)	0.19 (0.13-0.24)	0.05 (0.04-0.06)	0.05 (0.04-0.06)	0.20 (0.15-0.27)	0.72 (0.62-0.88)	0.13 (0.10-0.16)	0.24 (0.21-0.29)
exam. 4	0.64 (0.55-0.74)	0.06 (0.05-0.09)	0.04 (0.03-0.05)	0.06 (0.05-0.07)	0.09 (0.07-0.15)	1.31 (1.08-1.43)	0.06 (0.05-0.08)	0.43 (0.32-0.52)
PAT.1 exam. 1	0.29 (0.24-0.34)	0.83 (0.56-1.10)	0.24 (0.17-0.30)	0.33 (0.24-0.43)	1.35 (0.98-1.83)	0.18 (0.16-0.23)	0.17 (0.12-0.20)	0.17 (0.13-0.21)
exam. 2	0.07 (0.04-0.11)	0.35 (0.25-0.45)	0.02 (0.02-0.03)	0.03 (0.02-0.04)	0.22 (0.16-0.29)	0.40 (0.35-0.47)	0.15 (0.11-0.17)	0.12 (0.09-0.15)
exam. 3	0.21 (0.13-0.31)	0.27 (0.14-0.43)	0.05 (0.02-0.10)	0.07 (0.03-0.14)	0.39 (0.13-0.72)	0.42 (0.26-0.72)	0.11 (0.06-0.16)	0.18 (0.13-0.24)
exam. 1	0.32 (0.13-0.62)	1.43 (0.97-1.96)	0.42 (0.13-0.94)	0.63 (0.17-1.78)	2.77 (0.95-8.38)	0.19 (0.16-0.22)	0.26 (0.21-0.33)	0.13 (0.09-0.18)
exam. 2	0.02 (0.01-0.04)	2.34 (1.64-3.00)	0.04 (0.02-0.08)	0.05 (0.02-0.09)	0.29 (0.08-0.51)	0.12 (0.11-0.16)	0.29 (0.24-0.34)	0.18 (0.12-0.31)
exam. 3	0.10 (0.07-0.16)	0.99 (0.69-1.36)	0.08 (0.06-0.14)	0.10 (0.07-0.17)	0.54 (0.36-1.09)	0.22 (0.18-0.25)	0.21 (0.16-0.26)	0.15 (0.12-0.19)
exam. 4	0.43 (0.23-0.66)	0.18 (0.07-0.34)	0.12 (0.01-0.14)	0.22 (0.01-0.26)	0.27 (0.13-0.29)	0.35 (0.28-0.43)	0.21 (0.16-0.31)	0.45 (0.10-0.49)

^aThe values are in the format mean ± standard deviation, or median (25th, 75th percentile), depending on the given source. Cases, in which the null hypothesis, namely that two baseline examinations (exam 1 and exam 2) resulted in estimates with the same medians, cannot be rejected (Mann-Whitney U test, $P > 0.05$), are in bold.

DISCUSSION AND CONCLUSIONS

An extension to the published blind multi-channel deconvolution methods for AIF estimation was presented and tested on synthetic and clinical data. The standard extended-Tofts IRF model was replaced by the more realistic DCATH model, which describes the vascular distribution phase of the tracer in more detail. To compensate for the increase of the number of parameters to be estimated by blind deconvolution, the standard Parker's AIF model (described by 10 parameters) was used instead of the AIF model used in the blind-deconvolution approach (9,15,16) (described by 11 parameters).

The dependence of the AIF-estimation accuracy on the number of channels and SNR was demonstrated on simulated data. In general, the results show that the AIF can be estimated with a high accuracy (relative error 5% and less under realistic conditions, i.e. SNR 30, four channels or more). The choice of the number of channels (tissue ROIs) should be as high as possible for the given application, depending on the number of different tissue types in the imaged region.

On the other hand, the number of tissue ROIs is limited by the fact that tissue ROIs too remote from the analyzed tissue might degrade the AIF estimation because of different dispersion of their local AIFs (in multi-channel blind deconvolution, the dispersion of AIF is assumed the same for all tissue ROIs). This might be solved by including the dispersion term (42,43) in the model used in the blind-deconvolution algorithm.

The evaluation of the multi-channel blind deconvolution algorithm on clinical data was used for an illustration of the method performance. The results indicate that blind multi-channel deconvolution leads to perfusion-parameter estimates which are fairly reproducible and consistent with theoretical expectations of the treatment effects. The blind-deconvolution based AIF estimates were more reliable (in terms of reproducibility and consistency) than the population based Parker's AIF and the measured AIFs. In addition, the examination-specific blind-deconvolution AIFs were more reliable than patient-specific blind-deconvolution AIFs (taken as the average of all examination-specific blind-deconvolution AIFs for a given patient), which indicates the importance of examination-specific AIF estimation.

The lower performance of Parker's population-based AIF compared to the blind-deconvolution based AIFs can be explained by inpatient differences in the vascular system, in the therapy- and disease-induced vascular tree change and by differences in manual injection speed. These effects are not accounted for when using the same AIF for all experiments. The lowest performance of the measured AIFs compared to the blind-deconvolution and Parker's AIFs was due to signal saturation (for arterial tracer concentration higher than a certain level, the longitudinal magnetization reaches the steady state during inversion time) and flow artifacts.

It should be noted that in most DCE-MRI studies, the nonblind deconvolution relies on the simple Tofts or extended Tofts IRF model. Here, the DCATH IRF model (with fixed σ parameter) was used instead. The use of such more complex IRF model puts more demands on

the accuracy of the AIF. This might explain the fairly poor performance when using Parker's population AIF and the measured AIF.

An extended evaluation on a larger patient group will be performed to test the validity of the blind-deconvolution approach in clinical settings.

In conclusion, blind multi-channel deconvolution appears to be a good method of AIF estimation avoiding the problems of AIF measurement artifacts and avoiding simplification induced by the use of population-based AIF models. It might be the method of choice when complex IRF models (such as AATH, DCATH, 2CXM) are to be applied in nonblind deconvolution.

REFERENCES

1. Jackson A, Buckley D, Parker G. Dynamic contrast-enhanced magnetic resonance imaging in oncology. Berlin: Springer; 2005. 312 p.
2. Collins DJ, Padhani AR. Dynamic magnetic resonance imaging of tumor perfusion. *IEEE Eng Med Biol Mag* 2004;23:65–83.
3. Fournier LS, Oudard S, Thiam R, Trinquart L, Banu E, Medioni J, Balvay D, Chatellier G, Fria G, Cuenod CHA. Metastatic renal carcinoma: evaluation of antiangiogenic therapy with dynamic contrast-enhanced CT. *Radiology* 2010;256:511–518.
4. Barrett T, Brechbiel M, Bernardo M, Choyke PL. MRI of tumor angiogenesis. *J Magn Reson Imaging* 2007;26:235–249.
5. Sourbron SP, Buckley DL. Classic models for dynamic contrast-enhanced MRI. *NMR Biomed* 2013;26:1004–1027.
6. Sourbron SP, Buckley DL. Tracer kinetic modelling in MRI: estimating perfusion and capillary permeability. *Phys Med Biol* 2012;57:R1–R33.
7. Koh TS, Bisdas S, Koh DM, Thng CHH. Fundamentals of tracer kinetics for dynamic contrast-enhanced MRI. *J Magn Reson Imaging* 2011;34:1262–1276.
8. Parker GJM, Roberts C, Macdonald A, Buonaccorsi GA, Cheung S, Buckley DL, Jackson A, Watson Y, Davies K, Jayson GC. Experimentally-derived functional form for a population-averaged high-temporal-resolution arterial input function for dynamic contrast-enhanced MRI. *Magn Reson Med* 2006;56:993–1000.
9. Fluckiger JU, Schabel MC, DiBella EVR. Model-based blind estimation of kinetic parameters in dynamic contrast enhanced (DCE)-MRI. *Magn Reson Med* 2009;62:1477–1486.
10. Riabkov D, Di Bella EVR. Estimation of kinetic parameters without input functions: analysis of three methods for multi-channel blind identification. *IEEE Trans Biomed Eng* 2002;49:1318–1327.
11. Taxt T, Jiřík R, Rygh CB, Grüner R, Bartoš M, Andersen E, Curry F-R, Reed RK. Single-channel blind estimation of arterial input function and tissue impulse response in DCE-MRI. *IEEE Trans Biomed Eng* 2012;59:1012–1021.
12. Yang C, Karzmar GS, Medved M, Stadler WM. Multiple reference tissue method for contrast agent arterial input function estimation. *Magn Reson Med* 2007;58:1266–1275.
13. Jiřík R, Bartoš M, Standara M, Taxt T. Blind multi-channel estimation of arterial input function in dynamic contrast-enhanced MRI. In *Proceedings of Biosignal 2010: Analysis of Biomedical Signals and Images*. Brno: University of Technology; 2010, p 373–377.
14. YuLin Y-C, Chan T-H, Chi C-Y, Ng S-H, Liu H-L, Wei K-C, Wai Y-Y, Wang C-C, Wang J-J. Blind estimation of the arterial input function in dynamic contrast-enhanced MRI using purity maximization. *Magn Reson Med* 2012;68:1439–1449.
15. Fluckiger JU, Schabel MC, DiBella EVR. The effect of temporal sampling on quantitative pharmacokinetic and three-time-point analysis of breast DCE-MRI. *Magn Reson Imaging* 2012;30:934–943.
16. Schabel MC, Fluckiger JU, DiBella EVR. A model-constrained Monte Carlo method for blind arterial input function estimation in dynamic contrast-enhanced MRI: I. Simulations. *Phys Med Biol* 2010;55:4783–4806.
17. Tofts PS, Brix G, Buckley DL, et al. Estimating kinetic parameters from dynamic contrast-enhanced t1-weighted MRI of a diffusible tracer: Standardized quantities and symbols. *Magn Reson Imaging* 1999;10:223–232.

18. Schabel MC, Morell GR, Oh KY, Walczak CHA, Barlow RB, Neumayer LA. Pharmacokinetic mapping for lesion classification in dynamic breast MRI. *J Magn Reson Imaging* 2010;31:1371–1378.
19. Jansen JFA, Carlson DL, Lu Y, et al. Correlation of a priori DCE-MRI and 1H-MRS data with molecular markers in neck nodal metastases: Initial analysis. *Oral Oncol* 2012;48:717–722.
20. Brix G, Kiessling F, Lucht R, Darai S, Wasser K, Delorme S, Griebel J. Microcirculation and microvasculature in breast tumors: pharmacokinetic analysis of dynamic MR image series. *Magn Reson Med* 2004;52:420–429.
21. Bains LJ, McGrath DM, Naish JH, Cheung S, Watson Y, Taylor MB, Logue JP, Parker GJM, Waterton JC, Buckley DL. Tracer kinetic analysis of dynamic contrast-enhanced MRI and CT bladder cancer data: a preliminary comparison to assess the magnitude of water exchange effects. *Magn Reson Med* 2010;64:595–603.
22. St Lawrence KS, Lee TY. An adiabatic approximation to the tissue homogeneity model for water exchange in the brain: I. theoretical derivation. *J Cereb Blood Flow Metab* 1998;18:1365–1377.
23. Kershaw LE, Buckley DL. Precision in measurements of perfusion and microvascular permeability with T1-weighted dynamic contrast-enhanced MRI. *Magn Reson Med* 2006;56:986–992.
24. Koh TS, Zeman V, Darko J, Lee TY, Milosevic MF, Haider M, Warde P, Yeung IWT. The inclusion of capillary distribution in the adiabatic tissue homogeneity model of blood flow. *Phys Med Biol* 2001;46:1519–1538.
25. Bartoš M, Jiřík R, Kratochvíla J, Standara M, Starčuk Z Jr, Taxt T. The precision of DCE- MRI using the tissue homogeneity model with continuous formulation of the perfusion parameters. *Magn Reson Imaging* 2014;32:505–513.
26. Jacobs I, Srijkers G, Keizer H, Janssen H, Nicolay K, Schabel M. A novel approach to tracer-kinetic modeling of (macromolecular) multi-bolus DCE-MRI data, applied in a murine tumor model. In Proceedings of the 22nd Annual Meeting of ISMRM, Milan Italy, 2014. Abstract 0042.
27. Jiřík R, Soucek K, Drazanova E, Grossova L, Standara M, Kratochvíla J, Macicek O, Mala A, Taxt T, Starčuk Z Jr. Blind multi-channel deconvolution for estimation of a parametric AIF in DCE-MRI of mice. In Proceedings of the 22nd Annual Meeting of ISMRM, Milan Italy, 2014. Abstract 2754.
28. Jiřík R, Souček K, Mézl M, et al. Blind deconvolution in dynamic contrast-enhanced MRI and ultrasound. In Proceedings of 36th Annual International Conference of the IEEE Engineering in Medicine and Biology Society (EMBC'14), Chicago IL, 2014. p 4276–4279.
29. Mitchell CL, O'Connor JPB, Roberts C, et al. A two-part phase II study of cediranib in patients with advanced solid tumours: the effect of food on single-dose pharmacokinetics and an evaluation of safety, efficacy and imaging pharmacodynamics. *Cancer Chemother Pharmacol* 2011;68:631–641.
30. O'Connor JPB, Rose CJ, Jackson A, et al. DCE-MRI biomarkers of tumour heterogeneity predict CRC liver metastasis shrinkage following bevacizumab and FOLFOX-6. *Br J Cancer* 2011;105:139–145.
31. Calcagno C, Ramachandran S, Izquierdo-Garcia D, et al. The complementary roles of dynamic contrast-enhanced MRI and 18F-fluorodeoxyglucose PET/CT for imaging of carotid atherosclerosis. *Eur J Nucl Med Mol Imaging* 2013;40:1884–1893.
32. Dcemri: A package for medical image analysis [online] 2009. <http://dcemri.sourceforge.net/index.shtml>. Cited October 6, 2014.
33. Kratochvíla J, Jiřík R, Standara M, Bartoš M, Taxt T, Starčuk Z Jr. Blind parametric multi-channel deconvolution for estimation of arterial input function in dynamic contrast-enhanced MRI. In ESMRB 2012 Congress, Lisbon, Portugal, 2012, Book of Abstracts. p. 228–229.
34. Gill PE, Murray W, Wright MH. Practical optimization. London: Academic Press; 1981.
35. Luenberger DG. Linear and nonlinear programming (2nd ed). London: Addison-Wesley; 1984. 491 p.
36. Henderson E, Sykes J, Drost D, Weinmann HJ, Rutt BK, Lee TY. Simultaneous MRI measurement of blood flow, blood volume, and capillary permeability in mammary tumors using two different contrast agents. *J Magn Reson Imaging* 2000;12:991–1003.
37. Goh V, Halligan S, Hugill JA, Bartram CI. Quantitative assessment of tissue perfusion using MDCT: comparison of colorectal cancer and skeletal muscle measurement reproducibility. *AJR Am J Roentgenol* 2006;187:164–169.
38. Galbraith SM, Lodge MA, Taylor NJ, Rustin GJS, Bentzen A, Stirling JJ, Padhani AR. Reproducibility of dynamic contrast-enhanced MRI in human muscle and tumours: comparison of quantitative and semi-quantitative analysis. *NMR Biomed* 2002;15:132–142.
39. Lammertsma AA, Brooks DJ, Beaney RP, Turton DR, Kensett MJ, Heather JD, Marshall J, Jones T. In vivo measurement of regional cerebral haematocrit using positron emission tomography. *J Cereb Blood Flow Metab* 1984;4:317–322.
40. McGill R, Tukey JW, Larsen WA. Variations of box plots. *Am Stat* 1978;32:12–16.
41. Notohamiprodjo M, Sourbron S, Staehler M, et al. Measuring perfusion and permeability in renal cell carcinoma with dynamic contrast-enhanced MRI: a pilot study. *J Magn Reson Imaging* 2010;31:490–501.
42. Calamante F, Yim PJ, Cebra JR. Estimation of bolus dispersion effects in perfusion MRI using image-based computational fluid dynamics. *Neuroimage* 2003;19:341–353.
43. Calamante F. Bolus dispersion issues related to the quantification of perfusion MRI data. *J Magn Reson Imaging* 2005;22:718–722.

4.2.2 Paper IV

R. Jiřík, T. Taxt, O. Macíček, M. Bartoš, J. Kratochvíla, K. Souček, E. Dražanová, L. Krátká, A. Hampl, Z. Starčuk, Blind deconvolution estimation of an arterial input function for small animal DCE-MRI, *Magn. Reson. Imaging.* 62 (2019) 46–56.

<https://doi.org/10.1016/J.MRI.2019.05.024>.

(IF 2.053)

Author's contribution:

- co-author of the main idea
- methodological design
- implementation
- data acquisition (partly)
- data processing
- data evaluation
- paper writing



Contents lists available at ScienceDirect

Magnetic Resonance Imaging

journal homepage: www.elsevier.com/locate/mri

Original contribution

Blind deconvolution estimation of an arterial input function for small animal DCE-MRI

Radovan Jiřík^{a,*}, Torfinn Taxt^b, Ondřej Macíček^a, Michal Bartoš^c, Jiří Kratochvíla^a, Karel Souček^{d,e,f}, Eva Dražanová^a, Lucie Krátká^a, Aleš Hampl^g, Zenon Starčuk Jr.^a^a Institute of Scientific Instruments of the Czech Academy of Sciences, Kralovopolska 147, 61264 Brno, Czech Republic^b Department of Biomedicine, University of Bergen, Jonas Lies vei 91, 5009 Bergen, Norway^c Institute of Information Theory and Automation of the Czech Academy of Sciences, Pod Vodarenskou vezi 4, 18208 Praha, Czech Republic^d Department of Cytokinetics, Institute of Biophysics of the Czech Academy of Sciences, Kralovopolska 135, 61265 Brno, Czech Republic^e Center of Biomolecular and Cellular Engineering, International Clinical Research Center, St. Anne's University Hospital Brno, Pekarska 53, 65691 Brno, Czech Republic^f Department of Experimental Biology, Faculty of Science, Masaryk University, Kotlarska 2, 61137 Brno, Czech Republic^g Department of Histology and Embryology, Faculty of Medicine, Masaryk University, Kamenice 3, 62500 Brno, Czech Republic

ARTICLE INFO

Keywords:

DCE-MRI

Blind deconvolution

Arterial input function

ABSTRACT

Purpose: One of the main obstacles for reliable quantitative dynamic contrast-enhanced (DCE) MRI is the need for accurate knowledge of the arterial input function (AIF). This is a special challenge for preclinical small animal applications where it is very difficult to measure the AIF without partial volume and flow artifacts. Furthermore, using advanced pharmacokinetic models (allowing estimation of blood flow and permeability-surface area product in addition to the classical perfusion parameters) poses stricter requirements on the accuracy and precision of AIF estimation. This paper addresses small animal DCE-MRI with advanced pharmacokinetic models and presents a method for estimation of the AIF based on blind deconvolution.

Methods: A parametric AIF model designed for small animal physiology and use of advanced pharmacokinetic models is proposed. The parameters of the AIF are estimated using multichannel blind deconvolution.

Results: Evaluation on simulated data show that for realistic signal to noise ratios blind deconvolution AIF estimation leads to comparable results as the use of the true AIF.

Evaluation on real data based on DCE-MRI with two contrast agents of different molecular weights showed a consistence with the known effects of the molecular weight.

Conclusion: Multi-channel blind deconvolution using the proposed AIF model specific for small animal DCE-MRI provides reliable perfusion parameter estimates under realistic signal to noise conditions.

1. Introduction

Dynamic contrast-enhanced (DCE) MRI is an important method characterizing the status of tissue microvasculature. This is important for diagnosis and assessment of response to treatment mainly in oncology [1]. Small animal (mice, rats) DCE-MRI [2] is an important tool for development of new drugs, typically for anti-cancer therapy, such as anti-angiogenic drugs [3–5].

The aim of this paper is to improve the quality of small animal quantitative DCE-MRI. In DCE-MRI, contrast agent concentration time curves of tissue regions of interest (ROI, e.g. the whole tumor or each voxel) are derived from MR image sequences acquired before, during and after contrast agent administration. In quantitative DCE-MRI, each tissue curve is approximated by an arterial input function (AIF)

convolved with an impulse residue function (IRF) multiplied by plasma flow. The AIF is the contrast agent concentration curve in the arterial input of the tissue ROI. Estimation of a reliable AIF for each ROI is a challenge. Presently, it is one of the major factors causing low reliability of DCE-MRI.

Arterial input functions. There are several approaches to estimate the AIF. The first approach is to derive it from the acquired image sequence as the contrast agent concentration curve in a large artery [6]. However, such a measurement is distorted by flow artifacts, partial volume effects, saturation, T_2^* effects and dispersion. The partial volume artifact is more pronounced in small animal recordings. This is because of substantially smaller animal body size and the consequent need for coarser spatial resolution relative to the vessel size in small animal versus clinical DCE-MRI in order to achieve acceptable signal to noise

* Corresponding author.

E-mail address: jirik@isibrno.cz (R. Jiřík).<https://doi.org/10.1016/j.mri.2019.05.024>

Received 3 January 2019; Received in revised form 2 May 2019; Accepted 19 May 2019

0730-725X/© 2019 Elsevier Inc. All rights reserved.

ratio (SNR). Flow artifacts are also more severe for small animal DCE-MRI because of higher ratio of flow velocity to slice thickness in small animals.

The second approach is to use a population based AIF [7]. This ignores the differences in the vascular tree between different individuals and depends on the AIF acquisition method and the contrast agent used for creation of these populations based “standards”.

The third approach is based on analysis of arterial blood samples taken during the bolus application [8]. It is a fairly invasive method and suffers from AIF shape dispersion (blood samples are taken far from the arterial input of the tissue ROI).

The fourth approach is based on a reference tissue (e.g. muscle) [9]. The AIF is estimated from the tissue curve in this reference tissue and the presumably known perfusion parameters. This approach has been shown for the Tofts model. For advanced pharmacokinetic models, the complete set of perfusion parameters in the reference tissue would have to be known, which is not realistic.

This paper is focused on a very different approach to estimate the AIF – blind deconvolution [10,11]. When imposing prior knowledge (e.g. positivity of the signals, a parametric AIF model and a parametric model for the IRF) and a suitable initial estimation scheme, it is possible to estimate simultaneously the parameters of the AIF and the perfusion parameters from the measured tissue ROI contrast agent concentration curves. This provides examination specific AIF estimates.

Impulse residue functions. In DCE-MRI, the usual pharmacokinetic models for the IRF are the Tofts and extended Tofts models [12,13]. The estimated perfusion parameters included in these models are the rate parameters K^{trans} , k_{ep} and v_e (and also v_p for the extended Tofts model), see Table 1 for description of perfusion parameters. To estimate a more complete perfusion parameter set, including blood plasma flow, F_p , and vessel permeability surface area product, PS , advanced pharmacokinetic models [12,13] must be applied. The most relevant are the two compartment exchange model (2CXM) [14], the tissue homogeneity model (TH) [15], the adiabatic approximation to the tissue homogeneity model (ATH) [16], the distributed parameter (DP) model [17], the distributed capillary adiabatic tissue homogeneity model (DCATH) [18], and the Gamma Capillary Transit Time (GCTT) model [11]. However, the parameter estimation of these advanced pharmacokinetic models requires a high SNR in order not to be ill-conditioned. Furthermore, application of these models assumes a high temporal resolution of the acquisition to capture the vascular distribution phase of the bolus. These are the main reasons why most quantitative DCE-MRI studies are based on the Tofts or extended Tofts models.

This paper is focused on blind-deconvolution AIF estimation in small animal DCE-MRI using advanced pharmacokinetic models. As a realistic AIF model is an important prior information, we concentrate

Table 1
Description of symbols.

Quantity	Description	Unit
F_p	Plasma flow	mL/min/ mL
PS	Permeability-surface area product	mL/min/ mL
v_p	Plasma volume	mL/mL
v_e	Interstitial volume	mL/mL
K^{trans}	Volume transfer constant	1/min
k_{ep}	Interstitial-to-plasma rate constant	1/min
E	Extraction fraction	–
T_c	Capillary mean transit time	min
Δt	Delay between the common AIF and the ROI-specific local AIF	min
μ	Mean of the nontruncated normal distribution of T_c (DCATH model)	min
σ	standard deviation of the nontruncated normal distribution of T_c (DCATH model)	min
T_s	sampling interval	min

on parametric AIF formulations. To the authors' knowledge, only two papers [19,20] have been published on this topic. They are based on an AIF model proposed originally for clinical DCE-MRI [10,11], described by 10 parameters, and do not contain any analysis of the accuracy and precision of the estimated AIFs.

The contribution of this paper is two-fold. First, we propose a 7-parameter AIF model tailored to small animal DCE-MRI to take advantage of the fact that a small animal AIF is usually of a simpler shape than a clinical AIF, see below. This reduction of AIF parameters (7 versus 10) helps to reduce the ill-conditioned character of blind deconvolution. Second, we propose an evaluation method on real data (where no ground-truth is available) based on use of two contrast agents with very different molecular weights. The known effects of the molecular weight on the shape of the AIF estimates are assessed. Furthermore, the consistency of the estimated perfusion parameters with the known effect of the contrast agent molecular weight is quantified. For example, the values of F_p and v_p should be molecular weight independent, while PS should decrease with increasing molecular weight [21–24]. This perfusion parameter evaluation approach has been used only in [24] for non-blind deconvolution (measured AIF) and it was applied to the mean signals of the tumor regions in a tumor canine model. We present a voxel-based analysis.

This work is a substantial extension of our initial study [25,26]. The proposed blind deconvolution AIF estimation method gave consistent results suggesting that it can be used as a reliable AIF estimation scheme.

2. Material and methods

2.1. Perfusion modeling and parameter estimation

The tissue contrast agent concentration time curve in a ROI, $C(t)$, is given by the time-domain convolution of the AIF common for all ROIs, $C_p(t)$, and the delayed local IRF, $R(t - \Delta t)$, multiplied by the local plasma flow, F_p [13]:

$$C(t) = F_p \cdot C_p(t) * R(t - \Delta t) \quad (1)$$

The parameter Δt , is the delay between the common AIF and the ROI-specific local AIF, formulated as a part of the IRF as it is ROI specific.

Arterial input function. For the AIF, the standard model for small animal DCE-MRI is a bi-exponential function [27–29]. While this model is probably sufficient for the Tofts and extended Tofts pharmacokinetic models, it is not suitable for advanced pharmacokinetic models, such as the ATH model. The need for finer time domain sampling and more perfusion parameters inherent in these advanced IRF models require a more flexible AIF model. Especially the sharp peak of the bi-exponential AIF is unrealistic.

The AIF is a convolution of the bolus application function (contrast agent concentration versus time at the location of the cannula) and the remaining vascular distribution components. Assuming a typical case of a mouse examination with a constant speed of the contrast agent application (using a linear infusion pump) of 1 mL/min, the injection of a 0.1 mL dose of the contrast agent would take 6 s. This corresponds to the convolution of a rectangular blurring function of width 6 s with an ideal AIF which would be obtained for an instantaneous bolus application.

To model this blurring and to allow more degrees of freedom needed for a more detailed AIF, the AIF model proposed here is the sum of three gamma variate functions:

$$C_p(t) = t^\beta \sum_{n=1}^3 \alpha_n e^{-\tau_n t}. \quad (2)$$

Here, t is time in minutes, while β , α_n and τ_n are the model parameters. To keep the number of AIF parameters low, the parameter β is

common for all three gamma variate functions. The number of gamma variate functions was set to three as a compromise between a too high flexibility of the AIF model and the need for a low number of AIF parameters, based on our preliminary experiments. The same number of gamma variate functions is used also in the clinical AIF model of [19,20] applied in the context of blind deconvolution in mice.

No delay between the gamma variate functions is modeled because the dynamics of the cardiovascular system in small animals is very fast and multiple passes of the contrast agent bolus are not visible in the AIF, contrary to the case of human AIFs. More specifically, for humans the whole blood volume is pumped through heart in approx. 1 min (cardiac output 5 L/min, blood volume 5 L [30]), while for mice in about 0.15 min (cardiac output 15 mL/min, blood volume 2.25 mL [30]). As in human AIF, the distance between the 1st and 2nd pass peaks is approx. 12 s [31], we can expect the corresponding distance in mice to be $12/1 \cdot 0.15 = 1.8$ s. Assuming the above described rectangular blurring function of width 6 s, the 2nd pass peak is very likely to be filtered out. In support of this assumption, no second pass peak is observable in measured mouse AIFs [27–29], nor in blind deconvolution AIF estimates of mice in [19] (Supporting information 3).

A more specific argument about the presence of the 2nd pass peak in mouse AIFs follows from a study in [32]. First, the authors state that the fastest application of the contrast agent bolus tolerated well by mice was 2 mL/min. With this maximal infusion-pump rate, lower volumes of the contrast-agent bolus (0.025 mL and 0.050 mL) were applied in murine DCE-MRI, corresponding to bolus administration durations of 0.75 s and 1.50 s. This led to a visible 2nd pass peak in the AIFs measured in the left ventricle. On the other hand, application of a full bolus (0.100 mL, bolus administration duration of 3 s), has blurred the 2nd pass peak out. This implies that the proposed AIF model (2) is suitable for a contrast-agent bolus of 0.100 mL or more, assuming the infusion-pump rate 2 mL/min, i.e. bolus administration duration of 3 s or more. This is the case of the most published studies on murine DCE-MRI.

Our AIF model could be treated as a simplified version of Schabel's AIF model [11,19], where we leave out the sigmoid curve and the delays between the gamma variate functions. An example of a measured AIF and its approximation by the proposed model is shown in Supplemental Fig. 1.

Tissue residue function. The constrained DCATH model of the IRF [18] is used here because of its continuous formulation of T_c , which leads to the advantage of a smooth transition between the vascular and parenchymal distribution phases of the IRF. Thus, the criterion function of the blind deconvolution task is continuous in T_c . This is in contrast to the more commonly used model ATH [33]. As in [34], a fixed dispersion of the capillary transit time T_c is used to decrease the number of free parameters and to avoid the ill-posed character of deconvolution when using the DCATH model [35]. With this simplification, the IRF model can be viewed as an approximation of the ATH model.

Using the assumption of a truncated normal distribution for T_c , the DCATH model of $F_p \cdot R(t)$ is parametrized by five parameters, $\Psi = \{F_p, E, k_{ep}, \mu, \sigma\}$ (see Table 1).

$$\begin{aligned} R(t) &= R_v(t) + R_p(t), \\ R_v(t) &= 1 - \frac{\operatorname{erf}\left(\frac{t-\mu}{\sqrt{2}\sigma}\right) + \operatorname{erf}\left(\frac{\mu}{\sqrt{2}\sigma}\right)}{1 + \operatorname{erf}\left(\frac{\mu}{\sqrt{2}\sigma}\right)} \\ R_p(t) &= E \exp\left(\frac{1}{2}k_{ep}^2\sigma^2 + k_{ep}(\mu - t)\right) \cdot \frac{\operatorname{erf}\left(\frac{t-\mu}{\sqrt{2}\sigma} - \frac{k_{ep}\sigma}{\sqrt{2}}\right) + \operatorname{erf}\left(\frac{\mu}{\sqrt{2}\sigma} + \frac{k_{ep}\sigma}{\sqrt{2}}\right)}{1 + \operatorname{erf}\left(\frac{\mu}{\sqrt{2}\sigma}\right)} \end{aligned} \quad (3)$$

The error function erf is defined as

$$\operatorname{erf}(t) = \frac{2}{\sqrt{\pi}} \int_0^t dx \exp(-x^2). \quad (4)$$

The dispersion of T_c , σ , was fixed to T_s . This value is high enough to

preserve the continuous formulation of the impulse residue function inherent to the DCATH model and low enough to consider the model as an approximation of the ATH model. A high value of σ is more likely to lead to a non-unique IRF model, see [35].

The mean of the nontruncated normal distribution of T_c , μ , is a good approximation of T_c [18] if the ratio σ/μ is sufficiently small (no greater than 1/3) [18]. This allows replacement of μ by T_c in (3).

With F_p and E known, the permeability surface area product, PS [mL/min/mL], is expressed as $PS = -F_p \ln(1 - E)$.

Similarly, v_p [mL/mL] and v_e [mL/mL] are given by $v_p = F_p \cdot T_c$ and $v_e = (E \cdot F_p)/k_{ep}$.

Parameter estimation. The first step is the estimation of the parameters of the common AIF, $C_p(t)$. The mean contrast agent concentration time curves in several manually selected ROIs (channels) are calculated. Then, the curves are simultaneously approximated by the convolutional model (1). This task is formulated as a minimization problem where the criterion function is a sum of squared differences between the samples of the contrast agent concentration time curve and its convolutional model for all channels. Hence, the blind deconvolution algorithm results in estimates of the $C_p(t)$ parameters (common for all channels) and of the IRF parameters and F_p (perfusion parameters) of each channel. The estimates of IRF parameters and F_p are not used in the subsequent processing.

The blind deconvolution algorithm starts with an initial AIF estimate and initial estimates of F_p and IRF. The minimization problem is solved by using an iterative alternating optimization scheme [10]. Each iteration (10 iterations are used here) consists of two parts: 1. Update of the IRFs' parameters and F_p of each channel while the AIF parameters are fixed to the actual estimate. 2. Update of the AIF parameters while the IRFs' parameters and F_p of each channel are fixed to the actual estimates. Each update is done using the Active-Set optimization algorithm as implemented in the Matlab™ Optimization toolbox (MathWorks, USA), function *fmincon*.

To account for the ROI-specific time delay between the estimated AIF and the tissue curve (i.e. the bolus arrival time), the IRF of each channel is formulated to include a delay parameter, Δt (see (1)). However, the time-domain sampling of the tissue curves causes discontinuities of the blind deconvolution criterion function [33]. In order to avoid this problem, the IRF delay is implemented as a convolution with a narrow Gaussian function of unity area under the curve and with the mean value equal to the delay. The width of this Gaussian function must be small enough to avoid any significant blurring of the IRF. It must also be high enough to avoid a discontinuous formulation of the delay due to the temporal undersampling of the Gaussian function.

By its nature, blind deconvolution provides estimation of the AIF shape, not its scale. A scaling factor needs to be estimated by an additional procedure, see Section 2.8.

After the common AIF has been estimated and scaled, it can be used in a voxel-by-voxel non-blind deconvolution calculating the perfusion parameter maps. The IRF model is the same as in the blind deconvolution (3) and the implementation is according to [35].

2.2. Simulated data

Synthetic data were generated as a convolution of a reference AIF (Fig. 1) and $F_p \cdot R(t - \Delta t)$ (see (1)), with additive Gaussian white noise. The sampling interval and the number of samples were as for the in vivo recordings (see below): $T_s = 1.05$ s, $N = 800$.

The reference AIF, $C_p \text{ ref}(t)$, was a parametric AIF according to (2) derived from an AIF measured in aorta descendens in one of the in vivo recordings (Magnevist recording of mouse M1, see below). This measured AIF was selected manually based on visual assessment of the arterial voxel contrast agent concentration signals by selecting the signal with the steepest rising and falling parts and minimum noise. The measured AIF was then approximated by the AIF model (2) in order to obtain parameters of $C_p \text{ ref}(t)$, see Supplemental Fig. 1.

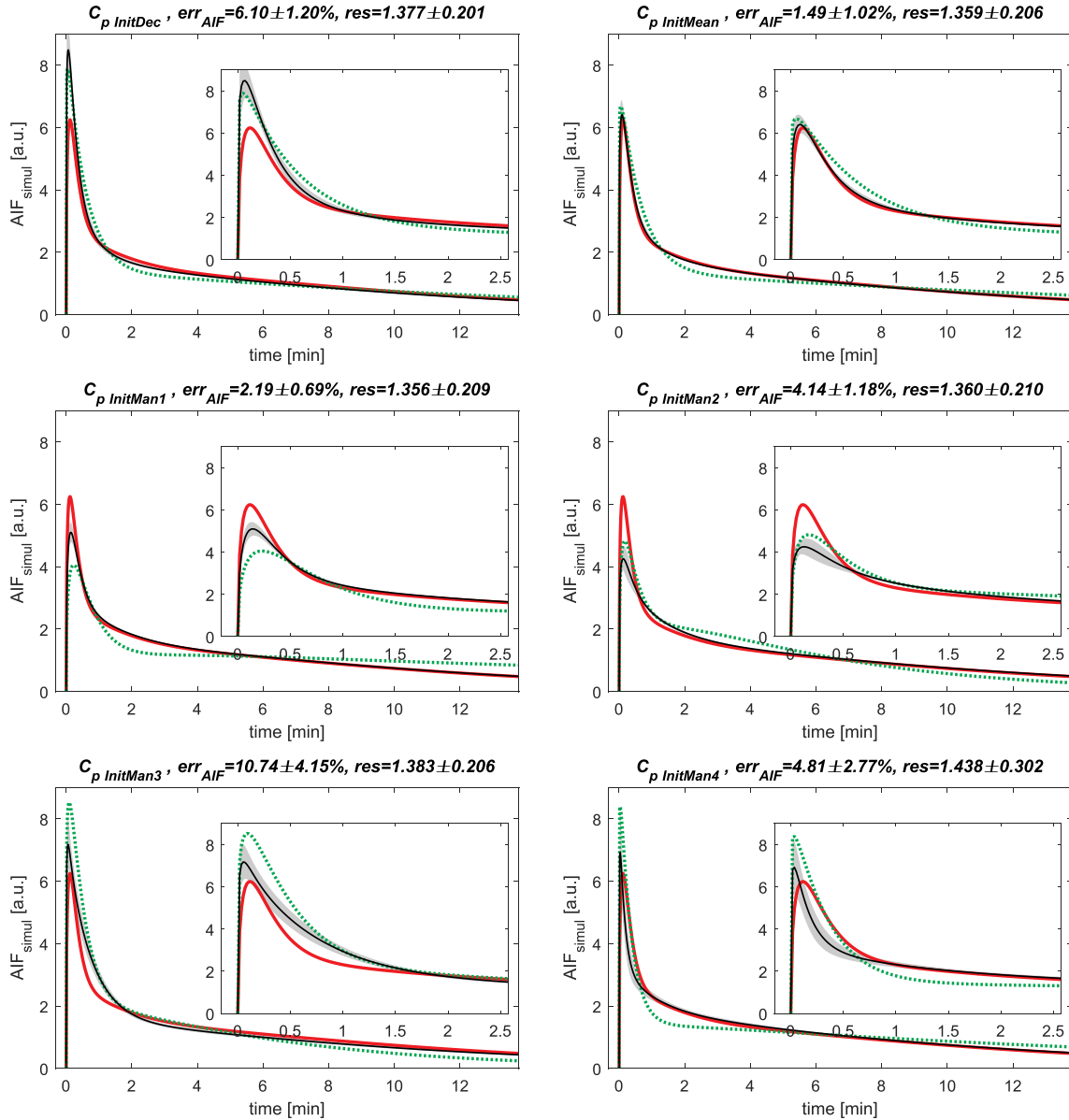


Fig. 1. AIF estimates for several initial AIFs, 6 channels, $SNR_{blind}=7$. Reference AIF (red line), AIF estimates – mean (solid black) \pm standard deviation (gray area) and initial AIF estimates (dotted green). Plot titles: AIF estimation error – err_{AIF} (see (5)), sum of squares of fitting residuals – res (see (6)). AIFs normalized to unity area under the curve $\times 1000$, a.u.: arbitrary units. (For interpretation of the references to colour in this figure legend, the reader is referred to the web version of this article.)

Two synthetic datasets were generated, one for evaluation of the blind deconvolution method alone and one for evaluation of its effect on the accuracy and precision of the subsequent voxel-by-voxel non-blind deconvolution. The first synthetic dataset (for testing of blind deconvolution) was generated for 5 SNR_{blind} levels, $W = 50$ noise realizations per SNR_{blind} level and 8 channels. This corresponded to $5 \cdot 50 \cdot 8 = 2000$ synthetic tissue curves.

For each of these tissue curves, different parameters of $F_p \cdot R(t - \Delta t)$ were chosen randomly (uniform distribution) within the following ranges: $F_p = [0.1 - 0.8]$ mL/min/mL, $E = [0.3 - 0.7]$, $T_c = \mu = [5 - 15]$ s and $v_e = [0.1 - 0.5]$ mL/mL ($k_{ep} = (E \cdot F_p)/v_e$). The Gaussian function modeling the IRF delay was used with a standard deviation $\sigma_{delay} = 0.06$ s and a random (uniform distribution) mean value in the interval $\Delta t = [0 - 2]$ s.

The noise was generated as a Gaussian random signal multiplied by a factor according to the intended level of SNR_{blind} . The SNR was defined as the mean of the noiseless signal ($F_p \cdot C_{p,ref}(t) * R(t - \Delta t)$) divided

by the standard deviation of the noise.

This synthetic dataset was used for the evaluation of the performance of the blind deconvolution algorithm with respect to the initial AIF estimate, SNR and the number of channels. For testing of the effect of the initial AIF estimate, the blind deconvolution algorithm was run using several different initial AIF estimates (i.e. initial parameters of the AIF model (2)).

The first initial AIF candidate, $C_{p,InitDec}$, was the result of our initial study [25]. The second initial AIF candidate, $C_{p,InitMean}$, was obtained from blind deconvolution of five recordings of this study (see Section 2.4, Magnevist recordings) by using the initial AIF estimate $C_{p,InitDec}$ as follows: the mean of the five resulting AIF estimates was approximated by the AIF model (2), thus providing the parameters of $C_{p,InitMean}$. Other initial AIF candidates, $C_{p,InitManX}$, were generated by manual modification of the AIF model parameters so that the set of initial AIFs covered the cases with a narrow and broad peak and with a slow and a fast decay of the AIF tail.

2.3. Evaluation on simulated data

Quantitative evaluation of the AIF estimation was based on the relative AIF estimation error:

$$err_{AIF} = \frac{1}{WN} \sum_{w=1}^W \sum_{n=1}^N \frac{|C_{p,w}[n] - C_{p,ref}[n]|}{C_{p,ref}[n]} \cdot 100\%, \quad (5)$$

where $C_{p,w}[n]$ is the AIF estimate for the w -th noise realization. The time variable t has been replaced by the time index, n , to account for the time domain sampling and N is the number of samples. In addition to err_{AIF} , the sum of squares of the fitting residuals, res , was calculated over all channels as

$$res = \frac{1}{RN} \sum_{r=1}^R \sum_{n=1}^N (C_r[n] - \hat{C}_r[n])^2. \quad (6)$$

Here, $C_r[n]$ is the synthetic contrast agent concentration sequence of the r -th ROI (channel), $\hat{C}_r[n]$ is its approximation according to (1) given by blind deconvolution and R is the number of channels.

For the assessment of the accuracy of the voxel-by-voxel perfusion parameter estimates obtainable using the common blind deconvolution AIF estimate, non-blind deconvolution was applied to another set of synthetic contrast agent concentration sequences. These sequences were generated using the reference AIF, $C_{p,ref}$, and three tumor types. The first was a prostate tumor ($F_p = 0.21$ mL/min/mL, $E = 0.65$, $T_c = 18.6$ s and $v_e = 0.35$ mL/mL [36]). The second was a glioblastoma ($F_p = 0.052$ mL/min/mL, $E = 0.161$, $T_c = 11.82$ s and $v_e = 0.076$ mL/mL [37]). The third was a colorectal tumor ($F_p = 0.256$ mL/min/mL, $E = 0.54$, $T_c = 15.5$ s and $v_e = 0.57$ mL/mL [19]).

For each tumor type and $SNR_{non-blind}$, $U = 200$ noise realizations were generated and added to the contrast agent concentration sequence. The perfusion parameter estimation error was quantified for each tissue and each $SNR_{non-blind}$ level as

$$err_{par} = \frac{1}{4UW} \sum_{u=1}^U \sum_{w=1}^W \left(\frac{|\hat{F}_{p,u,w} - F_{p,ref}|}{F_{p,ref}} + \frac{|\hat{PS}_{u,w} - PS_{ref}|}{PS_{ref}} + \frac{|\hat{v}_{p,u,w} - v_{p,ref}|}{v_{p,ref}} + \frac{|\hat{v}_{e,u,w} - v_{e,ref}|}{v_{e,ref}} \right) \cdot 100\%. \quad (7)$$

Here, w is the index of the blind deconvolution AIF estimate (see (5)) and u is the index of noise realization added to the contrast agent concentration sequence of the given tumor type. The hat symbol denotes perfusion parameter estimates and the subscript “ref” stands for the reference value of the given perfusion parameter used in generation of the synthetic signal of the given tumor type.

A relative estimation error is evaluated also for each perfusion parameter separately.

2.4. Animal handling

The proposed AIF estimation method was evaluated on real data from five BALB/c mice (experiment approved by the National Animal Research Authority) with murine colon tumor cells CT26.WT (ATCC, CRL-2638) subcutaneously implanted into the left flank (10^6 cells in HC Matrigel). The mice were anesthetized with a mixture of isoflurane (2%) and O_2 (800 mL/min), and monitored continuously for respiratory rate and body temperature.

Each mouse was examined with two separate DCE-MRI recordings which were subsequently separately processed, the first one with a high molecular weight contrast agent (GadoSpin P, Miltenyi Biotec, Bergisch Gladbach, Germany, molecular weight 200 kDa), and the second one with a standard low molecular weight contrast agent (Magnevist, Bayer HealthCare Pharmaceuticals, Berlin, Germany, molecular weight 0.9 kDa). The delay between the bolus injections was 30 min. A high molecular weight contrast agent was injected first because its concentration can be assumed constant after 30 min, so that its effect on the

tissue curves of the following low molecular weight contrast agent is minimized [24].

A linear infusion pump was used with injection speed of 1 mL/min. The dose of Magnevist was 0.3 mmol/kg weight. Magnevist was first diluted 1:5 with saline and 0.08 mL of this solution was injected, followed by 0.2 mL saline flush. For GadoSpin P, the dose of 0.1 mL of the supplied solution (25 mM gadolinium concentration) was applied, as recommended by the manufacturer, followed by the same saline flush as for Magnevist. When no mixing of the contrast agent and the saline flush is considered, for simplicity, the applied injection speed corresponds to the contrast agent injection duration of 4.8 s and 6 s for Magnevist and GadoSpin P, respectively.

2.5. MRI protocol

A 9.4 T BioSpin (Bruker Biospin MRI, Ettlingen, Germany) scanner was used. Anatomical images were recorded using the RARE sequence (T_2 -weighted and T_1 -weighted pre- and post-contrast). The parameter values for the T_2 -weighted sequence were: TR/TE = 3500/36 ms, FOV 23×35 mm², image matrix 256×256 , 20 axial slices with the thickness of 0.7 mm and no interslice gap. The parameter values for the T_1 -weighted sequences were: TR/TE = 666/10 ms, with the same geometry as for the T_2 -weighted sequence.

Before the first bolus administration, calibration scans were recorded and used for the conversion of the dynamic image sequences to the corresponding contrast agent concentration sequences. The acquisition was done using a 2D FLASH sequence with TR = 14, 30, 50, 100, 250, 500 ms, TE = 2.5 ms, flip angle 25°, image matrix 128×96 voxels, one axial slice located in the tumor center, slice thickness 1 mm, 15 images per sequence.

The DCE-MRI recordings (same acquisition parameters for both GadoSpin P and Magnevist recordings) were acquired using the 2D FLASH sequence with TR = 14 ms. The remaining parameters were the same as for the calibration scans. The sampling interval was 1.05 s and the acquisition time was 14 min (800 images).

2.6. Preprocessing

From multiple-TR calibration recordings, images of $k\rho$ (ρ is the spin density and k is a spatially invariant factor accounting for gain in the acquisition chain) and of the native T_{10} were obtained by approximation of the image data with the model of the FLASH acquisition (similarly to [38]), Eq. (6).

The multiple-TR method provides more reliable estimation than the standard method based on multiple flip angle recordings [38]. The multiple-TR method is less sensitive to B_1 field inhomogeneity and imperfections of the excitation profile of the RF pulses.

Subsequently, the same equation of the FLASH acquisition, including the estimated $k\rho$ values, was fitted to the DCE-MRI image data so that the relaxation rate $R_1[n]$ in each voxel at each time point n could be estimated. Then, the baseline, R_{10} , was estimated for each voxel as the mean R_1 in the time interval preceding the arrival of the contrast agent. The contrast agent concentration sequence of each voxel was calculated as $C[n] = (R_1[n] - R_{10})/r_1$ (assuming that the relaxivity r_1 is tissue independent).

The SNR of in vivo signals $C[n]$ was estimated as the mean of $C[n]$ divided by the standard deviation of the noise. The noise signal was estimated by approximation of the later part of $C[n]$ (i.e. a phase with slow changes, second half of $C[n]$ chosen here) by a second-order polynomial and subtraction of this polynomial from $C[n]$.

2.7. Initialization of blind deconvolution for real data

Due to local optima in the blind deconvolution optimization problem, the AIF estimate depends on its initial estimate. A possible solution would be to implement the blind deconvolution algorithm as a

global optimization scheme where the optimization would be performed several times, each time starting from a different initial AIF estimate. Then, the initial AIF estimate giving the best fit of the convolution model (1) to the tissue signals would be chosen. However, this approach resulted in a fairly high variability of the peaks of the AIF estimates when comparing different real data recordings with the same contrast agent.

Hence, another approach was chosen here. A common initial AIF estimate was set for all mouse recordings with both contrast agents and used as a common prior knowledge stabilizing the blind deconvolution algorithm. This initial AIF was found in two steps. First, the AIF was estimated several times by blind deconvolution with different initial AIF candidates. Then out of these initial AIF candidates the one giving the best fits over all recordings was selected as the single initial AIF.

Five initial AIF candidates were tested. The first initial AIF candidate, $C_p^{InitDec}$, was the result of our initial study [25]. The second initial AIF candidate, $C_p^{InitMean}$, was obtained from blind deconvolution Magnevist recordings of all five mice by using the initial AIF estimate $C_p^{InitDec}$ as follows: The mean of the five resulting AIF estimates was approximated by the AIF model (2), thus providing the parameters of $C_p^{InitMean}$. The other three candidates, $C_p^{InitRagan}$, $C_p^{InitCheckley}$ and $C_p^{InitHeilmann}$, were derived from dual exponential AIFs from the literature [27–29] by imposing a smooth rising phase ($\beta = 0.1$ for time in minutes in (2)) and setting the amplitude of the third AIF model term (α_3) to zero. The best fits of the convolution model (1) to the tissue signals were obtained in almost all in vivo recordings for the initial AIF estimate $C_p^{InitMean}$. Thus, the results below are given for this initial AIF.

2.8. Blind deconvolution and AIF scaling for real data

Blind deconvolution was performed using 6 channels, each corresponding to a tumor voxel with a high SNR (manually selected in the nonnecrotic region).

AIF scaling was done for each recording. For each recording using Magnevist, a case specific area under the curve of the AIF, AUC_{Mag} , was derived according to the above mentioned reference tissue approach as follows. In the first step, the AIF was scaled approximatively based on the property of convolution stating that the area under the curve of a convolution result is the product of areas under the curves of the convolved functions. Thus, the area under the curve of $C_p(t)$ was calculated as the area under the curve of $C(t)$ in a reference tissue divided by the area under the curve of $F_p R(t)$. For the ATH model of $R(t)$, the area under the curve of $F_p R(t)$ is equal to $v_e + v_p$. Erector spinae muscle was used as the reference tissue, with the literature based value of $v_e + v_p$ of 0.13 mL/g according to v_e of mouse masseter muscle in [39] and assuming v_p to be 5% of v_e .

The above procedure neglected the fact that both $C(t)$ and $C_p(t)$ were sampled in a time limited window. Consequently, the available sequences did not decay completely to zero. This was taken into account by the following step.

The contrast agent concentration sequences of the reference region (erector spinae muscle) voxels were deconvolved with the approximatively scaled AIF. Then the median of $v_e + v_p$ estimated in the reference region was calculated. The ratio of this median and the literature value of $v_e + v_p$ was used for refinement of the AIF scale.

For GadoSpin P this procedure was not reliable because of low SNR. Instead, the AIF area under the curve for GadoSpin P, AUC_{GSP} , was calculated as $AUC_{GSP} = AUC_{Mag}(D_{GSP}r_{1GSP})/(D_{Mag}r_{1Mag})$, where D_{GSP} and D_{Mag} are contrast agent doses. The quantities r_{1GSP} and r_{1Mag} are the T_1 relaxivities for GadoSpin P and Magnevist, respectively. The relaxivities were measured in a separate in vitro experiment performed using the same NMR scanner. Using this procedure, we relied on a precise knowledge of the contrast agent doses.

2.9. Evaluation on real data

The variability of the blind deconvolution AIF estimates and the shape difference between the Magnevist and GadoSpin P groups were assessed visually. Perfusion parameters were validated based on their consistency with the expected effects of high and low molecular weight contrast agents. The intravascular parameters, v_p and F_p , should not be affected by the contrast agent molecular size. In contrast, PS should increase with decreasing molecular weight [19,21–23]. The volume of the extravascular extracellular space, v_e , should not be affected by the contrast agent molecular weight. However, a smaller fraction of this space might be accessible for high molecular weight contrast agent particles [40], leading to a possible underestimation of v_e .

The voxels for this evaluation were selected from manually drawn tumor regions (based on anatomical T_2 -weighted images), excluding necrotic areas and fulfilling the condition of a sufficiently high SNR ($SNR > 1$) in both the Magnevist and GadoSpin P recordings. In necrotic regions, the usual pharmacokinetic models are not valid because the distribution of the contrast agent is affected by passive diffusion throughout neighboring voxel regions [2].

The voxels were assumed to be outside of necrotic areas when $k_{ep} > 0.2 \text{ min}^{-1}$. This perfusion parameter was chosen because it is independent of AIF scaling and its maps were spatially consistent (more than the maps of another scaling independent parameter, E). The threshold of k_{ep} was selected from visual assessment of the perfusion parameter maps, T_2 -weighted and post-contrast T_1 -weighted anatomical images.

The estimated perfusion parameters were evaluated using boxplots, correlation coefficients and proportionality coefficients of the scatter plots, relating the perfusion parameters obtained for low and high molecular weight contrast agents.

3. Results

3.1. Simulated data

Arterial input functions. The peak of the estimated AIFs depended on the initial AIF estimate, while the AIF tail did not, as shown for a realistic $SNR_{blind} = 7$ (see Table 2 for SNRs of real data) and 6 channels (Fig. 1). The AIF estimation error (5) was related to the goodness of fit measure, res (Fig. 1). Lower res resulted mostly in a lower AIF estimation error.

The relative AIF estimation error (5) decreased when increasing the number of channels, as shown for realistic SNR_{blind} in Fig. 2 (a). The relative AIF estimation error also decreased when increasing SNR_{blind} (Fig. 2 (b)). In addition, for high SNR_{blind} (approx. for $SNR_{blind} > 5$), the AIF estimation error reflected a systematic error, i.e. accuracy limits due to the remaining level of ill-conditioning of the blind deconvolution process and due to numerical errors (Fig. 2 (b)). For low SNR_{blind} (approx. for $SNR_{blind} < 5$), the AIF estimation error reflected the precision limits due to the measurement noise.

Perfusion parameter estimates. Fig. 3 shows the mean relative error of the perfusion parameter estimates (7) in the subsequent nonblind deconvolution for the three tumor types (estimation errors of each single perfusion parameter are shown in Supplement fig. 2). As expected, the error decreased with increasing $SNR_{non-blind}$. In the ideal case, with the reference AIF, the error approached asymptotically zero (except for tissue 2). When using blind deconvolution AIF estimates, the perfusion parameter estimation error did not decrease below approx. 5%, even with high $SNR_{non-blind}$ for all three tumor types. This reflected the deviation of the blind deconvolution AIFs from the reference AIF. However, for the SNR observed in preclinical data ($SNR_{non-blind} < 10$), the achieved perfusion parameter estimation error was practically the same for the reference and blind deconvolution AIFs.

Table 2

Overview of mice recordings: numbers of analyzed voxels and SNRs for the Magnevist and GadoSpin P recordings, correlation and regression coefficients relating the perfusion parameters of the Magnevist recordings to the GadoSpin P recordings.

Mouse no.	No. of voxels	SNR Magnevist	SNR GadoSpin P	Correlation coefficients				Regression coefficients			
				F_p	PS	v_p	v_e	F_p	PS	v_p	v_e
1	63	9.0	5.1	0.61	0.79	0.86	0.67	1.08	0.39	0.72	0.68
2	53	8.0	4.5	0.83	0.70	0.86	0.36	1.09	0.36	1.36	1.06
3	199	6.6	2.2	0.28	0.89	0.61	0.82	0.93	0.73	0.91	0.87
4	82	4.4	3.3	0.06	0.27	0.52	0.73	1.02	0.63	0.83	1.16
5	19	4.8	2.3	0.85	0.60	0.56	0.81	1.71	0.23	0.92	0.98
Mean	83	6.6	3.5	0.53	0.65	0.68	0.68	1.17	0.47	0.95	0.95
SD	69	2.0	1.3	0.35	0.24	0.17	0.19	0.31	0.21	0.24	0.18

3.2. Real data

The mean SNR values in the evaluated tumor voxels (necrotic, $SNR > 1$) were clearly higher for Magnevist compared to GadoSpin P (Table 2, columns 3, 4). This corresponded to higher extravasation rate of the low molecular weight contrast agent. The recordings from mice 1 and 2 had a clearly higher SNR than the other recordings. This was most probably due to higher volume fraction of vessels in the tumors of these mice, see below.

The contrast agent concentration sequences of the Magnevist and GadoSpin P recordings had a similar appearance (Supplement fig. 3). The decay of the GadoSpin P contrast agent concentration sequences was slower, compared to the Magnevist sequences. This reflected a slower renal clearance and a slower extravasation and intravasation of the high molecular weight contrast agent [21–23,40].

Arterial input functions. AIFs estimated for both Magnevist and GadoSpin P examinations had a low variance within each contrast agent group (Fig. 4). On the other hand, there was a clear difference between the mean AIFs of each contrast agent (Fig. 4) which was in line with the expected difference between high and low molecular weight contrast agents [21,40]. Compared to the mean Magnevist AIF, the mean GadoSpin P AIF had a broader peak. This reflected slower extravasation (i.e. a smaller extraction fraction, E) of GadoSpin P. The flatter later part of the mean GadoSpin P AIF reflected the smaller glomerular extraction rate of GadoSpin P.

Table 3 gives the parameters of the mean AIFs estimated from the Magnevist and GadoSpin P recordings. They were obtained by approximation of the mean contrast agent specific AIF (solid lines in Fig. 4) with the model (2). Each of the two mean AIFs was scaled using the median of AIF scaling factors (Section 2.4) calculated within the given contrast agent group.

Perfusion parameter estimates. The resulting DCE-MRI perfusion parameter maps (Fig. 5) were spatially consistent and in the expected range. They reflected the assumed histological composition. There was

a clear distinction between the tumor rim and the more central part. High values of F_p and v_p in the outer lesion margin corresponded to a highly vascularized tumor rim.

In line with the theory, the estimates of F_p (Fig. 6) were not affected by the molecular weight of the contrast agent (with the exception of mouse 5).

The estimates of v_p (calculated as $v_p = F_p \cdot T_c$) were in good agreement with the expected molecular weight independence (Fig. 6). The parameter v_p was the intravascular perfusion parameter with the best agreement between the low and high molecular weight contrast agents.

The estimates of PS (Fig. 6) were clearly lower for the high molecular weight contrast agent, again in agreement with the known capillary membrane properties [21–23].

The estimates of v_e for the high and low molecular weight contrast agents were comparable, showing no clear trend of v_e with respect to the molecular weight of the contrast agent. In the recordings from mice 1 and 2, some values of v_e were higher than 1. This was probably due to AIF scaling problems, see discussion below. The boxplots of E , k^{cp} and T_c are shown and commented in Supplement Fig. 4.

The analysis of correlation and regression coefficients included F_p , v_p , PS and v_e . These perfusion parameters were the parameters where the physiological effect of the contrast agent molecular size was the easiest to interpret.

Table 2, columns 5–8, gives the correlation coefficient for each mouse and the selected perfusion parameters. Each correlation coefficient is for a single perfusion parameter estimated from the low and high molecular weight contrast agent recordings (see example scatter plots in Fig. 7).

There was a clear difference between the correlation coefficients estimated for the examined mice. For mice 1, 2 and 5 the achieved correlation coefficients were largely around 0.7. More variable values were achieved for mice 3 and 4. These mice had substantially lower F_p , PS and v_p values than mice 1, 2 and 5 (Fig. 6), which might be the explanation for the lower correlation coefficients. This was also partly

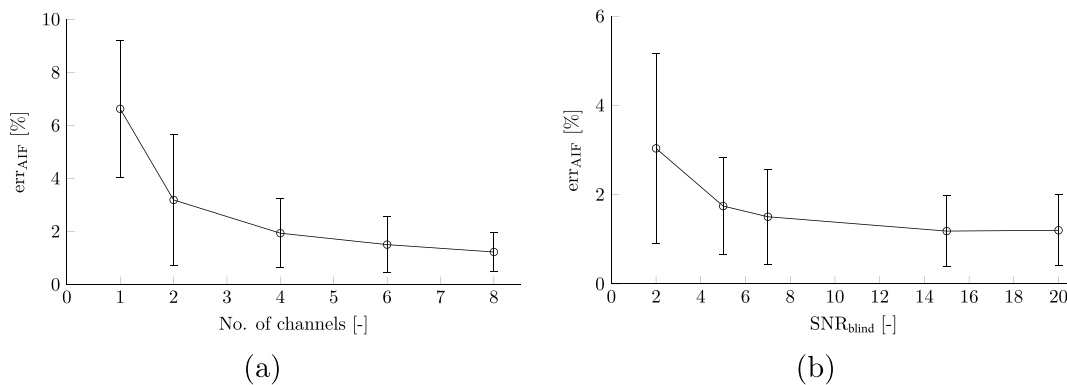


Fig. 2. AIF estimation errors. Initial AIF estimate: $C_p^{InitMean}$. (a) AIF estimation error versus number of channels ($SNR_{blind} = 7$). (b) AIF estimation error versus SNR_{blind} (6 channels). Confidence intervals defined as mean AIF estimation error (5) \pm standard deviation of the results of the inner summation operation in (5).

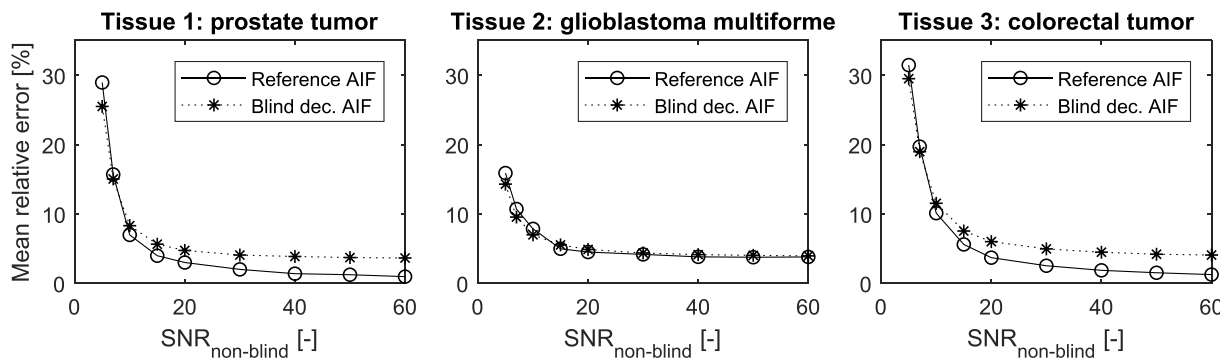


Fig. 3. Mean relative perfusion parameter estimation error (7) of non-blind deconvolution for the reference AIF and for blind deconvolution AIF estimates. Blind deconvolution AIFs were estimated from 6 channels with $SNR_{blind} = 7$, initial AIF estimate $C_p_{InitMean}$. Three tissue types.

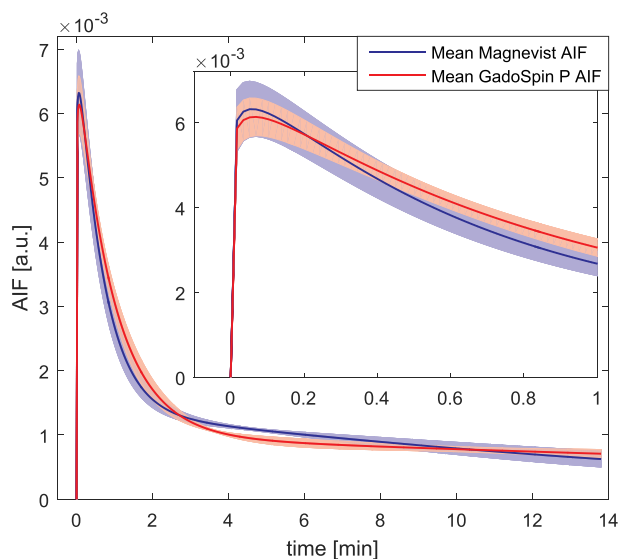


Fig. 4. AIFs estimated from Magnevist and GadoSpin P recordings. Shaded areas denote the mean \pm standard deviation. AIFs normalized to unity area under the curve.

Table 3
Parameters of mean AIFs estimated from Magnevist and GadoSpin P recordings (see (2)).

Parameter [unit]	Magnevist	GadoSpin P
β [-]	0.0847	0.0755
α_1 [mM min ^{-β}]	2.2540	0.6998
α_2 [mM min ^{-β}]	0.8053	0.2597
α_3 [mM min ^{-β}]	0.5381	0.1206
τ_1 [min ⁻¹]	1.4330	0.9755
τ_2 [min ⁻¹]	2.6349	2.3751
τ_3 [min ⁻¹]	0.0700	0.0327

reflected by the SNR values (Table 2). The lowest correlation factors were observed for mouse 4, which was in line with the low SNR of its Magnevist recording.

The slopes of the regression curves estimated for each scatter plot (Table 2, columns 9–12) showed the consistency of the estimated perfusion parameters with the contrast agent molecular weight. The slopes of scatter plots for F_p , v_p and v_e were close to 1 (slope 1 corresponds to a perfusion parameter independent of the contrast agent molecular weight). The slope for PS was clearly lower than one, which corresponds to higher PS for low molecular weight contrast agents.

4. Discussion and conclusions

The presented blind deconvolution approach is based on an AIF model designed for small animal physiology and applied in combination with an advanced pharmacokinetic model.

So far, the only AIF model used for blind deconvolution AIF estimation in small animal DCE-MRI using an advanced pharmacokinetic model [19,20] was Schabel's model [11]. Here, we decrease the complexity of the AIF model by assuming a much faster blood recirculation in mice compared to humans. Hence no delay between the main and the recirculation peaks is modeled. This assumption is supported by the fact that no recirculation peaks are observable in Scabel's-model blind AIF estimates (supporting information 3 of [19]) and in the mouse AIFs measured in the left ventricle [27–29], as well as in our measurements in aorta descendens (Supplemental fig. 1).

Our proposed AIF model is not suitable for a low-volume contrast-agent bolus of 0.050 mL or less (assuming the fastest well tolerated infusion-pump rate 2 mL/min), prepared by application of a less diluted contrast agent [20] or a lower dose [32,41]. For such cases, Schabel's AIF model is more appropriate [11]. However, with lower bolus volumes, the uncertainty about the applied dose becomes high and requires additional correction, such as inductively coupled plasma-optical emission spectrometry proposed in [20].

Analysis of synthetic and real data showed a dependence of the peak of the blind deconvolution AIF estimate on the initial AIF estimate. The peak represents the high frequency band in the Fourier domain. Assuming model (1), this band is almost removed by the convolution of the AIF with the IRF because this operation acts like a low-pass filter. The retrieval of the AIF peak is the most demanding task of the algorithm. The above loss of information was overcome by applying good priors. It included relevant parametric models for the AIF and IRF, and a realistic initial AIF estimate.

Another possibility to cope with the dependence of the blind deconvolution on the initial AIF estimate is to use a global optimization approach where the curve fitting is repeated for several initial AIFs, and the best result in terms of fitting residuals is selected for each recording. This global optimization approach was also tested (data not shown). It led to worse results than the use of one fixed initial AIF estimate. This was because the best AIF solution might be found in a local rather than a global optimum, due to noise.

The fixed initial AIF estimate turned out to be an important part of prior information, preventing optimization from being trapped in an incorrect local or global optimum. From this point of view, the blind deconvolution AIF estimation can be understood as a method for the adjustment of a population based AIF so that it reflects the case specific vascular properties.

The results of this study show that a realistic case specific AIF can be estimated using the proposed blind deconvolution method. This conclusion is supported by the fact that a fairly small variation of the AIF

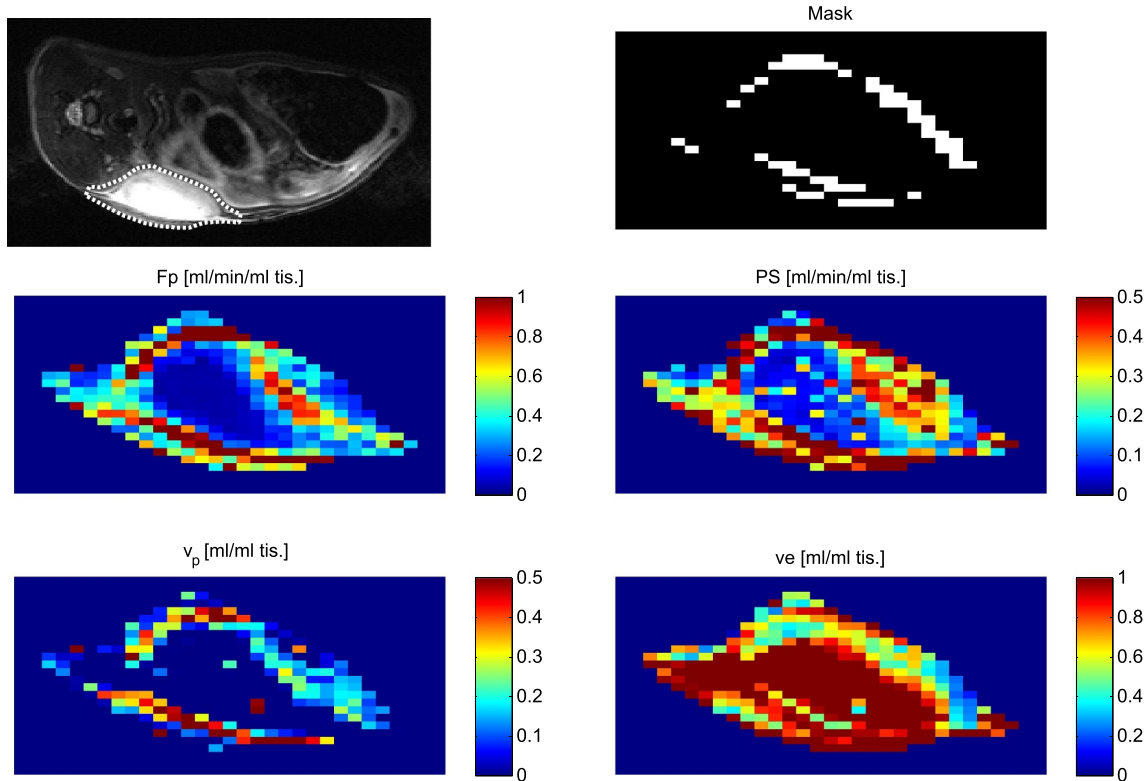


Fig. 5. Example images for mouse 2, Magnevist. T_2 -weighted anatomical image (dotted line delineates the tumor, upper left region is a cross section of spine and spinal muscles). Estimated DCE-MRI perfusion parameter maps and the mask of high SNR voxels outside the necrotic area used for evaluation.

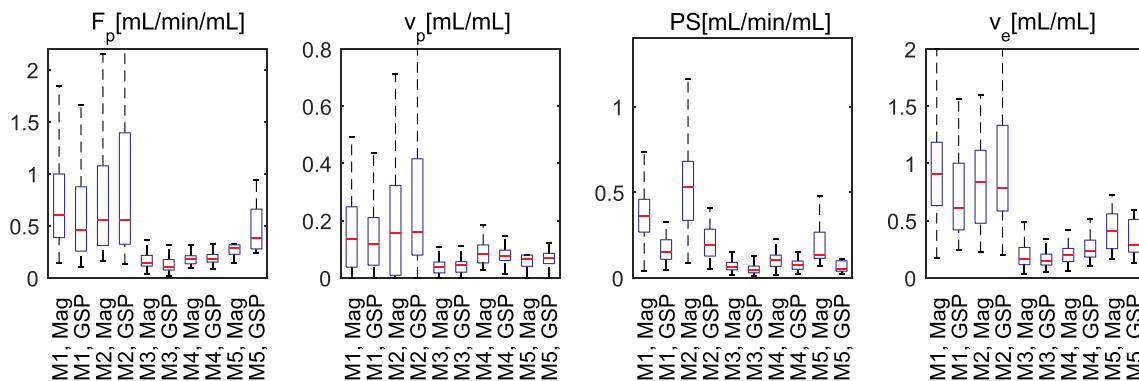


Fig. 6. Boxplots of estimated perfusion parameters. Mx – Mouse number, Mag – Magnevist, GSP – GadoSpin P.

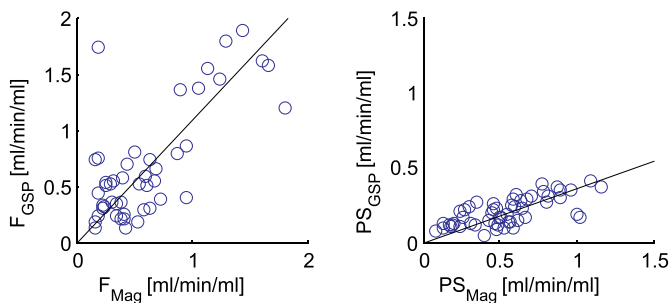


Fig. 7. Example of scatter plots and regression lines for mouse 2. Each circle corresponds to one high SNR voxel outside necrosis. Left: F_p , corr. coef. = 0.83, slope = 1.09. Right: PS , corr. coef. = 0.70, slope = 0.36.

estimates was observed within the contrast agent groups. In addition, a clear difference between the mean contrast agent specific AIFs was visible, which was according to the known differences in pharmacokinetics of the applied contrast agents.

Analysis of simulated data with $SNR_{non-blind}$ comparable to the SNR of in vivo data ($SNR_{non-blind} = 7$) showed that a similar accuracy of the perfusion parameter estimates can be achieved when using the correct (reference) AIF and when using a blind deconvolution AIF estimate.

The inaccuracy in blind deconvolution AIF estimation became visible in perfusion parameter estimates only for higher $SNR_{non-blind}$ of the synthetic voxel specific tissue curves ($SNR_{non-blind} > 10$). This shows that for real case SNRs, the accuracy of the perfusion parameter estimates is limited by the accuracy of the non-blind rather than the proposed blind deconvolution procedure. Our preliminary tests indicate

that more reliable perfusion parameter estimates can be obtained by the non-blind Lucy-Richardson algorithm in [43], probably due to its use of a non-parametric deconvolution prior to the parametric one. Also, the use of additional prior information taking the relationship of neighboring pixels into account, as in [44,45], will improve the performance of non-blind deconvolution.

The use of several contrast agents with different molecular weights in DCE-MRI based on advanced pharmacokinetic models has been proposed also in [19]. The prior information of the molecular weight independent perfusion parameters F_p , v_p and T_c was used in simultaneous fitting of multiple contrast agent curves. This led to more reliable perfusion parameter estimates. Here we propose to use this prior information solely for evaluation.

The differences in the physiological properties of the tumors (Fig. 6) and their SNR values (Table 2, columns 3, 4) had a clear effect on the achievable accuracy of the perfusion parameter estimates. The estimated perfusion parameters showed a higher plasma volume fraction of the tumors in mice 1, 2 and partly 5. There was also a higher SNR in these recordings than in the recordings of mice 3 and 4. The above two factors explain better consistency of the results with the two contrast agents observed for mice 1, 2 and partly 5, compared to mice 3 and 4.

The estimated correlation coefficients were still fairly low (Table 2, columns 5–8). This was probably the result of several factors. One factor degrading the correlation coefficient was motion of the mouse between (and during) the DCE-MRI acquisitions of the two contrast agents. This might be partly prevented by better fixation of the animal or by a respiration triggered acquisition. Respiration triggering would require a more sophisticated method coping with the impaired steady state of the FLASH acquisition due to nonconstant TR. A saturation-recovery prepared FLASH acquisition might be a good method of choice [24]. This would however lead to a decreased temporal and/or spatial resolution.

The procedure for AIF scaling is another source of inaccuracy of the perfusion parameter estimates. It might be too simplistic to assume the same $v_e + v_p$ for the erector spinae muscle of all mice, even if the same measurement conditions are kept. Also, the reference literature based value for $v_e + v_p$ might deviate from the true value. The literature values for skeletal muscles vary in a fairly wide range depending on the measurement method and the physiological state of the tissue. These scaling factor errors might be the reason for high v_e values, especially visible for mice 1 and 2 in Fig. 6 where $v_e > 1$ for some voxels. Another possibility would be scaling with respect to the “tail” level of a measured AIF. This approach was not reliable here due to a high variability in the arterial signal related mostly to its variable contamination by the partial volume effect and motion artifacts.

The reliability of the present blind deconvolution method might be further improved in several ways. A reparametrization of the applied pharmacokinetic model might help to improve the conditioning of the blind deconvolution process. Another possibility is to find a more realistic AIF model with parameters of a known physiological range connected with application of constraints on these parameters. To use more additional information, a combination of DCE-MRI with another MRI technique, such as DSC-MRI, might be considered [46].

The choice of the model might be another source of inaccuracy. The ATH model (implemented as a constrained DCATH model) was chosen as one of the available 4-parameter models. Other 4-parameter models include the 2CXM, TH and DP models. The 5-parameter models, such as the DCATH and GCTT models, were not considered due to the potentially worse conditioning of the approximation problem [35]. The choice of the ATH model was motivated by our previous comparisons of the 2CXM versus ATH in the context of blind deconvolution [43,47]. The ATH model could be also implemented as a constrained GCTT model. Whether the constrained GCTT model, the TH or DP model would lead to more reliable results is an open question to be addressed. These models are more realistic and might lead to better results, providing that the complexity of their corresponding criterial functional is

comparable with the used ATH model.

In summary, we believe that this study may contribute to the acceptance of blind deconvolution for AIF estimation in small animal DCE-MRI. Our results showed that reliable perfusion parameter estimates can be obtained for a sufficiently high, but still realistic SNR.

Supplementary data to this article can be found online at <https://doi.org/10.1016/j.mri.2019.05.024>.

Acknowledgements

This study was supported by the Czech Science Foundation (GA16-13830S), Ministry of Education, Youth and Sports of the Czech Republic (CZ.1.05/2.1.00/01.0017, LO1212, LQ1605, CZ.02.1.01/0.0/0.0/16.013/0001775), The Czech Academy of Sciences (RVO:68081731), by the project ICRC-ERA-Human Bridge (No. 316345) funded by the 7th Framework Programme of the European Union and by the project HistoPARK – Centre for analysis and modeling of tissues and organs (Reg. no.: CZ.1.07/2.3.00/20.0185). We are also grateful to Eva Janoušová for consultations on evaluation methods.

References

- [1] Jackson A, Buckley DL, Parker GJM. Dynamic contrast-enhanced magnetic resonance imaging in oncology. Berlin: Springer Science & Business Media; 2005.
- [2] Barnes SL, Whisenant JG, Loveless ME, Yankeelov TE. Practical dynamic contrast enhanced MRI in small animal models of cancer: data acquisition, data analysis, and interpretation. *Pharmaceutics* 2012;4(3):442–78.
- [3] Lee L, Sharma S, Morgan B, et al. Biomarkers for assessment of pharmacologic activity for a vascular endothelial growth factor (VEGF) receptor inhibitor, PTK787/ZK 222584 (PTK/ZK): translation of biological activity in a mouse melanoma metastasis model to phase I studies in patients with advanced colorectal cancer with liver metastases. *Cancer Chemother Pharmacol* 2006;57(6):761–71.
- [4] Keunen O, Johansson M, Oudin A, et al. Anti-VEGF treatment reduces blood supply and increases tumor cell invasion in glioblastoma. *Proc Natl Acad Sci U S A* 2011;108(9):3749–54.
- [5] Obad N, Espedal H, Jirik R, et al. Lack of functional normalisation of tumour vessels following anti-angiogenic therapy in glioblastoma. *Journal of Cerebral Blood Flow & Metabolism* 2018;38(10):1741–53.
- [6] Pike MM, Stoops CN, Langford CP, et al. High-resolution longitudinal assessment of flow and permeability in mouse glioma vasculature: sequential small molecule and SPIO dynamic contrast agent MRI. *Magn Reson Med* 2009;61(3):615–25.
- [7] Loveless ME, Halliday J, Liess C, et al. A quantitative comparison of the influence of individual versus population-derived vascular input functions on dynamic contrast enhanced-MRI in small animals. *Magn Reson Med* 2012;67(1):226–36.
- [8] Verhoye M, van der Sanden BPJ, Rijken PFJW, et al. Assessment of the neovascular permeability in glioma xenografts by dynamic T1 MRI with Gadomer-17. *Magn Reson Med* 2002;47(2):305–13.
- [9] Heisen M, Fan X, Buurman J, ter Haar Romeny BM. Effects of reference tissue AIF derived from low temporal resolution DCE-MRI data on pharmacokinetic parameter estimation. ISMRM-ESMRMB Joint Annual Meeting 2010. Sweden, Stockholm, Stockholm. 2010. p. 4802.
- [10] Fluckiger JU, Schabel MC, DiBella EVR. Model-based blind estimation of kinetic parameters in dynamic contrast enhanced (DCE)-MRI. *Magn Reson Med* 2009;62(6):1477–86.
- [11] Schabel MC, Fluckiger JU, DiBella EVR. A model-constrained Monte Carlo method for blind arterial input function estimation in dynamic contrast-enhanced MRI: I. simulations. *Phys Med Biol* 2010;55(16):4783–806.
- [12] Sourbron SP, Buckley DL. Tracer kinetic modelling in MRI: estimating perfusion and capillary permeability. *Phys Med Biol* 2012;57(2):R1–33.
- [13] Sourbron SP, Buckley DL. Classic models for dynamic contrast-enhanced MRI. *NMR Biomed* 2013;26(8):1004–27.
- [14] Brix G, Kiessling F, Lucht R, Darai S, Wasser K, Delorme S, et al. Microcirculation and microvasculature in breast tumors: pharmacokinetic analysis of dynamic MR image series. *Magn Reson Med* 2004;52(2):420–9.
- [15] Johnson JA, Wilson TA. A model for capillary exchange. *Am J Physiol* 1966;210(6):1299–303.
- [16] St Lawrence KS, Lee TY. An adiabatic approximation to the tissue homogeneity model for water exchange in the brain: I. Theoretical derivation. *J Cereb Blood Flow Metab* 1998;18(12):1365–77.
- [17] Larson KB, Markham J, Raichle ME. Tracer-kinetic models for measuring cerebral blood flow using externally detected radiotracers. *J Cereb Blood Flow Metab* 1987;7(4):443–63.
- [18] Koh TS, Zeman V, Darko J, et al. The inclusion of capillary distribution in the adiabatic tissue homogeneity model of blood flow. *Phys Med Biol* 2001;46(5):1519–38.
- [19] Jacobs I, Strijkers GJ, Keizer HM, Janssen HM, Nicolay K, Schabel MC. A novel approach to tracer-kinetic modeling for (macromolecular) dynamic contrast-enhanced MRI. *Magn Reson Med* 2016;75(3):1142–53.
- [20] Hectors SJ, Jacobs I, Lok J, et al. Improved evaluation of Antivascular Cancer

- therapy using constrained tracer-kinetic modeling for multiagent dynamic contrast-enhanced MRI. *Cancer Res* 2018;78(6):1561–70.
- [21] Zhou Z, Lu Z-R. Gadolinium-based contrast agents for magnetic resonance cancer imaging. *Wiley Interdiscip Rev Nanomed Nanobiotechnol* 2013;5(1):1–18.
- [22] Delrue LJ, Casneuf V, Van Damme N, et al. Assessment of neovascular permeability in a pancreatic tumor model using dynamic contrast-enhanced (DCE) MRI with contrast agents of different molecular weights. *Magnetic Resonance Materials in Physics, Biology and Medicine* 2011;24(4):225–32.
- [23] Daldrup H, Shames DM, Wendland M, et al. Correlation of dynamic contrast-enhanced MR imaging with histologic tumor grade: comparison of macromolecular and small-molecular contrast media. *AJR Am J Roentgenol* 1998;171(4):941–9.
- [24] Henderson E, Sykes J, Drost D, et al. Simultaneous MRI measurement of blood flow, blood volume, and capillary permeability in mammary tumors using two different contrast agents. *J Magn Reson Imaging* 2000;12(6):991–1003.
- [25] Jiřík R, Souček K, Dražanová E, et al. Blind multichannel deconvolution for estimation of a parametric AIF in DCE-MRI of mice. *ISMRM proceedings 2014*. vol. 4. 2014. p. 2754.
- [26] Jiřík R, Souček K, Mézl M, et al. Blind deconvolution in dynamic contrast-enhanced MRI and ultrasound. 36th Conf. Of the IEEE engineering in medicine and biology society 2014. 2014. p. 4276–9.
- [27] Heilmann M, Walczak C, Vautier J, et al. Simultaneous dynamic T1 and T2* measurement for AIF assessment combined with DCE MRI in a mouse tumor model. *Magma* 2007;20(4):193–203.
- [28] Ragan D, Lai S, Bankson J. Fast, reproducible measurement of the vascular input function in mice using constrained reconstruction and cardiac sampling. *NMR Biomed* 2011;24:373–84.
- [29] Checkley D, Tessier J, Wedge S, et al. Dynamic contrast-enhanced MRI of vascular changes induced by the VEGF-signalling inhibitor ZD4190 in human tumour xenografts. *Magn Reson Med* 2003;21:475–82.
- [30] Treuting PM, Dintzis SM, Montine KS. *Comparative anatomy and histology: A mouse, rat and human atlas*. London: Academic Press; 2017.
- [31] Parker GJM, Roberts C, Macdonald A, et al. Experimentally-derived functional form for a population-averaged high-temporal-resolution arterial input function for dynamic contrast-enhanced MRI. *Magn Reson Med* 2006;56(5):993–1000.
- [32] van Nierop BJ, Coolen BF, Dijk WJ, Hendriks AD, de Graaf L, Nicolay K, et al. Quantitative first-pass perfusion MRI of the mouse myocardium. *Magn Reson Med* 2013;69(6):1735–44.
- [33] Koh TS, Cheong DLH, Hou Z. Issues of discontinuity in the impulse residue function for deconvolution analysis of dynamic contrast-enhanced MRI data. *Magn Reson Med* 2011;66(3):886–92.
- [34] Kratochvíla J, Jiřík R, Bartoš M, et al. Distributed capillary adiabatic tissue homogeneity model in parametric multi-channel blind AIF estimation using DCE-MRI. *Magn Reson Med* 2016;75(3):1355–65.
- [35] Bartoš M, Jiřík R, Kratochvíla J, et al. The precision of DCE-MRI using the tissue homogeneity model with continuous formulation of the perfusion parameters. *Magn Reson Imaging* 2014;32(5):505–13.
- [36] Kershaw LE, Buckley DL. Precision in measurements of perfusion and microvascular permeability with T1-weighted dynamic contrast-enhanced MRI. *Magn Reson Med* 2006;56(5):986–92.
- [37] Schabel MC. A unified impulse response model for DCE-MRI. *Magn Reson Med* 2012;68(5):1632–46.
- [38] Li K-L, Zhu XP, Waterton J, Jackson A. Improved 3D quantitative mapping of blood volume and endothelial permeability in brain tumors. *J Magn Reson Imaging* 2000;12(2):347–57.
- [39] Reed RK, Viig H. Compliance of the interstitial space in rats. I. Studies on hindlimb skeletal muscle. *Acta Physiol Scand* 1981;113(3):297–305.
- [40] Vexler VS, Clément O, Schmitt-Willich H, Brasch RC. Effect of varying the molecular weight of the MR contrast agent Gd-DTPA-polylysine on blood pharmacokinetics and enhancement patterns. *J Magn Reson Imaging* 1994;4(3):381–8.
- [41] Jiang K, Tang H, Mishra PK, Macura SI, Lerman LO. Measurement of murine single-kidney glomerular filtration rate using dynamic contrast-enhanced MRI. *Magn Reson Med* 2018;79(6):2935–43.
- [42] Taxt T, Pavlin T, Reed RK, et al. Using single-channel blind deconvolution to choose the most realistic pharmacokinetic model in dynamic contrast-enhanced MR imaging. *Applied Magnetic Resonance* 2015;46(6):643–59.
- [43] Jiřík R, Bartoš M, Souček K, et al. Dynamic contrast-enhanced MRI using spatial prior knowledge. *ISMRM annual meeting 2017*. 2017. p. 2895. USA, Honolulu.
- [44] Bartoš M, Šorel M, Mangová M, et al. DCE-MRI perfusion analysis with L1-norm spatial regularization. *ISMRM-ESMRMB joint annual meeting 2018*. France, Paris. 2018. p. 2826.
- [45] Sourbron S, Heilmann M, Walczak C, et al. T2*-relaxivity contrast imaging: first results. *Magn Reson Med* 2013;69(5):1430–7.
- [46] Jiřík R, Taxt T, Souček K, et al. Comparison of the ATH and 2CXM models using low- and high-molecular-weight contrast agents in DCE-MRI. *Abstracts of ESMRMB Conf., magnetic resonance materials in physics, biology and medicine*. vol. 29(Suppl 1). 2016. p. S447–8.

4.2.3 Paper V

N. Obad, H. Espedal, R. Jiřík, P.O. Sakariassen, C. Brekke Rygh, M. Lund-Johansen, T. Taxt, S.P. Nicolou, R. Bjerkvig, O. Keunen, Lack of functional normalisation of tumour vessels following anti-angiogenic therapy in glioblastoma, *J. Cereb. Blood Flow Metab.* 38 (2018) 1741–1753.

<https://doi.org/10.1177/0271678X17714656>.

(IF 6.040)

Author's contribution:

- co-author of the perfusion-analysis methodology
- perfusion analysis of measured MRI data (except for blind-deconvolution AIF estimation)
- providing consultations on evaluation methodology
- paper co-writing



Lack of functional normalisation of tumour vessels following anti-angiogenic therapy in glioblastoma

Nina Obad^{1,2,3}, Heidi Espedal^{1,3}, Radovan Jirik⁴, Per Oystein Sakariassen¹, Cecilie Brekke Rygh^{1,5}, Morten Lund-Johansen^{2,6}, Torfinn Taxt¹, Simone P Niclou^{3,7}, Rolf Bjerkvig^{1,3,7} and Olivier Keunen⁷

Abstract

Neo-angiogenesis represents an important factor for the delivery of oxygen and nutrients to a growing tumour, and is considered to be one of the main pathodiagnostic features of glioblastomas (GBM). Anti-angiogenic therapy by vascular endothelial growth factor (VEGF) blocking agents has been shown to lead to morphological vascular normalisation resulting in a reduction of contrast enhancement as seen by magnetic resonance imaging (MRI). Yet the functional consequences of this normalisation and its potential for improved delivery of cytotoxic agents to the tumour are not known. The presented study aimed at determining the early physiologic changes following bevacizumab treatment. A time series of perfusion MRI and hypoxia positron emission tomography (PET) scans were acquired during the first week of treatment, in two human GBM xenograft models treated with either high or low doses of bevacizumab. We show that vascular morphology was normalised over the time period investigated, but vascular function was not improved, resulting in poor tumoural blood flow and increased hypoxia.

Keywords

Angiogenesis, bevacizumab, glioblastoma, hypoxia, perfusion, VEGF

Received 13 November 2016; Revised 11 April 2017; Accepted 18 April 2017

Introduction

Glioblastomas (GBMs) are highly heterogeneous tumours, characterised by angiogenesis and necrosis.¹ In 2009, the FDA approved bevacizumab, a monoclonal antibody against circulating vascular endothelial growth factor (VEGF), for second line treatment of patients with recurrent GBM. The accelerated approval was granted on the basis of two single arm trials, showing strong radiological responses in comparison to historical data,^{2,3} assessed by the Macdonald criteria.⁴ However, although progression-free survival (PFS) was prolonged, bevacizumab treatment did not improve overall survival (OS), when given alone or in combination with traditional chemotherapeutic regimens, whether for recurrent or newly diagnosed GBM.^{5–7} The radiological response was attributed to a reduced blood brain barrier (BBB) permeability, rather than a true anti-tumour effect.⁸ Several clinical

trials in recurrent GBM have also attempted to combine bevacizumab therapy with alternative chemotherapeutic regimens.^{9,10} The phase II BELOB trial,

¹Department of Biomedicine, University of Bergen, Bergen, Norway

²Department of Neurosurgery, Haukeland University Hospital, Bergen, Norway

³KG Jebsen Brain Tumor research Center, University of Bergen, Bergen, Norway

⁴Institute of Scientific Instruments of the Czech Academy of Sciences, Brno, Czech Republic

⁵Bergen University College, Bergen, Norway

⁶Department of Clinical Science, University of Bergen, Bergen, Norway

⁷Norlux Neuro-Oncology Laboratory, Department of Oncology, Luxembourg Institute of Health, Luxembourg, Luxembourg

Corresponding author:

Olivier Keunen, Norlux Neuro-Oncology Laboratory, Department of Oncology, Luxembourg Institute of Health, 84, Val Fleuri, L-1526 Luxembourg, Luxembourg.
Email: olivier.keunen@lih.lu

for example showed improved OS in patients treated with a combination of lomustine and bevacizumab.¹⁰ Unfortunately, a subsequent randomised phase III trial did not validate these results, leaving the future of anti-angiogenic treatment in GBM highly uncertain.¹¹

According to Folkman's hypothesis, anti-angiogenic therapy should prevent the formation of new blood vessels, leading to a nutrient- and oxygen-deprived tumour that subsequently ceases to progress.¹² As tumour vessels are highly irregular, tortuous and leaky, the delivery of oxygen and nutrients is inefficient. Jain et al. proposed that anti-angiogenic therapy may lead to a transient window of tumour vessel normalisation, shortly after treatment initiation, with increased pericyte coverage and a thickening of the basal membrane, resulting in increased blood flow with improved oxygen and drug delivery.^{13,14} In GBMs, preclinical studies have suggested that VEGF receptor 2 blockade can normalise the tumour vessels transiently by up-regulating angiopoietin 1 (Ang-1), leading to the stimulation and recruitment of pericytes with an increased tumour perfusion and decreased hypoxia.¹⁵ It has also been proposed that this normalisation leads to a decreased interstitial pressure that facilitates drug delivery and an improved tumour oxygenation that increases tumour sensitivity to radiation.^{16,17} In contrast, other studies indicate that anti-angiogenic treatment may lead to a reduced drug delivery caused by a restoration of the BBB.^{18,19} Support for the former view is found among a subset of patients treated with cediranib, a VEGFR tyrosine kinase inhibitor (TKI), where increased tumour perfusion was observed in some patients.^{20–22}

The proposed window of vascular normalisation is expected to occur transiently during the first days of treatment. In previous studies, our group has shown that bevacizumab treatment leads to morphological vessel normalisation without an increase in blood flow in human GBM patient-derived xenograft (PDX) models.^{23,24} Since blood flow was evaluated several weeks after the initiation of the treatment, the transient window of vascular normalisation might have been missed in these studies. We thus designed the present study to establish whether our clinically relevant PDX models display such a window of vascular normalisation or not, by repeatedly assessing perfusion parameters during the early courses of bevacizumab treatment. We used two different models displaying the properties of a purely angiogenic and a mixed angiogenic/infiltrative phenotype, closely mimicking the features of clinical GBM. The animals were treated with bevacizumab in doses equivalent to their clinical counterparts or in lower doses to see whether tumour vessel normalisation represents a dose-dependent effect. Dynamic Contrast Enhanced magnetic resonance

imaging (DCE-MRI) and histological analysis were used to assess vessel morphology and function, and Fluorine-18 Fluoromisonidazole (¹⁸F-FMISO) PET was used to assess tumoural hypoxia.

The results presented here do not support the hypothesis that bevacizumab treatment causes a transient window of normalisation of tumour vessels function during the early stages of treatment. Instead, tumoural blood flow remained heterogeneous and inefficient during the period analysed. Moreover, ¹⁸F-FMISO PET imaging showed a progressive increase in hypoxia in bevacizumab treated tumours, consistent with the reduced blood flow observed by magnetic resonance imaging (MRI).

Materials and methods

Xenograft models

A total of 37 nude male or female adult rats (rnu-/rnu-Rowett) were used for the studies (29 in the perfusion study and 8 in the hypoxia study). Group sizes were calculated according to expected variance in tumours growth, on the basis of previous similar studies. Animals were grouped in cages, fed ad libitum with standard food pellets, and their welfare was monitored through daily routine checks with increased daily frequency as animals were approaching the end stage. We used GBM spheroids generated from two different patients, Patient 3 (P3) and Patient 13 (P13) as previously described.²⁵ Tumour tissue was harvested during surgery and subsequently serially transplanted orthotopically in the animals. The tumours were passaged for either 32 (P3) or 7 (P13) generations in vivo. Both these models have been characterised in detail and recapitulate patient GBMs features by showing vascular proliferation, diffuse tumour cell infiltration and pseudopalisading necrosis.²⁶ They have the following genomic characteristics; P3: +[Chr 7, Chr19, 20q], -[1q42-q43, Chr9, Chr10, 20p] – [PIK3R1, CDKN2A/B]; P13: +[Chr7, Chr19, Chr20], -[6q16.2-16.3, Chr10, 17q12], – CDKN2A/B.²⁷ P13 is a highly angiogenic model with pronounced necrosis and little invasion. It displays contrast enhancement on T1-weighted images after injection of a gadolinium-based contrast agent, and responds to bevacizumab by a strong reduction in contrast enhancement. In comparison, P3, which is angiogenic as well, is more invasive and displays a less aggressive progression. It responds to bevacizumab by reduced contrast enhancement too, and has also been shown to increase glycolytic activity and invasion.^{23,24} Pimonidazole staining shows increased hypoxia after bevacizumab treatment in both models. The key histological features of the P3 and P13 animal models are summarised in online Supplementary Figure S1.

The collection of biopsy tissue was approved by the regional ethical committee at the Haukeland University Hospital, Bergen, Norway (REK 013.09).

Intracranial implantation

All animal experiments were performed within a facility that was recently certified by the Association for Assessment and Accreditation of Laboratory Animal Care (AAALAC) International. All experiments were done in accordance with the Norwegian Animal Act. The protocols were approved by the Animal Welfare Body of the University of Bergen, and are in compliance with the ARRIVE guidelines (www.nc3rs.org.uk/arrive-guidelines). P3 or P13 spheroids were implanted stereotactically into the brains of nude immunodeficient rats, as described previously.²⁸ A burr hole was made 3 mm lateral and 1 mm posterior to the bregma on the right side and the spheroids were injected 3.5 mm below the cortical surface. The animals were euthanized when neurological signs were evident, by CO₂ inhalation, and perfused intracardially with 0.9% NaCl. The brains were removed, the caudal half was fixed in formalin and further processed for histological and immunohistological examination.

Bevacizumab treatment

Treatment was initiated once the tumours reached an average size of about 50 mm³ as measured by MRI (typically 3 weeks after implantation for P13 and 4 weeks for P3). Animals were then divided randomly into treatment groups or controls. Bevacizumab (Avastin, Genentech, San Francisco, CA, USA) was injected i.v twice a week, at 10 mg/kg (high dose) or 5 mg/kg (low dose). The control animals received i.v saline following the same schedule. Separate groups of P13 implanted animals were used for the perfusion MRI studies and the hypoxia PET studies. The generic design of the studies is summarised in online Supplementary Figure S2, together with the number of animals used in each study.

Immunohistochemistry

Immunohistochemistry was performed as described previously.²⁴ Paraffin-embedded formalin-fixed tissue sections were de-paraffinized and brought to a temperature of 99°C for 20 min using a 10 mM citrate buffer at pH 6.0 or incubated with proteinase K diluted in 0.05 M Tris-Cl, at pH 7.5 and a temperature of 37°C for 10 min. The following primary antibodies were used during sections incubation: anti-von Willebrand factor (vWf) (1:1000; A0082; DAKO; Oslo, Norway), pimonidazole (1:200; Hypoxyprobe 9.7.11; HPI Inc;

Burlington, MA, USA) and anti-human nestin (1:1000; MAB5326; Millipore; Billerica, MA, USA). Incubation of primary antibodies lasted 90 min at RT. A biotinylated secondary antibody (Vector Laboratories, Trondheim, Norway) was used for detection, amplified with Vectastain ABC Reagent (Vector). Development of the sections was done with 3′3-diaminobenzidine (DAB, DAKO Cytomation), according to the manufacturer's instructions. Pictures were obtained using a Nikon light microscope (Nikon Eclipse E600) and Nikon imaging software (Nikon NIS Elements v 4.11).

MRI

MRI was used to screen the animals after implantation and randomly split them into treatment and control groups according to tumour volumes. Extensive MRI sessions, including perfusion series, were then conducted longitudinally throughout the treatment. Images were acquired on a 7T horizontal PharmaScan (Bruker Biospin) using either a quadratic volume coil or a four-channel surface coil designed for rat brain imaging. Animals were placed prone in a cradle and kept asleep with gas anaesthesia. We used 1–2% isoflurane mixed with 50% air for the first series of experiments, then switched to 50% O₂ or 1–3% sevoflurane mixed with 100% O₂, following an institutional decision motivated by animals stability, accelerated recovery, and unchanged blood flow and oxygenation. To avoid introducing experimental bias, groups compared within a study were always anaesthetised with the same gas at all time points throughout the study. Body temperature was kept constant at 37°C and breathing was monitored throughout the scan sessions. The following acquisition parameters were used: (1) T2-weighted (T2w): method RARE, spatial resolution (SR) 137 μm × 137 μm × 1000 μm, echo time (TE) 36 ms, repetition time (TR) 3500 ms, rare factor (RF) 8, averages (AVG) 3; (2) T1-weighted (T1w): method RARE, SR 137 μm × 137 μm × 1000 μm, TE 9 ms, TR 1000 ms, RF 4, AVG 4; (3) Diffusion Weighted Imaging (DWI): method DtiEpi, SR 125 μm × 125 μm × 1000 μm, 3 directions, 6 b-values per direction from 0 to 1664 s/mm²; (4) Dynamic Contrast Enhanced (DCE): method FLASH, SR 156 μm × 156 μm × 1000 μm, TE 2.1 ms, TR 8 ms, FA 17°, time resolution 0.7 s, total scan time 12′48″, Contrast Agent 0.1 mmol/kg of Omniscan (GE Healthcare) injected intravenously after 25″. The animals were scanned every other day for 8 days, and treatment was started after the first scan (Day 1).

Analysis of the MRI data was performed in Paravision 5.1 (Bruker Biospin) and with routines custom developed in Matlab 2015b (MathWorks,

MA, USA) and C. Specifically, the perfusion analysis was based on the pharmacokinetic modelling of the DCE-MRI data using the adiabatic approximation of the tissue homogeneity model and blind deconvolution arterial input functions (AIFs), as described previously,^{23,29} to separate the contributions of perfusion and vessels permeability changes to tumour physiology. The blind deconvolution AIFs were scaled so that a value known from the literature (12.8 mL/100 mL for the interstitial space + plasma fraction) was achieved for the reference tissue (left and right temporalis muscles).²³ Datasets that displayed poor signal-to-noise ratio (SNR) as a result of sub-optimal experimental conditions such as incomplete injection of the contrast agent or excessive rat motion, were excluded from the quantification. Tumour volume (TV) was defined as the part of the tumour visible on MRI, and measured by delineating tumour on consecutive 2D T2-weighted sections, multiplied by section thickness. Growth rate (GR) was calculated using the TV measurement at the first and last time points as $GR = 100 \times \log(TV_f / TV_0) / (t_f - t_0)$, where TV_f and TV_0 are the tumour volumes at the last and first time points, respectively, and $t_f - t_0$ is the difference in days between the time points. Tumour volumes are expressed in mm^3 and GR in ‘% per day’.

PET/CT imaging and data analysis

In vivo tumour hypoxia was evaluated by PET using in-house produced ^{18}F -fluoromisonidazole (^{18}F -FMISO) (ABX GmbH, Radeberg, Germany). PET/CT images were acquired on a small-animal nanoScan PET scanner (Mediso Medical Imaging Systems, Budapest, Hungary). An activity of ~ 30 MBq (31.8 ± 4.1) of ^{18}F -FMISO was injected in the tail-vein and the rats were left awake for 120 min prior to a 30 min acquisition scan (coincidence 1:5, normal count mode) as previously described.²⁴ Animals were anaesthetised with 3% sevoflurane mixed in air throughout the scans, and monitored for breathing and temperature. CT semi-circular scans (50 kVp, 300 ms, 480 projections) were performed for anatomical reference and attenuation correction of PET images. PET reconstruction was performed by Nucline nanoscan (Mediso Medical Imaging Systems) from list-mode using the following parameters: reconstruction algorithm Tera-Tomo 3D, full detector model, 4 iterations/6 subsets, 1:3 coincidence mode and a voxel size of 0.4 mm.

The images were quantified using InterView Fusion v3.01 (Mediso Medical Imaging Systems). A 3 mm sphere-shape volume of interest was placed in both the tumour and the contralateral hemisphere to calculate tumour-to-brain ratios using standard uptake value (SUV) mean.

Statistics

Individual animals were used as observations when assessing tumour volumes and tumour voxels were used as observations when assessing perfusion parameters, to account for the heterogeneity within the tumours. Mean values for each time point are reported for the treated and control animals. A Student's *t*-test was used to assess the statistical significance of differences between groups, calculated in Matlab (MathWorks). *p* Values < 0.05 were considered statistically significant.

Results

Tumour progression

Twenty-nine animals were used in the perfusion MRI studies, split for both the P3 and P13 models into controls versus treatment groups, as detailed in online Supplementary Figure S2. MRI showed a continuous growth in both tumour models during the time period of 1–8 days, for both the controls and the bevacizumab treated tumours in P13 implanted animals (Figure 1(a) and (b)) and P3 implanted animals (Figure 1(e) and (f)). Tumour volume progression during that time window was exponential for all models and treatment groups (Figure 1(c) and (g)). Quantification of tumour volumes indicated a tendency toward lower growth rate in the bevacizumab treated group compared to the controls for the P13 model ($12\% \pm 2\%$ versus $16\% \pm 2\%$ per day) (Figure 1(d)). Changes were however not statistically significant for the small cohorts used. For the P3 implanted animals, the tendency toward smaller growth rate in the treated animals was less pronounced ($12\% \pm 3\%$ vs. $14\% \pm 4\%$ per day) (Figure 1(h)), suggesting a weaker response to bevacizumab at the onset of treatment, possibly due to the less angiogenic and more infiltrative nature of this model. The changes were nevertheless not statistically significant either in the cohorts used.

We also acquired DWI data at each time point and calculated apparent diffusion coefficients (ADC), which have previously been related to cellularity, to see if longitudinal changes in ADC could inform us on a possible increase of the infiltrative compartment of the tumours. ADC was however stable for both tumour models over the time period investigated and no statistically significant changes were observed (data not shown).

Morphological normalisation of tumour vessels

DCE-MRI was used to obtain quantitative values of perfusion and vessel permeability parameters over

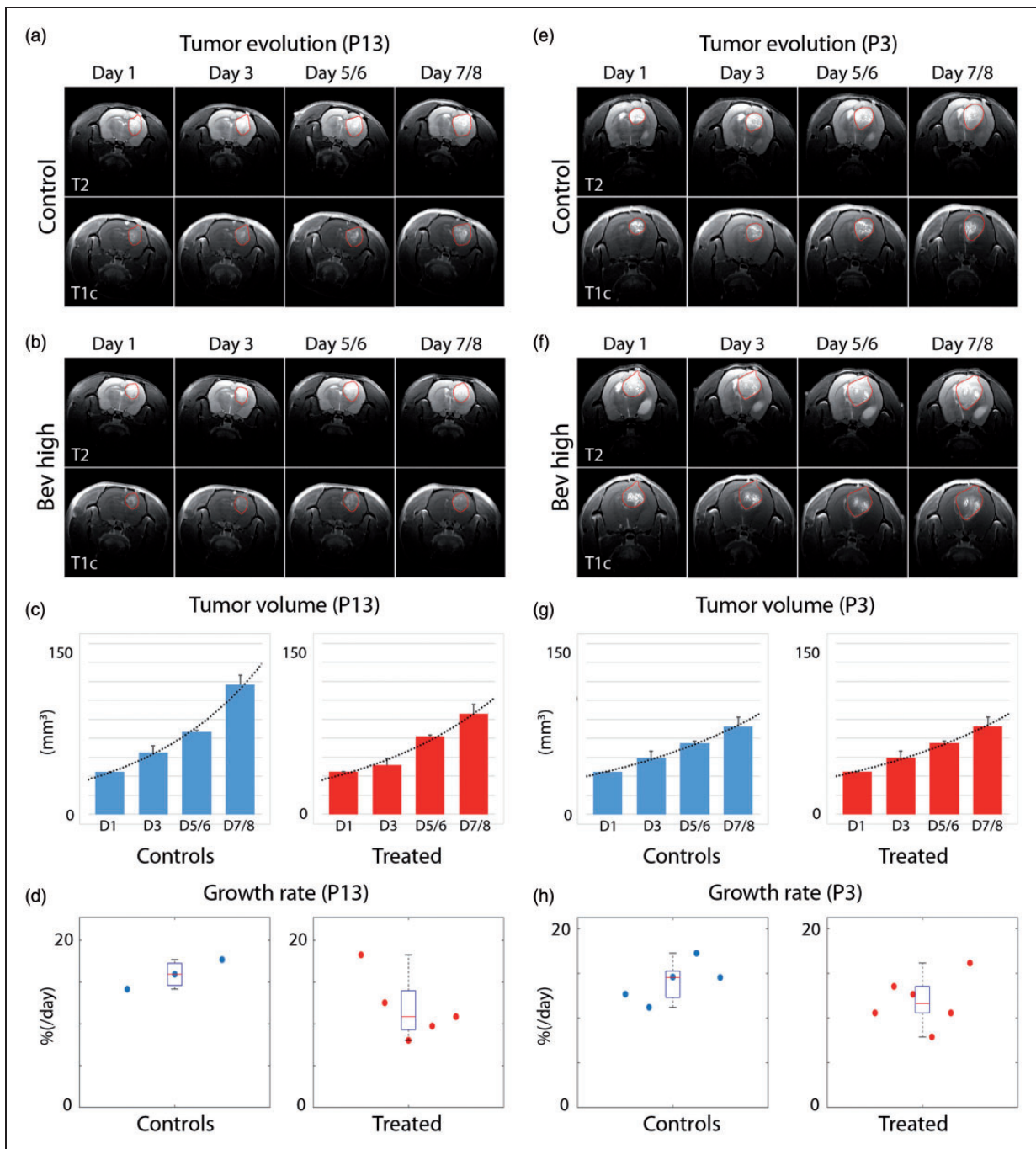


Figure 1. Tumor size evolution: Representative cases of tumour evolution for the animals implanted with the angiogenic P13 phenotype, showing one control (a), and one animal treated with high doses of bevacizumab (b). Images represent T2 weighted MRI acquisitions (top rows) and contrast enhanced T1 weighted MRI (bottom rows). Quantification of corresponding tumour volumes (c) and growth rates (d) for P13 animals per group. Whiskers boxes show percentile 25, median and percentile 75 values. Representative cases of tumour evolution for the animals implanted with the more infiltrative P3 phenotype, showing one control (e), and one animal treated with high doses of bevacizumab (f). Quantification of corresponding tumour volumes (g) and growth rates (h) for P3 animals per group. Tumour volumes show an exponential progression in all groups for P13 (c) and P3 (g) during the time window of observation. Growth rates were higher for controls than for bevacizumab treated animals in both the P13 (d) and the P3 (h) tumour models, and this difference was more pronounced for the more angiogenic P13 tumour model. Tumour volumes expressed in mm³ and growth rates in % per day. Animals per group: P13 Controls-5, P13 Bev high-5, P3 Controls-5, P3 Bev high-6. High dose: 10 mg/kg. (Scale bars: ± SE).

time, and to assess if anti-angiogenic therapy induces a window of normalisation of tumour vessels for the two GBM models used. For the more angiogenic model (P13), high and low doses of bevacizumab were used to further evaluate whether this putative normalisation was associated with a dose-dependent effect. Mean tumour values as well as tumoural (voxels) values were examined to account for the spatial heterogeneity of the parameters within the tumour.

We observed that tumour blood volume (V_b) increased over time in the control (untreated) animals for the angiogenic P13 model, as illustrated by one representative animal in this group (Figure 2(a), top line). This increase was less pronounced in the treated animals, whether given high doses (10 mg/kg) or low doses

(5 mg/kg) of bevacizumab (Figure 2(a), middle and bottom lines). Quantification of the mean tumoural V_b (Figure 2(b), top line) revealed a steady progression over time in the control animals, and for the treated animals a reduction first, followed by a steady progression. In comparison to controls, tumoural V_b mean values in the treated animals were 39% and 46% lower on Day 5/6 for the animals treated with 10 mg/kg doses of bevacizumab (Bev high) and those treated with the 5 mg/kg doses of bevacizumab (Bev low) groups, respectively ($p < 0.001$). Histogram analysis of tumoural V_b values distribution (Figure 2(b), bottom line) showed a progressive increase in the fraction of high V_b values (dark blue) compared to medium V_b (hatched blue) and low V_b (light blue) values over

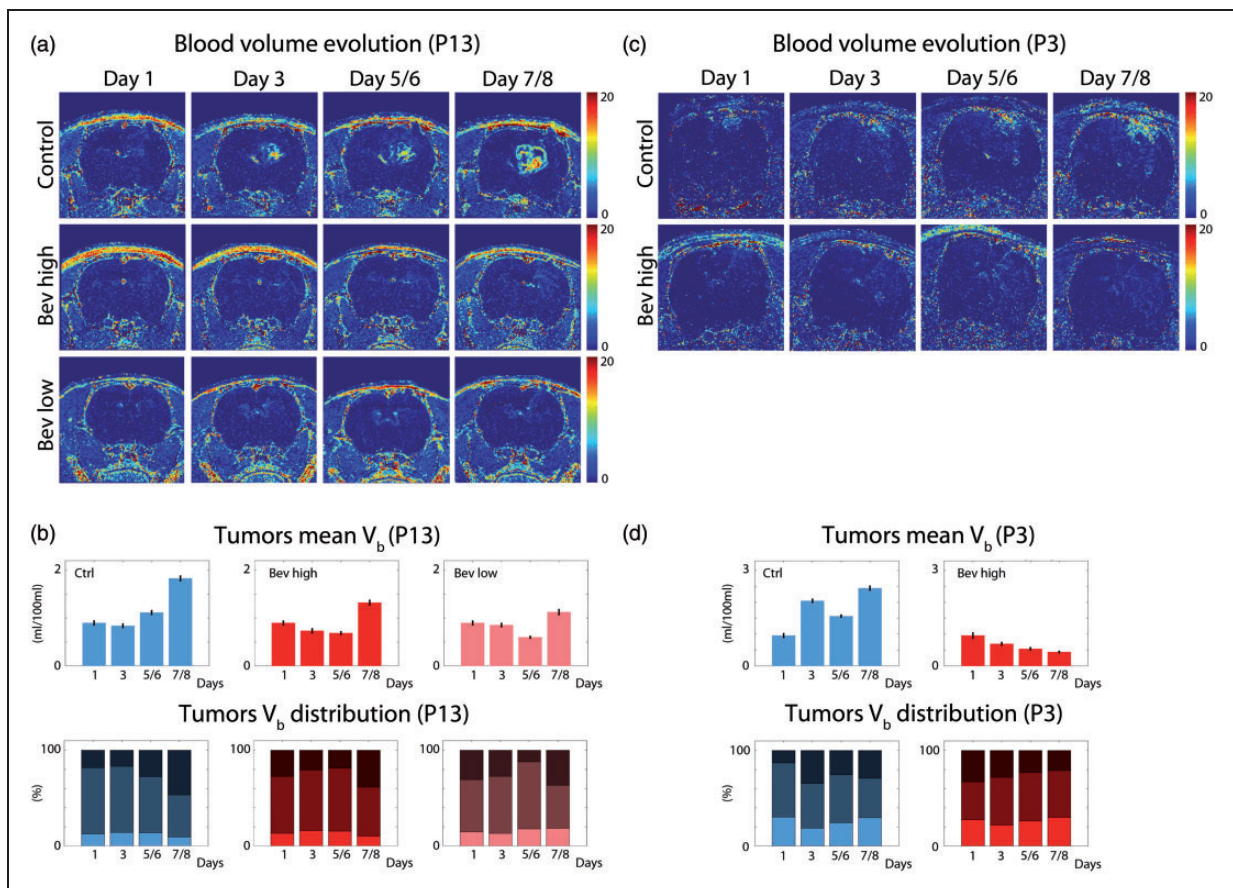


Figure 2. Tumoural blood volume evolution. (a) Illustrative maps of blood volume (V_b) evolution for animals implanted with the highly angiogenic P13 tumour model, showing one control (top line) and two animals treated with respectively high and low doses of bevacizumab (middle and bottom lines). (b) Quantification of tumour mean V_b for P13 animals (top line) and histogram analysis of tumoural V_b values distribution (bottom line). In comparison to controls, animals treated with bevacizumab high or low doses, show a reduced tumour mean V_b and a reduced fraction of high V_b values shortly after the start of the treatment, suggesting a normalisation of blood vessel morphology. Similar results are observed for the less angiogenic more infiltrative P3 model (c and d), where the normalisation window extends throughout the whole observation period. V_b expressed in absolute values of mL/100 mL of tissue. Thresholds for the high, medium and low values (dark, hatched and light blue/red) were defined by the 75% and 25% percentiles of the whole voxel population for the given tumour model. Animals per group: P13 Controls-5, P13 Bev high-5, P13 Bev low-5, P3 Controls-7, P3 Bev high-7. Bev high: 10 mg/kg, Bev low: 5 mg/kg.

time for the control animals. In the animals treated with high or low doses of bevacizumab, a reduction of the fraction of high V_b values was observed early after the start of the treatment, suggesting a possible morphological normalisation effect caused by the treatment.

For the less angiogenic and more infiltrative P3 model, tumour V_b also increased steadily over time for the control animals (Figure 2(c)), with mean tumour V_b and distribution showing more fluctuations (Figure 2(d)). For animals treated with high doses of bevacizumab, the normalisation effect suggested by progressive decrease of mean tumoural V_b and progressive reduction of the fraction of high V_b values, lasted

throughout the whole observation period. In comparison to controls, mean tumoural V_b in the treated animals was 82% lower on Day 7/8 ($p < 0.001$).

The permeability of blood vessels was also assessed, using the permeability surface (PS) area product parameter that represents the product of the permeability (leakiness) of vessel wall by the area of vessel wall. Similarly to V_b , PS increased in the P13 control animals (Figure 3(a), top line). Quantification of mean tumoural PS (Figure 3(b), top line) revealed a sustained progression of this parameter over time in this group, with a progressive increased fraction of high PS values (Figure 3(b), bottom line). For the animals treated with bevacizumab, PS was more stable over time

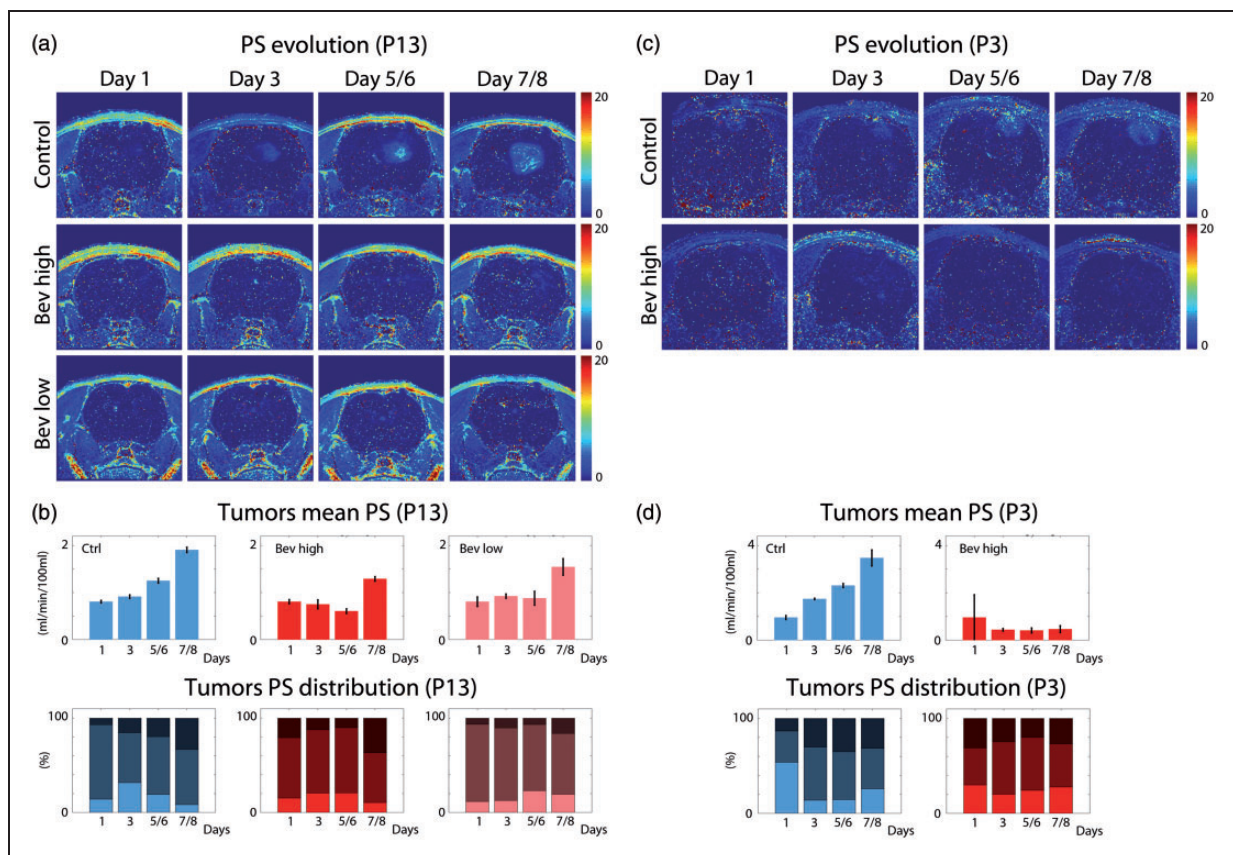


Figure 3. Tumoural vessel permeability evolution. (a) Illustrative maps of the permeability surface area product (PS) evolution for animals implanted with the highly angiogenic P13 tumour model, showing one control (top line) and two animals treated with respectively high and low doses of bevacizumab (middle and bottom lines). (b) Quantification of tumours mean PS for P13 animals (top line) and histogram analysis of tumoural voxels PS distribution (bottom line). In comparison to controls, animals treated with bevacizumab high or low doses, show a reduced tumour mean PS and a reduced fraction of high PS voxels shortly after the start of the treatment, again suggesting a normalisation of blood vessel morphology. For the less angiogenic, more infiltrative P3 model (c and d), the normalisation window extends throughout the whole observation period. Datasets displaying poor SNR as a result of experimental conditions, such as on Day 1 for the represented P3 Control (C), were not considered in the quantification. PS expressed in absolute values of mL/min/100 mL of tissue. Thresholds for the high, medium and low values (dark, hatched and light blue/red) were defined by the 75% and 25% percentiles of the whole voxels population for the given tumour model. Animals per group: P13 Controls-5, P13 Bev high-5, P13 Bev low-5, P3 Controls-7, P3 Bev high-7. Bev high: 10 mg/kg, Bev low: 5 mg/kg.

(Figure 3(a), middle and bottom lines). Quantification of mean tumoural PS for the animals treated with high doses of bevacizumab showed a reduction first, followed by a steady increase (Figure 3(b), top line), similar to what was observed for the tumoural blood volumes (Figure 2(b), top line). In comparison to controls, PS in this treatment group was 52% lower on Day 5/6 ($p < 0.001$). The distribution of tumoural PS (Figure 3(b), bottom line) showed a reduction of the high PS values fraction first, followed by a steady increase, again suggestive of a transient normalisation of this parameter following anti-angiogenic therapy. This effect was less pronounced for the animals treated with the low dose of bevacizumab.

For the less angiogenic, more infiltrative P3 model (Figure 3(c)), mean tumour PS also increased steadily in the controls and was more stable for the animals treated with high doses of bevacizumab (Figure 3(d), top line). In comparison to controls, PS in the treatment group was 82% lower on Day 7/8 ($p < 0.001$). The distribution of tumoural PS values showed a progressive increase of the fraction of high PS values in the controls, and a more stable or slightly decreasing fraction of high PS values in the bevacizumab treated animals (Figure 3(d), bottom line).

In many studies on brain tumour perfusion, K^{trans} , a parameter that represents the outflow of contrast agent from the vascular compartment to the tissue is used, to provide an indication of vessel permeability. It should however be noted that K^{trans} is also influenced by blood flow. This makes interpretation of changes in this parameter more complex, especially in studies involving treatments with anti-angiogenic agents that are known to interfere with vessel permeability. PS, on the contrary, is independent of blood flow, such that changes in PS more accurately reflect changes in the permeability of blood vessels. Nevertheless, the longitudinal changes in K^{trans} in our study closely followed those of PS (online Supplementary Figure S3). Thus, changes in vessel permeability, when further used in the text, can here indifferently be regarded as referring to changes in PS or K^{trans} .

Details of mean tumour V_b , PS and K^{trans} for all time points are provided in online Supplementary Tables S1 and S2, together with the ratio of values for bevacizumab treated versus control animals and associated p -values.

In summary, the longitudinal study on changes in blood volume and vessel permeability parameters suggests a morphological normalisation of the blood vessels early after the start of the anti-angiogenic therapy, whether given in high or low doses, for both the more angiogenic and the less angiogenic, more infiltrative, tumour phenotypes used in this study.

Functional normalisation of tumour vessels

For the P13 model, blood flow (F) fluctuated over time in the tumours of the control animals (Figure 4(a), top line), with a tendency of mean tumour F to slightly increase over time (Figure 4(b), top line), and a progressive increase of the high F voxels fraction (Figure 4(b), bottom line). In the treated animal groups, tumour F values fluctuated but to a lesser extent compared to controls (Figure 4(a), middle and bottom lines). In comparison to controls, animals treated with high doses of bevacizumab showed a more stable but lower increase in mean tumour F values (fluctuating from +47% to -6% during the observation window) and the fraction of high F values increased slightly (Figure 4(b)). For the animals treated with low doses of bevacizumab, the mean tumour F values kept fluctuating over time and also increased less than for the controls. Mean tumour F ranged from +47% to -39% in comparison to controls (with varying p -values at each time point) during the observation window. The distribution of F values also fluctuated over time with no clear evolutionary trend (Figure 4(b)).

For the P3 control animals (Figure 4(c), top line), both the mean tumour F and the fraction of high tumour F increased over time (Figure 4(d)). For the animals treated with high doses of bevacizumab (Figure 4(c), bottom line), mean tumour F values remained stable over time and was significantly lower than controls (down to 45% of controls on Day 7/8, $p < 0.001$). The fraction of high F values remained constant during the observation window (Figure 4(d)).

Details of mean tumour F for all time points are provided in online Supplementary Tables S1 and S2, together with the ratio of values for bevacizumab treated versus control animals and associated p -values.

We also quantified perfusion parameters in other regions to verify the consistency of the results obtained. Assessment of perfusion parameters in the contralateral brain is challenging because an uncompromised BBB results in limited leakage of the contrast agent and poor SNR with the method used. Quantification results in this region are therefore to be considered with caution. We thus additionally quantified perfusion parameters in the temporalis muscle where the SNR is much higher. Overall F, V_b and PS remained stable and homogeneous over time in the muscle. In comparison to tumours, F and V_b had a similar range of values while PS was higher in the muscles than in the tumours, for both models. All perfusion parameters seemed unaffected by the treatment in the muscles while they were reduced in the treated tumours. In the contralateral brain, F, V_b and PS also remained rather stable and homogeneous over time and were not affected by the treatment. Most parameters were significantly lower in

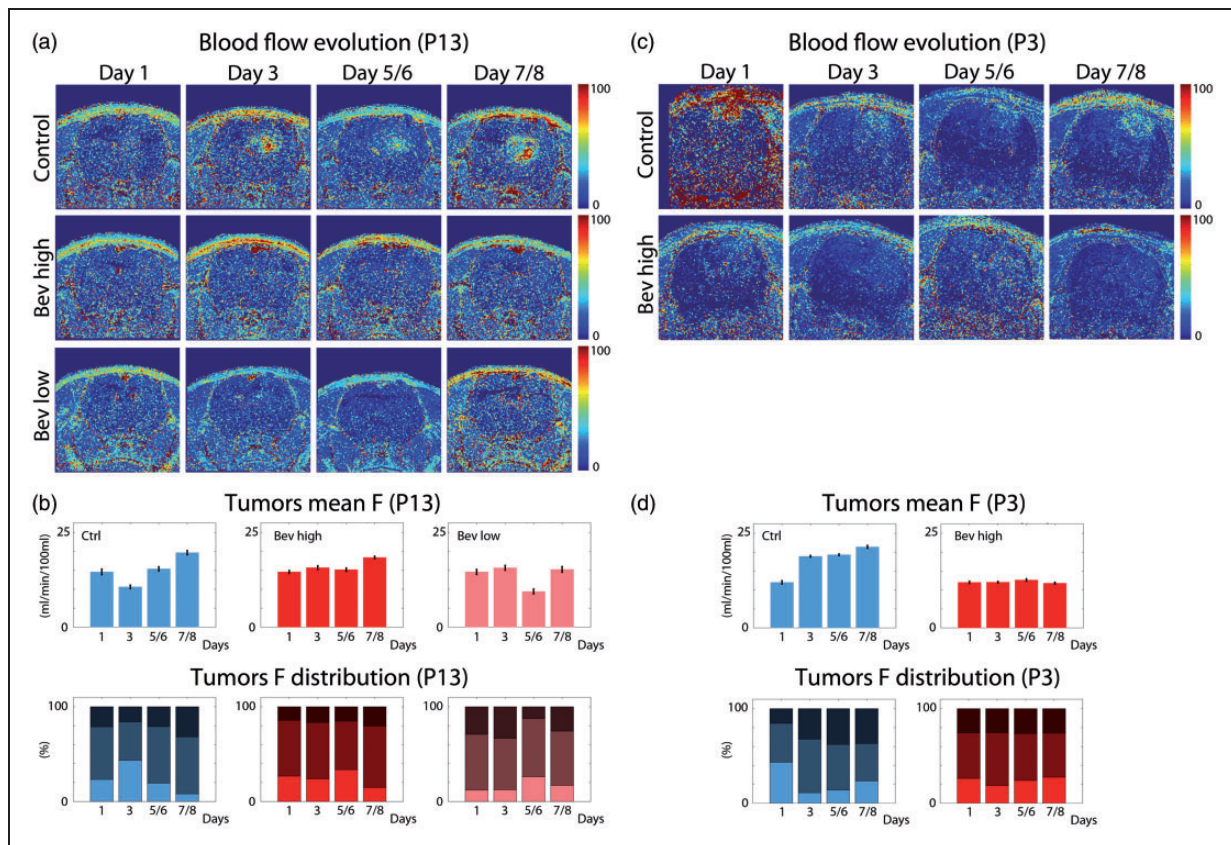


Figure 4. Tumoural blood flow (F) evolution. (a) Illustrative maps of F evolution for animals implanted with the highly angiogenic P13 tumour model, showing one control (top line) and two animals treated with respectively high and low doses of bevacizumab (middle and bottom lines). (b) Quantification of tumour mean F for P13 animals (top line) and histogram analysis of tumour F value distribution (bottom line). In control animals, F is heterogeneous and shows a tendency to increase over time. For animals treated with high or low doses of bevacizumab, F is not improved in comparison to controls and the distribution remains heterogeneous. Similar results can be observed for the less angiogenic more infiltrative P3 model (c and d), suggesting that the morphological normalisation does not result in a functional normalisation with improved and homogenous blood flow. F expressed in absolute values of mL/min/100 mL of tissue. Thresholds for the high, medium and low values (dark, hatched and light blue/red) were defined by the 75% and 25% percentiles of the whole voxels population for the given tumour model. Animals per group: P13 Controls-5, P13 Bev high-5, P13 Bev low-5, P3 Controls-7, P3 Bev high-7. Bev high: 10 mg/kg, Bev low: 5 mg/kg.

the brain than in the tumours. A rigorous comparison would however be hazardous given the somewhat unreliability of parameters estimation in this region with poor SNR.

In summary, the results presented here demonstrate that anti-angiogenic therapy causes a morphological normalisation of blood vessels, evidenced by a statistically significant decrease in tumoural blood volume and vessel permeability, early after the start of the treatment. In this time window however, no functional normalisation was observed in the tumours of the treated animals that would have resulted in an improved blood flow. Instead, tumoural blood flow remains heterogeneous over time, and shows no improvement in comparison to the values observed for the control animals.

Hypoxia

Eight animals implanted with the angiogenic model P13 were used in the PET study, split in controls versus treatment group (bevacizumab high doses). Hypoxia was assessed by ^{18}F -FMISO PET. The signal obtained with this tracer is indeed from hypoxic regions and not healthy tissue since the tracer freely diffuses into all tissues but is only trapped in hypoxic tissue. The optimal timing between injection of the tracer and acquisition was determined from dynamic scans in pilot studies. Longitudinal PET imaging with ^{18}F -FMISO on Day 1, 3, 7 and 12 after treatment start demonstrated a slow increase of the tracer in the control group (Figure 5(a), top line). The uptake of the tracer was strikingly faster in the bevacizumab treated

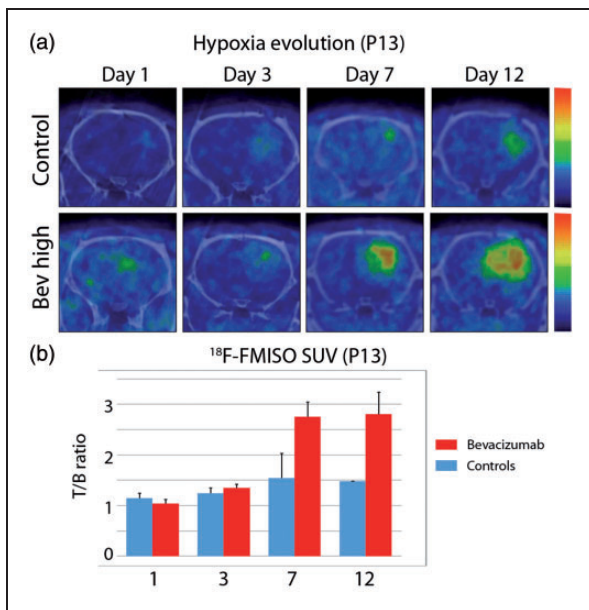


Figure 5. Tumoural hypoxia evolution. (a) Representative images of the longitudinal changes in hypoxia for P13 animals, assessed ¹⁸F-FMISO PET, illustrate the high increased uptake of this tracer following treatment with bevacizumab (high dose) compared to the controls. SUV in arbitrary units. (b) Quantification of the ratio of ¹⁸F-FMISO standard uptake value (SUV) in tumour versus brain confirms these findings. The following numbers of animals were used (Controls: 4, Bev 10 mg/kg: 4). (Scale bars: SEM).

animals (Figure 5(a), bottom line), accelerating after a few days of treatment. Quantification of the tracer uptake (Figure 5(b)), using the tumour-to-brain ratio of the mean SUV, further confirmed the results. The poor oxygenation of the tumour evidenced here after anti-angiogenic therapy is consistent with the poor tumour perfusion and lack of functional normalisation showed by MRI.

Discussion

As several clinical trials have shown no improvement in OS after treatment of GBM with anti-angiogenic therapy, the focus has now shifted to the identification of the mechanisms of treatment resistance and potential bio- and imaging markers for a subgroup of patients that may respond to this therapy.

Traditionally, the proposed mechanism of action of anti-angiogenic treatment was an inhibition of tumour vessel growth, depriving the tumour of nutrients and oxygen.¹² The vascular normalisation hypothesis emerged as an alternative mechanism of action, through which normalised vessels would lead to an improved blood flow and oxygenation of the tumour.^{13,14}

Our group has previously shown that anti-angiogenic treatment with bevacizumab decreases contrast enhancement and blood supply to the tumour in clinically relevant GBM xenografts, increasing hypoxia and invasion.²³ These studies focused on the long-term effects of the therapy, assessed after 3 weeks of treatment with a dose of 10 mg/kg given twice a week. No information was provided then about the short-term effects of the therapy and the possible existence of a window of vascular normalisation early after treatment. In the present work, we addressed this issue by determining dynamic changes in brain tumour perfusion parameters induced by bevacizumab over time, assessed within the first week of treatment. We show that, during this time window, bevacizumab treatment tends to slow down tumour growth, with a more pronounced effect in the purely angiogenic phenotype compared to the mixed angiogenic/infiltrative phenotype. This may reflect an initial treatment response, before adaptation mechanisms occur. We have also previously shown that bevacizumab treatment can lead to an up-regulation of glycolysis, increased lactate accumulation and invasion of tumour cells, possibly highlighting an adaptation mechanism that enables a more infiltrative tumour growth.^{23,24}

Using DCE-MRI perfusion analysis, we show that treatment with both high (10 mg/kg) and low (5 mg/kg) doses of bevacizumab leads to a transient normalisation of the vessel morphology, evidenced by stable or marginally decreased blood volume values, and further confirmed this by immunohistochemistry and histology. The treatment also caused a strong decrease in tumour vessel permeability parameters, evidenced by the permeability surface area product PS and the vessel-to-tissue transfer constant K^{trans} that characterises the transport of contrast-agent across the capillary endothelium.³⁰ At the same time, blood flow did not improve during the time window of the treatment, and remained heterogeneous as evidenced by histogram analysis. This suggests that the morphological normalisation of blood vessels induced by anti-angiogenic therapy was not sufficient to achieve a functional normalisation. The same results were achieved for the two PDX used in the study, which have previously been shown to display purely angiogenic or mixed angiogenic/infiltrative phenotypes.³¹ Taken together, these results suggest that poor tumour perfusion and reduced vessel permeability after anti-angiogenic therapy are likely to impede systemic drug delivery, possibly explaining the disappointing results of combined anti-angiogenic/chemotherapy regimens in the clinic so far.^{5-7,10}

The method used for perfusion analysis dictates to a large extent the interpretation of putative results obtained. Several reports on the effects of

anti-angiogenic therapy in the brain have used DSC-MRI, a data acquisition method commonly used in the clinic. This approach suffers from the limitation that only relative perfusion parameters can be derived. With this method, blood vessels are also assumed to be non-leaky, such that pre-loading of contrast agent is needed to compensate for the leakiness of blood vessels typically observed in tumours. The contribution of changes in the permeability of blood vessels to the observed changes in blood flow is thus difficult to appreciate with this method. DCE-MRI on the other hand, provides absolute perfusion parameter estimates. Most studies conducted with this method have been based on the (extended) Tofts model for pharmacokinetic analysis, which also makes separation of blood flow from vessel permeability parameter impossible. DCE-MRI, based on the ATH pharmacokinetic model as used in the present study, by introducing one additional parameter in the analysis, makes it however possible to evaluate blood flow and vessels permeability separately. This observation is of importance in the context of treatment with anti-angiogenic agents that are known to modulate the permeability of blood vessels. More information on the methodology used for perfusion analysis in this study is provided in the online Supplementary material, together with examples of raw signal curves and a discussion on the robustness of the model.

Finally, whether DSC-MRI or DCE-MRI is used to derive perfusion parameters maps, averaging blood flow values over the whole tumour may also hide a heterogeneous distribution of blood flow values that would still result in poor perfusion of tumour sub-regions. Histogram analysis of tumoural perfusion parameters values makes it possible to capture this heterogeneity dimension into the analysis, providing additional information to parameters values averaged over the whole tumour. Different studies have started to recognise the role of using histogram and image features analysis to account for the spatial heterogeneity of tumours with benefits related to grading, prognosis and assessment of therapy responses.³²

In support of our results, a recent clinical study showed no improvement in tumour oxygenation, despite morphological vessel normalisation, assessed in 71 patients with recurrent GBM treated with bevacizumab.³³ Using ¹⁸F-FMISO PET to assess hypoxia, we observed an increased uptake of the tracer both shortly after treatment initiation, and during the first 12 days of treatment, suggesting that the oxygenation of the tumour was decreased rather than increased during the first week of treatment. Poor tumour oxygenation and hypoxia may also contribute to the poor performance of anti-angiogenic therapy combined with standard radio-chemotherapy regimens, by reducing the

efficacy of the radiotherapy part of standard GBM treatment.

The observation that bevacizumab treatment decreases contrast enhancement by normalising the vessel morphology, despite the lack of benefit in OS, has been considered of high clinical relevance, as it identified the need for revised radiological response criteria.^{8,34,35} Consequently, several studies have tried to identify new radiological biomarkers to predict and measure treatment responses. Schmainda et al.³⁶ assessed changes in relative cerebral blood volume (rCBV) by DSC-MRI and found that an early decrease in rCBV was predictive of improved survival in patients with recurrent GBM treated with bevacizumab. Other studies have shown that pre-treatment rCBV is a potential predictive biomarker for bevacizumab treatment in patients with recurrent GBM.³⁰ It has also been proposed that markers derived from diffusion weighted MRI could be used to predict responses to anti-angiogenic therapies.^{37,38} ADC has been shown to inversely correlate with cellularity in the brain,³⁹ providing a potential indicator of infiltrative tumour progression. Indeed, in the study we performed on the long-term effects of bevacizumab,²³ ADC was reduced in the periphery of the tumours suggesting an increased tumour cell infiltration, which was further confirmed by histology. In the present study, changes in ADC values in the tumour periphery early after the start of the treatment were only marginal, suggesting that the evolution to a more infiltrative progression of the tumour is a process that happens at a later stage, after an initial adaptation to treatment.

The bevacizumab dose has also been discussed in the context of vessel normalisation, as it was proposed that lower doses may be more suitable to normalise vessels. A recent meta-analysis revealed that there are no differences in patient outcome whether treated with 10 mg/kg or 5 mg/kg,⁴⁰ supporting our results in the present study.

In conclusion, in our orthotopic GBM PDX models, a transient functional window of normalisation of vessels could not be identified following anti-angiogenic therapy. Blood supply to the tumour remains heterogeneous and hypoxia increases while the permeability of tumoural blood vessels is reduced, shedding a causal light on the disappointing results of clinical trials where anti-angiogenic therapies have been combined with systemic delivery of chemotherapeutic agents. This study also shows that MRI combined to PET gives valuable insight into responses to anti-angiogenic therapies, by assessing physiological changes in the tumour in addition to the classically used morphological responses. Such a multimodal imaging approach thus holds a great potential for assessing responses to therapy in both pre-clinical and clinical research.

Funding

The author(s) disclosed receipt of the following financial support for the research, authorship, and/or publication of this article: This work was supported by the Kristian Gerhard Jebsen Foundation, The Research Council of Norway, Stiftelsen Kristian Gerhard Jebsen, Helse Vest, Haukeland University Hospital, the Bergen Medical Research Foundation, the Czech Science Foundation (16-13830S) and the Luxembourg Institute of Health.

Acknowledgements

The MR- and PET-imaging was performed at the Molecular Imaging Center (MIC) and was thus supported by the Department of Biomedicine and the Faculty of Medicine and Dentistry, at the University of Bergen, and its partners. We thank the patients for consenting to donate the tumour tissue and the Department of Neurosurgery at Haukeland University Hospital for the collaboration. We also thank Tina Pavlin for the fruitful discussion on MR protocols optimisation. N Obad was supported by a PhD fellowship from the Norwegian Cancer Society.

Declaration of conflicting interests

The author(s) declared no potential conflicts of interest with respect to the research, authorship, and/or publication of this article.

Access to research materials

Researchers interested in data, samples or models used in the present study are invited to contact the corresponding author.

Authors' contributions

NO, SPN, RB and OK designed the study. NO, HE, POS, CBR, RJ, TT and OK designed the instrumentation, collected and analysed the data. NO drafted the manuscript. NO, HE, MLJ, RJ, TT, SPN, RB and OK revised the manuscript and approved the final version.

Supplementary material

Supplementary material for this paper can be found at the journal website: <http://journals.sagepub.com/home/jcb>

References

- Louis DN, Ohgaki H, Wiestler OD, et al. The 2007 WHO classification of tumours of the central nervous system. *Acta Neuropathol* 2007; 114: 97–109.
- Vredenburg JJ, Desjardins A, Herndon JE 2nd, et al. Phase II trial of bevacizumab and irinotecan in recurrent malignant glioma. *Clin Cancer Res* 2007; 13: 1253–1259.
- Kreisl TN, Kim L, Moore K, et al. Phase II trial of single-agent bevacizumab followed by bevacizumab plus irinotecan at tumor progression in recurrent glioblastoma. *J Clin Oncol* 2009; 27: 740–745.
- Macdonald DR, Cascino TL, Schold SC Jr, et al. Response criteria for phase II studies of supratentorial malignant glioma. *J Clin Oncol* 1990; 8: 1277–1280.
- Friedman HS, Prados MD, Wen PY, et al. Bevacizumab alone and in combination with irinotecan in recurrent glioblastoma. *J Clin Oncol* 2009; 27: 4733–4740.
- Chinot OL, Wick W, Mason W, et al. Bevacizumab plus radiotherapy-temozolomide for newly diagnosed glioblastoma. *N Engl J Med* 2014; 370: 709–722.
- Gilbert MR, Dignam JJ, Armstrong TS, et al. A randomized trial of bevacizumab for newly diagnosed glioblastoma. *N Engl J Med* 2014; 370: 699–708.
- van den Bent MJ, Vogelbaum MA, Wen PY, et al. End point assessment in gliomas: novel treatments limit usefulness of classical Macdonald's criteria. *J Clin Oncol* 2009; 27: 2905–2908.
- Reardon DA, Desjardins A, Peters KB, et al. Phase 2 study of carboplatin, irinotecan, and bevacizumab for recurrent glioblastoma after progression on bevacizumab therapy. *Cancer* 2011; 117: 5351–5358.
- Taal W, Oosterkamp HM, Walenkamp AM, et al. Single-agent bevacizumab or lomustine versus a combination of bevacizumab plus lomustine in patients with recurrent glioblastoma (BELOB trial): a randomised controlled phase 2 trial. *Lancet Oncol* 2014; 15: 943–953.
- Wick W. Phase III trial exploring the combination of bevacizumab and lomustine in patients with first recurrence of a glioblastoma: the EORTC 26101 trial. *Neuro Oncol* 2015; 17(suppl-5): v1.
- Folkman J. Tumor angiogenesis: therapeutic implications. *N Engl J Med* 1971; 285: 1182–1186.
- Jain RK. Normalizing tumor vasculature with anti-angiogenic therapy: a new paradigm for combination therapy. *Nat Med* 2001; 7: 987–989.
- Carmeliet P and Jain RK. Principles and mechanisms of vessel normalization for cancer and other angiogenic diseases. *Nat Rev Drug Discov* 2011; 10: 417–427.
- Winkler F, Kozin SV, Tong RT, et al. Kinetics of vascular normalization by VEGFR2 blockade governs brain tumor response to radiation: role of oxygenation, angiotensin-1, and matrix metalloproteinases. *Cancer Cell* 2004; 6: 553–563.
- Tong RT, Boucher Y, Kozin SV, et al. Vascular normalization by vascular endothelial growth factor receptor 2 blockade induces a pressure gradient across the vasculature and improves drug penetration in tumors. *Cancer Res* 2004; 64: 3731–3736.
- McGee MC, Hamner JB, Williams RF, et al. Improved intratumoral oxygenation through vascular normalization increases glioma sensitivity to ionizing radiation. *Int J Radiat Oncol Biol Phys* 2010; 76: 1537–1545.
- Claes A, Wesseling P, Jeuken J, et al. Antiangiogenic compounds interfere with chemotherapy of brain tumors due to vessel normalization. *Mol Cancer Ther* 2008; 7: 71–78.
- Arjaans M, Oude Munnink TH, Oosting SF, et al. Bevacizumab-induced normalization of blood vessels in tumors hampers antibody uptake. *Cancer Res* 2013; 73: 3347–3355.
- Sorensen AG, Emblem KE, Polaskova P, et al. Increased survival of glioblastoma patients who respond to antiangiogenic therapy with elevated blood perfusion. *Cancer Res* 2012; 72: 402–407.

21. Batchelor TT, Sorensen AG, di Tomaso E, et al. AZD2171, a pan-VEGF receptor tyrosine kinase inhibitor, normalizes tumor vasculature and alleviates edema in glioblastoma patients. *Cancer Cell* 2007; 11: 83–95.
22. Batchelor TT, Gerstner ER, Emblem KE, et al. Improved tumor oxygenation and survival in glioblastoma patients who show increased blood perfusion after cediranib and chemoradiation. *Proc Natl Acad Sci U S A* 2013; 110: 19059–19064.
23. Keunen O, Johansson M, Oudin A, et al. Anti-VEGF treatment reduces blood supply and increases tumor cell invasion in glioblastoma. *Proc Natl Acad Sci U S A* 2011; 108: 3749–3754.
24. Fack F, Espedal H, Keunen O, et al. Bevacizumab treatment induces metabolic adaptation toward anaerobic metabolism in glioblastomas. *Acta Neuropathol* 2015; 129: 115–131.
25. Bjerkvig R, Tonnesen A, Laerum OD, et al. Multicellular tumor spheroids from human gliomas maintained in organ culture. *J Neurosurg* 1990; 72: 463–475.
26. Wang J, Miletic H, Sakariassen PO, et al. A reproducible brain tumour model established from human glioblastoma biopsies. *BMC Cancer* 2009; 9: 465.
27. Stieber D, Golebiewska A, Evers L, et al. Glioblastomas are composed of genetically divergent clones with distinct tumorigenic potential and variable stem cell-associated phenotypes. *Acta Neuropathol* 2014; 127: 203–219.
28. Sakariassen PO, Prestegarden L, Wang J, et al. Angiogenesis-independent tumor growth mediated by stem-like cancer cells. *Proc Natl Acad Sci U S A* 2006; 103: 16466–16471.
29. Taxt T, Jirik R, Rygh CB, et al. Single-channel blind estimation of arterial input function and tissue impulse response in DCE-MRI. *IEEE Trans Biomed Eng* 2012; 59: 1012–1021.
30. Kickingreder P, Wiestler B, Graf M, et al. Evaluation of dynamic contrast-enhanced MRI derived microvascular permeability in recurrent glioblastoma treated with bevacizumab. *J Neurooncol* 2015; 121: 373–380.
31. Bougnaud S, Golebiewska A, Oudin A, et al. Molecular crosstalk between tumour and brain parenchyma instructs histopathological features in glioblastoma. *Oncotarget* 2016; 7: 31955–31971.
32. O'Connor JP, Rose CJ, Waterton JC, et al. Imaging intratumor heterogeneity: role in therapy response, resistance, and clinical outcome. *Clin Cancer Res* 2015; 21: 249–257.
33. Bonekamp D, Mouridsen K, Radbruch A, et al. Assessment of tumor oxygenation and its impact on treatment response in bevacizumab-treated recurrent glioblastoma. *J Cereb Blood Flow Metab* 2016; 37(2): 485–494.
34. Wen PY, Macdonald DR, Reardon DA, et al. Updated response assessment criteria for high-grade gliomas: response assessment in neuro-oncology working group. *J Clin Oncol* 2010; 28: 1963–1972.
35. Sorensen AG, Batchelor TT, Wen PY, et al. Response criteria for glioma. *Nat Clin Pract Oncol* 2008; 5: 634–644.
36. Schmainda KM, Zhang Z, Prah M, et al. Dynamic susceptibility contrast MRI measures of relative cerebral blood volume as a prognostic marker for overall survival in recurrent glioblastoma: results from the ACRIN 6677/RTOG 0625 multicenter trial. *Neuro Oncol* 2015; 17: 1148–1156.
37. Pope WB, Kim HJ, Huo J, et al. Recurrent glioblastoma multiforme: ADC histogram analysis predicts response to bevacizumab treatment. *Radiology* 2009; 252: 182–189.
38. Ellingson BM, Cloughesy TF, Lai A, et al. Graded functional diffusion map-defined characteristics of apparent diffusion coefficients predict overall survival in recurrent glioblastoma treated with bevacizumab. *Neuro Oncol* 2011; 13: 1151–1161.
39. Chen L, Liu M, Bao J, et al. The correlation between apparent diffusion coefficient and tumor cellularity in patients: a meta-analysis. *PLoS One* 2013; 8: e79008.
40. Wong ET, Gautam S, Malchow C, et al. Bevacizumab for recurrent glioblastoma multiforme: a meta-analysis. *J Natl Compr Canc Netw* 2011; 9: 403–407.

4.2.4 Paper VI

M. Bartoš, P. Rajmic, M. Šorel, M. Mangová, O. Keunen, R. Jiřík, Spatially regularized estimation of the tissue homogeneity model parameters in DCE-MRI using proximal minimization, *Magn. Reson. Med.* 82 (2019) 2257–2272.

<https://doi.org/10.1002/mrm.27874>.

(IF 3.635)

Author's contribution:

- co-author of the main idea
- setup of the clinical-data acquisition method
- design and implementation of synthetic-data generation
- providing consultations on data processing and evaluation methodology
- paper co-writing

Spatially regularized estimation of the tissue homogeneity model parameters in DCE-MRI using proximal minimization

Michal Bartoš¹  | Pavel Rajmic² | Michal Šorel¹ | Marie Mangová² |
Olivier Keunen³  | Radovan Jiřík⁴

¹The Czech Academy of Sciences, Institute of Information Theory and Automation, Prague, Czech Republic

²SPLab, Department of Telecommunications, FEEC, Brno University of Technology, Brno, Czech Republic

³Norlux Neuro-Oncology Laboratory, Department of Oncology, Luxembourg Institute of Health, Luxembourg, Luxembourg

⁴The Czech Academy of Sciences, Institute of Scientific Instruments, Brno, Czech Republic

Correspondence

Michal Bartoš, ÚTIA AV ČR, Pod
Vodárenskou věží 4, CZ-182 08 Prague,
Czech Republic.
Email: bartos@utia.cas.cz

Funding information

Akademie Věd České Republiky, Grant/
Award Number: MSM100751802;
Ministerstvo Školství, Mládeže a
Tělovýchovy, Grant/Award Number:
CZ.02.1.01/0.0/0.0/16_013/0001775,
CZ.1.05/2.1.00/01.0017, LO1212 and
LO1401; Grantová Agentura České
Republiky, Grant/Award Number: GA16-
13830S

Purpose: The Tofts and the extended Tofts models are the pharmacokinetic models commonly used in dynamic contrast-enhanced MRI (DCE-MRI) perfusion analysis, although they do not provide two important biological markers, namely, the plasma flow and the permeability-surface area product. Estimates of such markers are possible using advanced pharmacokinetic models describing the vascular distribution phase, such as the tissue homogeneity model. However, the disadvantage of the advanced models lies in biased and uncertain estimates, especially when the estimates are computed voxelwise. The goal of this work is to improve the reliability of the estimates by including information from neighboring voxels.

Theory and Methods: Information from the neighboring voxels is incorporated in the estimation process through spatial regularization in the form of total variation. The spatial regularization is applied on five maps of perfusion parameters estimated using the tissue homogeneity model. Since the total variation is not differentiable, two proximal techniques of convex optimization are used to solve the problem numerically.

Results: The proposed algorithm helps to reduce noise in the estimated perfusion-parameter maps together with improving accuracy of the estimates. These conclusions are proved using a numerical phantom. In addition, experiments on real data show improved spatial consistency and readability of perfusion maps without considerable lowering of the quality of fit.

Conclusion: The reliability of the DCE-MRI perfusion analysis using the tissue homogeneity model can be improved by employing spatial regularization. The proposed utilization of modern optimization techniques implies only slightly higher computational costs compared to the standard approach without spatial regularization.

KEYWORDS

DCE-MRI, perfusion parameter estimation, proximal methods, spatial regularization, tissue homogeneity model, total variation

1 | INTRODUCTION

Dynamic contrast-enhanced magnetic resonance imaging (DCE-MRI) is becoming an established tool in obtaining information about tissue perfusion and capillary permeability. The trend today is to represent such information as a set of images/maps of physiological parameters related to the perfusion, for example, blood plasma flow, permeability surface area product, and plasma or extracellular-extravascular-space volumes. The type and number of the parameters represented by perfusion maps depend on the pharmacokinetic model used. To estimate the perfusion parameters, the respective model is typically fitted to the concentration-time curve of each voxel. These curves are calculated from a T1-weighted MR image sequence recorded before, during, and after administration of a contrast agent bolus.¹

The problem of fitting the concentration-time curves is unfortunately a nontrivial optimization problem due to the model nonlinearity, insufficient temporal sampling, poor signal-to-noise ratio, and uncertainties in the model and the measurement. This results in bias and uncertainty in the estimates or even wrong estimates because of the presence of local minima. The estimation problems are often categorized as a priori structural identifiability and a posteriori identifiability. The a priori identifiability is influenced by the nonlinear model structure itself²⁻⁴ and by the experimental design – sampling and duration of the experiment.⁵⁻¹⁰ The a posteriori identifiability includes the errors in the measurement – the signal-to-noise ratio, arterial input function errors, and the inaccuracy of conversion from the T1-weighted image sequence to the concentration-time curves.¹⁰⁻¹⁴ Additionally, the local minima may also be caused by an improper discretization of the model.¹⁵⁻¹⁷

One way to reduce the uncertainties caused by errors is an incorporation of a spatial prior into the modeling. Such a means of regularization is based on the assumption that neighboring voxels in the parameter maps belonging to the same tissue should have similar values: that is, the perfusion maps should be piecewise smooth. Although using spatial priors is usual in image reconstructions including MRI, they have been used only occasionally in the DCE-MRI analysis. To the authors' knowledge, it has been used by only a few groups.¹⁸⁻²⁴ The priors in the mentioned papers are based on image gradients of perfusion maps except for²⁴ using a wavelet transform and²³ using the difference of the image from its denoised variant. The denoising is guided by the input DCE-MRI sequence. All three mentioned transformations generate so-called feature images on which a metric is computed to express, by one value, the spatial consistency of the voxels. The metrics used range from the smoothing ℓ^2 norm^{18,20,22,23} to an approximation of the edge-preserving ℓ^1 norm.^{22,24} The minimization of these spatial-regularization criterial functions is problematic because the voxels cannot be processed independently as in the case without the regularization.

Compared to^{22,24} where an approximate ℓ^1 norm was used, in the present paper we derive a solution to the strict sparsity-inducing ℓ^1 norm regularizer operating on image gradients, that is, the total variation regularization. This reduces smoothing of edges between different tissues. Since the strict ℓ^1 norm is not differentiable, we use proximal algorithms²⁵⁻²⁷ to find the numerical solution. They are based on alternating minimization of the data and regularization terms and are the state of the art for solving image-processing problems such as image denoising, deconvolution, or MRI reconstruction. However, the adaptation of these algorithms to DCE-MRI is not straightforward, because the data formation model in DCE-MRI is not linear. Motivated by good performance of the Levenberg-Marquardt (LM) method^{28,29} in DCE-MRI perfusion parameter estimation,^{30,31} we decided to use the proximal Newton method²⁶ adapted to employ the LM keeping good convergence and low computational costs. The derived algorithm iteratively performs one step of the LM method in each voxel followed by an image-denoising step in all parameter maps.

All the preceding spatial regularization approaches are based on the Tofts³² or extended Tofts³³ model. On the contrary, this paper proposes a spatial regularization for DCE-MRI based on the tissue homogeneity (TH) pharmacokinetic model.^{16,34} Use of the TH model provides estimates of additional perfusion parameters such as the plasma flow and the permeability surface area product, as opposed to the use of the Tofts models. But its use is not widespread because of its complexity (number of parameters, nonlinearity, a posteriori identifiability). In this paper we show that spatial regularization stabilizes the estimation procedure and makes use of such more complicated pharmacokinetic models feasible.

2 | THEORY

2.1 | Problem description

The goal of the DCE-MRI analysis is to estimate perfusion parameters from a sequence of N images capturing the distribution of the administered contrast agent bolus in time. The image intensity values are related to the actual concentration of the contrast agent in the voxel. The voxels from a region of interest are extracted and rearranged to form a matrix \mathbf{S} of size $I \times N$ (number of selected voxels \times number of observations in time). The values in \mathbf{S} can be described by the model

$$\begin{aligned} S_{i,n} &= \bar{S}_{i,n} + \epsilon_{i,n}, \quad i = 0, \dots, I-1, n = 0, \dots, N-1; \\ \epsilon_{i,n} &\sim \text{Rice}(\bar{S}_{i,n}, \sigma_R), \end{aligned} \quad (1)$$

where $S_{i,n}$ is a single measured element of \mathbf{S} (i^{th} voxel, n^{th} time sample) and $\bar{S}_{i,n}$ is the true value, not distorted by the noise $\epsilon_{i,n}$. The noise follows the signal-dependent Rice distribution,³⁵

assuming Cartesian imaging for simplicity. Major mathematical notations used throughout the paper can be found in Table 1.

The intensity values \mathbf{S} are transformed to represent concentration of the contrast agent \mathbf{S}^ϕ :

$$S_{i,n}^\phi = \phi_i(S_{i,n}) \approx \bar{S}_{i,n}^\phi + \epsilon_{i,n}^\phi, \quad \forall i, n \quad (2)$$

where ϕ_i is a nonlinear transformation function derived from the precontrast measurements (e.g. with several different flip angles);¹ thus the additive-noise model is not exact. The values $\bar{S}_{i,n}^\phi$ can be modeled as samples of a nonlinear pharmacokinetic model $c(n\Delta t, p_{i,\cdot})$. It describes the contrast agent concentration within voxel i in time $t = n\Delta t$, where Δt is the sampling interval, and it is parametrized by the vector $p_{i,\cdot}$ of length J , consisting of the perfusion parameters. A consequence of the transformation ϕ_i is that the noise $\epsilon_{i,n}^\phi$ now follows a complicated distribution. Thus, it is usually approximated by normal distribution; that is, $\epsilon_{i,n}^\phi \sim N(0, \sigma_i)$, $\forall n$, σ_i is noise standard deviation in voxel i , which neglects variations in time and asymmetry [in the case of low signal-to-noise ratio (SNR < 10 dB)^{36,37} or for strongly nonlinear ϕ_i].

The goal of the DCE-MRI analysis is to estimate parameters $p_{i,\cdot}$ of the pharmacokinetic model c by fitting it to the curve $S_{i,\cdot}^\phi$ in each voxel i . Let \mathbf{p} denote the matrix gathering the perfusion parameters such that $p_{i,\cdot}$ is the i^{th} row of \mathbf{p} . The maximum a posteriori probability estimate $\hat{\mathbf{p}}$ of the perfusion parameters \mathbf{p} of the size $I \times J$ (I – number of voxels, J – number of perfusion parameters), assuming Gaussian noise, can be formulated as:

$$\begin{aligned} \hat{\mathbf{p}} &= \arg \min_{\mathbf{p} \in P^I} \sum_{i=0}^{I-1} \sigma_i^{-2} \sum_{n=0}^{N-1} \left(S_{i,n}^\phi - c(n\Delta t, p_{i,\cdot}) \right)^2 + \psi(\mathbf{p}) \\ &= \arg \min_{\mathbf{p} \in P^I} \sum_{i=0}^{I-1} f(p_{i,\cdot}) + \psi(\mathbf{p}) \end{aligned} \quad (3)$$

where P is the feasible domain of the perfusion parameters. The regularization term $\psi(\mathbf{p})$ describes the a priori knowledge about the problem and the first term, that is, the data term, describes the fidelity of the fit. If no prior information is known or available in a suitable form, ψ is substituted by a zero function making the optimization problem to reduce to the standard nonlinear least squares problem solvable by minimizing $f(p_{i,\cdot})$ independently for each voxel.^{11,16}

2.2 | Pharmacokinetic model

The core of the functional in Equation (3) is a pharmacokinetic model c defined in general by a set of differential equations. This model can be transformed to the Laplace domain, where it has the form of multiplication of the Laplace spectra of two functions: the arterial input function (AIF) describing concentration of the contrast agent in voxels' arterial input and the impulse residue function of the tissue voxel. If both functions have a closed-form expression in the time domain, the model can also be represented in the time domain, either as a convolution integral or even better in a closed form.¹⁵ If the closed forms are not available, as in our case of the TH model, the multiplication in the Laplace domain can be transformed to the Fourier domain.¹⁶ In a discrete setting, the Laplace operator s is substituted by the sampling at discrete angular frequencies $j\Delta\omega$, where $\Delta\omega$ is the sampling angular frequency, \mathbf{w} is a vector of indices, and the model is evaluated as:

$$c(n\Delta t, p_{i,\cdot}) = \text{DFT}^{-1} \left\{ C_a(j\Delta\omega) H(j\Delta\omega, p_{i,\cdot}) \right\} \quad (4)$$

where the multiplication of the Fourier spectra of the AIF and impulse residue function is elementwise and DFT^{-1} is the inverse discrete Fourier transform. The symbol \mathbf{n} represents a vector of time indices meaning that the discrete Fourier transform returns N values. The vector of frequency indices is $\mathbf{w} = (0, 1, \dots, (N' - \text{mod}(N', 2)) / 2)$, where mod is the modulo operation and N' is the number of time-domain

TABLE 1 Mathematical notations

Symbol	Description
\mathbf{A}, \mathbf{p}	Matrices
\mathbf{x}	Vector
x_j	The j^{th} element of \mathbf{x}
A_{ij}	One element of \mathbf{A} in the i^{th} row and the j^{th} column
$p_{i,\cdot}$	The i^{th} row of \mathbf{p}
$p_{\cdot,j}$	The j^{th} column of \mathbf{p}
\mathbf{H}_i	The i^{th} matrix from the array of matrices
\mathbf{y}^k	Vector \mathbf{y} in the k^{th} iteration
θ	Constant
$\hat{\mathbf{p}}, \mathbf{p}^*$	Estimate, ground truth of \mathbf{p}
$\ \cdot\ $	Magnitude of a vector field or a number
$\ \cdot\ _1$	ℓ^1 norm

samples that guarantee avoidance of the time-domain aliasing; see Refs. 16 and 38. The sampling angular frequency is then $\Delta\omega = 2\pi/N'\Delta t$. To use the defined representations of the functions, the DFT^{-1} includes complex conjugate symmetrization and final truncation to N samples. Additionally, we assume that the AIF is represented as a vector of time-domain samples $c_a(\mathbf{n}\Delta t)$ that are transformed to the Fourier domain: $C_a(j\Delta\omega) = \text{DFT}\{c_a(\mathbf{n}\Delta t)\}$ as in Ref. 16 with zero-padding to N' and the truncation to the half-spectrum. The impulse residue function is represented by the TH model in the Laplace domain, $H_{\text{TH}}(s, \mathbf{p})$. In comparison with Refs. 16, 39, the parametrization is modified and a bolus arrival time is added, $\mathbf{p} = \{F_p, T_c, T_e, \alpha, \tau\}$, see Table 2 for descriptions. An additional modification is that we use a windowed version of the TH model, $H_{\text{TH}}^w(s, \mathbf{p}, t_w)$. This speeds up the evaluation keeping the number of samples low, $N' = 3N$, limited by the time-domain aliasing; see Ref. 38 for more details. The TH model is evaluated as:

$$H_{\text{TH}}(s, \mathbf{p}) = \frac{F_p(1 - e^{-(\alpha + T_c s)})(T_c + \alpha T_e + T_c T_e s)(\alpha + T_c s)}{\alpha(1 - e^{-(\alpha + T_c s)}) + s(T_c + \alpha T_e + T_c T_e s)(\alpha + T_c s)} \quad (5)$$

$$H_{\text{TH}}^w(s, \mathbf{p}, t_w) = H_{\text{TH}}(s, \mathbf{p}) - F_p E e^{-k_{\text{ep}}(t_w - \tau - T_c)} \frac{e^{-s t_w}}{s + k_{\text{ep}}}$$

where $E = 1 - e^{-\alpha}$, $k_{\text{ep}} = E / (T_e \alpha)$ and $t_w = (N - 1) \Delta t$.

2.3 | Regularization function

The stabilizing factor in Equation [3] is the regularization function $\psi(\mathbf{p})$. Here, we describe the prior knowledge in the form of an image prior taking spatial relations of the voxels into account. The image prior in the form of a sparsifying ℓ^1 norm of a linearly transformed image is a widely used option in the image and signal processing community.^{27,40,41}

The transformation can be, for example, a wavelet transform or image gradients. It is in the form of a linear operator \mathbf{A} transforming the vector of parameters, $p_{\cdot,j}$, of the length I to a domain, where most of the values are close to zero. This so-called sparsifying transform \mathbf{A} can be represented by a set of V matrices \mathbf{A}_v , $v \in \{1, \dots, V\}$ each corresponding to one sparse feature. We suppose the case of the image gradients; that is, there are two matrices $\mathbf{A} = (\nabla_r, \nabla_c)$ representing forward differences with respect to rows and columns and taking into account the spatial position of the voxels.⁴² Applying this operator, a vector field is obtained. Before the application of ℓ^1 norm usually a magnitude of this vector field is computed (represented by $|\cdot|$). This is repeated for J perfusion parameters leading to:

$$\psi(\mathbf{p}) = \sum_{j=0}^{J-1} \gamma_j \left\| \|\mathbf{A} p_{\cdot,j}\|_1 \right\|_1 = \sum_{j=0}^{J-1} \gamma_j \sum_{i=0}^{I-1} \sqrt{\sum_v |\mathbf{A}_v p_{\cdot,j}|^2} \quad (6)$$

$$= \sum_{j=0}^{J-1} \gamma_j \sum_{i=0}^{I-1} \sqrt{(\nabla_r p_{\cdot,j})^2 + (\nabla_c p_{\cdot,j})^2}$$

where γ_j is a regularization weight for particular parameter $p_{\cdot,j}$. The magnitude in the middle term reduces to elementwise absolute value, and the square and the square root act elementwise. The last term represents the discrete isotropic total variation regularization used in this paper.

2.4 | Optimization methods

For the spatially regularized estimation of the perfusion maps, we use two proximal optimization methods, the proximal Newton method²⁶ and the primal-dual algorithm.²⁷ Both methods are applicable to the class of problems of the form

TABLE 2 Definitions of perfusion parameters and related quantities

Perfusion parameter	Description	Units	Starting point, p^0	Constraints, P	Relative weight, γ'
F_p	Plasma flow ^a	mL/min/mL	1	$[10^{-3}, 10^2]$	0.025
T_c	Mean capillary transit time	min	0.1	$[\Delta t, 3]$	0.283
T_e	Mean transit time of EES ^b	min	2.5	$[\Delta t, 10^2]$	0.024
α	$= PS/F_p = -\ln(1 - E)$	–	0.4	$[10^{-4}, 3]$	0.103
τ	Bolus arrival time	min	0	$[-0.5, 1]$	0.565
PS	Permeability-surface area product	mL/min/mL			
E	Extraction fraction	–			
v_p	Plasma volume	mL/mL			
v_e	EES ^b volume	mL/mL			
k_{ep}	EES ^b -to-plasma rate constant	1/min			
K^{trans}	Volume transfer constant	mL/min/mL			

^aValues take the reweighting by α_{TRF} , α_{AIF} into account.

^bEES, Extravascular extracellular space.

$$\arg \min_{\mathbf{x}} d(\mathbf{x}) + r(\mathbf{A}\mathbf{x}) \quad (7)$$

where d , r are convex lower-semicontinuous, not necessarily differentiable functions. In our case, d and r represent the data and regularization terms, respectively. \mathbf{A} is an arbitrary linear operator possibly in matrix form.

2.4.1 | Proximal Newton method

The proximal Newton method²⁶ is a variant of the Newton method^{28,29} for nondifferentiable functions applicable for functions in the form of Equation [7] if d is twice differentiable. Similarly to the Newton method, it exploits the Hessian of d , which improves the convergence of the algorithm. Since r is typically not differentiable, its gradient is replaced by the so-called proximal operator, a useful tool proximal methods use to treat nondifferentiable functions.

The proximal operator of an arbitrary convex function $f(\mathbf{x})$ can be defined⁴³ as:

$$\text{prox}_{r(\mathbf{A}\cdot)}^{\mathbf{A}}(\mathbf{y}) = \arg \min_{\mathbf{x}} (f(\mathbf{x}) + (\mathbf{x} - \mathbf{y})^{\top} \mathbf{\Lambda}^{-1} (\mathbf{x} - \mathbf{y})) \quad (8)$$

where \mathbf{y} is a point at which the proximal operator is evaluated and $\mathbf{\Lambda}$ is called the scaling matrix. Note that in the majority of the literature, $\mathbf{\Lambda}$ is the identity matrix. In the proximal Newton method, $\mathbf{\Lambda}$ is necessary to compensate for the scaling implied by the Hessian in the Newton step.

The proximal Newton method iteratively performs two steps until convergence:

1. Do a Newton step in d , where ∇d and \mathbf{H} are the gradient and Hessian of d :

$$\mathbf{y}^k = \mathbf{x}^k - \mathbf{H}^{-1} \nabla d(\mathbf{x}^k) \quad (9)$$

2. Evaluate the proximal operator of $r(\mathbf{A}\mathbf{x})$ at the point \mathbf{y}^k scaled by \mathbf{H}^{-1} :

$$\mathbf{x}^{k+1} = \text{prox}_{r(\mathbf{A}\cdot)}^{\mathbf{H}^{-1}}(\mathbf{y}^k) = \arg \min_{\mathbf{x}} \left(r(\mathbf{A}\mathbf{x}) + \frac{1}{2} (\mathbf{x} - \mathbf{y}^k)^{\top} \mathbf{H} (\mathbf{x} - \mathbf{y}^k) \right) \quad (10)$$

Since this subproblem 2) is solved in every iteration, it must be done efficiently. It resembles Equation [7], but d is now much simpler – a quadratic function. This case can be computed again by a proximal method, such as the nested primal-dual algorithm²⁷ described in Section 2.4.2. Let us note that in the case of a nonconvex d , as in our case, the proximal Newton method converges to the closest minimum,^{44,45} if the minimization steps are not too large.

2.4.2 | Primal-dual algorithm

Another proximal method for solving problems in the form of Equation [7] is the primal-dual algorithm,²⁷ especially suitable for quadratic d . The algorithm is initialized by choosing constants influencing the convergence: $\tau, \sigma > 0, \theta \in [0, 1]$, setting starting-point variables: $\mathbf{u}^0 = \mathbf{y}^k, \mathbf{v}^0 = \mathbf{A}\mathbf{u}^0, \mathbf{x}^0 = \mathbf{u}^0$, and proceeds by iterative updates until convergence:²⁷

$$\begin{aligned} \text{a) } \mathbf{v}^{n+1} &= \text{prox}_{r^*}^{\sigma}(\mathbf{v}^n + \sigma \mathbf{A}\mathbf{x}^n) \\ \text{b) } \mathbf{u}^{n+1} &= \text{prox}_d^{\tau}(\mathbf{u}^n - \tau \mathbf{A}^* \mathbf{v}^{n+1}) \\ \text{c) } \mathbf{x}^{n+1} &= \mathbf{u}^{n+1} + \theta (\mathbf{u}^{n+1} - \mathbf{u}^n) \\ \text{d) Repeat a)–c) until convergence} \end{aligned} \quad (11)$$

Here, r^* is the convex conjugate²⁵ of r and \mathbf{A}^* is the adjoint operator to \mathbf{A} ; see Equation [22] for details in the case of the total variation.

2.5 | Estimation of perfusion parameters

The final goal is to estimate perfusion parameter maps, that is, to minimize Equation [3] using total variation regularization in Equation [6]:

$$\hat{\mathbf{p}} = \arg \min_{\mathbf{p} \in \mathcal{P}^I} \sum_{i=0}^{I-1} f(p_{i,\cdot}) + \sum_{j=0}^{J-1} \gamma_j \left\| \mathbf{A} \mathbf{p}_{\cdot,j} \right\|_1 \quad (12)$$

This problem is solved by the proximal Newton method (Section 2.4.1). Unfortunately, the computation of the Hessian matrices \mathbf{H}_i of the data term $f(p_{i,\cdot})$ for each curve i is computationally demanding and their inversions are unstable. For this reason we replace them by the Levenberg-Marquardt modification²⁹: $\mathbf{H}_i = 1/\lambda_i^k \mathbf{I} + 2\mathbf{J}_i^{\top} \sigma_i^{-2} \mathbf{J}_i$, where λ_i^k is related to the step length in the iteration k and \mathbf{J}_i is the Jacobian matrix of $c(\mathbf{n}T_s, \hat{\mathbf{p}}_{i,\cdot}^k)$ of the size $N \times J$. Then, the proximal Newton method has the form:

1. Do a Newton (Levenberg-Marquardt) step [9] in terms of $f(\hat{\mathbf{p}}_{i,\cdot}^k)$ for each voxel:

$$\begin{aligned} \mathbf{y}_{i,\cdot}^k &= \hat{\mathbf{p}}_{i,\cdot}^k - \mathbf{H}_i^{-1} \nabla f(\hat{\mathbf{p}}_{i,\cdot}^k) \\ &\cong \hat{\mathbf{p}}_{i,\cdot}^k - \lambda_i^k (\mathbf{I} + \lambda_i^k 2\mathbf{J}_i^{\top} \sigma_i^{-2} \mathbf{J}_i)^{-1} \nabla f(\hat{\mathbf{p}}_{i,\cdot}^k), \forall i, \end{aligned} \quad (13)$$

- where λ_i^k is estimated by the LM scheme according to Ref. 29.
2. Evaluate the scaled proximal operator [10] of the regularization function in [12]:

$$\hat{\mathbf{p}}^{k+1} = \arg \min_{\mathbf{p} \in P^I} \left(\sum_{j=0}^{J-1} \gamma_j \left| \mathbf{A} \mathbf{p}_{\cdot,j} \right|_1 + \frac{1}{2} \sum_{i=0}^{I-1} \left(p_{i,\cdot} - y_{i,\cdot}^k \right) \mathbf{H}_i \left(p_{i,\cdot} - y_{i,\cdot}^k \right)^\top \right),$$

where $\mathbf{H}_i = (\lambda_i^k)^{-1} (\mathbf{I} + \lambda_i^k 2 \mathbf{J}_i^\top \sigma_i^{-2} \mathbf{J}_i)$, $\forall i$. (14)

The resulting functional [14] is minimized using the primal-dual algorithm [11]. After initialization of the starting point $\mathbf{u}^0 = \mathbf{y}^k$, $v_{\cdot,j}^0 = \gamma_j \mathbf{A} \mathbf{u}_{\cdot,j}^0$, $\forall j$, $\mathbf{x}^0 = \mathbf{u}^0$ and setting the constants $\tau, \theta; \sigma \leq \frac{1}{8\tau}$ {valid for the operator of forward differences [6]}, the algorithm iterates through the following steps:

- (a) Evaluate the proximal operator [11] of the convex conjugate of the regularization function in the form of $r(\mathbf{x}) = \|\mathbf{A} \mathbf{x}\|_1$. This is well known in image reconstruction problems and the required proximal operator of its convex conjugate gets the form of a projection onto unit ball²⁷:

$$v_{\cdot,j}^{n+1} = \frac{v_{\cdot,j}^n + \sigma \gamma_j \mathbf{A} x_{\cdot,j}^n}{\max \left(1, \left| v_{\cdot,j}^n + \sigma \gamma_j \mathbf{A} x_{\cdot,j}^n \right| \right)}, \forall j \quad (15)$$

that is, the vector field is in each point divided either by its magnitude or by unity.

- (b) Evaluate the proximal operator of a quadratic function [11]:

$$\mathbf{u}^{n+1} = \arg \min_{\mathbf{x}} \left(\frac{1}{2} \sum_{i=0}^{I-1} \left(x_{i,\cdot} - y_{i,\cdot}^k \right) \mathbf{H}_i \left(x_{i,\cdot} - y_{i,\cdot}^k \right)^\top + \sum_{i=0}^{I-1} \frac{1}{2\tau} \left(x_{i,\cdot} - u_{i,\cdot}^n + \tau \left(\gamma_j \mathbf{A}^* v_{\cdot,j}^{n+1} \right)_{i,\cdot} \right) \cdot \left(x_{i,\cdot} - u_{i,\cdot}^n + \tau \left(\gamma_j \mathbf{A}^* v_{\cdot,j}^{n+1} \right)_{i,\cdot} \right)^\top \right), \forall j \quad (16)$$

The optimizer of this quadratic form was derived as:

$$u_{i,\cdot}^{n+1} = (\tau \mathbf{H}_i + \mathbf{I})^{-1} \left(\tau \mathbf{H}_i y_{i,\cdot}^k + u_{i,\cdot}^n - \tau \left(\gamma_j \mathbf{A}^* v_{\cdot,j}^{n+1} \right)_{i,\cdot} \right), \quad \forall j, i,$$

where $(\cdot)_{i,\cdot}$ stands for the row i of the result of the parenthesized operation and \mathbf{A}^* is the adjoint operator [22].

- (c) Update estimate [11]:

$$\mathbf{x}^{n+1} = \mathbf{u}^{n+1} + \theta \left(\mathbf{u}^{n+1} - \mathbf{u}^n \right) \quad (17)$$

- (d) Repeat steps a), b), c) until convergence and then set:

$$\hat{\mathbf{p}}^{k+1} = \mathbf{x}^{n+1} \quad (18)$$

3. Repeat main steps 1), 2) until convergence.

3 | METHODS

3.1 | Experimental data

For the comparisons with the ground truth, we have designed a numerical DCE-MRI rat phantom. The phantom was based on a DCE-MRI examination of a real rat with implanted glioblastoma⁴⁶ (next paragraph). A high-resolution image (1024×1024 pixels) of an axial slice of head including the tumor was based on manual segmentation of a real DCE-MRI image sequence into 41 homogeneous regions (Figure 1). Each region was described by a set of perfusion parameters based on literature and on perfusion analysis results from Ref. 46. For each set of parameters, a concentration-time curve was generated using the TH model and a predefined AIF⁴⁷ in high temporal resolution (sampling period equal to repetition time, TR). The curves were converted to signal-intensity curves based on the acquisition model of the FLASH acquisition with no T_2^* effect and assuming a constant contrast-agent relaxivity r_1 and spatially invariant native relaxation time T_{10} and proton density. The signal intensity curves were used to construct a high-spatial-resolution image at each TR. These images, multiplied by coil sensitivities (estimated from real measurements), were then Fourier transformed to the k-space and echoes extracted as k-space lines corresponding to the acquisition scheme (next paragraph). Complex uncorrelated zero-mean Gaussian noise was added to obtain SNR according to real conditions (Figure 1). In addition to the dynamic DCE-MRI scans, multi-flip-angle pre-contrast scans were simulated. The simulated dynamic sequence was converted to the contrast-agent concentration using the pre-contrast images according to.⁴⁸

A real DCE-MRI recording of a glioblastoma-bearing rat was used as a testing preclinical dataset (detailed description in Ref. 46), acquired on a 7 T horizontal PharmaScan (Bruker Biospin, Germany) with a four-channel rat head surface coil using the FLASH acquisition: one 1mm slice, TR/TE 8/2.1 ms, FA 17°, acquisition matrix 128×128, temporal resolution 0.768 s, total scan time ~13 min. The contrast agent (Omniscan – GE Healthcare, Norway) of 0.1 mmol/kg was injected intravenously after 25 s of recording. The pre-contrast scans were acquired using the same parameters except for the FA (5°, 10°, 15°, 20°, 25°, 30°). These scans were used to convert the dynamic sequence to the contrast-agent concentration images.⁴⁸ The AIF was derived using multichannel blind deconvolution⁴⁹ as stated in the original paper.⁴⁶

A testing clinical dataset of a renal-cell-carcinoma-metastasis patient (details in Ref. 50) was acquired on a Magnetom Avanto 1.5 T MRI scanner (Siemens AG, Munich, Germany) using the T1-weighted 2D saturation-recovery prepared Turbo FLASH (nonselective SR pulse): TR/TE/TI 400/1.09/200 ms, FA 16°, acquisition matrix 128×128, temporal resolution 1.2 s, three coronal slices, total scan time 10 min.

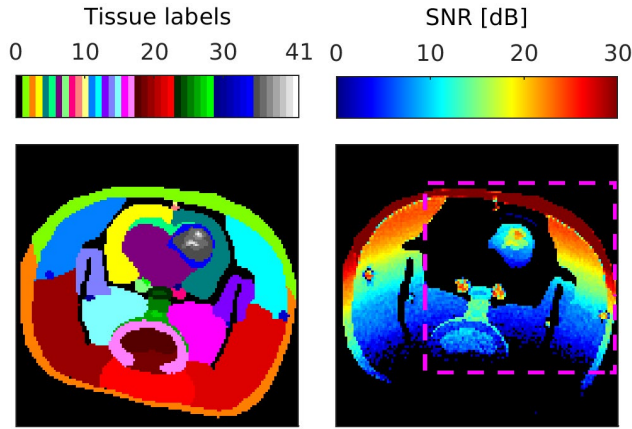


FIGURE 1 Numerical rat phantom: 41 different color-coded tissues (left) and the SNR induced to the phantom data by adding noise (right). The magenta rectangle shows the close-up used in Figure 2. SNR, signal-to-noise ratio

The contrast agent bolus of 7.5 ml (Gadovist – Bayer Schering Pharma, Berlin, Germany) was injected into antecubital vein. The pre-contrast scans acquisition preceded with the same parameters except TI (500, 1000, 3000 ms, five frames per each) to perform conversion to contrast-agent concentration.⁵¹ The AIF was estimated using multi-channel blind deconvolution.⁵⁰

3.2 | Initial setup

To keep the regularization weights unchanged across measurements and AIFs with different energies, the measured perfusion curves and the AIF were normalized by scalar constants α_{TRF} , α_{AIF} to obtain similar ratio of the data and regularization term values for any scenario. Additionally, we have separated relative weights γ'_j and the global weight Γ such that $\gamma_j = \Gamma \gamma'_j$. This extended the functional [12] to:

$$\hat{\mathbf{p}}' = \arg \min_{\mathbf{p}' \in P'} \sum_{i=0}^{I-1} \sigma_i^{-2} \sum_{n=0}^{N-1} \left(\alpha_{\text{TRF}}^{-1} S_{i,n}^{\phi} - \alpha_{\text{AIF}}^{-1} c(n\Delta t, p'_{i,\cdot}) \right)^2 + \Gamma N \sum_{j=0}^{J-1} \gamma'_j \left| \mathbf{A} p'_{\cdot,j} \right| \quad (19)$$

where α_{TRF} , α_{AIF} are estimated from the measured data and AIF using:

$$\alpha_{\text{TRF}} = \text{quantile}_{0.75} \left(\text{median} \left(S_{i,\cdot}^{\phi} \right), i=0, 1, \dots, I-1 \right), \quad (20)$$

$$\alpha_{\text{AIF}} = \text{median} \left(c_a(n\Delta t) \right)$$

The estimates are finally computed as: $\hat{\mathbf{p}} = \hat{\mathbf{p}}'$ except for $\hat{p}_{\cdot,1} = \alpha_{\text{TRF}} \alpha_{\text{AIF}}^{-1} \hat{p}'_{\cdot,1}$, since only the perfusion map F_p is influenced by the energy of the inputs. It is worth noting that the number of samples N was included in [19] to eliminate a possibly different number of time samples in the measured data S^{ϕ} .

The relative weights were estimated on the basis of the numerical phantom using the maximum likelihood approach,⁵²

that is, $\gamma''_j = I / \left\| \mathbf{A} p'_{\cdot,j} \right\|_1$, $\forall j$, transformed to $\gamma'_j = \gamma''_j / \sum \gamma''$, $\forall j$. The minimization was run from only one starting point based on the authors' experience and results in¹⁶ using the TH model. The relative weights, the starting point, as well as the constraints of the parameters are defined in Table 2. The estimates were projected onto the constraints P before any evaluation of the pharmacokinetic model throughout the iterative procedure.⁴⁴ This was done to ensure the respective physiological ranges and numerical stability. The stopping criterion in the main loop of the algorithm (proximal Levenberg-Marquardt) was set experimentally to 50 iterations and each subproblem (primal-dual) was stopped after 200 iterations. The estimates of noise standard deviations (σ_i , $\forall i$) were computed using the median of the absolute deviation estimator with the Daubechies wavelet.⁵³ The source code of the algorithm is available at: https://github.com/Bartolomejka/DCE-MRI_Regularization_MRM.

4 | RESULTS

4.1 | Strength of regularization

The goal of this numerical-phantom experiment was to analyze the influence of the global regularization weight Γ on the perfusion parameter estimates. The proposed algorithm was run for 16 values of Γ spread logarithmically from 10^{-3} to 10^2 . The results are shown in Figure 2 and Supporting Information Figures S1 and S2 as perfusion-parameter maps and in Figure 3 as the mean absolute error (MAE) for each perfusion parameter and as the mean, $\mu(\cdot)$, of the reduced chi-squared statistic, χ_{red}^2 , computed per voxel, which is related to the data-term value in [12]. The metrics were defined as:

$$\text{MAE}_j = \frac{1}{I} \sum_{i=0}^{I-1} \left| \hat{p}_{\cdot,j} - p_{\cdot,j}^* \right|$$

$$\chi_{\text{red}}^2 = \frac{1}{(N-J)} \left(\sigma_i^* \right)^{-2} \sum_{n=0}^{N-1} \left(S_{i,n}^{\phi} - c(n\Delta t, \hat{p}_{i,\cdot}) \right)^2 \quad (21)$$

where $p_{\cdot,j}^*$, $\forall j$ is the ground truth. The noise standard deviation σ_i^* , $\forall i$ was estimated using the ground truth. Additional metrics showing the bias and precision are plotted in Supporting Information Figure S3. The areas where the model is invalid or unstable, that is, bones (no signal), arteries (no extravascular space), brain tissue (no contrast-agent extravasation), and areas where $\text{SNR} < 5$ dB (areas far from surface coils), were excluded from the analysis.

When Γ increased, the MAE values (Figure 3) decreased until their minima, after which they started increasing, exhibiting an overregularization effect. The minima are achieved for $\Gamma = 0.22$, except for F_p , v_p , where the optimum is $\Gamma = 4.64$. The value $\Gamma = 0.22$ also corresponded to the best perfusion-parameter maps visually (Figure 2). The optimal value $\Gamma = 0.22$ was also consistent with the visual analysis of the bias and precision (Supporting Information Figure S3) for most perfusion parameters. Supporting Information Figure S3 shows that increasing

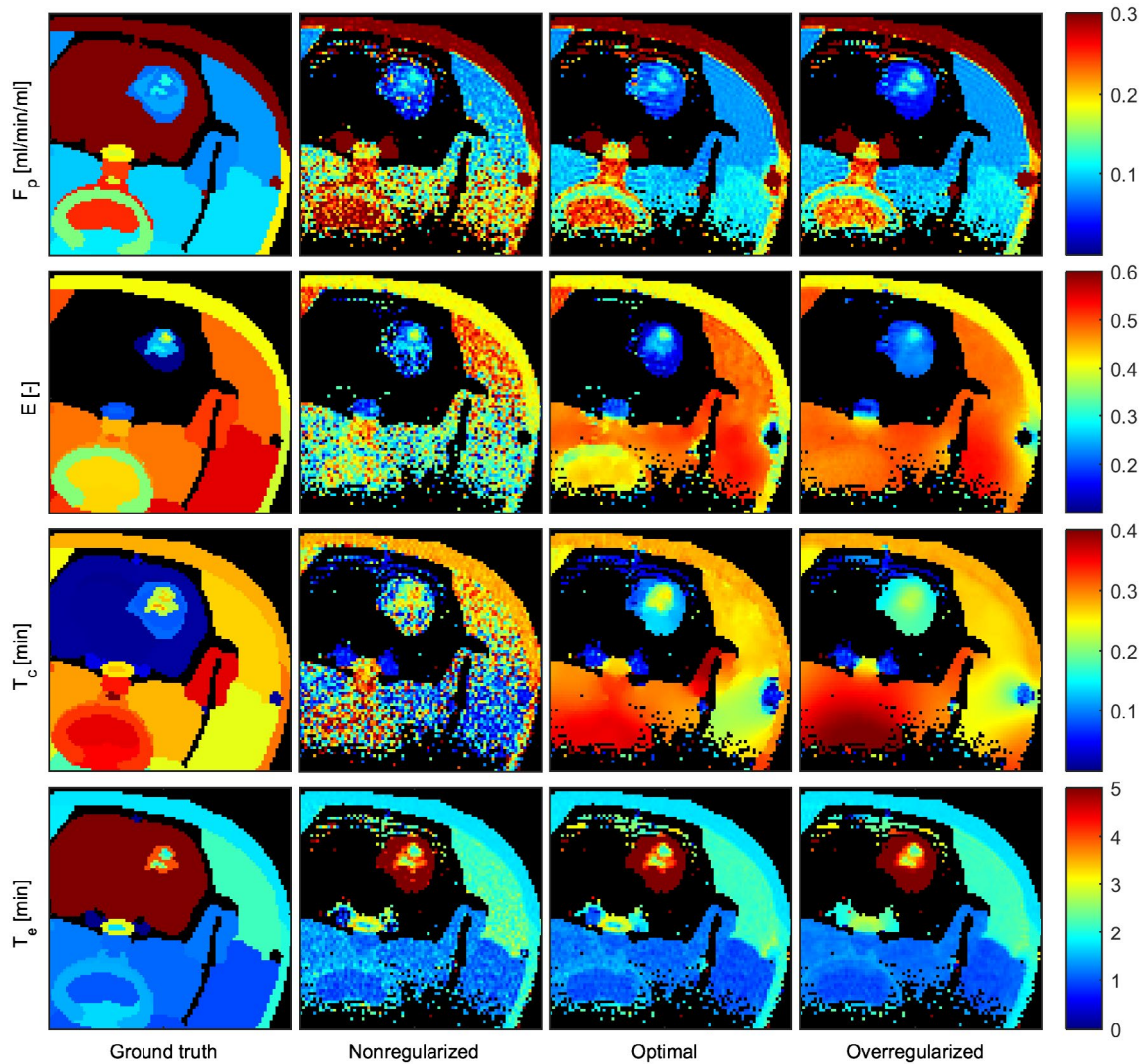


FIGURE 2 Effect of the regularization on perfusion parameters estimated from synthetic data in comparison with the ground truth. Only results for selected perfusion parameters and regularization weights are shown in a close-up defined in Figure 1. The black areas (e.g. brain tissue surrounding the tumor and areas far from the used surface coils) had $\text{SNR} < 0$ dB (cf. Figure 1) and were excluded from the computation. The closest MAE distance to GT for most of the parameters is obtained for $\Gamma = 0.22$ – column “Optimal” (cf. Figure 3). For $\Gamma = 2.2$ – column “Overregularized,” the maps are too smooth, causing loss of details. MAE, mean absolute error; SNR, signal-to-noise ratio

Γ could further improve precision but at the cost of increased bias. Mean absolute error shapes similar to ours were reported also in Ref. 22; however, in Ref. 22 the shape of the curve equivalent to our $\mu(\chi_{\text{red}}^2)$ (Figure 3) was similar to the MAE curves. This was not observed here. A probable explanation is that our pharmacokinetic model and minimizer are more robust in terms of local optima. Interestingly, $\mu(\chi_{\text{red}}^2) \approx 1$ for any Γ , meaning that the estimated concentration-time curves fitted the data well even for high regularization (cf. Supporting Information Figure S1 showing χ_{red}^2 per voxel).

4.2 | Bias and precision of the estimator

The proposed method (with fixed $\Gamma = 0.22$) was quantitatively compared to the standard nonregularized method (Table 3 – tumor tissues, Supporting Information Table S1 –

all tissues). The metrics used were the mean and the standard deviation of perfusion-parameter estimates within each simulated tissue region, representing the bias and precision of the estimator, respectively. They were estimated from a single numerical rat phantom dataset (i.e., one realization of noise). The proposed method performed the best for large tissue areas with low SNR, as expected. The nonregularized version led to slightly less biased or more precise estimates only in some small tissue areas or regions with high SNR.

We additionally tested the performance of the nonregularized and the proposed methods with the optimal setting (Section 4.1) on the numerical phantom for 50 noise realizations. To measure the bias and the precision of the estimators, the mean and the standard deviation of the perfusion-parameter estimates were computed for each voxel. Supporting Information Figure S4 (Mean) shows a distinct systematic difference between the

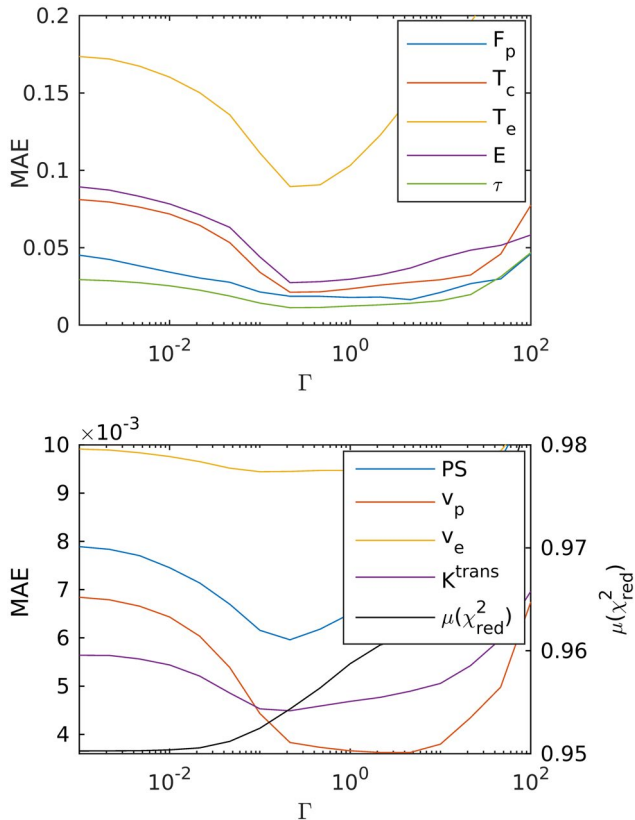


FIGURE 3 Effect of the regularization weight Γ on the distance of the parameter estimates from the ground truth (MAE) for the regularized parameters (top) and for the derived parameters (bottom – color curves). The effect of the regularization on the quality of fit represented by the mean of the reduced chi-squared statistic $\mu(\chi_{red}^2)$ is also shown (bottom – black line). MAE, mean absolute error

methods in the low-SNR areas, that is, a clearly lower bias of the regularized estimation. In addition, the standard deviation of the proposed estimator is lower (i.e. higher precision), leading to an improved readability of perfusion maps (cf. Figure 2 with Supporting Information Figure S4 – standard deviation, parameter F_p in tumor outer region).

To compare the two estimators quantitatively, we have again estimated their bias and precision per tissue (Supporting Information Table S2) by averaging their mean and standard deviation in Supporting Information Figure S4 within each simulated tissue region. In agreement with the evaluation based on a single noise realization, the proposed method enjoyed consistently better precision and in the majority of the cases also a lower bias (Supporting Information Table S2).

4.3 | Computational demands

To assess the time requirements of the proposed method, additional data from the experiment in Section 4.1 were analyzed. They included the number of evaluations of the pharmacokinetic model $c(nT_s, p'_i)$ for each voxel i and the total

duration of the minimization procedure measured on a 6-core Intel^R CoreTM i7-8700K CPU @ 3.70 GHz, implementation in Matlab without parallelization. The same was analyzed for the standard method without regularization; that is, the denoising step [14] was excluded. Additionally, the standard nonregularized method was accelerated by including a stopping criterion of a minimal change in its data term.

The proposed regularized perfusion analysis with $\Gamma = 0.22$ needed 36 min to finish in comparison with 20 min in the nonregularized case. The data consisted of 9916 curves, with 1000 time points each. The evaluation of the LM step [13] took 80% and the denoising step [14] took 15% of the total time in the proposed algorithm.

As the calculation of the pharmacokinetic model [4] was the most time-demanding operation, the distribution of the number of model evaluations in each pixel and their total count were analyzed (Figure 4). Theoretically, the number of model evaluations in the regularized method is at least twice the number of iterations times the number of the concentration-time curves, since recalculation of the gradients after each denoising step is needed. Contrarily, the nonregularized method can perform almost an arbitrary number of model evaluations, since the number of iterations is not fixed for particular curves. However, the regularized method does not need twice the nonregularized method model evaluations (black points in Figure 4). This means that the recomputations of the model and its derivatives inside one iteration to estimate the LM step length are reduced in the case of the regularized method. This stabilizing effect of the regularization is also visible in the distribution of the model evaluations in pixels (box plots in Figure 4). As the regularization grows, the numbers of model evaluations in each pixel reduce: that is, the pixels with problematic convergence are now converging better.

4.4 | Real datasets

The results of the experiments on real preclinical and clinical data are shown in Figures 5 and 6, respectively; data were acquired under the approval of an Institutional Review and Ethics Boards. In both cases, the number of outlier perfusion-parameter estimates was clearly reduced and the spatial correspondence of the maps to the underlying anatomy was substantially improved.

5 | DISCUSSION

The goal of this work was to improve the accuracy and precision of perfusion-parameter estimates in DCE-MRI. In the standard voxel-by-voxel approach, errors in the estimates are mainly caused by the presence of local minima of the curve-fitting problem and appear mainly in low-SNR conditions starting at approximately 13 dB (cf. Figure 1 – SNR,

TABLE 3 Quantitative comparison of the proposed TV with $\alpha = 0.22$ and nonregularized VW estimations with the GT numerical rat phantom evaluated statistically per tissue in tumor

Tissue ^a [label]	Area [voxels]	SNR ^b [dB]	Method	F_p [mL/mL/min]		T_c [min]		E [-]		v_p [mL/mL]		K^{trans} [mL/mL/min]		
				μ	σ	μ	σ	μ	σ	μ	σ	μ	σ	μ
41	1	23.0	GT	0.13	0.27	1.85	0.41	0.033	0.052					
			VW	0.12	0.24	1.95	0.39	0.029	0.047					
			TV	0.13	0.23	1.99	0.37	0.029	0.046					
39	5	22.1	GT	0.12	0.23	1.98	0.39	0.028	0.047					
			VW	0.12	0.01	0.27	0.03	0.09	0.38	0.02	0.032	0.001	0.046	0.002
			TV	0.13	0.00	0.25	0.01	2.12	0.09	0.36	0.02	0.031	0.001	0.046
37	7	20.9	GT	0.12	0.27	2.39	0.35	0.032	0.041					
			VW	0.11	0.02	0.27	0.04	0.26	0.34	0.04	0.028	0.004	0.037	0.007
			TV	0.11	0.01	0.24	0.01	2.52	0.32	0.03	0.028	0.004	0.037	0.007
40	4	18.4	GT	0.12	0.29	2.23	0.30	0.035	0.036					
			VW	0.12	0.01	0.26	0.04	0.20	0.28	0.03	0.030	0.002	0.033	0.003
			TV	0.12	0.01	0.24	0.01	2.45	0.26	0.01	0.030	0.001	0.033	0.003
38	8	17.2	GT	0.11	0.25	2.77	0.27	0.027	0.029					
			VW	0.11	0.02	0.25	0.04	0.30	0.26	0.02	0.026	0.002	0.028	0.003
			TV	0.11	0.01	0.23	0.01	2.95	0.31	0.25	0.01	0.026	0.002	0.028
36	57	15.4	GT	0.07	0.22	3.97	0.25	0.016	0.018					
			VW	0.08	0.02	0.22	0.05	0.54	0.25	0.04	0.017	0.004	0.019	0.004
			TV	0.08	0.01	0.20	0.03	0.50	0.24	0.03	0.016	0.004	0.019	0.004
35	116	8.7	GT	0.09	0.08	6.11	0.10	0.007	0.009					
			VW	0.07	0.06	0.16	0.09	1.52	0.18	0.09	0.008	0.003	0.009	0.002
			TV	0.07	0.03	0.12	0.02	5.88	0.15	0.03	0.008	0.003	0.009	0.002
34	97	7.2	GT	0.07	0.09	6.93	0.10	0.006	0.007					
			VW	0.07	0.07	0.16	0.08	1.91	0.16	0.09	0.007	0.003	0.007	0.002
			TV	0.06	0.02	0.11	0.02	6.37	0.12	0.05	0.007	0.002	0.007	0.002

Notes: Complete table can be found in Supporting Information Table S1. Bold values indicate lower bias or higher precision.

Abbreviations: μ , mean; σ , standard deviation; GT, ground truth; SNR, signal-to-noise ratio; TV, TV-regularized; VW, voxelwise.

^aPosition of the labels can be found in Figure 1.

^bMean SNR in the tissue.

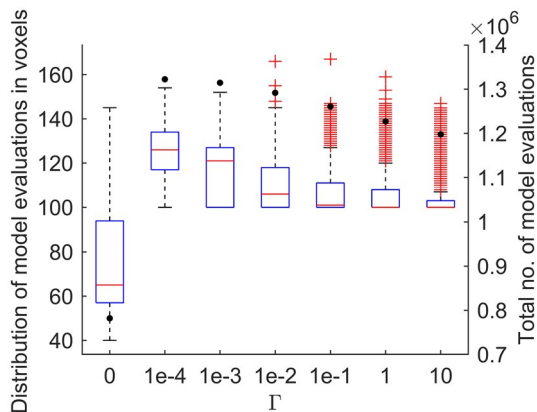


FIGURE 4 Distribution of the number of pharmacokinetic model evaluations in voxels shown in box plots together with the total number of function evaluations (black points) as a function of the regularization strength. $\Gamma=0$ stands for the standard nonregularized algorithm. The number of voxels was $I=9916$; the maximum number of iterations was 50

Figure 2 – Nonregularized). However, it can differ on the basis of tissue type. Erroneous estimates reduce the readability of the perfusion maps and their usability in practice. Not only is the estimation error in perfusion-parameter estimates random but the estimates are also biased, as was demonstrated in Supporting Information Figure S4 (Mean, Nonregularized).

Using spatial regularization, we were able to stabilize the estimates. The introduction of additional prior information led to a distinct improvement in the parameter estimates (Figure 2 or Supporting Information Figures S1 and S2 for $\Gamma=0.22$). The improvements were of two types: our method has improved the precision (i.e. reduced the variance of the estimates in homogeneous regions) and the readability of the parameter maps (e.g. Figure 2 – T_c map of the tumor), and it has reduced the bias of the estimates in areas with low SNR (see e.g. Figure 2 – bottom of the maps for F_p , E , T_c). These observations were supported by the quantitative evaluation of the bias and precision per tissue (Table 3 and Supporting Information Tables S1, S2).

In comparison with previous publications¹⁸⁻²⁴ our work was based on the TH model as a natural successor of the previously used simpler models. Our study showed that the increased complexity of the TH model can still be handled using spatial prior. In addition, as opposed to the relaxed ℓ^1 norm or ℓ^2 norm used by other groups, our prior is the total variation using exact ℓ^1 norm. This leads to a nondifferentiable criterion functional of the estimator. As was derived in the paper, application of the state-of-the-art minimization techniques, that is, proximal algorithms, solved this fundamental drawback efficiently.

In contrast to the previous spatially regularized DCE-MRI approaches, our spatial-regularization model [12] adjusts the strength of regularization automatically to the spatially

varying noise level. Hence, voxels with high noise level are regularized more than those with low noise level. To utilize this property, the standard deviations of noise in each voxel were estimated using an independent estimator⁵³ prior to the minimization. Alternatively, estimates from nonregularized curve fits similar to Ref. 22 can be used; this alternative method is more precise but time-consuming. A more challenging approach would be estimation of noise standard deviations for each time instant or formulating the problem using an exact noise distribution model. We assume a zero-mean Gaussian noise with spatial-variant standard deviation, which is not valid for low-SNR areas.

The method presented is an experimental method pushing the DCE-MRI limits utilizing the modern image processing techniques. The target application is preclinical DCE-MRI data processing, where strongly inhomogeneous coil sensitivities are causing dramatic reduction of SNR in areas distant from the coils. Similarly, the clinical datasets may suffer from insufficient SNR, for instance, in the case of 3D imaging. The target application of our minimizer is defined by the model used in the core of the algorithm, that is, the pharmacokinetic model. Its replacement by another pharmacokinetic model or a completely different model with a similar structure can solve nonlinear minimization problems with regularization in other applications, such as arterial spin labeling or diffusion tensor imaging.

Another aspect that deserves discussion is the regularization function used and its relation to the properties of the numerical rat phantom. We have used the total variation, which is a simple regularization function that favors piecewise-constant functions. In this way, we incorporated the assumption that tissues contain a small number of homogeneous regions with constant perfusion properties. To model real semihomogeneous tissues better, we could choose one of the more complex alternatives {by replacing the image gradients of the total variation \mathbf{A} in [6]}. These are for example the wavelet transform as in Ref. 24 favoring piecewise-polynomial functions or the total generalized variation⁵⁴ favoring piecewise linear functions. However, in our experience, the real-life difference between them is not large. What is important is to apply any regularization with a preference for piecewise-smooth functions, even a simple one.

Our numerical rat phantom contains several dozens of regions, where all the voxels have the same perfusion parameters. We are aware of the fact that this simplistic choice in a sense favors the regularization function used. We cannot solve this problem by using another regularization function, because all common functions favor piecewise constant functions. On the other hand, we are not aware of any good model to describe the change in perfusion parameters within the same tissue. Any ad hoc noise introduced into the parameters could influence the results in an unpredictable way. These considerations lead us to the nonideal but plausible choice of

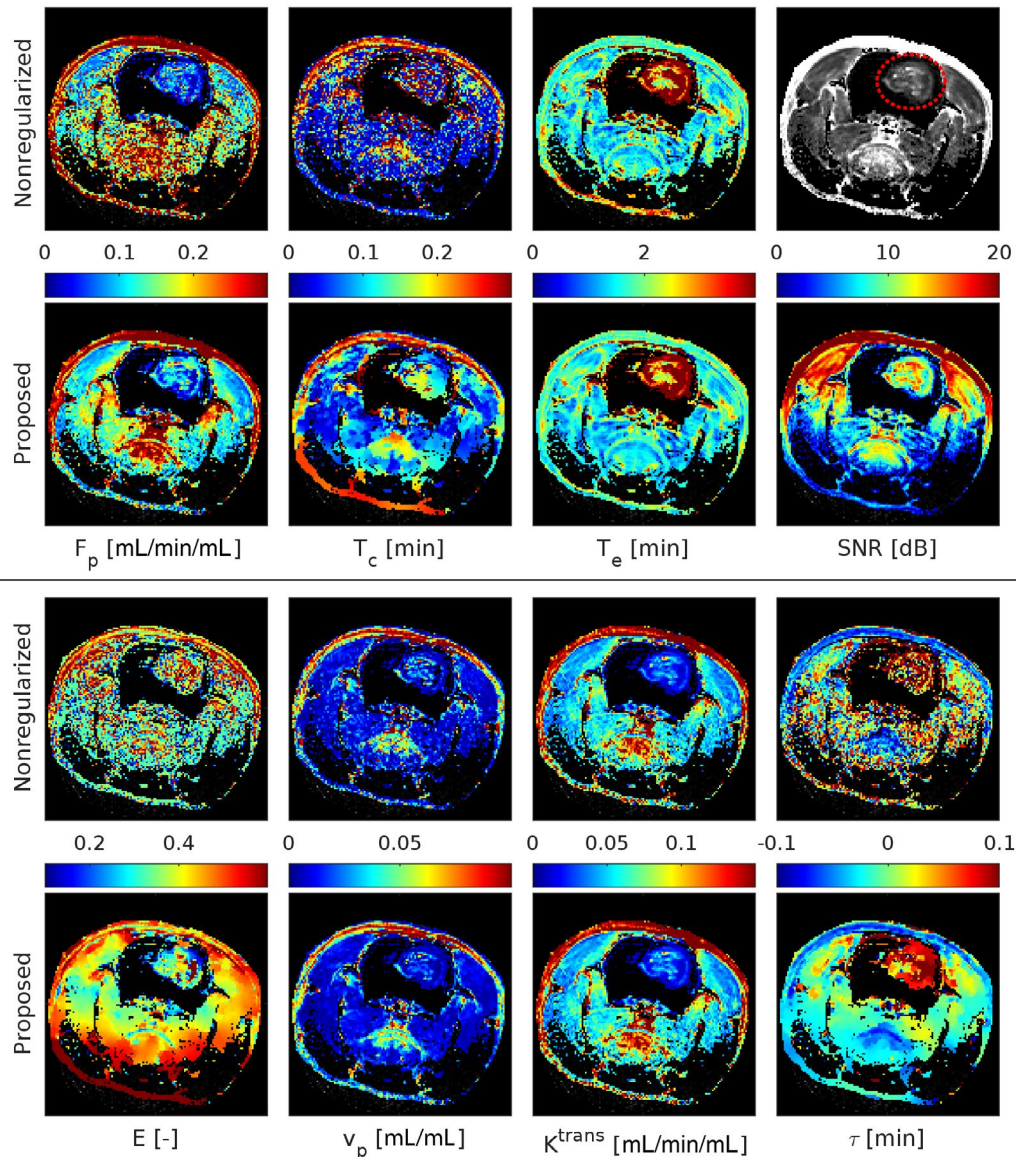


FIGURE 5 Preclinical data (rat brain with glioblastoma). Comparison of the perfusion parameter maps estimated without and with spatial regularization (top, bottom row in a group, respectively). The dotted circle in the anatomical image (top right) indicates the tumor. The final SNR map is shown only once since it was similar for both methods. The perfusion parameters were calculated only for curves satisfying $SNR > 0$ dB. SNR, signal-to-noise ratio

the total variation regularization and the simple numerical rat phantom with constant regions.

In general, to set up the regularization strength is challenging even for the standard problem when regularizing a single image. In the DCE-MRI, there are five perfusion-parameter maps to regularize simultaneously: that is, five regularization weights have to be set. The weights are not independent, since each of them affects the others via the pharmacokinetic model. If, for example, one perfusion-parameter map is forced to be too smooth (by setting its weight high), the estimates of the remaining perfusion parameters compensate for this effect to preserve a good fit in the data term. Thus their maps become uneven (data not shown but similar behavior is visible in Figure 2 or Supporting Information Figure S1, right column,

parameters F_p vs. E, T_c). Therefore, the weights must not take only the values of the perfusion parameters into account but also their interconnection through the data-term fitting.

We have approached the problem of setting the relative regularization weights by the maximum likelihood estimation on a realistic numerical phantom. The optimal global weight Γ was chosen on the basis of knowledge of the ground truth and the estimated perfusion parameters. We have applied these weights to the real dataset and obtained a substantial improvement of the spatial consistency between the perfusion-parameter maps and the anatomical images when compared to the nonregularized version. However, the accuracy improvement gained from the proposed spatial regularization is difficult to quantify for the real data

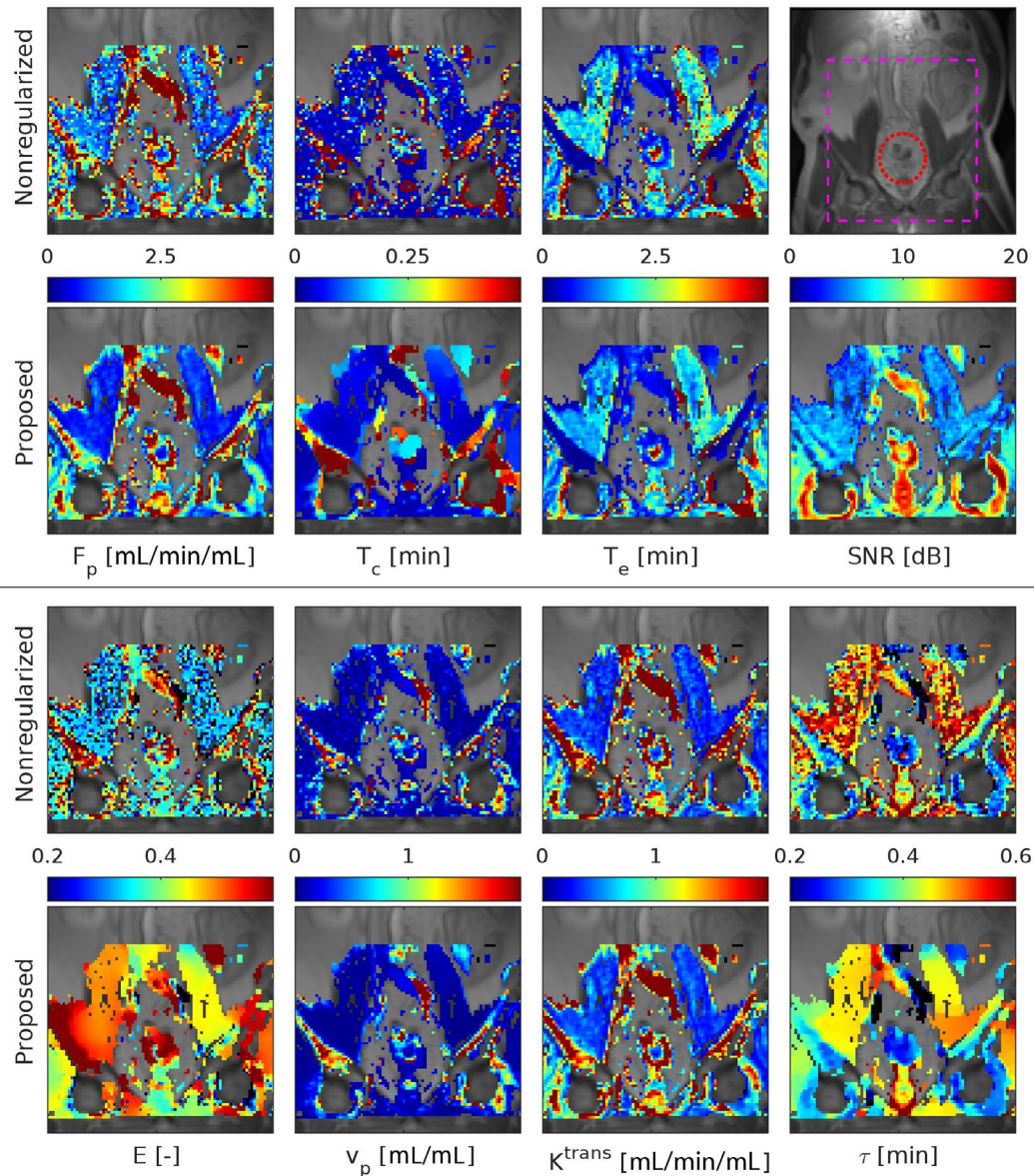


FIGURE 6 Clinical data (abdomen area with renal cell carcinoma metastasis). Comparison of the perfusion parameter maps estimated without and with spatial regularization (top, bottom row in a group, respectively). The dotted circle in the anatomical image (top right) indicates the tumor; the magenta rectangle indicates the close-up. The final SNR map is shown only once since it is similar for both methods. The perfusion parameters were calculated only for curves in a rectangular ROI satisfying $\text{SNR} > 0$ dB. ROI, region of interest; SNR, signal-to-noise ratio

where no ground truth is available. Since the proposed algorithm utilizes data normalization and an estimator of the noise variance based on the input data, it should not be necessary to change the global regularization weight Γ nor the relative regularization weights γ for new datasets. However, this beneficial property is difficult to test thoroughly and thus a slight modification of Γ can improve the estimates in new scenarios.

A related question is, which perfusion parameters should be spatially regularized. In this paper, the same parameters as the parameters of the pharmacokinetic model are regularized: T_c, T_e, α, τ (parameters independent of AIF and concentration-time curves scaling) and F_p (dependent

on scaling of the curves). This choice of the regularized parameters was also motivated by the fact that F_p, T_c, α are hard to estimate in comparison with the derived perfusion parameters such as $v_p, v_e, K^{\text{trans}}$. Despite the fact that the derived parameters were not regularized, their estimates were stable and robust to overregularization contrary to the regularized parameters; see perfusion-parameter maps of $v_p = F_p T_c$ and $K^{\text{trans}} = F_p E$ in Supporting Information Figures S1 and S2.

Although we have justified the set of parameters for regularization, it is not clear whether this set is equal to an optimal set of parameters to parametrize the model in the minimization, which influences convergence. In the

nonregularized case, the optimal parametrization was studied in Ref. 55 for the extended Tofts model, but in our work, the parameterization was not studied and the selection of the parameters was driven by the regularization and practical reasons.

6 | CONCLUSION

Incorporation of spatial prior information in terms of total variation helps to improve the estimates of perfusion parameters. This was clearly shown on realistically simulated data. Perfusion maps estimated from preclinical and clinical data showed a substantially better consistency with anatomical images than in the case of the traditional estimation with no spatial prior.

Our implementation of the spatial prior incorporates an additional image denoising step applied to the perfusion maps after each iteration of the voxelwise Levenberg-Marquardt algorithm. The time demands of the denoising step are negligible in comparison to the evaluation of the pharmacokinetic model and its gradients keeping the presented algorithm tractable. However, the algorithm needs more model evaluations than the nonregularized algorithm, because of the additional model evaluations after each denoising step and a missing smart stopping criterion.

ACKNOWLEDGMENT

This study was supported by the Czech Science Foundation (GA16-13830S); Ministry of Education, Youth and Sports of the Czech Republic (CZ.1.05/2.1.00/01.0017, LO1212, LO1401, CZ.02.1.01/0.0/0.0/16_013/0001775); and the Czech Academy of Sciences (MSM100751802). Infrastructure of the SIX Center was used. We would like to thank Michal Standara for providing the clinical data.

ORCID

Michal Bartoš  <https://orcid.org/0000-0003-4389-7703>

Olivier Keunen  <https://orcid.org/0000-0003-2203-7026>

REFERENCES

- Schabel MC, Parker DL. Uncertainty and bias in contrast concentration measurements using spoiled gradient echo pulse sequences. *Phys Med Biol*. 2008;53:2345–2373.
- Koh TS. On the a priori identifiability of the two-compartment distributed parameter model from residual tracer data acquired by dynamic contrast-enhanced imaging. *IEEE Trans Biomed Eng*. 2008;55:340–344.
- Brix G, Zwick S, Kiessling F, Griebel J. Pharmacokinetic analysis of tissue microcirculation using nested models: multimodel inference and parameter identifiability. *Med Phys*. 2009;36:2923–2933.
- Brix G, Salehi Ravesh M, Griebel J. Two-compartment modeling of tissue microcirculation revisited. *Med Phys*. 2017;44:1809–1822.
- Lopata RGP, Backes WH, van den Bosch PPJ, van Riel NAW. On the identifiability of pharmacokinetic parameters in dynamic contrast-enhanced imaging. *Magn Reson Med*. 2007;58:425–429.
- Henderson E, Rutt BK, Lee T-Y. Temporal sampling requirements for the tracer kinetics modeling of breast disease. *Magn Reson Imaging*. 1998;16:1057–1073.
- Aerts H, Jaspers K, Backes WH. The precision of pharmacokinetic parameters in dynamic contrast-enhanced magnetic resonance imaging: the effect of sampling frequency and duration. *Phys Med Biol*. 2011;56:5665–5678.
- Larsson C, Kleppesø M, Rasmussen I, et al. Sampling requirements in DCE-MRI based analysis of high grade gliomas: simulations and clinical results. *J Magn Reson Imaging*. 2013;37:818–829.
- Evelhoch JL. Key factors in the acquisition of contrast kinetic data for oncology. *J Magn Reson Imaging*. 1999;259:254–259.
- Kershaw LE, Cheng H-LM. Temporal resolution and SNR requirements for accurate DCE-MRI data analysis using the AATH model. *Magn Reson Med*. 2010;64:1772–1780.
- Bartoš M, Jiřík R, Kratochvíla J, Standara M, Starčuk Z, Taxt T. The precision of DCE-MRI using the tissue homogeneity model with continuous formulation of the perfusion parameters. *Magn Reson Imaging*. 2014;32:505–513.
- Garpebring A, Brynolfsson P, Yu J, et al. Uncertainty estimation in dynamic contrast-enhanced MRI. *Magn Reson Med*. 2013;69:992–1002.
- Dale BM, Jesberger JA, Lewin JS, Hillenbrand CM, Duerk JL. Determining and optimizing the precision of quantitative measurements of perfusion from dynamic contrast enhanced MRI. *J Magn Reson Imaging*. 2003;18:575–584.
- De Naeyer D, De Deene Y, Ceelen WP, Segers P, Verdonck P. Precision analysis of kinetic modelling estimates in dynamic contrast enhanced MRI. *MAGMA*. 2011;24:51–66.
- Koh TS, Cheong D, Hou Z. Issues of discontinuity in the impulse residue function for deconvolution analysis of dynamic contrast-enhanced MRI data. *Magn Reson Med*. 2011;66:886–892.
- Garpebring A, Östlund N, Karlsson M. A novel estimation method for physiological parameters in dynamic contrast-enhanced MRI: application of a distributed parameter model using Fourier-domain calculations. *IEEE Trans Med Imaging*. 2009;28:1375–1383.
- Bartoš M, Keunen O, Jiřík R, Bjerkvig R, Taxt T. Perfusion analysis of dynamic contrast enhanced magnetic resonance images using a fully continuous tissue homogeneity model with mean transit time dispersion and frequency domain estimation of the signal delay. In *Analysis of Biomedical Signals and Images*. Vol. 20. Brno, Czech Republic: Brno University of Technology; 2010:269–274.
- Sommer JC, Gertheiss J, Schmid VJ. Spatially regularized estimation for the analysis of dynamic contrast-enhanced magnetic resonance imaging data. *Stat Med*. 2014;33:1029–1041.
- Sommer JC, Schmid VJ. Spatial two-tissue compartment model for dynamic contrast-enhanced magnetic resonance imaging. *J R Stat Soc Ser C. (Applied Stat)*. 2014;63:695–713.
- Schmid VJ, Whitcher B, Padhani AR, Taylor NJ, Yang G-Z. Bayesian methods for pharmacokinetic models in dynamic contrast-enhanced magnetic resonance imaging. *IEEE Trans Med Imaging*. 2006;25:1627–1636.
- Feilke M, Bischl B, Schmid VJ, Gertheiss J. Boosting in nonlinear regression models with an application to DCE-MRI data. *Methods Inf Med*. 2016;55:31–41.

22. Kelm BM, Menze BH, Nix O, Zechmann CM, Hamprecht FA. Estimating kinetic parameter maps from dynamic contrast-enhanced MRI using spatial prior knowledge. *IEEE Trans Med Imaging*. 2009;28:1534–1547.
23. Yang W, Yu L, Lu Z, et al. Estimating pharmacokinetic parameter maps from breast DCE-MRI with implicit regularization by guided image filtering. IEEE 11th International Symposium on Biomedical Imaging (ISBI). *IEEE*. 2014;2014:878–881.
24. Guo Y, Lingala SG, Zhu Y, Lebel RM, Nayak KS. Direct estimation of tracer-kinetic parameter maps from highly undersampled brain dynamic contrast enhanced MRI. *Magn Reson Med*. 2017;78:1566–1578.
25. Parikh N, Boyd S. Proximal algorithms. *Found Trends Optim*. 2013;1:123–231.
26. Lee JD, Sun Y, Saunders MA. Proximal Newton-type methods for minimizing composite functions. *SIAM J Optim*. 2014;24:1420–1443.
27. Chambolle A, Pock T. A first-order primal-dual algorithm for convex problems with applications to imaging. *J Math Imaging Vis*. 2011;40:120–145.
28. Seber G, Wild CJ. *Nonlinear Regression (Wiley Series in Probability and Statistics)*. Hoboken, NJ: Wiley-Interscience; 2003.
29. Madsen K, Nielsen HB, Tingleff O. *Methods for Non-Linear Least Squares Problems*, 2nd ed. Lyngby: Informatics and Mathematical Modelling, Technical University of Denmark, DTU; 2004.
30. Ahearn TS, Staff R, Redpath T, Semple S. The use of the Levenberg-Marquardt curve-fitting algorithm in pharmacokinetic modelling of DCE-MRI data. *Phys Med Biol*. 2005;50:N85–N92.
31. Feilke M, Bischl B, Schmid VJ, Gertheiss J. Web-based appendix for boosting in nonlinear regression models with an application to DCE-MRI data: details on the optimization in the boosting algorithm. *Methods Inf Med*. 2016;55:31–41.
32. Tofts PS, Brix G, Buckley DL, et al. Estimating kinetic parameters from dynamic contrast-enhanced T1-weighted MRI of a diffusable tracer: Standardized quantities and symbols. *J Magn Reson Imaging*. 1999;10:223–232.
33. Sourbron SP, Buckley DL. Classic models for dynamic contrast-enhanced MRI. *NMR Biomed*. 2013;26:1004–1027.
34. Johnson JA, Wilson TA. A model for capillary exchange. *Am J Physiol Heart Circ Physiol*. 1966;210:1299–1303.
35. Baselice F, Ferraioli G, Pascasio V. Relaxation time estimation from complex magnetic resonance images. *Sensors*. 2010;10:3611–3625.
36. Nowak RD. Wavelet-based Rician noise removal for magnetic resonance imaging. *IEEE Trans Image Process*. 1999;8:1408–1419.
37. Gudbjartsson H, Patz S. The Rician distribution of noisy MRI data. *Magn Reson Med*. 1995;34:910–914.
38. Bartoš M, Šorel M, Jiřík R. Time-efficient Fourier domain evaluation of pharmacokinetic model in dynamic contrast-enhanced magnetic resonance imaging. *IFMBE Proc*. 2019;68:777–781.
39. Sourbron SP, Buckley DL. Tracer kinetic modelling in MRI: estimating perfusion and capillary permeability. *Phys Med Biol*. 2011;57:R1–R33.
40. Rudin LI, Osher S, Fatemi E. Nonlinear total variation based noise removal algorithms. *Phys D Nonlinear Phenom*. 1992;60:259–268.
41. Rajmic P, Novosadova M. On the limitation of convex optimization for sparse signal segmentation. *2016 39th Int Conf Telecommun Signal Process*. TSP 2016;2016:550–554.
42. Michel V, Gramfort A, Varoquaux G, Eger E, Thirion B. Total variation regularization for fMRI-based prediction of behaviour. *IEEE Trans Med Imaging*. 2011;30:1–12.
43. Rakotomamonjy A, Flamary R, Gasso G. DC proximal Newton for nonconvex optimization problems. *IEEE Trans Neural Networks Learn Syst*. 2016;27:636–647.
44. Salzo S, Villa S. Convergence analysis of a proximal Gauss-Newton method. *Comput Optim Appl*. 2012;53:557–589.
45. Maier O, Schoormans J, Schloegl M, et al. Rapid T1 quantification from high resolution 3D data with model-based reconstruction. *Magn Reson Med*. 2019;81:2072–2089.
46. Obad N, Espedal H, Jirik R, et al. Lack of functional normalisation of tumour vessels following anti-angiogenic therapy in glioblastoma. *J Cereb Blood Flow Metab*. 2018;38:1741–1753.
47. Jirik R, Soucek K, Mezl M, et al. Blind deconvolution in dynamic contrast-enhanced MRI and ultrasound. In 2014 36th Annual International Conference of the IEEE Engineering in Medicine and Biology Society. Vol. 2014. IEEE, 2014. pp. 4276–4279.
48. Li KL, Zhu XP, Waterton J, Jackson A. Improved 3D quantitative mapping of blood volume and endothelial permeability in brain tumors. *J Magn Reson Imaging*. 2000;12:347–357.
49. Taxt T, Jiřík R, Rygh CB, et al. Single-channel blind estimation of arterial input function and tissue impulse response in DCE-MRI. *IEEE Trans Biomed Eng*. 2012;59:1012–1021.
50. Kratochvíla J, Jiřík R, Bartoš M, Standara M, Starcuk Z, Taxt T. Distributed capillary adiabatic tissue homogeneity model in parametric multi-channel blind AIF estimation using DCE-MRI. *Magn Reson Med*. 2016;75:1355–1365.
51. Henderson E, Sykes J, Drost D, Weinmann H-J, Rutt BK, Lee T-Y. Simultaneous MRI measurement of blood flow, blood volume, and capillary permeability in mammary tumors using two different contrast agents. *J Magn Reson Imaging*. 2000;12:991–1003.
52. Šorel M, Bartoš M. Fast Bayesian JPEG decompression and denoising with tight frame priors. *IEEE Trans Image Process*. 2017;26:490–501.
53. Foi A. Noise estimation and removal in MR imaging: the variance-stabilization approach. In *Proceedings of the International Symposium on Biomedical Imaging*. 2011;1809–1814.
54. Bredies K, Holler M. A TGV-based framework for variational image decompression, zooming, and reconstruction. Part I: Analytics. *SIAM J Imaging Sci*. 2015;8:2814–2850.
55. Fusco R, Sansone M, Petrillo M, Petrillo A. Influence of parameterization on tracer kinetic modeling in DCE-MRI. *J Med Biol Eng*. 2014;34:157–163.

SUPPORTING INFORMATION

Additional supporting information may be found online in the Supporting Information section at the end of the article.

FIGURE S1 Effect of the global regularization weight Γ on perfusion parameters estimated from the numerical rat phantom in comparison with the ground truth (GT). Estimates of the regularized perfusion parameters and the reduced χ^2 metric are shown for selected regularization weights. The location of the used close-up is defined in Figure 1

FIGURE S2 Effect of the global regularization weight Γ on perfusion parameters estimated from the numerical rat phantom in comparison with the ground truth (GT). Estimates of the derived perfusion parameters and for selected regularization weights are shown in a close-up defined in Figure 1

FIGURE S3 Simulated data, effect of the regularization weight Γ on the bias (estimated within a tissue) averaged using its absolute value over all tissues (left column) for the regularized parameters (top) and for the derived parameters (bottom). Similarly, the mean of tissue standard deviations is shown (measure of precision – right column). In the formulas, \mathbf{K} , k relate to tissue indices and \mathbf{N} , n relate to indices of voxels inside the tissues

FIGURE S4 Effect of the regularization (Proposed, $\Gamma = 0.22$) on the mean and standard deviation of the perfusion-parameter estimates from 50 noise realizations of the numerical rat phantom in comparison with the ground truth (GT)

TABLE S1 Quantitative comparison of the proposed TV and nonregularized VW estimations from a single noise realization with the ground truth of the numerical rat phantom

TABLE S2 Statistical quantitative comparison of the proposed TV and nonregularized VW estimations from 50 noise realizations with the ground truth of the numerical rat phantom

How to cite this article: Bartoš M, Rajmic P, Šorel M, Mangová M, Keunen O, Jiřík R. Spatially regularized estimation of the tissue homogeneity model parameters in DCE-MRI using proximal minimization. *Magn Reson Med.* 2019;82:2257–2272. <https://doi.org/10.1002/mrm.27874>

APPENDIX A

A1. ADJOINT OPERATOR OF THE IMAGE GRADIENT

The adjoint operator \mathbf{A}^* , required in the primal-dual algorithm, for the image gradient has the form of a negative discrete divergence:²⁷

$$\mathbf{A}^* \begin{pmatrix} \mathbf{X}_1 \\ \mathbf{X}_2 \end{pmatrix} = \nabla_r^\top \mathbf{X}_1 + \nabla_c^\top \mathbf{X}_2 = -\text{div} \begin{pmatrix} \mathbf{X}_1 \\ \mathbf{X}_2 \end{pmatrix}, \quad (\text{A1})$$

where \mathbf{X}_1 , \mathbf{X}_2 are respective components of the vector field with size equivalent to the result of the gradient operator in [6]. The divergence takes the position of the voxels in the image into account.⁴²